

DOCTORAL THESIS

Intra- and Extracellular chips for cell mechanics

Author:

María Isabel Arjona Hidalgo

Under the supervision of:

Prof. José Antonio Plaza Plaza

*A thesis submitted in fulfillment of the requirements
for the degree of Doctor of Philosophy in the*

Programa de Doctorado en Física y Ciencias del Espacio



**UNIVERSIDAD
DE GRANADA**

with university tutor:

Prof. Salvador Rodríguez Bolívar

Departamento de Electrónica y Tecnología de Computadores



February 25, 2021

Editor: Universidad de Granada. Tesis Doctorales
Autor: Arjona Hidalgo, María Isabel
ISBN: 978-84-1306-835-0
URI: <http://hdl.handle.net/10481/68002>

Agradecimientos

Ahora que ya están escritas todas las páginas de esta tesis, tengo que enfrentarme de nuevo a un folio en blanco. Mi primera reflexión es sobre el talento. Uno puede tener o no talento para conseguir lo que se proponga, pero no se nace sabiendo. Es por eso por lo que estoy agradecida a todas las personas que me han enseñado algo, en la vida en general, y en mi carrera científica, en particular, porque definitivamente yo no nací sabiendo sobre dispositivos de silicio intracelulares. Por eso, pienso en todo lo que quiero dejar escrito con la mirada puesta en el transcurso de estos años, y en cómo, las decisiones que he ido tomando a lo largo de la vida me han llevado a cruzarme con personas que han marcado mi destino.

Cuando empecé, hace ya cinco años, lo único que sabía con claridad era quién era una de estas personas. Sin duda, llegar hasta donde estoy nunca habría sido posible sin la confianza que ha tenido en mí Francisco Manuel Gómez-Campos. Admiro tu entusiasmo, tu dedicación, tu pasión por enseñar; eres la mejor definición de la palabra profesor. Gracias Francisco. Esta tesis tiene sus raíces en todo lo que tú me has enseñado, porque has sido la persona decisiva en el inicio de mi carrera científica. Siempre, siempre te estaré agradecida. Gracias también a Salvador Rodríguez Bolívar, por darme su tiempo y darme la oportunidad de poder aprender de él.

Cuando en 2016 me uní al grupo de Micro- y NanoTooLs (MNTL) en el Instituto de Microelectrónica de Barcelona (IMB-CNM, CSIC), todo eran caras nuevas, solamente reconocía a dos personas, José Antonio Plaza y Marta Duch. Hoy el grupo MNTL es familia, amigos y compañeros de trabajo, junto a un gran número de personas del IMB-CNM, ya siempre van a formar parte de mi trayectoria personal y profesional. Gracias José Antonio, por todo. Gracias por elegirme, por creer en mí, por enseñarme, por apoyarme siempre, por animarme a avanzar y a lanzarme con seguridad a tantas cosas en las que me sentía insegura. Eres el mejor director de tesis que podría haber soñado y una de las mejores personas que he conocido. ¡Qué suerte he tenido! En el grupo he encontrado mi lugar en la investigación, gracias por hacerme partícipe, espero que podamos seguir compartiendo la ciencia y la vida mucho tiempo más. Gracias a ti también, Marta. Me has enseñado todo sobre el mundo de la microfabricación. Me has ayudado y dedicado tu tiempo con la alegría y el entusiasmo con el que lo haces todo. Gracias también por los momentos de amistad que hemos compartido. Te admiro en mucho, eres una gran profesional y una gran persona. Eres mi referente en la ciencia, me gustaría llegar a ser como tú eres.

En el grupo MNTL, somos pocos, pero es un grupo grande por la calidad de las personas que lo componen. Juan Pablo Aguil, es una de esas personas. Gracias Juan Pablo, por ser mi hermano mayor en la vida científica. Siempre has sido un apoyo para mí, escuchando mis frustraciones y animándome a seguir. Me has enseñado tantas cosas en el laboratorio, que casi me convierto en química. Gracias también a Jaume Esteve, porque siempre se ha interesado y preocupado por cómo avanzaba mi trabajo. Pero para mí,

el grupo no acaba aquí, porque hay un electrón desapareado al que tengo mucho que agradecer. Mi chica de los grabados, Ana Sánchez, sin tu ayuda no existirían la mitad de los dispositivos que hay en esta tesis, ni otros que no aparecen. Gracias por las horas de EBL, de FIB y de SEM, en las que trabajamos y nos poníamos al día de tantas cosas. Gracias por compartir junto a mí tantos dolores de cabeza en la fabricación de nuestro maravilloso sensor de presión. He aprendido mucho de ti, de tu inteligencia y serenidad a la hora de enfrentar los percances que iban surgiendo. Gracias Ana, por enseñarme siempre y por tus consejos en momentos de desilusión. También quiero agradecer a personas que formaron parte del grupo MTNL, y que, de algún u otro modo, han contribuido en el desarrollo de esta tesis. Gracias a Rodrigo Gómez-Martínez, por su ayuda con el sensor de presión, a Sara Durán, por esas charlas de tesis llenas de consejos, a Carolina Vargas, por todas nuestras conversaciones de despacho y a Núria Torras, por los excels embrionarios, porque siempre has encontrado un hueco para ayudarme, has sido muy generosa conmigo. Gracias, porque esta tesis está aquí por vuestro trabajo previo.

En el IMB-CNM tengo la suerte de formar parte de otro grupo, el Grupo Tupper. La ciencia es importante, pero todos sabemos lo relevantes que son las cosas del comer. Gracias a todos los miembros de este selecto grupo, Juan Pablo A., Juan Pablo E., Marta, Alberto, Neus, Nuria, Ana, Leyre, Xavi y Carlos. Espero que esta pandemia pase pronto y podamos recuperar nuestras rutinas culinarias, nuestro confesionario cafetil y las salidas gastronómicas en las que tendremos que brindar por todas las celebraciones pendientes. Nuria Torres, gracias por invitarme al mundo de la costura del que ahora ya no puedo salir. Gracias por todo lo que me has ayudado y enseñado, por las pruebas de grabado de óxido, de decapado de resina, por los ánimos con la tesis, y por hacer de mensajera en tiempos COVID. Eres una de las personas más trabajadoras que conozco. Gracias a ti también, Leyre, siempre me has transmitido una comprensión y conexión muy especial. Gracias Eli Prats, un placer compartir contigo los trayectos al trabajo, ojalá vuelvan pronto. Me gustó mucho vivir la experiencia Agustina contigo, de la que tanto disfrutamos y de la que tanto aprendí.

Gracias a todos los miembros del IMB-CNM: administración, conserjería, mantenimiento, informática, biblioteca, D+T, personal investigador y personal de la Sala Blanca, porque todos habéis aportado en el desarrollo de este trabajo.

Gracias al Centro de Investigaciones Biológicas-Margarita Salas (CIB, CSI C), por acogerme como una más en todas mis estancias en el Laboratorio 3D. Gracias a todos sus miembros, a Enrique de la Rosa, Flora de Pablo, Teresa Suárez, Mariano Redondo, Patricia Vázquez, Consuelo González y Alberto Hernández. He aprendido mucha biología en estos años gracias a vosotros. Gracias también a Maite y Gema, del servicio de Microscopía Láser Confocal y Multidimensional in vivo, por vuestro cariño y trabajo tan profesional. En especial, me gustaría dar las gracias a Teresa Suárez. Gracias por hacer que me interese tanto la biología, por enseñarme absolutamente todo lo que

sé de células, por estar siempre dispuesta a hacer una probatina más, por los paseos por Madrid, por acogerme y cuidarme siempre y por compartir conmigo tantas cosas. Qué alegría haberte encontrado en este camino, que espero que sigamos recorriendo juntas mucho tiempo más.

A Llüisa Pérez y Elvira Gómez, de la Universitat de Barcelona, por todo lo que me habéis enseñado sobre el desarrollo de algunos procesos químicos. A Rafael Pérez del Real, del Instituto de Ciencia de Materiales de Madrid (ICMM, CSIC), por acercarme a otras ramas de la física con las caracterizaciones magnéticas, de manera divertida y didáctica. Gracias a Roberto Castilla, de la Universidad Politécnica de Cataluña (UPC), por su implicación en los análisis viscoelásticos. Gracias a Jon Molina Aldareguia y a Miguel Monclús, de IMDEA, por las caracterizaciones mecánicas, por recibirme tan bien y estar dispuestos a trabajar con nuestros dispositivos. I also want to thank Tony Perry and Maki Asami, from University of Bath, for allowing me to participate in such relevant work and teaching me so much about embryos. We have some English or Spanish celebration beers pending.

A Mijal y Laura, gracias por vuestro apoyo, ahora os toca a vosotras. Gracias Mijal, por compartir tantos momentos conmigo, por ser amiga y compi de piso a la vez. A mis Techumbres, gracias Vane, María del Mar, Nati, Bea y Analú, por estar desde el minuto cero, por nuestros viajes que ahora se han convertido en videollamadas, por la amistad. Gracias Analú, por compartir conmigo tantos momentos para el recuerdo en Barcelona, y otros que quizás no recordemos; gracias por estar siempre, amiga. Gracias a todos mis amigos fiZicos de Granada, a pesar del espacio-tiempo encontramos un lugar y momento en el mundo para encontrarnos. Gracias a Alfonso, Cuchi, Pablo, Javi y Berni. Y a las niñas del Canal Cotilleo, gracias por todos estos años, Nuri, Alba, Hiren, Gema, Marta, Bea, Yeye, Marisol y Ester, no sabéis lo importantes que sois para mí. Y especialmente a ti, Rebe, mi amiga, mi parte complementaria, que ahora estás a años luz y no verás este final, pero al menos pudimos vivir, reír y bailar juntas durante el desarrollo. Gracias por haber estado. Volveremos a bailar y reír.

Quiero agradecer a toda mi familia, en especial a mi madre, Reme, por su apoyo durante todo el recorrido de esta tesis y el de toda la vida, por enseñarme a luchar por lo que uno quiere y por poner a mi alcance lo necesario para llegar a donde estoy. Mis logros son sus logros. A mis hermanas, Ana y María, que a pesar de la distancia siempre están cerca. Siempre haciendo planes de reencuentros divertidos, viajes, celebraciones y sorpresas, y siempre apoyándome. A mis tíos y a mis tías, por sus llamadas, sus consejos y su confianza. No podría tener una familia mejor. A ti, papá, porque esto también es gracias a ti, aunque no puedas vivirlo. Y a mi familia Colombano-Sosa, Mónica, Luis, Renzo, Flavia y Mica, gracias por vuestro apoyo y estar siempre ahí.

Y a ti Martín, que siempre confiaste más en mí que yo misma. Por estar incondicionalmente y animarme a comenzar esta etapa tan bonita que hemos recorrido juntos. Porque tú también eres mi Constante.

Financial Support

The investigation within this doctoral thesis has been financed by the Spanish Government through a pre-doctoral grant *Ayuda para la Formación de Personal Investigador* (FPI) with reference BES-2015-075932. Moreover, the investigation has been sustained by the financial support of the projects TEC2014-51940-C2-1-R (MINAHE5) and TEC2017-85059-C3-1-R (MINAHE6) of the *Ministerio de Economía y Competitividad* of the Spanish Government with Feder funding. This author also appreciates the resources provided from the *Instituto de Microelectrónica de Barcelona* (IMB-CNM, CSIC) Clean Room facilities in the development of her doctoral thesis.

Abstract

The *Micro- and NanoTools* group, as a worldwide pioneer in the development of silicon-based suspended chips, has previously enabled the development of micro- and nanodevices small enough to be internalized by living cells. Passive devices, as barcodes, or active devices as biochemical sensors, electrical stimulators or nanomechanical sensors have been developed for *chip-in-a-cell* and *chip-on-a-cell* applications. From the previous achievement of developing and testing an intracellular pressure sensor, motivated by the mechanical analysis of cells, a new line was opened within the group covering one of the most promising current research hot-topic in cell biology: **Cell Mechanics**.

This thesis has been focused on the development of innovative tools to explore cellular mechanical properties from inside and outside the cell. This development consisted in the design, fabrication, characterization, mechanical simulation and biological validation of micro- and nanodevices.

Chips were fabricated with the required design using micro and nanofabrication processes based on silicon technologies. Hence, these technologies allow the development of tools with functional parts at the micro- and nanometer scale. The mechanical behaviour of these devices was analysed by finite element method simulations, and was compared with an experimental mechanical characterization of fabricated samples. The biological application of the devices is presented as a final step in most of the tools developed on this thesis, with the analysis of their biocompatibility as a mandatory study.

Here, we have demonstrated the integration of multiple functionalities within a single chip. To accomplish this, intracellular magnetic biocompatible barcodes were developed enabling both, the labelling, and the magnetic mechanical-manipulation of living cells. Moreover, the second generation of an intracellular pressure sensor has been designed and fabricated through the advances of the technological development of the sealing of a cavity at room temperature and atmospheric pressure to reach millibar sensitivities. Furthermore, the mechanical characterization of the cytoplasm in mouse one-cell embryo development has been accomplished through the use of an intracellular nanodevice, being the basis for the development of new intracellular tools for mechanical sensing within eukaryotic cells. Finally, an extracellular system based on the mechanical failure of silicon chips anchored to the substrate has been designed, fabricated, characterized and validated as a tool for the sensing of cell ultimate traction forces. Overall, the obtained results highlight the reliability of the silicon micro- and nanotechnologies for the fabrication of mechanical chips for and at the scale of living cells.

Contents

Declaration of Authorship	iii
Agradecimientos	v
Financial Support	ix
Abstract	xi
Contents	xiii
List of Figures	xvii
List of Tables	xxiii
1 General introduction	1
1.1 Introduction	2
1.2 General objectives	4
1.3 Chapters overview	4
Bibliography	6
2 Magnetic barcodes development for labelling and magnetic mechanical-manipulation	9
2.1 Introduction	10
2.2 Previous background of the group on CoNi barcodes	11
2.2.1 Design of the magnetic barcodes	12
2.2.2 Fabrication of the inverted barcode pattern	13
2.2.3 Fabrication of the CoNi barcodes	13
2.2.4 Etching of the sacrificial and seed layers to release the CoNi barcodes	14
2.3 CoNi-based barcodes	16
2.3.1 Alternative releasing method	16
2.3.2 Characterization of the CoNi barcodes	17
2.3.3 Biological validation of the CoNi barcodes	19
2.3.4 CoNi barcode encapsulation through a gold covering layer	20
2.3.5 Biological validation of Au-encapsulated CoNi barcodes	22
2.4 Toxicity analysis of the CoNi and Ni compounds through substrates for cell seeding	22

2.5	Ni-based barcodes	24
2.5.1	Fabrication of the Ni barcodes	24
2.5.2	Characterization of the Ni barcodes	24
2.5.3	Biological validation of the Ni barcodes	26
2.6	Ni-based barcodes for cell labelling and magnetic mechanical-manipulation	26
2.6.1	Ni magnetic barcodes for cell labelling	26
2.6.2	Characterization of the magnet for the magnetic set-up	27
2.6.3	Cell magnetic manipulation	28
2.7	Discussion	31
	Bibliography	33
3	Second generation of an intracellular pressure sensor with high sensibility and a reference cavity	39
3.1	Introduction	40
3.1.1	Previous background of the group	41
3.2	Design proposal for a more sensitive cavity	44
3.3	Mechanical analysis of the pressure sensor	46
3.4	Optical analysis of the pressure sensor	48
3.5	Technological development for the fabrication of a sealed cavity	52
3.5.1	Development of a thin-nongrainy polysilicon layer	53
3.5.2	Fabrication of the pressure sensor devices	54
3.5.3	Cavity sealing development for the tightness of the pressure sensors	57
3.5.4	Summary of the complete fabrication process of the pressure sensors with polyimide cap for sealing the cavities	67
3.5.5	Releasing of the pressure sensors	69
3.6	Preliminary characterization and validation of the first devices	70
3.6.1	Morphological characterization of the fabricated devices	70
3.6.2	Validation of the pressure sensor operation principle by bright-field optical microscopy	71
3.7	Discussion	76
	Bibliography	78
4	H-comb polysilicon devices for tracking intracellular forces and mechanical property changes in mouse one-cell embryo development	81
4.1	Introduction	83
4.2	Design and operational principle of the mechanical sensor	84
4.3	Technological development for the fabrication process of the H-comb mechanical sensors	87
4.3.1	Fabrication steps of the H-comb mechanical sensors	87
4.3.2	Reproducibility of nanodevice dimensions	88
4.4	Theoretical and numerical analysis of the device through FEM simulations	91
4.4.1	Determination of the Young's modulus for the theoretical analysis	91

4.4.2	Calculation of the devices sensitivity by Finite Element Method	96
4.4.3	Simulation analysis of an initial curvature of the nanodevices.	97
4.4.4	Effects of geometrical and material property errors on device sensitivity	99
4.5	H-comb deflection measure within mouse one-cell embryos for cytoplasm mechanical characterization	101
4.5.1	From device bending measurements to the mechanical description of the cytoplasm behaviour	101
4.5.2	Device bending limitation under experimental conditions	104
4.5.3	Development of optical structures for the calculation of the device bending limitation	107
4.5.4	Measure limitation inside embryos due to optical noise	109
4.6	Normal embryo development injected with H-comb nanodevices	112
4.7	Detailed analysis of the mouse one-cell embryo development stages	113
4.7.1	SDR-phase. Major mechanical activity during paternal genome reprogramming	113
4.7.2	PM-phase. Membrane ruffling detected close to the embryo center	114
4.7.3	PEB-phase. Low cytoplasmic mechanical activity during spindle formation	117
4.7.4	EL-phase. Cytoplasmic stiffening governs embryo elongation	117
4.7.5	DIV-phase. Cytoplasmic softening and the largest forces during division	119
4.8	Experimental perturbation of the mouse cytoplasm mechanical program	120
4.9	Suspended intracellular devices developed for mechanical actuation inside eukaryotic living cells	122
4.10	Discussion	126
	Bibliography	128
5	Anchored silicon chips for cell traction forces determination	133
5.1	Introduction	134
5.2	Electron Beam lithography patterning for a PDMS-based cell TFM	136
5.2.1	Design of a patterned substrate as a TFM	136
5.2.2	Technological development for the fabrication of a periodically-spaced dots substrate	137
5.2.3	Characterization of the TFM	140
5.3	Design of the silicon-pillars platforms	144
5.4	Technological development of a narrow anchor for the fabrication of high sensitive mechanical silicon-based platforms	148

5.5	Physical characterization of the silicon standing nanopillar chips	151
5.6	Mechanical experimental characterization and simulation analysis for the determination of the fracture force of the nanopillars	155
5.6.1	Preliminary nano-indentation analysis of pillars fracture	156
5.6.2	Theoretical analysis of the mechanical performance through FEM simulations	159
5.7	Biological application: preliminary results of the cell force measurements	162
5.8	Discussion	170
	Bibliography	172
6	General conclusions and perspectives	177
	Bibliography	182
7	Resumen en Español	183
7.1	Introducción	184
7.2	Objetivos generales	186
7.3	Descripción general de los capítulos	187
7.4	Conclusiones y perspectivas	188
	Bibliography	193
	Collaborations and Stays in Research Institutions	197
	Scientific Contribution	199
	Scientific Dissemination	203

List of Figures

2.1	Designed barcodes	12
2.2	Fabrication of the inverted pattern	13
2.3	Fabrication of the CoNi barcodes	14
2.4	Releasing of the CoNi barcodes by the wet etching of the sacrificial layer	15
2.5	Suspended CoNi barcodes after wet etching	15
2.6	Fabricated CoNi barcodes before their releasing	16
2.7	Current release of the CoNi barcodes	17
2.8	CoNi barcodes after new releasing	18
2.9	Characterization of the fabricated CoNi barcodes	18
2.10	Released CoNi-Au-1 barcodes	20
2.11	Released CoNi-Au-2 barcodes	21
2.12	EDXS characterization of CoNi-Au barcodes	21
2.13	Biological validation CoNi-Au barcodes	22
2.14	CoNi and Ni substrates for cell toxicity analysis	23
2.15	Released Ni barcodes	25
2.16	Ni barcodes: physical and magnetic characterization	25
2.17	Biological validation of Ni barcodes co-cultured with HeLa cells	26
2.18	HeLa cell labelling and tracking by Ni barcodes	27
2.19	Characterization of the magnet for the magnetic set-up for cell manipulation	27
2.20	Magnetic manipulation of HeLa cells with internalized Ni barcodes	28
2.21	HeLa cells 4 days after magnetic manipulation using Ni barcodes	29
3.1	Cover of the publication of the previous IPS	41
3.2	Schematic of the device parts	41
3.3	Device dimensions	42
3.4	Schematics of the operational mode of the IPS	42
3.5	Fabricated devices	43
3.6	Measured reflected intensities through the pressure sensor in different environments versus an applied pressure	43
3.7	Scheme of the second-generation designed devices	44
3.8	Dimensions of the second-generation designed sensor	45
3.9	Schematics of the operational mode of the second-generation sensor	45
3.10	Applied pressure on a membrane	46
3.11	Analytical mechanical study	47

3.12	FEM simulation of the mechanical behaviour of the sensor . . .	48
3.13	Schematic of the multilayer optical system	49
3.14	Schematic of plane waves behaviour in a one-layer film optical system	49
3.15	Simulation of the reflection response through the cavity	51
3.16	Optical simulation of the reflection dependence with the tilt angle of the device for $\lambda = 580$ nm	52
3.17	Polysilicon deposit conditions	53
3.18	Polysilicon roughness	54
3.19	Detail of the pressure sensors fabrication steps before cavities etching	55
3.20	Partial SiO ₂ internal etching of the cavities	56
3.21	Complete SiO ₂ internal etching of the cavities	57
3.22	SU-8 photolithographic process	58
3.23	Photolithography SU-8 test for the definition of the sealing cap dimensions	58
3.24	SU-8 cap selected to fabricate the sensors	59
3.25	Evaluation of the SU-8 resistance to acetone exposition	59
3.26	Last steps in the sensors fabrication with SU-8 cap	60
3.27	Fabricated sensors SEM image with SU-8 cap	60
3.28	Sensors with SU-8 cap after FIB milling	61
3.29	EDXS analysis of the interior of the devices	62
3.30	Selected polyimide cap with and without dissolve	63
3.31	Analysis of the collapsed sensors sealed with the dissolved polyimide	64
3.32	Sensors with resist rests after the resist stripping	64
3.33	Complete stripping of the resist and polyimide caps	65
3.34	FIB milling to probe sensors have not collapsed with the ordinary polyimide as sealing cap	65
3.35	Optical images of the fabricated sensors with polyimide cap . .	66
3.36	Detail of the whole final fabrication of the pressure sensors . .	69
3.37	Releasing process of the sensors from the wafer	69
3.38	Confocal characterization of the devices	70
3.39	SEM and optical images of released devices	71
3.40	Scheme of the Ludin chamber	71
3.41	Pressure sensor validation subjected to a pressure sweep for different wavelengths	72
3.42	Scheme of the selected ROIs for the measure of the reflected intensity	73
3.43	Reflection intensities for different values of λ in a sweep of pressures, P	73
3.44	Surface plot of the reflected intensities of the sensor cavity . .	74
3.45	Normalized reflected intensities at the sensor cavity in a range of 0 to 50 mbar	74
3.46	Surface plot of the reflected intensities in a range of 0 to 50 mbar	75
4.1	Cytoskeletal structures	84
4.2	H-comb device design dimensions	84

4.3	Conceptualization of the operating principle	85
4.4	Cantilever schematic of errors induced by the optical projection	86
4.5	Representation of the three axes of rotation	86
4.6	Determination of the H-comb deflection	86
4.7	Schematic of the fabrication process of the H-comb devices . .	87
4.8	Fabricated chips	88
4.9	Released chips	89
4.10	Nanodevice area on a wafer	89
4.11	Wafer and chip points locations for polysilicon thickness mea- sure	90
4.12	Schematic of a nanodevice showing the lateral dimensions, L_c and w_c , of a cantilever	90
4.13	Stiffness dependence of an arbitrary geometry	92
4.14	SEM images of the dropped devices for mechanical determi- nation	93
4.15	FIB Lift-out with micromanipulator	94
4.16	H-comb nanodevices anchored at their centers	94
4.17	Peak Force mapping scheme	95
4.18	Schematic of the Force map curves for Young Modulus calcu- lation	95
4.19	25 nm-thick polysilicon layer Young's modulus estimation . .	96
4.20	Representation of the modelled device load state	97
4.21	Simulation results of applied pressure or force	98
4.22	Scheme of the layer modelling to simulate an initial curvature of the H-comb nanodevices	98
4.23	Scheme of the imposed load conditions on the modelling of an initial curvature of the devices	99
4.24	Scheme of the initial state under F and P loads to be simulated	99
4.25	Simulation results under F and P load states and considering an initial curvature on the devices	100
4.26	Representation of an applied pressure or force on a cantilever	100
4.27	Stages of the development of mouse one-cell embryo	102
4.28	Monitoring of H-comb during embryo development	102
4.29	Phase duration	103
4.30	Experimental results in control embryos	103
4.31	Experimental ad hoc parameters	104
4.32	Scheme of the z-stack images acquisition	104
4.33	Detail of the calculation method of the device deflection	105
4.34	Scheme of the resolving distances of different interference pro- files	106
4.35	Nanodevice intensity profile over a z-stack	106
4.36	Nanodevice intensity profile inside an embryo	107
4.37	Optical test structures fabricated by EBL to determine the min- imum curvature that can be solved	108
4.38	Fixed embryo with nanodevice for optical noise determination	110
4.39	Embryos within a 100 nm-thick device for optical noise deter- mination	111

4.40	Histogram levels in one-cell embryos of transcripts upregulated following embryonic genome activation determined by ratiometric, semiquantitative PCR (qPCR)	112
4.41	Development of 25 nm nanodevice-injected embryos	113
4.42	Rearrangement close to the sperm	113
4.43	PM movement towards embryo center	114
4.44	Membrane ruffling during pronuclear migration	115
4.45	Simulated normalized effective elastic and viscous constant	115
4.46	Endogenous embryonic particle trajectories analysis	116
4.47	Embryo pronuclear growth	116
4.48	Fluorescence confocal images of injected embryos during PEB	117
4.49	Morphological changes during elongation and division	118
4.50	Immunofluorescence images of embryo elongation and division	118
4.51	Embryo DIV-phase analysis	119
4.52	Blebbistatin treated embryos during PM-phase	120
4.53	Blebbistatin treated embryo underwent asymmetric division	121
4.54	Experimental measures with several devices on treated embryos	121
4.55	Star-shaped device design dimensions	122
4.56	Simplified working principle of star-shaped devices	122
4.57	Schematic of the fabrication process of the star-shaped devices	123
4.58	SEM image of the star-shaped fabricated devices	124
4.59	Simulation of the vertical displacement versus a pressure or force	124
4.60	Outline of the mechanical program of mouse embryo	127
5.1	Schematic of the working principle of the TFM for cell force measurements	136
5.2	Designed steps for the fabrication of the TFM	137
5.3	PMMA-Copolymer profile after EBL exposure	137
5.4	EBL process for the silicon master fabrication	138
5.5	Silicon master surface preparation	139
5.6	PDMS stamp fabrication	139
5.7	PDMS stamp on cell substrate	140
5.8	Characterization of high aspect ratio fabrication structures	141
5.9	Silicon master characterization	141
5.10	PDMS stamp characterization	142
5.11	Printed QD characterization by fluorescence microscopy	142
5.12	Printed QD characterization by SEM	143
5.13	Wrong printed QD zone characterization by SEM	143
5.14	Printed QD characterization with inked QD655	144
5.15	Scheme of the designed silicon pillars relating the anchor diameter and the applied force	144
5.16	Specimen behaviour with the magnitude of the applied force	145
5.17	Schematic of the pillar behaviour dependence between an applied force and the anchor size	145
5.18	Cell culture interaction with nanopillar chips	146
5.19	Design conception for the fabrication of an UTF with silicon chips anchored to the substrate	147

5.20	Schematic of the pillar behaviour dependence between an applied force and the size of the pillar head	148
5.21	Fabrication steps of the nanopillar chips	149
5.22	SEM images at some steps of the fabrication	149
5.23	Fabrication step options of the nanopillar sharpening	150
5.24	Detail of the nano-sharpening process of the nanopillars through <i>Option 2</i>	150
5.25	Wafer before cutting into chips	151
5.26	Process to determine the mean value of the anchor diameter for every Q and chip	152
5.27	Fabricated chip through the sharpening <i>Option 1</i> method	153
5.28	Analysis of the chip condition prior and after the SiO_2 wet etching	153
5.29	Analysis of the fabricated chips following the <i>Option 2</i>	154
5.30	Fabricated chips with different t_{head} values following <i>Option 2</i>	154
5.31	$Q64$ with fallen pillars on the edges	155
5.32	Set-up of the PI87 Picoindenter module inside the SEM chamber	156
5.33	Chip cut with a line of pillars accessible	157
5.34	Schematic representation of the experimental set-up using the PI-87 SEM PicoIndenter	157
5.35	Schematic and SEM images of the operational mode of the nanoindenter measurements	158
5.36	Load-displacement curve of a tested pillar from $Q62$	158
5.37	Fracture force versus the diameter of the nanopillars	159
5.38	Simulation results of the fracture force versus the diameter depending on the ultimate strength limit	160
5.39	Simulation results of the fracture force versus the diameter for multiple force application positions	161
5.40	Optical images conforming a quadrant after cells seeding	162
5.41	Optical images of the quadrant $Q42$ over the time	164
5.42	Simulated F_{fract} related to the anchor size of the pillar	165
5.43	Optical images of $Q35$ status from $t=0$ h to $t=168$ h	165
5.44	Optical images of quadrants with thicker anchor sizes at $t=96$ h h and $t=168$ h	166
5.45	Silicon stability test	167
5.46	CLSM images of HeLa cells adhered to the pillars of a silicon chip	168
5.47	SEM images of HeLa cells adhered to the pillars of a silicon chip	168

List of Tables

3.1	Thickness values of the fabricated polysilicon layers	51
3.2	Viscosity of the resist	62
3.3	ED and DOF for both polyimide configurations	63
4.1	Area and number of devices	90
4.2	Polysilicon thickness variations	90
4.3	Measured dimensions of a cantilever of the nanodevice	90
4.4	Young's Modulus of the measured samples	96
4.5	Calibration values of the optical test structures	109
5.1	Estimation of the number of cells in the experiment versus time	163
5.2	Anchor size and fracture force in quadrants Q42 to Q35	164
5.3	Anchor size and fracture force in quadrants Q34 to Q31	166

*Ir y venir, seguir y guiar,
dar y tener, entrar y salir de fase
Amar la trama más que el desenlace*

-Jorge Drexler-

Chapter 1

General introduction

1.1 Introduction

The cell is defined as the structural and functional unit of life and establishes the building block to form tissues, organs and organisms. Since the most relevant processes occur inside them, there is an enormous demand for innovative intracellular tools for biochemical but also biomechanical and bioelectrical applications.

Typically, cell analysis has been performed by measuring and averaging the response of a population of cells. Thus, it has been assumed that mean values are representatives of individual cells within a population. However, along the last decades it has been proved that cells are heterogeneous elements within the same population, this means that cells with similar phenotypes can react and behave in different ways to the same stimuli. Hence, the great interest in developing new tools to monitor, analyse and study individual cells has led an effort in the technology improvement[1].

Therefore, researchers at the microelectronic field realised that the tools to solve some of these questions were encompassed in typical application fields of chips. Thus, MEMS and NEMS (Microelectromechanical Systems and Nanoelectromechanical Systems) created new opportunities for spatial and temporal control of cell growth and stimuli, and showed new pathways for basic biomedical and pharmaceutical research. For instance, scanning probe microscopy emerged as an interesting tool for cell biology allowing high resolution scanning of cells[2-4].

In spite of the potential of these tools, these chips are larger than the cells and therefore they can only study the cells from the exterior or, few of them, perform intracellular measurements by puncturing the cell membrane, which can compromise cell viability. On this sense, the *Micro- and NanoTools* (MNTL) group at the IMB-CNM, CSIC, was a pioneer worldwide in the development of chips smaller than the cell scale. The design and fabrication of new devices for single cells applications have focused the work of the group, building a strong background on the field, coining two new terms: *chip-in-a-cell*[5] and *chip-on-a-cell*[6, 7].

Therefore, the use of microchips as intracellular passive devices has been demonstrated. Silicon barcodes were fabricated and internalized by macrophages cells[8] enabling their labelling and tracking. In addition, silicon-based devices were proved to be internalized by living eukaryotic cells without interfering their viability[9]. These initial exploratory ideas were the seed to an important line focused in the development of MEMS and NEMS with potential contribution to biology, nanobiotechnology and nanomedicine. Hence, chips which combine size smaller than cells, to allow cell internalization, with the possibility to study populations of cells but also obtain information from single cells, and with the possibility to perform mechanical and also biochemical, thermal and magnetic tasks, are of great interest[10-13].

Historically, the investigation about the cellular behaviour has been addressed from a chemical approximation, with great results in drug research

and the progress of medicine[14]. However, a great effort is being carried out during the last decades to perform a mechanical characterization of cells[15–20]. Cell mechanics is one of the most promising current research lines in cell biology[21]. The mechanical properties and mechanical behaviour of cells have a relevant impact in cell malfunction and are involved in many human diseases including vascular disorders[22], cancer[23] and neuronal affections[24]. Thus, mechanobiology, at the interface of biology and engineering, has become one of the most interesting emerging fields for science, with many good examples of devices from the field of micro- and nanotechnologies to contribute in the study of the interplay between the forces and the mechanical properties of living cells and cell function[15, 16, 25].

On this sense, the progress on the investigation of new tools led to the development (by our group) of a silicon chip which integrated two 50-nm thick polysilicon membranes, as mechanical sensors, and a Fabry-Perot optical resonator, as a transducer. This device, with dimensions of $6\ \mu\text{m} \times 4\ \mu\text{m} \times 0.4\ \mu\text{m}$, was able to measure pressure changes from the interior of a living cell[26] and was the inception of a new perspective in which the MNTL group advanced in the design and fabrication of new intracellular sensors to study cell mechanics.

On the one hand, to quantify forces produces by cells during migration, contraction or development, current techniques are mainly based on the measure of the deformation of materials whose properties are initially known, as Traction Force Microscopes (TFM) or Micropost arrays[27–30]. These systems consist of a polymeric substrate with embedded beads or micropost arrays commonly fabricated with polydimethylsiloxane (PDMS). Cells of interest are seeded over the device and the exerted forces can indirectly be measured from the displacement of the beads or the microposts positions. However, these techniques, despite being commonly used, only allow the study of cells from outside, providing information on the relationship between cells and their interaction with the environment that surrounds them. On the other hand, intracellular techniques can help to elucidate the cell mechanical behaviour from a direct internal detection. Thus, tools based on optical and magnetic techniques have been employed to directly measure forces acting within cells[31]. For instance, optical tweezers have been used to investigate the mechanical response of the F-actin cytoskeleton[32] or to analyse the rheological differences between normal and cancer cells[33], by trapping microbeads internalized by the cells. In addition, the viscoelastic behaviour of the nucleus and the cytoplasm has been investigated by the use of intracellular spherical magnetic beads[34] or magnetic nanorods[35]. Other methods based on nanowires bending have emerged as simple techniques for monitoring inter- or intracellular force dynamics[36]. Nonetheless, these methods usually offer local intracellular information and have to be extrapolated to reach a global characterization, and also, some of them, present limitation such as the use of high-powered lasers that can alter cell normal function.

Thus, from the challenge on the development of new tools to contribute on the knowledge of the cell mechanical behaviour arises the motivation

of this thesis. The main objectives are the design, fabrication, characterization and validation of intracellular or extracellular chips for cell mechanics. Our micro- and nanofabricated chips offer alternative tools to explore cell-mechanic properties from inside and outside the cell.

1.2 General objectives

This thesis is framed in a highly multidisciplinary nature, since it has been developed with the main general objective of obtaining micro- and nanotools which act as sensors in the mechanical characterization of living cells. Hence, micro- and nanofabrication technologies, physics, materials science and biology are the main disciplines covered.

To obtain the devices presented throughout this thesis, it has been devised the appropriate fabrication technology based on silicon microelectronic techniques. Previously, it was carried out the design of the micro- and nanodevices to later fabricate them by photolithography and Electron Beam Lithography (EBL) techniques. On the other hand, it was performed the physical characterization of the fabricated devices, after their fabrication, to validate its correct operation mode, but also in their application to living cells. Moreover, cell viability has been one of the necessary requirement that the devices must to fulfil so they can perform their function. In addition, simulations based on Finite Element Method (FEM) has been a central task in most devices, both in its conception and in their experimental application. Thus, the micro- and nanotools had to be simulated in order to verify that the experimental results corresponds to their expected behaviour. Hence, they are an additional method to optimize its design and fabrication to fulfil the technological and biological requirements.

1.3 Chapters overview

The devices presented in this thesis have been conceived with a common objective: their operation in the field of cell biology to act as mechanical sensors or actuators. Each chapter focuses independently on the presentation of each of the developed chips.

In Chapter 2 we show the progress on the integration of magnetic functionalities on intracellular chips for cell mechanical-manipulation. For that, we propose chips combining coding and magnetic capabilities, by developing a technology based on photolithographic processes in combination with electroplating methods to grow cobalt/nickel (CoNi) and nickel (Ni) layers. A vast number of suspended microbarcodes have been released from the wafer through an *ad hoc* process that combines a thermal shock and a subsequent peel-off method. Moreover, cell viability has been tested and Ni

devices were found to be internalized by cells without interfering their viability. Finally, chips were used in a proof of concept to manipulate cells from a culture.

In Chapter 3, we have improved the technology of a previous intracellular pressure sensor (developed by the group[26]) to refine its detection limit by following processes of silicon microelectronic technology. The sensor consists in two parallel polysilicon membranes separated by an air gap. To achieve this, the sealing of the sensor cavity has to be done at room temperature and atmospheric pressure conditions, with a baked-polyimide-cap by a photolithographic process. The risk of inflowing the polyimide in the sensor cavity makes the sealing a delicate step. Moreover, FEM simulations were used to calculate the deflection of the membranes for different values of an applied external pressure. Notwithstanding, large batch production remains as future work, some samples were tested confirming its operation mode.

Chapter 4 presents a new intracellular polysilicon tool for mouse-one cell embryo mechanical properties determination and mechanical load tracking during fertilization. This device has $22\ \mu\text{m}$ in length and $10.5\ \mu\text{m}$ in width, and is extremely thin, only 25 nm-thick, which allows its bending inside the embryo minimizing its impact on the cytoplasm. The cytoplasmic loads were estimated by measuring the real bending of the device inside the embryo and by FEM analysis. This tool enable the mechanical characterization of the embryo cytoplasm along the initial stages of the fertilization until the first cell division. Moreover, the measured program of intracellular force and mechanical property changes was measured to be altered on embryos treated with an actomyosin inhibitor. Additionally, it was established a mechanical model of the cytoplasm behaviour during the pronuclear migration stage of the embryo development.

Finally, Chapter 5 explores a new extracellular chip as a tester of the Ultimate Traction Force (UTF) exerted by living cells on their extracellular environment. The investigation started by fabricating a TFM, based on conventional methods, by stamping a Quantum Dot (QD) pattern on a substrate. The process was expected to be fast, so that in a stamping-step the whole TFM system was fabricated. However, it was not such, and an improved method would not be obtained compared to those systems that already exist. Thereby, based on the intracellular chips design, we devised and fabricated a highly sophisticated UTF consisting of standing mushroom-shaped silicon pillars with different values in their anchor diameters. Micro- and nanofabrication technology was the key on the sharpening of the anchors by the use of dry etching processes. These nanodevices were mechanically characterized in a preliminary nanoindentation test and simulated by FEM. Thus, a catalogue with the correspondence between the size and the fracture force of each pillar was elaborated. Finally, a chip was tested with HeLa cells validating their operation mode.

Bibliography

- [1] Daojing Wang and Steven Bodovitz. Single cell analysis: the new frontier in 'omics'. *Trends in biotechnology*, 28(6):281–290, 2010.
- [2] Yves F Dufrêne, Toshio Ando, Ricardo Garcia, David Alsteens, David Martinez-Martin, Andreas Engel, Christoph Gerber, and Daniel J Müller. Imaging modes of atomic force microscopy for application in molecular and cell biology. *Nature nanotechnology*, 12(4):295–307, 2017.
- [3] BJ Haupt, AE Pelling, and MA Horton. Integrated confocal and scanning probe microscopy for biomedical research. *TheScientificWorld-JOURNAL*, 6, 2006.
- [4] Kristina Haase and Andrew E Pelling. Investigating cell mechanics with atomic force microscopy. *Journal of The Royal Society Interface*, 12(104):20140970, 2015.
- [5] Petra S Dittrich. Research highlights. *The Royal Society of Chemistry. Lab Chip*, 10:541–543, 2010. <https://doi.org/10.1039/C000521P>.
- [6] S Durán, Sergi Novo, M Duch, R Gómez-Martínez, M Fernández-Regúlez, A San Paulo, C Nogués, J Esteve, E Ibañez, and JA Plaza. Silicon-nanowire based attachment of silicon chips for mouse embryo labelling. *Lab on a Chip*, 15(6):1508–1514, 2015.
- [7] Andreas Schmid, Hendrik Kortmann, Petra S Dittrich, and Lars M Blank. Chemical and biological single cell analysis. *Current opinion in biotechnology*, 21(1):12–20, 2010.
- [8] Elisabet Fernandez-Rosas, Rodrigo Gomez, Elena Ibanez, Leonardo Barrios, Marta Duch, Jaume Esteve, Carme Nogués, and José Antonio Plaza. Intracellular polysilicon barcodes for cell tracking. *Small*, 5(21):2433–2439, 2009.
- [9] Rodrigo Gómez-Martínez, Patricia Vázquez, Marta Duch, Alejandro Muriano, Daniel Pinacho, Nuria Sanvicens, Francisco Sánchez-Baeza, Patricia Boya, Enrique J de la Rosa, Jaume Esteve, et al. Intracellular silicon chips in living cells. *Small*, 6(4):499–502, 2010.
- [10] Xiaoyu Rayne Zheng and Xin Zhang. Microsystems for cellular force measurement: a review. *Journal of Micromechanics and Microengineering*, 21(5):054003, 2011.
- [11] Jun Liu, Jun Wen, Zhuoran Zhang, Haijiao Liu, and Yu Sun. Voyage inside the cell: Microsystems and nanoengineering for intracellular measurement and manipulation. *Microsystems & Nanoengineering*, 1(1):1–15, 2015.
- [12] James J Norman, Vikram Mukundan, Daniel Bernstein, and Beth L Pruitt. Microsystems for biomechanical measurements. *Pediatric research*, 63(5):576–583, 2008.

- [13] William J Polacheck and Christopher S Chen. Measuring cell-generated forces: a guide to the available tools. *Nature methods*, 13(5):415–423, 2016.
- [14] Jürgen Drews. Drug discovery: a historical perspective. *Science*, 287(5460):1960–1964, 2000.
- [15] Pere Roca-Cusachs, Vito Conte, and Xavier Trepap. Quantifying forces in cell biology. *Nature cell biology*, 19(7):742–751, 2017.
- [16] Marita L Rodriguez, Patrick J McGarry, and Nathan J Sniadecki. Review on cell mechanics: experimental and modeling approaches. *Applied Mechanics Reviews*, 65(6), 2013.
- [17] Daniel A Fletcher and R Dyche Mullins. Cell mechanics and the cytoskeleton. *Nature*, 463(7280):485–492, 2010.
- [18] Jochen Guck. Some thoughts on the future of cell mechanics. *Biophysical Reviews*, 11(5):667–670, 2019.
- [19] CT Lim, EH Zhou, and ST Quek. Mechanical models for living cells—a review. *Journal of biomechanics*, 39(2):195–216, 2006.
- [20] Charlotte Alibert, Bruno Goud, and Jean-Baptiste Manneville. Are cancer cells really softer than normal cells? *Biology of the Cell*, 109(5):167–189, 2017.
- [21] Emad Moendarbary and Andrew R Harris. Cell mechanics: principles, practices, and prospects. *Wiley Interdisciplinary Reviews: Systems Biology and Medicine*, 6(5):371–388, 2014.
- [22] Cornelia Hahn and Martin A Schwartz. Mechanotransduction in vascular physiology and atherogenesis. *Nature reviews Molecular cell biology*, 10(1):53–62, 2009.
- [23] Sarah E Cross, Yu-Sheng Jin, Jianyu Rao, and James K Gimzewski. Nanomechanical analysis of cells from cancer patients. *Nature nanotechnology*, 2(12):780–783, 2007.
- [24] Martin Chalfie. Neurosensory mechanotransduction. *Nature reviews Molecular cell biology*, 10(1):44–52, 2009.
- [25] Mustafa Unal, Yunus Alapan, Hao Jia, Adrienn G Varga, Keith Angelino, Mahmut Aslan, Ismail Sayin, Chanjuan Han, Yanxia Jiang, Zhehao Zhang, et al. Micro and nano-scale technologies for cell mechanics. *Nanobiomedicine*, 1(Godište 2014):1–5, 2014.
- [26] Rodrigo Gómez-Martínez, Alberto M Hernández-Pinto, Marta Duch, Patricia Vázquez, Kirill Zinoviev, J Enrique, Jaume Esteve, Teresa Suárez, and José A Plaza. Silicon chips detect intracellular pressure changes in living cells. *Nature nanotechnology*, 8(7):517, 2013.
- [27] Huw Colin-York, Christian Eggeling, and Marco Fritzsche. Dissection of mechanical force in living cells by super-resolved traction force microscopy. *Nature protocols*, 12(4):783–796, 2017.

- [28] Martin Bergert, Tobias Lendenmann, Manuel Zündel, Alexander E Ehret, Daniele Panozzo, Patrizia Richner, David K Kim, Stephan JP Kress, David J Norris, Olga Sorkine-Hornung, et al. Confocal reference free traction force microscopy. *Nature communications*, 7(1):1–10, 2016.
- [29] Manuel Zündel, Alexander E Ehret, and Edoardo Mazza. Factors influencing the determination of cell traction forces. *PLoS One*, 12(2): e0172927, 2017.
- [30] Sujin Lee, Juhee Hong, and Junghoon Lee. Cell motility regulation on a stepped micro pillar array device (smpad) with a discrete stiffness gradient. *Soft Matter*, 12(8):2325–2333, 2016.
- [31] Dedy Septiadi, Federica Crippa, Thomas Lee Moore, Barbara Rothen-Rutishauser, and Alke Petri-Fink. Nanoparticle–cell interaction: a cell mechanics perspective. *Advanced Materials*, 30(19):1704463, 2018.
- [32] Schanila Nawaz, Paula Sánchez, Kai Bodensiek, Sai Li, Mikael Simons, and Iwan AT Schaap. Cell visco-elasticity measured with afm and optical trapping at sub-micrometer deformations. *PloS one*, 7(9):e45297, 2012.
- [33] Kalpana Mandal, Atef Asnacios, Bruno Goud, and Jean-Baptiste Manneville. Mapping intracellular mechanics on micropatterned substrates. *Proceedings of the National Academy of Sciences*, 113(46):E7159–E7168, 2016.
- [34] Marie Versaevel, Maryam Riaz, Tobias Corne, Thomas Grevesse, Joséphine Lantoine, Danahe Mohammed, Céline Bruyère, Laura Alaimo, Winnok H De Vos, and Sylvain Gabriele. Probing cytoskeletal pre-stress and nuclear mechanics in endothelial cells with spatiotemporally controlled (de-) adhesion kinetics on micropatterned substrates. *Cell adhesion & migration*, 11(1):98–109, 2017.
- [35] Alfredo Celedon, Christopher M Hale, and Denis Wirtz. Magnetic manipulation of nanorods in the nucleus of living cells. *Biophysical journal*, 101(8):1880–1886, 2011.
- [36] John F Zimmerman, Graeme F Murray, Yucai Wang, John M Jumper, Jotham R Austin, and Bozhi Tian. Free-standing kinked silicon nanowires for probing inter-and intracellular force dynamics. *Nano letters*, 15(8):5492–5498, 2015.

Chapter 2

Magnetic barcodes development for labelling and magnetic mechanical-manipulation of living cells

In this chapter we report the technological development for the integration of magnetic capabilities on intracellular chips. Intracellular chips offer endless possibilities in cell biology and nanomedicine: as barcodes, biochemical sensors or mechanical sensors. The capabilities of these chips depend on the possibility to integrate more functionalities. Here, we study the integration of magnetic capabilities to allow cell manipulation. In particular, we integrate magnetic capabilities to intracellular barcodes to add magnetic cell manipulation to cell tagging. We explore the CoNi and Ni-based microbarcodes fabrication by electroplating processes on silicon substrates and, interestingly, we demonstrate a simple and non-destructive release method of the codes from the wafer. The magnetic properties of the devices are also characterised. Moreover, we evaluate cell viability with the developed barcodes and show that CoNi devices affect cell viability. On the contrary, internalization and non-toxic effects are achieved by the Ni-based barcodes. Finally, we performed experiments which demonstrate the cell tagging and cell manipulation capability of the Ni-based magnetic microbarcodes without cell cytotoxicity. This work opens a way to implement the manipulation on more sophisticated intracellular tools controlled by magnetic fields.

2.1 Introduction

There is an increasing demand for tracking, labelling and manipulate even smaller objects which is inspiring worldwide scientific researchers for a continuous exploration for newer and better techniques. Microtechnologies provide new opportunities for device miniaturization which allows the study of the microworld and its manipulation.

The identification of objects at the micro- and nanoscale has been challenging in many instances. Hence, researchers have used microbarcodes as labelling tools as they are representations of data attached to the object of interest for clear identification, avoiding misreading[1]. The applications of barcodes for investigation at the microscale have been continuously demonstrated, in various barcoding studies in molecular interaction[2–9] and combinatorial screening[10–14]. In fact, the constant research progress done in this field proves how much valuable microbarcodes are.

Complimentary techniques based on magnetic approaches have been followed to identify systems at the microscale. Thus, synthesized magnetic nanoparticles offer researchers worldwide labelling and identification tools with several applications in immunoassays[15], biomolecule detection[16], biomedical applications[17, 18], trap and control of bacteria[19], or chemotherapy[20]. In cell studies, researchers have used particle-based methods to manipulate cell orientation and migration using magnetic Iron oxide (Fe_3O_4) magnetic nanoparticles under directionalized magnetic fields[21], forfeiting cell identification. More commonly, the properties of the cells are exploited in magnetic identification and separation techniques. In some instances solely the physical characteristics, as size or density, have been used to obtain a levitation profile of different cellular types with the use of paramagnetic solutions[22]. However, many cells have similar shape and sizes and consequently these techniques could be proven limited. Instead, the intrinsic magnetic properties of the cells have been employed in microfluidic cell sorting for White Blood Cells (WBCs)[23], yet only few cell types have intrinsic magnetic properties. Thus, the addition of an external tag with customized physical and magnetic properties attached or internalized into the cells could offer identification and external magnetic manipulation.

In our group, we have previously used polysilicon, a material widely used in microelectronics, to develop chips smaller than cells for their use in cellular level identification[24–29] and identification and tracking of living embryos[24, 26–30]. The combination of the functional features of both, microbarcodes, for identification, and magnetic features, for magnetic manipulation, provides the means to develop a device able to be attached or internalized by living cells coupled with the capability to be manipulated by an external magnetic field.

In this work, we present a technological development of an initial top-down photolithographic microfabrication technology encompassing the batch

fabrication of millions of reproducible devices at the microscale, with complete control over their size, shape, and distribution. We subsequently demonstrate the bottom-up aggregation of magnetic materials with a specific electroplating process to obtain CoNi alloy and Ni magnetic suspended microdevices. Electroplating is one of many methods to deposit and eventually integrate magnetic materials into microfabrication processes. Besides being a cost effective technique, the whole process requires low energy: high deposition rates can be achieved by thermoregulation allowing a precise deposit thickness by controlling the deposition time, so complex geometries can be handled[31]. The electroplating set up is also easy to maintain and, what is most important, the properties of the deposited layer can be adjusted by modifying the solution composition.

We take a step forward and present a new generation of magnetic microbarcodes for labelling and manipulating living cells. In particular, we study HeLa cells viability with internalized magnetic barcodes with the purpose of optical cell identification and tracking. Finally, we investigate the magnetic separation and isolation of cells with internalized magnetic microbarcodes from the rest of the cell culture and study their viability past 4 days after the magnetic separation.

2.2 Previous background of the group on CoNi barcodes

As said above, in our group we have the experience of the fabrication of different polysilicon devices smaller than living cells for intracellular applications or for being adhered to the cell membrane. These devices have been developed to perform different applications as nanomechanical sensors in living cells[32, 33], biochemical sensing[34, 35] and tracking and labelling biological cells[24, 25, 27–30, 36, 37]. Polysilicon barcodes were developed as label tools[38, 39] and they were tested injected or attached to the Zona Pellicida (ZP) of mouse[24, 28, 29, 36], bovine[37] and human[30] embryos and also being internalized by living cells[25, 27], resulting a suitable material for biological experimentation.

As this investigation line is consolidated, the natural evolution is moving to new materials with further capabilities. Hence, our group developed the fabrication process of well-defined CoNi alloy barcodes[38] which could allow the labeling and tracking of microobjects and, in addition, its manipulation. On one hand, we have microtechnology expertise, such as the possibility to fabricate millions of reproducible devices, a complete control over the size and shape of the devices or the ability to achieve a low-cost fabrication. On the other hand, the magnetic material capabilities allow us to have control on the manipulation of the microbarcodes by the application of an external magnetic field.

These CoNi barcodes were previously designed, fabricated, chemically characterized by ensuring the homogeneity of the alloy, and magnetically by analysing its suitability as magnetic labels. Formerly, a detailed study on the etching of the sacrificial and seed layers for the releasing of CoNi barcodes were also performed[38]. In that work, first, layers were etched with HF vapors, which resulted to damage the devices and a formless CoNi layer was obtained. Secondly, it was tried a combination of etching steps (HF, HNO₃ and polyethylene glycol (PEG)) plus the approach of a magnet to collect the devices. Released CoNi devices could be obtained with this second method, but barcodes were rough and they were released in clusters because the use of the magnet, thus single device application was not feasible.

In the present section, an outlook of the previous design and fabrication process is going to be found. After that, all the development done during this thesis is going to be detailed in further sections.

2.2.1 Design of the magnetic barcodes

The new magnetic barcodes share the design of the previously developed polysilicon barcodes[24, 28–30, 36, 37]. Briefly, the design of the barcode consists in a two-dimensional matrix of 2 rows and 4 columns of individual bits (Figure 2.1a). The external lateral dimensions of the devices were fixed to 10.0 μm in length and 6.0 μm in width, in order to make them easily identifiable under an optical microscope. Bit lateral dimensions were fixed to 2.0 μm in length, 1.5 μm in width. The thickness of the devices were established to 1.0 μm. A solid-bit represented the value 1 (Bit =1) and a hole-bit represented the value 0 (Bit = 0). A start mark in the top left corner was designed in order to expedite the correct reading of data. In Figure 2.1b, it can be seen a detail of some of the codes used during this study (henceforth, a specific barcode will be designed by its decimal representation).

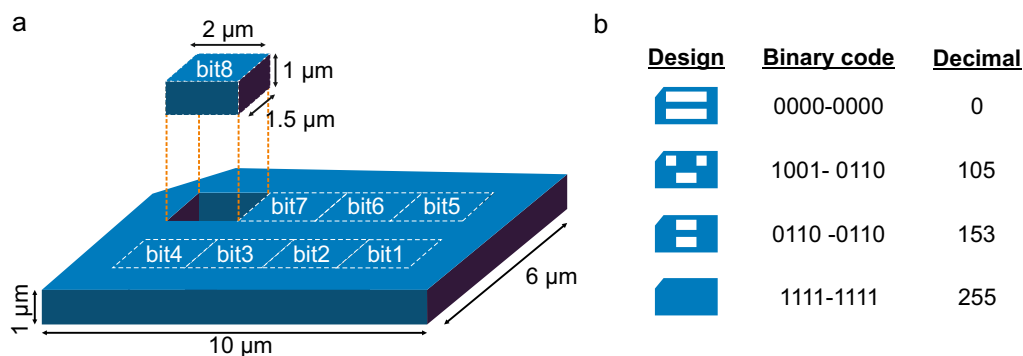


Figure 2.1. **Designed barcodes.** a) Schematic representation of the barcodes consisting in two rows of 4 rectangles areas representing bits. The presence of material in these areas indicates a '1' and the absence indicates a '0'. A mark (cut) on the top left corner indicates the start of the reading position. b) Representation of the physical design, binary code and decimal corresponding of some of the tested devices.

2.2.2 Fabrication of the inverted barcode pattern

Compared to the fabrication of the polysilicon barcodes, for the magnetic device fabrication, it was necessary to design a new mask to obtain inverted barcode photoresist patterns, as this mould should be filled with the electrodeposited material. The fabrication of the magnetic barcodes started with a 100 mm p-type silicon wafer (Figure 2.2a), where a 1 μm -thick silicon oxide (SiO_2) layer was deposited as a sacrificial layer (Figure 2.2b). 50 nm-thick Titanium (Ti) layer and a 50 nm-thick Ni layer were evaporated as seed layers to allow the further deposition of the magnetic materials (Figure 2.2c and 2.2d, respectively). Then, a 0.9 μm -thick photoresist (Fujifilm OiR 620-09) was spun (Figure 2.2e) and finally patterned by photolithography to define an inverted pattern of the devices on the wafer (Figure 2.2f).

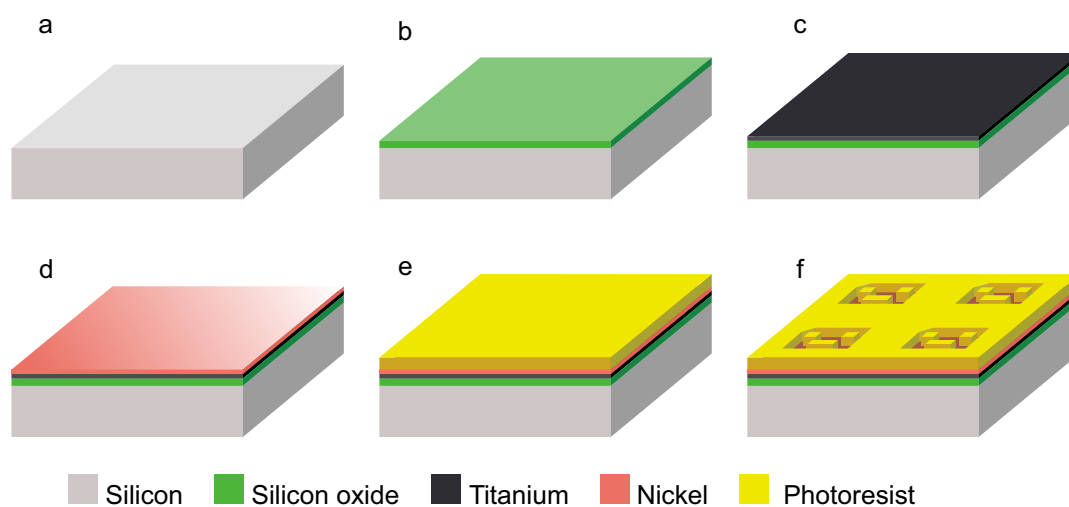


Figure 2.2. **Fabrication of the inverted pattern.** a) The magnetic barcodes fabrication started with a silicon wafer substrate. b) 1 μm of silicon oxide was deposited as a sacrificial layer. c) A 50 nm-thick of Ti and d) a 50 nm-thick of Ni were evaporated as seed layers. e) 0.9 μm of photoresist was spun over the surface. f) Patterned photoresist after exposure to UV through a photolithographic process to get the inverted barcode pattern.

2.2.3 Fabrication of the CoNi barcodes

For the fabrication of the CoNi alloy, firstly we started up the electroplating set-up and optimized the parameters and conditions for a high suitable electroplating bath. Hence, an appropriate chloride bath was needed to deposit CoNi alloys onto the selected substrate. The electrolytic bath consisted of a 0.9 M nickel chloride ($\text{NiCl}_2 \cdot 6\text{H}_2\text{O}$, Merck) and 0.2 M cobalt chloride ($\text{CoCl}_2 \cdot 6\text{H}_2\text{O}$, Merck), boric acid (H_3BO_3) aqueous solution buffered with addition of 30 g/l of boric acid (H_3BO_3 , Panreac) and 0.7 g/l of saccharine (Merck)[40, 41]. Boric acid acted as a weak pH buffer controlling the hydrogen evolution maintaining the pH in the range of 3-3.5. In addition, it improves the quality of the deposit, as the deposited layer may crack and burn at low boric acid concentrations[42]. Moreover, saccharine worked as

a de-stressing additive agent which helps to minimize the possible internal stresses of the CoNi alloy promoting a smooth alloy deposition[43]. Both, the boric acid and saccharine, were highly insoluble, hence the solution had to be stirred during some hours (>2 h). The preparation of deposits was performed under stirring conditions in order to assure homogeneous composition in the samples

As the electrodeposition is a temperature dependent process, the electroplating protocol requires an extremely accurate thermoregulation in order to assure constant deposition rates at the applied potential. For this reason, a precise thermostatic bath (Magnetic stirrer and heater, Lab-Mix 35, Fisher Scientific) was acquired. The complete set-up includes this bath, a thermometer probe which measures the temperature at all times, and a customized beaker lid with apertures to insert the reference, counter, and working electrodes comprising the three-electrode cell. The reference electrode is a silver/silver chloride ($\text{Ag}/\text{AgCl}/\text{Cl}^-$) electrode, the counter electrode is a Ni sheet and the working electrode is a piece of wafer (where the CoNi alloy is going to be deposited). The electrodes were connected to the potentiostat (Autolab 302N, Metrohm, AG) which regulates the applied potential and the deposition time.

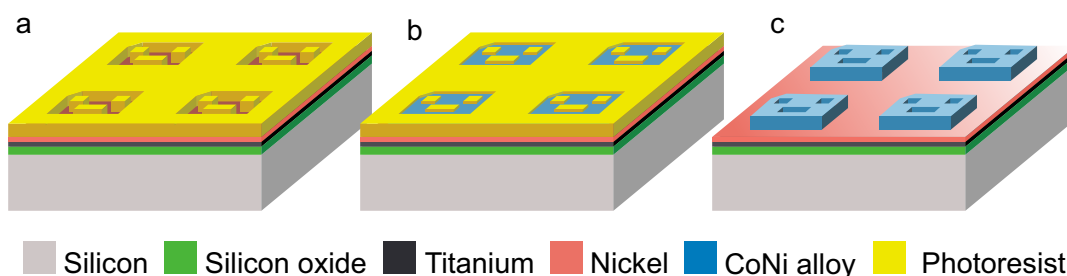


Figure 2.3. **Fabrication of the CoNi barcodes.** a) The devices were fabricated starting from the inverted photoresist pattern. b) $1\ \mu\text{m}$ CoNi was deposited with the electroplating process. c) Removal of the photoresist.

The whole fabrication starting from samples with the engraved photoresist pattern on their surfaces is schematized in Figure 2.3. First, several CoNi electroplating experiments (Figure 2.3b) were performed for different deposition times (from 50 s to 600 s) and for different bath temperatures (from $45\ ^\circ\text{C}$ to $65\ ^\circ\text{C}$) at fixed applied potential of $E = -0.8\ \text{V}$. Ultimately, the desired thickness of $1\ \mu\text{m}$, without losing the devices dimensions, was obtained at $55\ ^\circ\text{C}$ during 100 s. Lastly, the photoresist was removed with acetone, and sample was later rinsed with isopropyl alcohol and DI water for 1 min (Figure 2.3c).

2.2.4 Etching of the sacrificial and seed layers to release the CoNi barcodes

After the photoresist removal, to obtain suspend CoNi barcodes, we have to release the devices from the substrate by etching the sacrificial and seed

layers. As introduced before, a previous study on the group was performed to release CoNi barcodes. This study consisted in the development of a wet etching process of the layers.

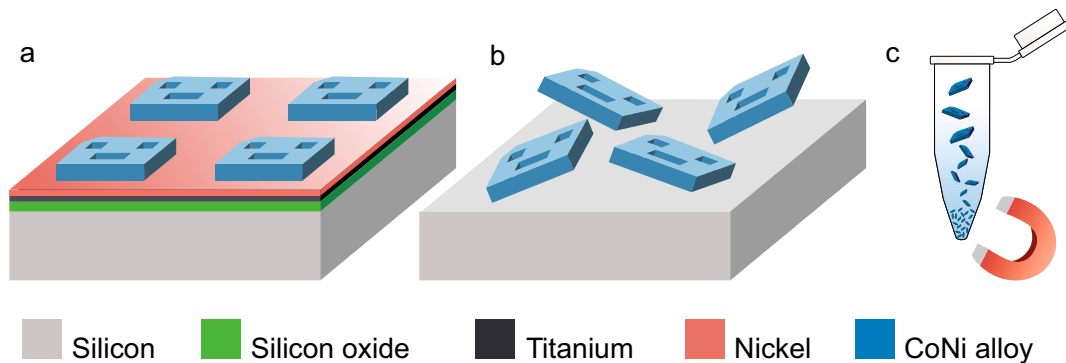


Figure 2.4. **Releasing of the CoNi barcodes by the wet etching of the sacrificial layer.** a) A piece of wafer with the CoNi barcodes after the photoresist removal. b) Wet etching of the Ti and Ni seed layers and the SiO₂ sacrificial layer. c) Finally, suspended CoNi barcodes were obtained by introducing the piece of wafer on an Eppendorf with 96% ethanol and by approaching a magnet to it.

It started from a sample where the CoNi alloy barcodes has been patterned and the photoresist were removed (Figure 2.4a). Then, the Ti and Ni 50 nm-thick seed layers were etched. First, the Ni layer was etched for 30 s with a mixture of 69% HNO₃ and double DI water in a ratio of 1:4, followed by a wash in water. Next, the Ti layer was etched in for 1 min on a bath composed of a 1:1 mixture of 10% HF and PEG. As this mixture is composed by HF, it was also used to attack the SiO₂ sacrificial layer (Figure 2.4b). Finally, the resulting piece of wafer was introduced in an Eppendorf with 96% ethanol and a magnet was approach to allow the CoNi barcode precipitation (Figure 2.4c)[38].

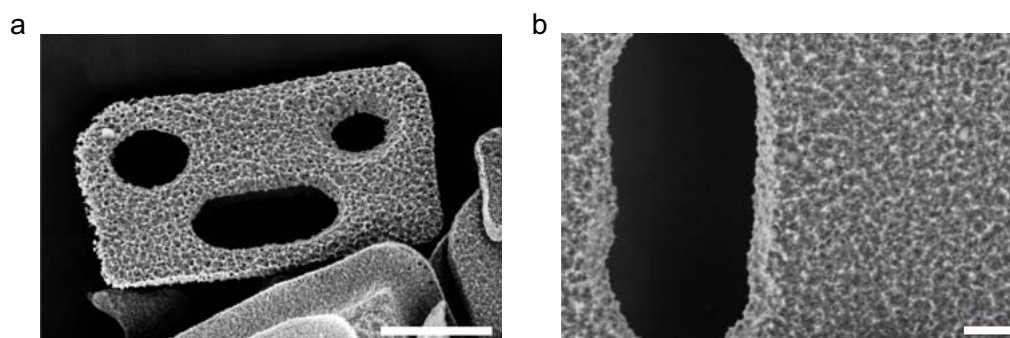


Figure 2.5. **Suspended CoNi barcodes after wet etching.** SEM images of a) a released barcode with a roughness appearance after the wet etching of the seed layers and b) a zoom of the same barcode. Scale bars: 3 μ m and 500 nm, respectively. Images extracted from[38].

These released devices were observed under the SEM showing a rough surface of the CoNi barcodes after the wet etching process. In addition, the

dimensions of the bits areas did not present their nominal shape (Figure 2.5a and b). This results could be caused by the presence of HNO_3 and HF on the wet etching solutions of the Ti and Ni seed layers, as the CoNi barcodes were also etched in these baths. In addition, collecting the devices by approaching a magnet to them produces large clusters of CoNi barcodes hardly to disaggregate without damaging them. Overall, this limitations prevents the use of the devices for cell labelling and manipulation.

2.3 CoNi-based barcodes

Here we commence a new investigation from the need of obtaining suitable suspended CoNi barcodes to manipulate a cell population and to label and track single cells. For that, we started from the development of a releasing method appropriate for single device applications.

2.3.1 Alternative releasing method

Above releasing method (etching the sacrificial and seed layers) affected the CoNi barcodes surface and turned this step into a critical process. To prevent this damage, we avoided the etching processes and we developed a two-step process to release the chips. For that, we started from a piece of wafer with the CoNi barcodes electrodeposited over them as seen in Figure 2.6 (code number 0000-0000 = 0).

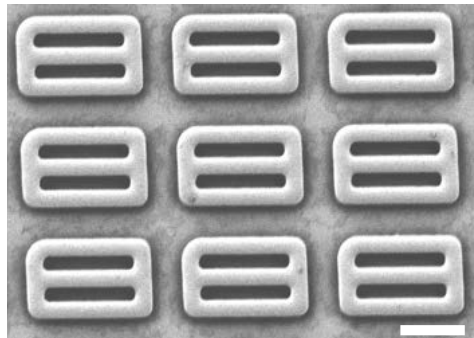


Figure 2.6. **Fabricated CoNi barcodes before their releasing.** SEM image of CoNi barcodes over a silicon wafer after removing the photoresist just before their releasing. Code number 0. Scale bar: 5 μm

Hence, a thermal shock was firstly done by placing the samples (Figure 2.7a) in an oven for 20 min at 200 °C and their subsequent rapid cooling to 21 °C (Figure 2.7b). The exposure to the high temperature and the posterior rapid cooling induced the thermal expansion and contraction of the layers on the wafer. This procedure increased the material stresses, weakening the adhesion at the interface between chips and the nickel layer. Afterwards, we used a simple but highly effective peel-off method that was previously developed to release Suspended Planar-Array (SPA) chips[35, 44]. This method

consisted in placing a drop of an aqueous mounting medium (Fluoromount, Sigma-Aldrich) directly on the top of the anchored chips and letting it to solidify at room temperature (RT) (Figure 2.7c). After that, a manual force was used to peel the solidified, flexible membrane encircling the chips (Figure 2.7d). Finally, the chips were collected by centrifugation after dissolving the water-soluble membrane (Figure 2.7e).

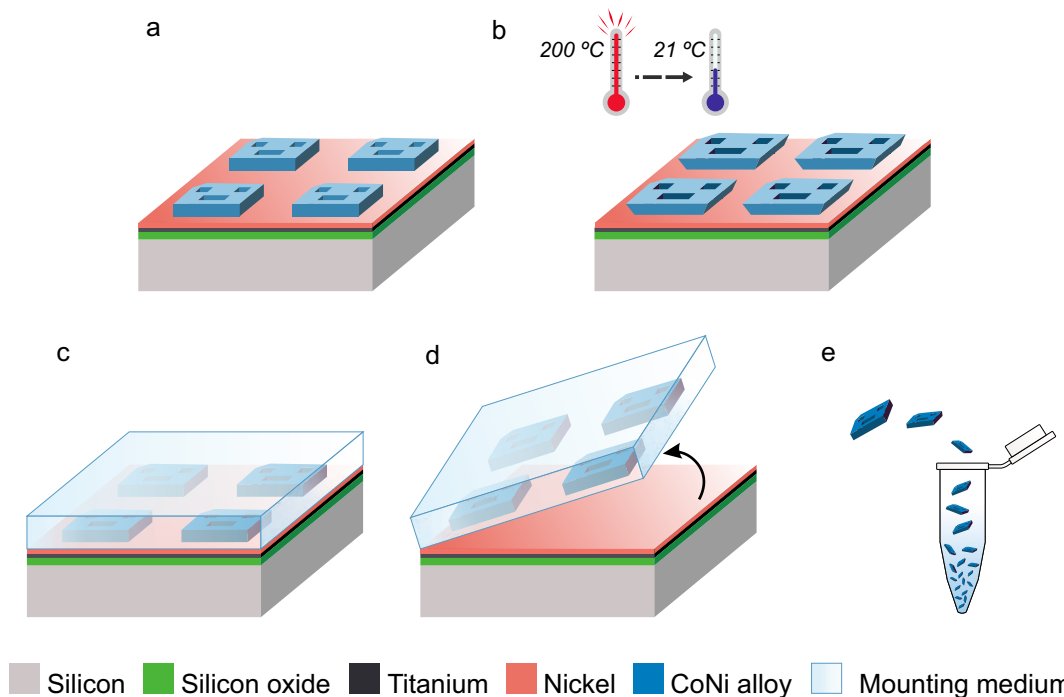


Figure 2.7. **Current release of the CoNi barcodes.** a) Starting from a wafer with the CoNi alloy deposited, the photoresist was removed. b) A thermal-shock was performed after heating the devices at 200 °C for 20 min and then a quick cooling down to RT. c) A drop of an aqueous mounting medium was casted over the devices. d) A manual peeling of the solidified membrane was performed to release the CoNi barcodes. e) Chips were collected in an Eppendorf by dissolving the membrane in water.

2.3.2 Characterization of the CoNi barcodes

After the releasing process CoNi barcodes were characterized by SEM (Carl Zeiss Auriga Microscope, GmbH, IncaX-act, Oxford Instruments) by placing a 2 μ l-drop of suspended devices in 96% ethanol on a piece of silicon wafer. Figure 2.8 shows some released barcodes with a well-defined shape and accurate dimensions of the code number 0110-1001 = 105. The upper side of the barcodes (devices pointed with green arrows) presented a smoother surface, but smaller dimensions on the bit areas, than the bottom side (devices pointed with red arrows).

The material composition of the barcodes 105 and 153 were analysed by EDXS (PentaFET-Precision attached to the SEM equipment) and was found that the deposit of these two barcodes were composed of only Ni and Co

without impurities. The characteristic peaks of cobalt and nickel signals at 0.776 keV and 0.851 keV, respectively, can be clearly observed in Figure 2.9a.

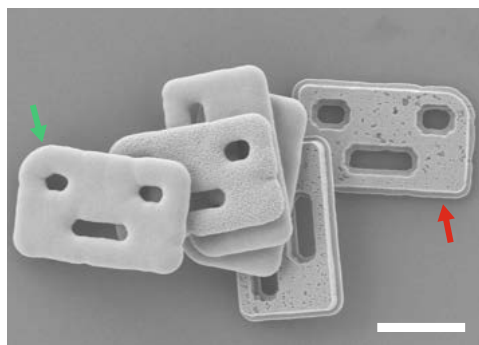


Figure 2.8. **CoNi barcodes after new releasing.** SEM images of the barcodes (upwards and downwards) after their release through a thermal shock and the use of water-soluble mounting medium casted on the devices. Green and red arrows point upwards and downwards barcodes, respectively. Code number 105. Scale bar: 5 μm .

Furthermore, XRF (Fisher scope system XDAL with DCM 3D optical image profiler software) analysis was carried out for more depth material composition. XRF results showed an equitable proportion and fairly constant ratio of Co and Ni in the fabricated barcodes, composed by an average of 45.4 ± 3.2 % of Co and by 54.6 ± 2.7 % of Ni (n=6).

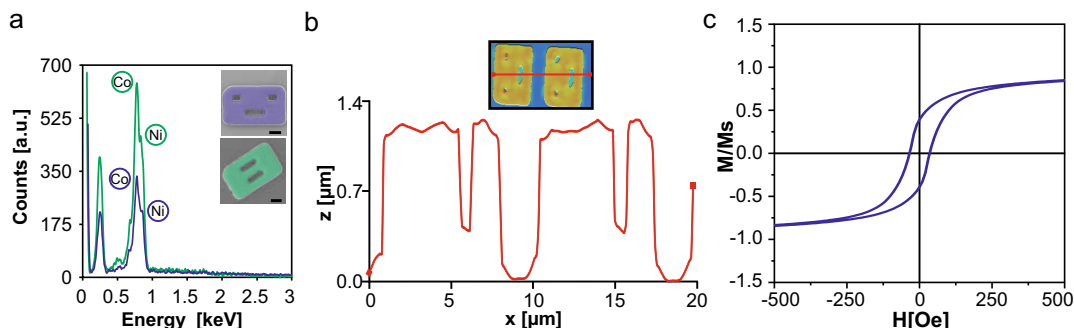


Figure 2.9. **Characterization of the fabricated CoNi barcodes.** a) EDXS spectrum of two different barcodes, shown in the insets, confirmed the presence of both material, Co and Ni. The signal showed the characteristic peak of Co and Ni at 0.776 keV and 0.851 keV respectively. Scale bars: 2 μm . b) Confocal profile of the thickness of the CoNi devices (inset shows the scanned line). z represents the vertical dimension and x the length along the scanned line. c) Hysteresis loop of CoNi barcodes measured with a VSM for magnetic characterization. M/M_s represents the magnetization of CoNi normalized by its saturation magnetization and H the magnetic field.

To evaluate the device thickness, the barcodes were measured with confocal microscopy (PLu neox, optical 3D surface profiler, Sensofar) before their release from the wafer (Figure 2.9b, barcode 105) showing a thickness of 1.24 μm .

Finally, magnetic characterization of the barcodes was performed. Figure 2.9c shows the hysteresis loop of an array of CoNi barcodes BC105, obtained

by the use of a VSM (LOT-Oriel EV7). CoNi barcodes were placed on a fragment of silicon wafer inside the equipment under a saturating magnetic field of 1.8 T in order to know the maximum magnetic moment of the array. All the magnetic characterizations present throughout this chapter were carried out at the *Instituto de Ciencias de Materiales de Madrid* (ICMM, CSIC) by Dr. Rafael Pérez del Real (see *Collaborations and Stays in Research Entities*). The magnetic moment of a single barcode, used to know the force under a magnetic field gradient, can be calculated following the equation[45]:

$$m_b = (M_{Co}x + M_{Ni}y)V \quad (2.1)$$

where m_b is the CoNi barcode saturation magnetic moment, M_{Co} ($\mu_0 M_{Co} = 1.8$ T) and M_{Ni} ($\mu_0 M_{Ni} = 0.61$ T) are the saturation magnetization of Co and Ni, x and y are the composition percentage of Co and Ni respectively, and V is the volume of the barcode.

2.3.3 Biological validation of the CoNi barcodes

The intended uses of the suspended CoNi barcodes encompass living cell labelling and cell manipulation, hence, cell toxicity studies on HeLa cells were done with these devices. All biological experiments conducted throughout this chapter were prepared and performed by Dr. Teresa Suárez and Dr. Consuelo González-Manchón at the *Centro de Investigaciones Biológicas Margarita Salas* (CIB-CSIC) (see *Collaborations and Stays in Research Entities*). The following protocol was established in order to facilitate cell-device contact as well as microscopic analysis. HeLa cells were grown on 12 mm-coverslips at a confluence of 40-50% and were incubated for 18 h with 80 μ l of growth medium containing \sim 2500 barcodes in a humid chamber. The coverslips were then transferred to wells of 12-well dishes with 0.5 ml of medium and incubation continued for additional 24 h. In this first analysis, a simple visual exploration under an optical microscope was enough to validate the effects of the CoNi devices on cells. The CoNi barcodes, even not being internalized appeared to be toxic to the cells, resulting in general cell death after the first day in co-culture. Incubation in the presence of lipofectamine (Invitrogen) to facilitate internalization of the devices did not improve the results.

Previous studies have reported that cobalt could be released from micro- and nanoparticles becoming toxic when interacting with the culture medium components[46, 47]. Therefore, to evade this direct interaction, we developed an encapsulation process to coat our CoNi barcodes with a gold nanolayer. This gold coating could preserve the magnetic properties of the CoNi chips while preventing the contact between HeLa cells and the CoNi alloy.

2.3.4 CoNi barcode encapsulation through a gold covering layer

The fabricated CoNi alloy barcodes were coated with a gold layer aimed as a protective film to prevent any potential toxicity when the devices interact with living cells. We identified and followed two different gold coating processes: the first, that we name as Au-1, was based on a Potassium Dicyanoaurate(I) solution ($\text{K}[\text{Au}(\text{CN})_2]$), and the second, named as Au-2, was based on a Gold (III) Chloride solution (AuCl_3). Both coating processes contain potentially toxic elements, therefore, we tested the two approaches to study whether the different bath components could affect the cell viability.

In the first approach, Au-1, we initially prepared a batch of electroless bath solution. To prepare 1 l of this solution, 750 ml of water were heated up to 50 °C, once the temperature was stable, 200 ml of Immersion gold complex B (MacDermid Enthone) were added. Then, 5.8 g of $\text{K}[\text{Au}(\text{CN})_2]$ (MacDermid Enthone) were incorporated into the solution to maintain a gold concentration of 4 g/l. Finally, the volume was made up to 1 l, the temperature raised to 80 °C and the solution was degassed with a constant bubbling of nitrogen. The previously liberated CoNi chips were re-suspended in 1 ml of this solution in an Eppendorf tube and left to react during 15 min while submerging the tube in a water bath at 80 °C. Afterwards, the suspended barcodes were centrifuged and the supernatant electroless solution discarded. The chips were rinsed and recollected with water at least 3 times before finally re-suspended and stored in an Eppendorf tube with ethanol. Suspended CoNi-Au-1 barcodes were observed under a SEM equipment by placing a 2 μl -drop of 96% ethanol with the recollected chips on a piece of silicon wafer (Figure 2.10).

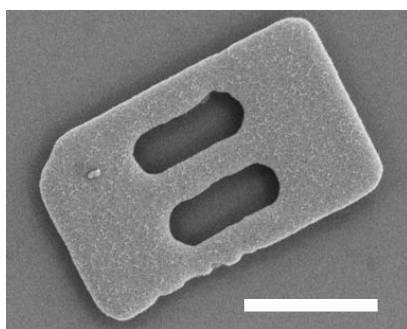


Figure 2.10. **Released CoNi-Au-1 barcodes.** SEM image of CoNi barcodes with an Au coating based on $\text{K}[\text{Au}(\text{CN})_2]$ solution, namely Au-1. Scale bars: 5 μm .

For the second Au coating approach (Au-2) based in galvanic displacement, we initially replaced the medium where the barcodes were suspended by centrifuging and re-suspending with 1 ml of a 0.34 mM HAuCl_4 (Sigma-Aldrich) aqueous solution. We ensured the solution was thoroughly mixed with a vortex, and left it to react at RT during 5 min. We then rinsed and recollected the barcodes as described previously. Detailed characterization by SEM provided an insight of the Au coating surrounding the barcodes. We

used this information to tune the coating concentration, as this coating resulted to be coarse, affecting the overall size of the device and by closing the open areas that define the bits (Figure 2.11, left).

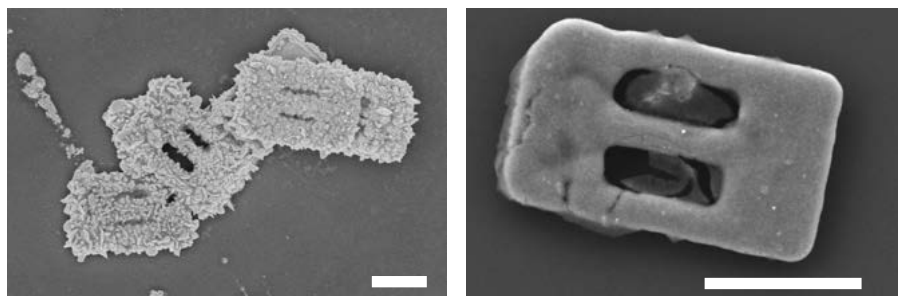


Figure 2.11. **Released CoNi-Au-2 barcodes.** SEM images of CoNi barcodes with an Au coating based on AuCl_3 solution with the original concentration (left), and with a diluted solution, namely Au-2, to decrease the thickness (right). Scale bars: $5 \mu\text{m}$.

To solve this problem, we decreased the original concentration of the AuCl_3 solution, at a ratio of $490 \mu\text{l H}_2\text{O} : 10 \mu\text{l of HAuCl}_4$ and proceeded with the same reaction parameters. These resulting devices were also examined by SEM, resulting in homogeneously distributed Au layer which preserved the size and encoding features of the designed devices (Figure 2.11, right). This second batch was used in all further Au-2 coating experiments.

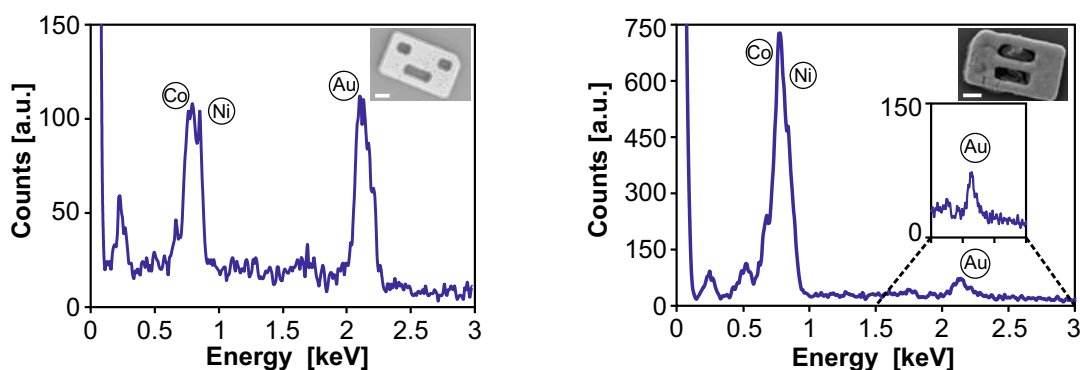


Figure 2.12. **EDXS characterization of CoNi-Au barcodes.** EDXS spectrum of a CoNi-Au barcodes (inset) with (left) the Au-1 and (right) with the Au-2 solution confirm the presence of Au. Inset graphic shows a zoom of the Au peak at 2.120 keV. Scale bars: $2 \mu\text{m}$.

We characterized the CoNi-Au devices fabricated through both coating processes. To confirm that the devices were coated with Au, an EDXS analysis was carried out on a device of each batch (Figure 2.12), demonstrating the gold deposition by the characteristic peak obtained at 2.120 keV. Moreover, from the inset images in Figure 2.12, and also from Figures 2.10 and 2.11(right), it was confirmed that there was no loss in bit dimension.

2.3.5 Biological validation of Au-encapsulated CoNi barcodes

A high concentration of both types of Au-coated magnetic barcodes (ranging from 2500 to 10000 barcodes/coverslip) were co-cultured with HeLa cells to test their toxicity. Experiments were performed as described above for CoNi barcodes, and after 24 h cells were incubated with 2 μ M calcein-AM (Sigma-Aldrich), a vital dye, for 30 min at 37 °C, fixed with 4% paraformaldehyde (PFA) and the nuclei stained with DAPI (Sigma-Aldrich). Coverslips were mounted with Fluoromount-G (Sigma-Aldrich) and cell viability was examined with Epifluorescence Microscopy (EFM, Zeiss Axioskop) exhibiting a lack of viability, such as rounded morphology and a marked reduction of calcein labelling (Figure 2.13).

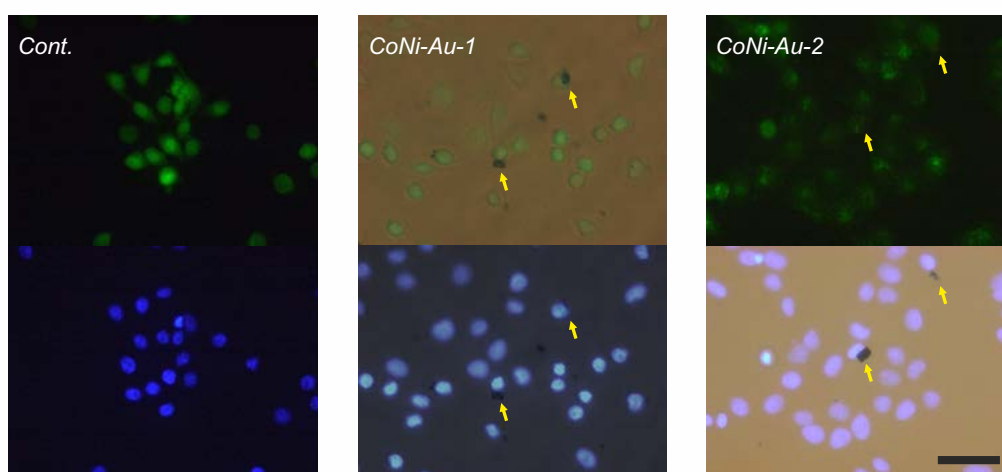


Figure 2.13. **Biological validation CoNi-Au barcodes.** EFM images of HeLa cells with and without barcodes stained with DAPI (blue, cell nuclei) and calcein-AM 2 μ M (green fluorescence) to study cell viability after 24 h in unlike control cells (Cont., left panel), cells incubated with (center) CoNi-Au-1 and (right) CoNi-Au-2. Yellow arrows point the position of the barcodes. Scale bar: 50 μ m.

Despite neither of the two Au coatings prevented cell toxicity, further analysis by confocal microscopy allowed us to detect a small percentage of internalized barcodes.

2.4 Toxicity analysis of the CoNi and Ni compounds through substrates for cell seeding

Some physical or chemical characteristics of the barcodes may interfere with extra- or intracellular mechanisms, thus, translating as toxicity factors. The barcode shape and dimensions in the range of microns as toxicity factors have been ruled out in previous studies[24–30, 32, 35]. Therefore, the chemical composition of the barcodes had to be thought as the root cause of cell death in the previous experiments. A possible explanation could encompass

the leakage of toxic ions of the material into the biological media. Accordingly, we fabricated a platform to test the toxicity over two distinct neighbouring regions consisting in the bare Ni and CoNi alloy in a single piece of wafer (Figure 2.14a). First, a Ni layer was deposited over a complete piece of wafer as showed in Figure 2.2. Next, CoNi alloy was grown over half of the previous Ni-coated wafer following the same protocol as that to fabricate the CoNi barcodes (Figure 2.3), albeit without the initial engraved photoresist barcode pattern (Figure 2.3a). Thus, the second half of the wafer maintained only the Ni seed layer. Otherwise, to fabricate a Co layer was not required as it has been already reported to be a toxic element for its oxidative stress[48]. Hence, with this fabrication we have the possibility of study cell viability over the CoNi alloy and the Ni layers.

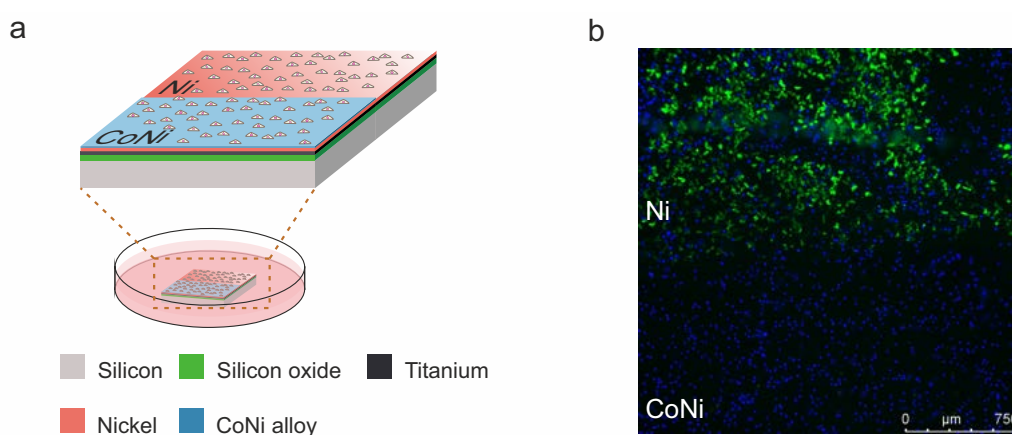


Figure 2.14. **CoNi and Ni substrates for cell toxicity analysis.** a) Schematic representation of a culture of HeLa cells on the fabricated double-layer (Ni and CoNi) chip. b) EFM image of HeLa cells stained with DAPI and 2 μ M calcein-AM 48 h after seeding on the substrate platform. DAPI labelling of nuclei (blue) indicates that cells adhere to both substrates but viability is markedly reduced in the CoNi layer as indicated by the practical absence of calcein fluorescence (green).

HeLa cells were seeded over this platform within a culture-dish (Figure 2.14a) and incubated in 2 ml of growth medium at 37 °C. After 48 h, the vital dye calcein-AM was added. Cells were fixed with 4 % PFA and the nuclei labelled with DAPI. For microscopic analysis, the platform chip was placed upside down on a glass bottom dish in a DMI6000B inverted Leica microscope coupled to a Hamamatsu CCD 9100-O2 camera.

Cells were clearly attached to the platform surface, as can be seen by DAPI labelling of nuclei (Figure 2.14b). However, viability was markedly reduced in cells adhered to substrate containing cobalt, as indicated by the absence of calcein fluorescence (Figure 2.14b). We did not observe cell death all over the culture, as seen with the previous CoNi and CoNi-Au barcodes. Most probably due to differences in the experiments, as with the substrates, incubations in small volumes, to increase the probability of chips getting internalised are not needed. Then, it could be safe to assume that CoNi barcode after its releasing, could be less compact for a living cell application,

and some parts of cobalt could have contaminated the culture. Cobalt compounds could remain in the medium after device releasing causing contamination of cell medium, being impossible to eliminate.

2.5 Ni-based barcodes

2.5.1 Fabrication of the Ni barcodes

As Ni layer was shown to be a viable material with HeLa cells, we proceeded to fabricate Ni barcodes. The fabrication started from samples with an inverted patterned fabricated with the same technology of CoNi barcodes (Figure 2.2). Ni barcodes fabrication was based on a different type of electroplating bath. A Watts nickel electroplating solution was used to deposit Ni onto the exposed areas of the substrates. The Watts Ni plating process consisted in an aqueous bath of 280 g/l of Nickel(II) sulfate hexahydrate ($\text{NiSO}_4 \cdot 6\text{H}_2\text{O}$, Merck) and 45 g/l of Nickel(II) chloride hexahydrate ($\text{NiCl}_2 \cdot 6\text{H}_2\text{O}$, Merck). 30 g/l of boric acid were added to keep the pH around 4, also acting as a reducer in the hydrogen production. Nickel sulphate was the main Ni supplier to the sample, given that it is easily soluble (as chloride) and a non-complex ion source. The nickel chloride improved the quality of the deposit since it allowed a high current density limit due to an increased ion diffusion coefficient, however it corroded the anode.

For the set-up, system of two electrodes was adequate to achieve an accurate Ni deposit, instead than for CoNi barcode fabrication where 3 electrodes were used to control the alloy deposit. The two electrodes comprise an anode of Ni and a cathode which consists in a $0.5 \text{ cm} \times 1.0 \text{ cm}$ piece of wafer to deposit the Ni layer. Both electrodes were connected to the potentiostat at a fixed working current of 15 mA during 40 s at RT, that results a current density of 30 mA/cm^2 . Afterwards, the photoresist was stripped and the devices were released using the thermal shock and peel-off method explained previously.

As in the CoNi deposition process, the electrode and the wafer piece were connected to the Autolab equipment fixing the working current at 15 mA and establishing a time of 40 s for the deposition process. After this process, the photoresist was removed.

2.5.2 Characterization of the Ni barcodes

The fabricated Ni barcodes were examined in SEM (Figure 2.15) to validate their correct shape and dimensions. Ni magnetic barcodes were also inspected by EDXS to confirm that the devices were only made of Ni, as shown in Figure 2.16a with the Ni characteristic peak of 0.851 keV. In addition, the device thickness was evaluated prior their release with confocal microscopy (Figure 2.16b) measuring a thickness of $0.81 \mu\text{m}$.

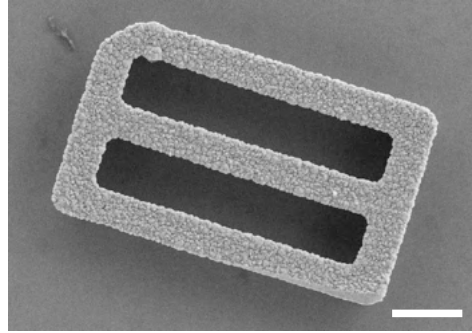


Figure 2.15. **Released Ni barcodes.** SEM image of a Ni fabricated barcode placed on a piece of wafer after their release. Scale bar: 2 μm .

Furthermore, we performed the magnetic characterization of the Ni barcodes with the VSM as described above for CoNi alloy barcodes. Figure 2.16c shows the hysteresis loop for some Ni barcodes spread on a piece of silicon wafer. Due to there was a small number of Ni barcodes, the measurement resulted noisy, obtaining a magnetic moment closed to the detection limit of the equipment.

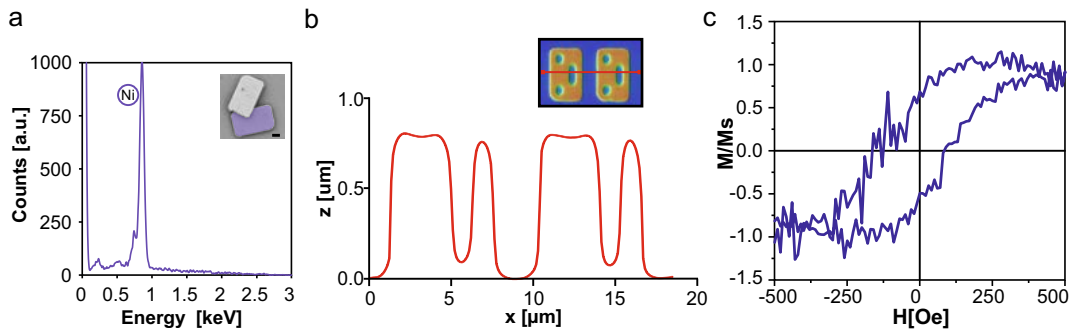


Figure 2.16. **Ni barcodes: physical and magnetic characterization.** a) EDXS spectrum a barcode, shown in the inset (code number 255), confirmed the only presence Ni. The signal showed the characteristic peak of Ni 0.851 keV. Scale bars: 2 μm . b) Vertical profile just before the releasing process (inset shows the scanned line). z represents the vertical dimension and x the length along the scanned line. c) Magnetic characterization of the Ni devices through the use of a VSM. M/M_s represents the magnetization of Ni normalized by its saturation magnetization and H the magnetic field.

Following equation (2.1), the magnetic moment of a single Ni barcode can be derived from as:

$$m_{Ni} = M_{Ni}V \quad (2.2)$$

where m_{Ni} is the Ni barcode saturation magnetic moment, M_{Ni} is the saturation magnetization of Ni, x and V is the volume of the barcode. The saturation magnetization of the Ni devices is lower than that of the CoNi barcodes due to the absence of Co.

2.5.3 Biological validation of the Ni barcodes

Additionally to the toxicity platform study, Ni suspended barcodes were biologically tested with HeLa cells. Cells were grown on glass coverslips as described before and, after 24 h, different concentrations ranging from 2500 to 10000 of Ni barcodes were added in different experiments, and incubation continued another 24 h. To analyse cell viability, cells were stained with the vital dye CellTracker (Thermo Fisher Scientific) for 45 min (as indicated by the manufacturer) and, then, fixed with 4% PFA and the nuclei stained with DAPI. Cells were mounted with Fluoromount-G and analysed under EFM.

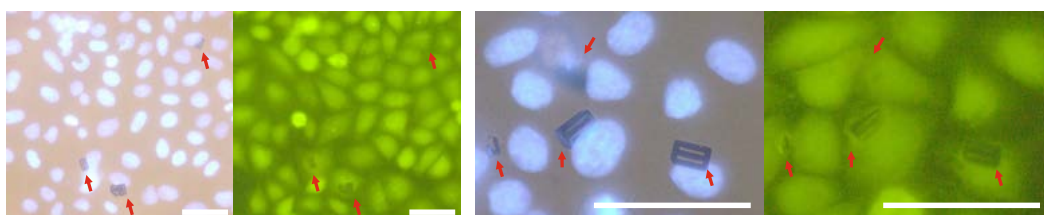


Figure 2.17. **Biological validation of Ni barcodes co-cultured with HeLa cells.** Images of HeLa cells viability after incubation with Ni barcodes. Fixed cells stained with CellTracker (green fluorescence) and DAPI (nuclei, blue). Red arrows point the position of the Ni barcodes. Scale bars: 40 μm .

Cell viability, using the different Ni barcodes concentrations, was assessed by fluorescence intensity after CellTracker labelling, and was unaffected in the whole culture, and barcode-bearing cells appeared identical to neighbouring cells (Figure 2.17). Furthermore, with the lowest cell-chip ratio (2:1) we were able to observe up to 10-13% of cells with internalized barcodes.

2.6 Ni-based barcodes for cell labelling and magnetic mechanical-manipulation

2.6.1 Ni magnetic barcodes for cell labelling

To demonstrate the labelling and tracking capabilities of the devices, HeLa cells were monitored under a DMI6000B inverted Leica microscope coupled to a Hamamatsu CCD 9100-O2 camera with time-lapse technology. A HeLa cell was identified bearing the barcode with decimal number 0 (= 0000-0000, binary code) and was tracked for more than 24 h (Figure 2.18) with a perfect identification of the cell by the Ni barcode.

Hence, Ni barcodes are demonstrated to employ for cell labelling along the complete cell cycle. Additionally, cells exhibited a normal functionality, showing that they underwent division cycles comparable to those of the surrounding control cells, namely Ni barcodes do not affect the cell cycle. Thus, after the cell division, the magnetic barcode will remain within one of the daughter cells.

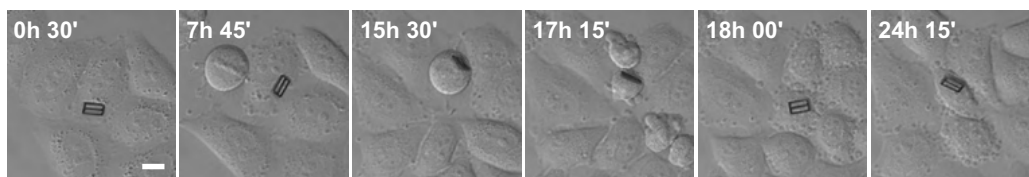


Figure 2.18. **HeLa cell labelling and tracking by Ni barcodes.** Images taken from a 24-hour videomicroscopy showing a HeLa cell with a Ni barcode inside (code number: 0000-0000 = 0). Cell before division (15h 30') and daughter cells (17h 15'). Scale bar: 10 μm

2.6.2 Characterization of the magnet for the magnetic set-up

After demonstrating their biological compatibility and their use for labelling in HeLa cells, the Ni barcodes were employed in the magnetic manipulation of cells. To accomplish this we will make use of a standard magnet.

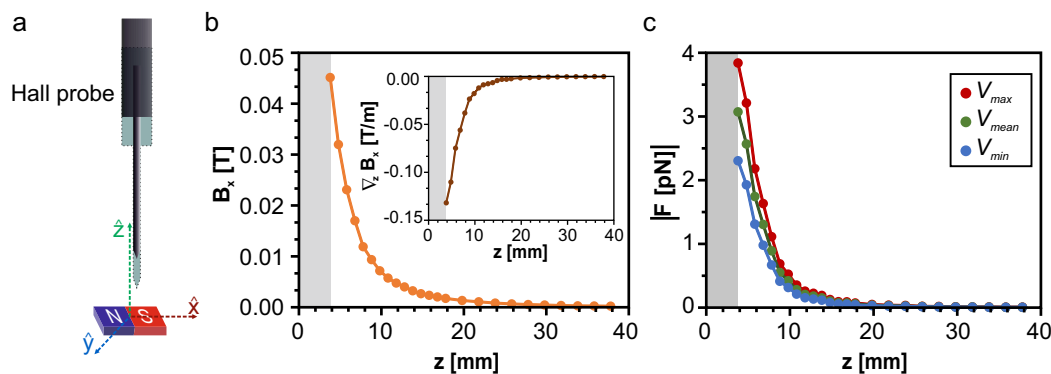


Figure 2.19. **Characterization of the magnet for the magnetic set-up for cell manipulation.** a) Schematic representation of the magnet characterization. The magnetic field of the magnet were measured along the z – axis with a Hall probe. b) Measured magnetic field, B_x , of the magnet and the calculated gradient of magnetic field, $\nabla_z B_x$. c) Estimated force, F , applied over the devices depending on the distance to the magnet for the maximum, mean and minimum barcode volumes. Measurements for Hall probe-magnet distances below 3.81 mm (grey area) were not carried out as this is the location from the tip of the Hall sensor inside the probe.

We performed a magnetic characterization of the magnet prior to its use on the set-up. For that, we employed a gaussmeter Lakeshore 475 DSP to measure the magnetic field along a perpendicular plane to the magnet, $\vec{B} = B_x$, (Figure 2.19a and 2.19b) in order to determine the gradient of this field, $\vec{\nabla}_z B_x$ (Figure 2.19b, inset). The magnetic force acting on a barcode (and therefore on the cell) can be expressed by way of:

$$F_z = m \nabla_z B_x \quad (2.3)$$

As the magnetic moment of the barcodes depends on their volume (see equation (2.2)), the magnetic force on the barcode was calculated depending on the design (binary code) (see Figure 1 and Supplementary Figure 1).

The maximum volume corresponds to the barcode 1111-1111 = 256 ($V_{max} = 60 \mu m^3$) and the minimum to 0000-0000 = 0 ($V_{min} = 36 \mu m^3$). A mean value of the volume corresponds to several barcodes such as the 0110-1001 = 105 or 1001-1001 = 153 ($V_{mean} = 48 \mu m^3$). Figure 2.19c represents the values of the magnetic force exerted on HeLa cells with internalized magnetic barcodes for those three barcode volumes. This force could reach up to 3.83 pN. As a first approximation, it is assumed that the barcode is magnetically saturated.

2.6.3 Cell magnetic manipulation

To demonstrate the cell manipulation capabilities, 50000 HeLa cells were initially seeded in triplicate in a 12-well plate and cultured with 25000 Ni barcodes (ratio cell-chip 2:1) over 24 h.

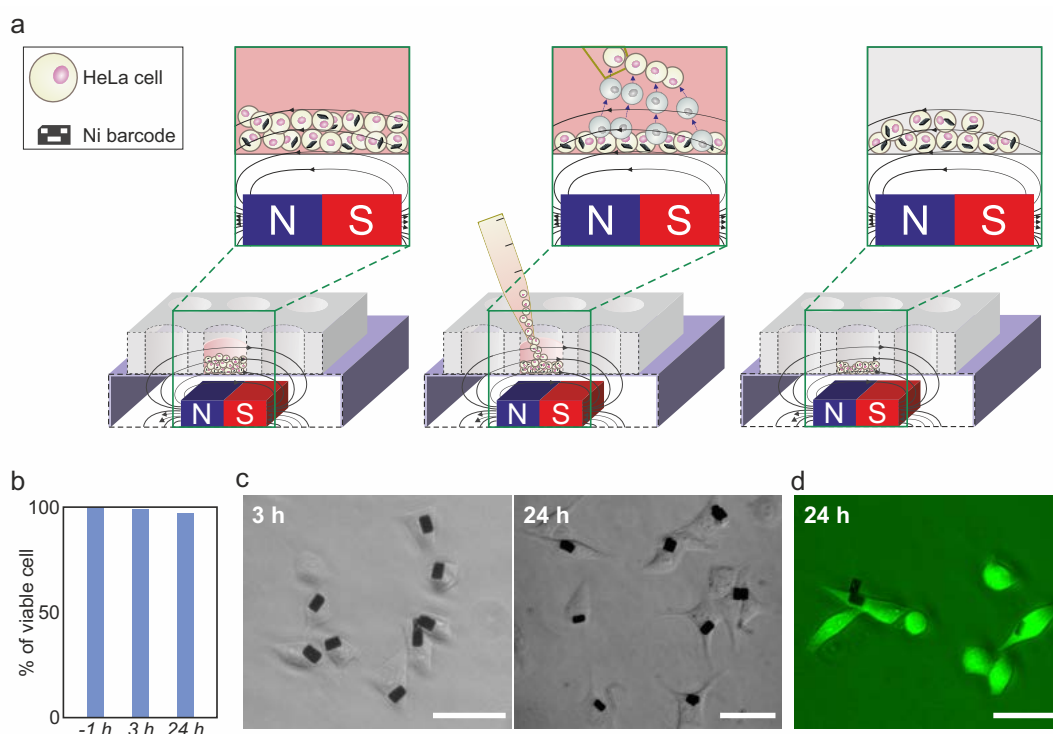


Figure 2.20. **Magnetic manipulation of HeLa cells with internalized Ni barcodes.** a) Schematic representation of the cell separation process. (left) A magnet was placed close to the bottom of the well containing the cell suspension. After a 15'' exposure, most of the cells without a device could be transferred to another well (centre), thus enriching the cell population with internalized Ni barcode that remains in the first well. b) Viability of cells cultured with Ni barcode before (-1 h) the magnetic separation and of those separated bearing Ni barcodes 3 h and 24 h after magnetic separation. Percentage values were obtained by analysing approximately 1000 cells for each condition. c) Optical images 3 h and 24 h after magnetic separation of HeLa cells bearing Ni barcodes. d) EFM images of HeLa cells stained with calcein-AM 2 μM (green fluorescence) 24 h after magnetic separation to assess cell viability. Scale bars: 40 μm

Then, cells were detached from the well substrate with 100 μl of trypsin and, after adding 0.5 ml of complete medium, the previously characterized magnet was located (4.9 mm) under the well dish to perform the magnetic separation (Figure 2.20a). Therefore, magnetic forces with a value of ~ 2.57 pN are expected to act over the cells-bearing Ni barcodes. After 15 s of magnet exposure and assuming that cells with internalized magnetic barcodes would remain at the bottom of the well, the rest of the culture medium, being hovering by the effect of the trypsin, was removed by micropipette aspiration, carrying along the cells without barcodes. The remaining cells with internalized Ni barcodes were re-suspended with new fresh medium after detaching the magnet.

These cells with internalized magnetic Ni barcodes were also observed 3 h after the exposure to the magnet to verify if cell viability and/or morphology seemed affected by the magnetic separation process. HeLa cells looked healthy and firmly attached to the plate (Figure 2.20b and 2.20c). Observation of the cells under the optical microscopy 3 h after magnetic separation showed a tenfold increase in the population of barcode-bearing cells, from 6% to 60%. It is important to state here that both the shape and the aspect of HeLa cells containing Ni barcodes were indistinguishable from the surrounding cells. Then, these cells were cultured at 37 $^{\circ}\text{C}$ and their proliferation analysed after 24 h. As expected, the percentage of cells with microdevices was reduced after 24 h of incubation, due to the dilution of the carrier cells in the proliferating population but the viability of cells 24 h after magnetic separation, assessed by calcein or CellTracker labelling, was similar to that of the cells analysed before separation (Figure 2.20b and 2.20c). In an independent experiment, we checked the viability of cells with devices up to 4 days after the magnetic separation, where cell population developed perfectly healthy (Figure 2.21).

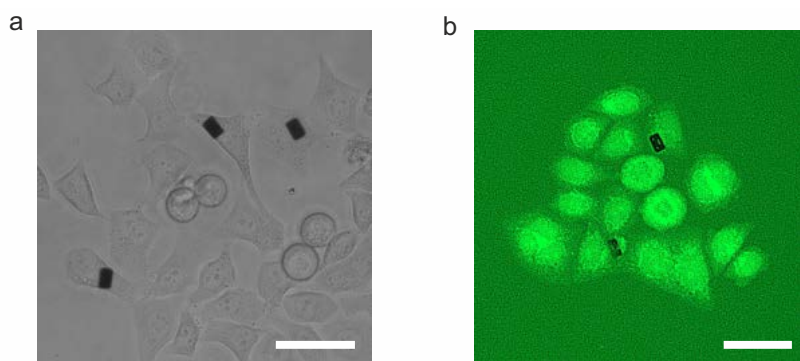


Figure 2.21. HeLa cells 4 days after magnetic manipulation using Ni barcodes. a) Optical image of HeLa cells 4 days after magnetic separation. b) EFM images of HeLa cells stained with 2 μM calcein-AM (green fluorescence) 4 days after magnetic separation to assess cell viability. Scale bars: 20 μm .

Notably, it has been demonstrated that HeLa cells with internalized magnetic barcodes can be recovered after magnetic separation, by re-suspending

the cells in new fresh medium and aspirated them to translate to another container.

2.7 Discussion

In this work, we present the development and fabrication of CoNi and Ni magnetic barcodes for cell labelling and manipulation. All the devices were fabricated with an initial photolithographic process to define their physical properties and subsequently complemented with the inclusion of an electroplating processes. Initially, the fabrication technology of CoNi alloy devices was developed to obtain homogeneous and smooth barcodes by optimizing the concentration of the different components of the electroplating bath. CoNi devices were found to be toxic for living HeLa cells due to the presence of cobalt.

Consequently, we studied the possibility of coating the CoNi alloy barcodes with a gold layer as an encapsulation method to avoid toxicity. Therefore, two different coating processes were developed and two batches of the CoNi alloy barcodes were coated. After analysing the cultured cells exposed to the Au-coated barcodes, we found that both coatings did not prevent the toxicity. Previous studies have reported that Co could be released from micro- and nanoparticles ensuring a toxic environment for living cells[46, 47]. This could explain that cells attached to the surface of CoNi alloy did not survive, even with an Au coating, and were unable to retain vital markers. Hence, we fabricated Ni barcodes to study the effects of this material on cell viability. We found that incubating cells with increasing concentrations of Ni barcodes did not affect their viability and that cells that had internalized these devices apparently preserved their functionality and ability to proliferate. Thereby, we characterized the magnetic properties of the Ni barcodes, resulting in a lower magnetic moment than that of CoNi alloy, yet still suitable for magnetic handling. We demonstrate a magnetic separation of HeLa cells with internalized Ni barcode, with the consequent enrichment of this cell population. The viability of these cells 24 h after separation was practically of 100%. More importantly, isolated cell with internalized barcodes grown properly 4 days after the exposure to the magnet. This result let a separated cell population being healthy and suitable for further experiments.

This study provides the development and demonstration of Ni barcodes as magnetic micrometric tools for easy cell manipulation and their potential emergence as viable tools for cell tracking in cell-based therapy. For instance, it is reasonable to suppose that this type of devices could be used to lead a specific cell type to a precise site. In this sense, the application of an external magnetic field to direct magnetic nanoparticles anchored to T-cells to the tumor site has recently been reported[49] and similarly with human mesenchymal stem cells, that have a significant potential for regenerative cell therapies[50]. Cell separation, sorting and targeting are necessary tasks in fundamental investigation in health science, thus, these type of devices are a step forward in the field of cell manipulation.

Moreover, our group, and also other groups are starting to work on a wide range of intracellular chips with several applications: polysilicon barcodes for cell tracking[25], mechanical sensors for pressure change measures[32,

33], biochemical sensors with the use of SPA chips[35, 44], and even a radio-frequency identification and transceiver systems for tracking and monitoring living cells[51]. Henceforth, we envision the integration of multiple functionalities in a single chip. In the next future, this work will contribute to the implementation of the manipulation of more sophisticated intracellular chips controlled by external magnetic fields.

Bibliography

- [1] Patrick J Sweeney et al. Rfid for dummies. 2010.
- [2] Sheila R Nicewarner-Pena, R Griffith Freeman, Brian D Reiss, Lin He, David J Peña, Ian D Walton, Remy Cromer, Christine D Keating, and Michael J Natan. Submicrometer metallic barcodes. *Science*, 294(5540): 137–141, 2001.
- [3] Warren CW Chan, Dustin J Maxwell, Xiaohu Gao, Robert E Bailey, Mingyong Han, and Shuming Nie. Luminescent quantum dots for multiplexed biological detection and imaging. *Current opinion in biotechnology*, 13(1):40–46, 2002.
- [4] David J Lockhart and Mark O Trulson. Multiplex metallica. *Nature biotechnology*, 19(12):1122–1123, 2001.
- [5] Randall J True, Micah K Taylor, Gabriela S Chakarova, and Ian D Walton. Microfabricated templates for the electrodeposition of metallic barcodes for use in multiplexed bioassays. *The 26th Annual International Conference of the IEEE Engineering in Medicine and Biology Society*, 1:2619–2622, 2004.
- [6] Joseph Wang, Guodong Liu, and Qiyu Zhu. Indium microrod tags for electrochemical detection of dna hybridization. *Analytical chemistry*, 75(22):6218–6222, 2003.
- [7] Sarah E Brunker, Kristin B Cederquist, and Christine D Keating. Metallic barcodes for multiplexed bioassays. 2007.
- [8] Tao Song, Junqing Liu, Wenbin Li, Yunhong Li, Qiuhua Yang, Xiaoqun Gong, Lixue Xuan, and Jin Chang. Self-healing encapsulation strategy for preparing highly stable, functionalized quantum-dot barcodes. *ACS applied materials & interfaces*, 6(4):2745–2752, 2014.
- [9] R Griffith Freeman, Paul A Raju, Scott M Norton, Ian D Walton, Patrick C Smith, Lin He, Michael J Natan, Y Sha Michael, and Sharron G Penn. Use of nanobarcode® particles in bioassays. *NanoBiotechnology Protocols*, pages 73–83, 2005.
- [10] Bronwyn J Battersby and Matt Trau. Novel miniaturized systems in high-throughput screening. *Trends in biotechnology*, 20(4):167–173, 2002.
- [11] Bronwyn J Battersby, Darryn Bryant, Wim Meutermans, Daniel Matthews, Mark L Smythe, and Matt Trau. Toward larger chemical libraries: encoding with fluorescent colloids in combinatorial chemistry. *Journal of the American Chemical Society*, 122(9):2138–2139, 2000.
- [12] Hicham Fenniri, Lunhan Ding, Alexander E Ribbe, and Yegor Zyrianov. Barcoded resins: A new concept for polymer-supported combinatorial library self-deconvolution. *Journal of the American Chemical Society*, 123(33):8151–8152, 2001.

- [13] Meihong Chen, Quan Du, Hong-Yan Zhang, Xiaoxia Wang, and Zicai Liang. High-throughput screening using sirna (rna) libraries. *Expert review of molecular diagnostics*, 7(3):281–291, 2007.
- [14] GS Galitonov, SW Birtwell, NI Zheludev, and H Morgan. High capacity tagging using nanostructured diffraction barcodes. *Optics express*, 14(4):1382–1387, 2006.
- [15] Guoxin Zhang, Yanbo Liu, Chunfu Zhang, Weiqing Hu, Wanbang Xu, Zheng Li, Sheng Liang, Jinqian Cao, and Yongxian Wang. Aqueous immune magnetite nanoparticles for immunoassay. *Journal of Nanoparticle Research*, 11(2):441–448, 2009.
- [16] Andrea Fornara, Petter Johansson, Karolina Petersson, Stefan Gustafsson, Jian Qin, Eva Olsson, Dag Ilver, Anatol Krozer, Mamoun Muhammed, and Christer Johansson. Tailored magnetic nanoparticles for direct and sensitive detection of biomolecules in biological samples. *Nano letters*, 8(10):3423–3428, 2008.
- [17] Rui Hao, Ruijun Xing, Zhichuan Xu, Yanglong Hou, Song Gao, and Shouheng Sun. Synthesis, functionalization, and biomedical applications of multifunctional magnetic nanoparticles. *Advanced materials*, 22(25):2729–2742, 2010.
- [18] Hakho Lee, Alfreda M Purdon, Vincent Chu, and Robert M Westervelt. Controlled assembly of magnetic nanoparticles from magnetotactic bacteria using microelectromagnets arrays. *Nano letters*, 4(5):995–998, 2004.
- [19] Morteza Mahmoudi, Shilpa Sant, Ben Wang, Sophie Laurent, and Tapas Sen. Superparamagnetic iron oxide nanoparticles (spions): development, surface modification and applications in chemotherapy. *Advanced drug delivery reviews*, 63(1-2):24–46, 2011.
- [20] Pedro Tartaj, Maria del Puerto Morales, Sabino Veintemillas-Verdaguer, Teresita González-Carreño, and Carlos J Serna. The preparation of magnetic nanoparticles for applications in biomedicine. *Journal of physics D: Applied physics*, 36(13):R182, 2003.
- [21] Jiaojiao Liu, Xiaodong Tian, Meimei Bao, Jingliang Li, Yujiang Dou, Bing Yuan, Kai Yang, and Yuqiang Ma. Manipulation of cellular orientation and migration by internalized magnetic particles. *Materials Chemistry Frontiers*, 1(5):933–936, 2017.
- [22] Naside Gozde Durmus, H Cumhur Tekin, Sinan Guven, Kaushik Sridhar, Ahu Arslan Yildiz, Gizem Calibasi, Ionita Ghiran, Ronald W Davis, Lars M Steinmetz, and Utkan Demirci. Magnetic levitation of single cells. *Proceedings of the National Academy of Sciences*, 112(28):E3661–E3668, 2015.
- [23] Shujing Lin, Xiao Zhi, Di Chen, Fangfang Xia, Yihuan Shen, Jiaqi Niu, Shiyi Huang, Jie Song, Jianmin Miao, Daxiang Cui, et al. A flyover style

- microfluidic chip for highly purified magnetic cell separation. *Biosensors and Bioelectronics*, 129:175–181, 2019.
- [24] Sergi Novo, Leonardo Barrios, Josep Santalo, Rodrigo Gómez-Martínez, Marta Duch, Jaume Esteve, José Antonio Plaza, Carme Nogués, and Elena Ibáñez. A novel embryo identification system by direct tagging of mouse embryos using silicon-based barcodes. *Human reproduction*, 26(1):96–105, 2011.
- [25] Elisabet Fernandez-Rosas, Rodrigo Gomez, Elena Ibanez, Leonardo Barrios, Marta Duch, Jaume Esteve, Carme Nogués, and José Antonio Plaza. Intracellular polysilicon barcodes for cell tracking. *Small*, 5(21):2433–2439, 2009.
- [26] Elisabet Fernández-Rosas, Rodrigo Gómez, Elena Ibañez, Lleonard Barrios, Marta Duch, Jaume Esteve, José A Plaza, and Carme Nogués. Internalization and cytotoxicity analysis of silicon-based microparticles in macrophages and embryos. *Biomedical microdevices*, 12(3):371–379, 2010.
- [27] E Fernandez-Rosas, A Baldi, E Ibañez, L Barrios, S Novo, J Esteve, JA Plaza, M Duch, R Gómez, O Castell, et al. Chemical functionalization of polysilicon microparticles for single-cell studies. *Langmuir*, 27(13):8302–8308, 2011.
- [28] Sergi Novo, Oriol Penon, Leonardo Barrios, Carme Nogués, Josep Santaló, Sara Durán, Rodrigo Gómez-Matínez, Josep Samitier, José Antonio Plaza, Luisa Pérez-García, et al. Direct embryo tagging and identification system by attachment of biofunctionalized polysilicon barcodes to the zona pellucida of mouse embryos. *Human Reproduction*, 28(6):1519–1527, 2013.
- [29] Oriol Penon, Sergi Novo, Sara Durán, Elena Ibañez, Carme Nogués, Josep Samitier, Marta Duch, José Antonio Plaza, and Lluïsa Pérez-García. Efficient biofunctionalization of polysilicon barcodes for adhesion to the zona pellucida of mouse embryos. *Bioconjugate chemistry*, 23(12):2392–2402, 2012.
- [30] Sergi Novo, Carme Nogués, Oriol Penon, Leonardo Barrios, Josep Santaló, Rodrigo Gómez-Martínez, Jaume Esteve, Abdelhamid Errachid, José Antonio Plaza, Lluïsa Pérez-García, et al. Barcode tagging of human oocytes and embryos to prevent mix-ups in assisted reproduction technologies. *Human reproduction*, 29(1):18–28, 2014.
- [31] Nosang V Myung, D-Y Park, B-Y Yoo, and Paulo TA Sumodjo. Development of electroplated magnetic materials for mems. *Journal of Magnetism and Magnetic Materials*, 265(2):189–198, 2003.
- [32] Rodrigo Gómez-Martínez, Alberto M Hernández-Pinto, Marta Duch, Patricia Vázquez, Kirill Zinoviev, J Enrique, Jaume Esteve, Teresa Suárez, and José A Plaza. Silicon chips detect intracellular pressure changes in living cells. *Nature nanotechnology*, 8(7):517, 2013.

- [33] Marta Duch, Núria Torras, Maki Asami, Toru Suzuki, María Isabel Arjona, Rodrigo Gómez-Martínez, Matthew D VerMilyea, Robert Castilla, José Antonio Plaza, and Anthony CF Perry. Tracking intracellular forces and mechanical property changes in mouse one-cell embryo development. *Nature Materials*, pages 1–10, 2020.
- [34] S Durán, M Duch, T Patiño, A Torres, O Penon, R Gómez-Martínez, L Barrios, J Esteve, C Nogués, L Pérez-García, et al. Technological development of intracellular polysilicon–chromium–gold chips for orthogonal chemical functionalization. *Sensors and Actuators B: Chemical*, 209: 212–224, 2015.
- [35] Núria Torras, Juan Pablo Aguil, Patricia Vázquez, Marta Duch, Alberto M Hernández-Pinto, Josep Samitier, Enrique J de la Rosa, Jaume Esteve, Teresa Suárez, Lluïsa Pérez-García, et al. Suspended planar-array chips for molecular multiplexing at the microscale. *Advanced Materials*, 28(7):1449–1454, 2016.
- [36] Oriol Penon, Dimitrios Siapkis, Sergi Novo, Sara Durán, Gerard Oncins, Abdelhamid Errachid, Lleonard Barrios, Carme Nogués, Marta Duch, José Antonio Plaza, et al. Optimized immobilization of lectins using self-assembled monolayers on polysilicon encoded materials for cell tagging. *Colloids and Surfaces B: Biointerfaces*, 116:104–113, 2014.
- [37] Sergi Novo, Roser Morató, Oriol Penon, Sara Duran, Leonardo Barrios, Carme Nogués, José Antonio Plaza, Luisa Pérez-García, Teresa Mogas, and Elena Ibáñez. Identification of bovine embryos cultured in groups by attachment of barcodes to the zona pellucida. *Reproduction, Fertility and Development*, 26(5):645–652, 2014.
- [38] Sara Durán Ibáñez. *Suspended micro-and nanotools for cell biology*. PhD thesis, Universitat Autònoma de Barcelona, 2014.
- [39] Rodrigo Gómez Martínez. *Intracellular silicon chips*. PhD thesis, Universitat Autònoma de Barcelona, 2016.
- [40] M Duch, J Esteve, E Gómez, R Pérez-Castillejos, and E Vallés. Development and characterization of co-ni alloys for microsystems applications. *Journal of the Electrochemical Society*, 149(4):C201–C208, 2002.
- [41] M Duch, J Esteve, E Gomez, R Perez-Castillejos, and E Valles. Electrodeposited co-ni alloys for mems. *Journal of Micromechanics and microengineering*, 12(4):400, 2002.
- [42] Mordechai Schlesinger and Milan Paunovic. Modern electroplating. 55, 2011.
- [43] Xinwei Cui and Weixing Chen. Saccharin effects on direct-current electroplating nanocrystalline ni–cu alloys. *Journal of The Electrochemical Society*, 155(9):K133–K139, 2008.
- [44] Juan Pablo Aguil, Núria Torras, Marta Duch, Jaume Esteve, Lluïsa Pérez-García, Josep Samitier, and José A Plaza. Highly anisotropic

- suspended planar-array chips with multidimensional sub-micrometric biomolecular patterns. *Advanced Functional Materials*, 27(13):1605912, 2017.
- [45] Cristina Bran, José A Fernández-Roldán, Esther M Palmero, Eider Berganza, J Guzman, RP Del Real, A Asenjo, A Fraile Rodríguez, M Forster, L Aballe, et al. Direct observation of transverse and vortex metastable magnetic domains in cylindrical nanowires. *Physical Review B*, 96(12):125415, 2017.
- [46] Enrico Sabbioni, Salvador Fortaner, Massimo Farina, Riccardo Del Torchio, Claudia Petrarca, Giovanni Bernardini, Renato Mariani-Costantini, Silvia Perconti, Luca Di Giampaolo, Rosalba Gornati, et al. Interaction with culture medium components, cellular uptake and intracellular distribution of cobalt nanoparticles, microparticles and ions in balb/3t3 mouse fibroblasts. *Nanotoxicology*, 8(1):88–99, 2014.
- [47] Naomi Lubick. Nanosilver toxicity: ions, nanoparticles- or both? *ACS Publications*, 2008.
- [48] Sourav Chattopadhyay, Sandeep Kumar Dash, Satyajit Tripathy, Balam Das, Debasis Mandal, Panchanan Pramanik, and Somenath Roy. Toxicity of cobalt oxide nanoparticles to normal cells; an in vitro and in vivo study. *Chemico-biological interactions*, 226:58–71, 2015.
- [49] Laura Sanz-Ortega, Yadileiny Portilla, Sonia Pérez-Yagüe, and Domingo F Barber. Magnetic targeting of adoptively transferred tumour-specific nanoparticle-loaded cd8+ t cells does not improve their tumour infiltration in a mouse model of cancer but promotes the retention of these cells in tumour-draining lymph nodes. *Journal of nanobiotechnology*, 17(1):1–24, 2019.
- [50] Natalia Landázuri, Sheng Tong, Jin Suo, Giji Joseph, Daiana Weiss, Diane J Sutcliffe, Don P Giddens, Gang Bao, and W Robert Taylor. Magnetic targeting of human mesenchymal stem cells with internalized superparamagnetic iron oxide nanoparticles. *Small*, 9(23):4017–4026, 2013.
- [51] Xiaolin Hu, Kamal Aggarwal, Mimi X Yang, Kokab B Parizi, Xiaoqing Xu, Demir Akin, Ada SY Poon, and H-S Philip Wong. Micrometer-scale magnetic-resonance-coupled radio-frequency identification and transceivers for wireless sensors in cells. *Physical Review Applied*, 8(1):014031, 2017.

Chapter 3

Second generation of an intracellular pressure sensor with high sensibility and a reference cavity

A high sensitive pressure sensor smaller than a living cell, based on a previously intracellular pressure sensor developed by the group, is presented in this chapter. Intracellular mechanical forces are involved in basic cellular processes, such as cell migration or development. The microelectronic techniques allow the miniaturization of complex micro- and nanosystems, thus, silicon-based intracellular devices can provide real-time monitoring of activity within individual living cells. The MNTL group has previously developed an intracellular pressure sensor capable to detect changes within the cell of external pressures, but not sensitive enough to measure internal forces. Here, to improve the sensitivity of the previous design we propose the fabrication of a silicon chip with a cavity sealed in air at room temperature and atmospheric pressure. This new design consist in two cavities: a sensing cavity, through which the pressure is measured; and a reference cavity, that compensates the measure from the sensing cavity when the device is tilted. The cavities of the sensor are structured by two polysilicon layers separated by an air gap. The ground of a technology development for a sealing process at room temperature and atmospheric pressure, with micro- and nanotechniques is established, in order to enclose air to improve the sensibility of the device. Different polymers were tested as a cap to seal the cavities through photolithographic processes. The inflowing of the polymer inside the cavities is a risk during the fabrication development, since it could disable the devices. Despite the low fabrication yield, pressure sensors have been properly fabricated attaining to measure pressure changes down to 25 mbar. The sealing of the devices has been the main challenge during the fabrication development in which further improvements should be done to achieve a stable mass production for a reliable intracellular pressure measure.

3.1 Introduction

Cells are heterogeneous mixtures of different components as organelles and a network of microtubules and filaments. Fundamental processes driving cell function are affected by changes in cell mechanical behaviour[1, 2]. Particularly, intracellular pressure is an important regulator in cell dynamics because it is involved in many important processes as cell shape, development, migration and differentiation[3, 4]. Thus, it is necessary to understand the changes in pressure *in situ* through the cell cycle, either in specific subcellular components, as vacuole, and cytoplasm.

Hence, the technology development of sophisticated miniaturized intracellular sensors able to monitor intracellular processes is in the focus of the research, from the need to detect the small variations that govern the mechanics of intracellular processes[5]. The integration of new tools with nanosized moving parts[6] offers enhanced mechanical sensing systems with higher resolution and sensitivity.

Current techniques for measuring cellular pressure can be classified in indirect and direct methods[3]. Indirect methods are based on an external exploration of the cell, as the measure of the cell shape change in response of an known external stimuli[7], or experiments that generate large deformation as micropipette cell aspiration[8]. However, these methods have the disadvantage of obtaining an indirect measure as they both, induce the load and read the response from the cell exterior. On the other hand, direct methods are based on pipette insertion[9], as servo-null technique where a micropipette is introduced into the cytoplasm as pressure probe, changes in the micropipette resistance translate into changes in cell pressure[10, 11]. This technique is highly invasive and can damage mechanically the cell membrane impacting in cell viability and pervert the study, both in the data collection and interpretation[12].

A step forward was done when a novel chip was internalized in living cells allowing a direct measure and monitoring of cell pressure[13]. These intracellular chips, as pressure sensors, consist in two polysilicon membranes separated by a vacuum gap. Their direct optical detection method enable to detect fluctuations in intracellular pressure by measuring the changes in the reflected light caused by the variation in the gap length between the membranes, being able to detect intracellular pressure changes of 1 bar. Nonetheless, to obtain more sensitive devices that allow to better characterize cell interior is still a challenge, both for biology and for the fabrication processes.

In this chapter, it is presented a new pressure sensor in which the technology of the first generation of sensors[13] have been improved to develop a more sensitive device. To achieve that, the main difference is that the sealing of the cavity has to be done at room temperature and atmospheric pressure conditions. Common processes of microsystem techniques used to work at very low pressure and high temperature conditions. Therefore, if the cavity of the sensor is sealed under these conditions, the membranes of the sensor

will suffer a high displacement when the device is in its working environment (atmospheric pressure and room temperature), with the risk of breaking the membranes under relevant changes. Thereby, we develop a sealing method with a baked-polymide-cap by a photolithographic process atmospheric pressure and room temperature. The risk of inflowing the polyimide in the sensor cavity makes the sealing a delicate step. Large batch production remains as future work. Besides, a reference cavity has been included in the new proposal, so that the measures can be calibrated and corrected easily when the device is tilted.

3.1.1 Previous background of the group

As mentioned in 3.1, a NanoOptoMechanical System (NOMS) as an Intracellular Pressure Sensor (IPS) were successfully developed previously in the group (Figure 3.1). This section of the chapter intends to be a contextualization looking at the previous IPS developed by the group which was published in *Nature Nanotechnology* (Figure 3.1)[13] and is widely described in Gómez-Martínez thesis[14].



Figure 3.1. Cover of the publication of the previous IPS. Cover from Nature Nanotechnology showing a HeLa cell taking a silicon pressure sensor.

These IPSs were internalized by living cells being able to detect intracellular pressure changes of 1 bar. The system allowed to directly have information of the pressure changes inside the cells.

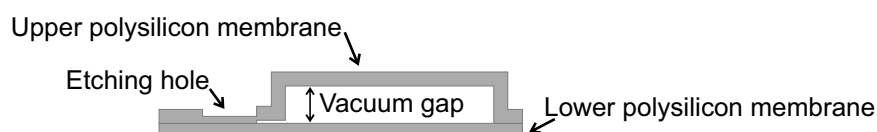


Figure 3.2. Schematic of the device parts. The device consists of two polysilicon membranes separated by a vacuum gap and an etching hole acting as an optical reference

The design consisted in a mechanical sensor defined by two polysilicon membranes separated by a vacuum gap, defining a Fabry-Perot cavity, and an etching hole uses as an optical reference area (Figure 3.2). The dimensions of this Fabry-Perot resonator were fixed to $3 \mu\text{m} \times 3 \mu\text{m} \times 0.4 \mu\text{m}$, based on prior analytical and simulated studies of the mechanical behaviour of the polysilicon layers and the optical response through them. Thus, the final lateral dimensions of the NOMS were suited to $6 \mu\text{m} \times 4 \mu\text{m}$, with an optical area as a reference of $\sim 1 \mu\text{m}$ of diameter, and a maximum height of 400 nm (Figure 3.3).

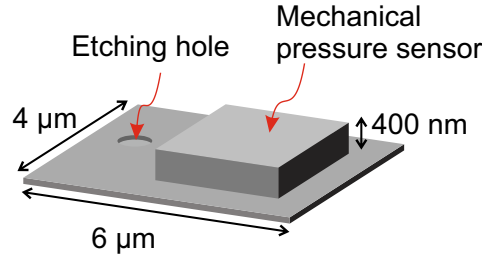


Figure 3.3. **Device dimensions.** Representation of the device dimensions. Red arrows point the delimited etching hole as a reference area and the cavity which acts as a mechanical pressure sensor.

The operational mode of the devices is as follows. The two polysilicon membranes constitute a Fabry-Perot interferometer[15] as they act as parallel reflecting mirrors, this means that the cavity is partially transparent for some wavelengths. When an external pressure, P , acts on the device, the membranes deflect and the gap distance between them, t_{gap} , changes (Figure 3.4). Hence, when the devices are observed under a microscope, the intensity of the reflected light at the centre of the sensor membranes, I'_{sensor} , is shaped by the applied external pressure. Moreover, an optical reference area is included, in order to focus and normalize the reflected intensity.

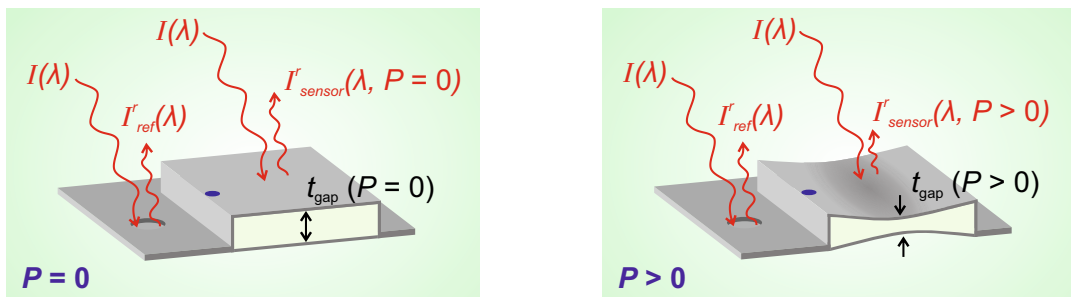


Figure 3.4. **Schematics of the operational mode of the IPS.** Working principle shows the incident light intensity, $I(\lambda)$, and the reflected light intensities from the reference area, $I'_{\text{ref}}(\lambda)$, and from the centre of the membrane, $I'_{\text{sensor}}(\lambda, P)$, depending on the mechanical deformation of the device membranes with and without applied pressure, P (right and left respectively). Blue dots represent the position where the reflected intensity is measured for tilt corrections.

Nonetheless, this design did not include a tilt compensation system. Hence, it was assumed that the deflection of the membranes will be negligible at the

border of the sensing cavity (Figure 3.4, blue dots) and this area was employed to compensate the device-tilt cross-sensitivities.

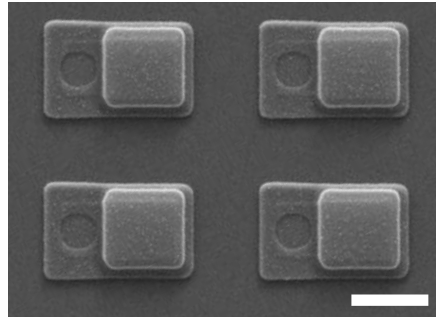


Figure 3.5. **Fabricated devices.** SEM top image of the fabricated pressure sensor chips before their release from the wafer. Scale bar: $3 \mu\text{m}$

The fabricated devices (Figure 3.5) were firstly validated using bright-field optical microscopy (Eclipse ME600 upright, Nikon) with a x100 magnification by a 0.8 NA long-distance objective (LU Plan ELWD 3.5, Nikon) and later intracellular pressure changes were detected by the chips and optically quantified through Confocal Laser Scanning Microscope (CLSM) (Figure 3.6, left).

For the intracellular pressure change measurements, the fabricated devices were subjected to a lipofection treatment, as described in previous works of the group[16], in order to promote their internalization in HeLa cells. Briefly, this method consist in encapsulate the material of interest (here, the IPS) in a lipid vesicle called a liposome which have the same composition than the cell membrane[17].

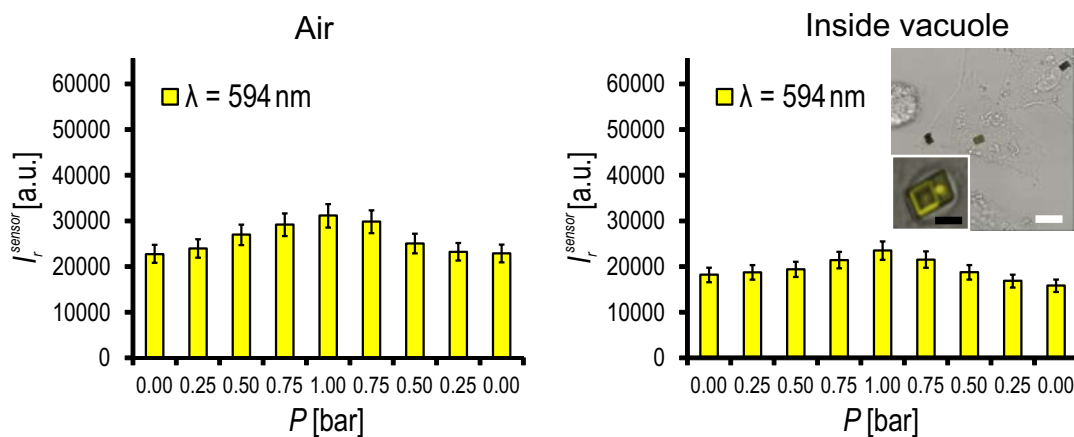


Figure 3.6. **Measured reflected intensities through the pressure sensor in different environments versus an applied pressure.** Reflected intensity values at the center of the sensor, I_r^{sensor} , for different applied pressures, P , for $\lambda = 594 \text{ nm}$. The device was immersed in (left) air medium for calibration, and (right) inside a vacuole in HeLa cells during experimental measures. Inset show CLSM images of HeLa cells with an internalized device in a vacuole and a detail of it. Scale bars: (white) $20 \mu\text{m}$ and (black) $5 \mu\text{m}$.

Hence, sensors were tested inside living cells after its internalization by lipofection and were located easily by optical light microscopy thanks to the high reflectivity of polysilicon. After sensor internalization, an external pressure was applied and the sensor was monitored to detect the reflected light at the center of the sensor cavity (I'_{sensor}) inside the cells (Figure 3.6, right). Devices in the cytoplasm or in a subcellular component as vacuoles were confirmed to detect pressure changes of up to 1 bar (Figure 3.6). This detection additionally confirms that the extracellular applied pressure is transmitted to the cell interior and even inside its subcomponents (as a vacuole).

As IPS were found to be able to detect intracellular pressure changes, it emerges the aim to improve the sensitivity of the sensors to be able to obtain more accurate pressure measures. Some studies have evidenced that subcellular components endured pressure changes in the mbar range. Therefore, devising devices with a lower detection limit of the pressure changes will allow us to study more precisely the mechanical changes produced inside cells and their components.

3.2 Design proposal for a more sensitive cavity

For the development of a more sensitive pressure sensor, we based the new design on the previous IPS[13, 14]. To decrease the detection limit it was needed to adjust the dimensions of the cavity, and at the same time to replace the contents of the cavity from vacuum to air at room conditions (room temperature and atmospheric pressure).

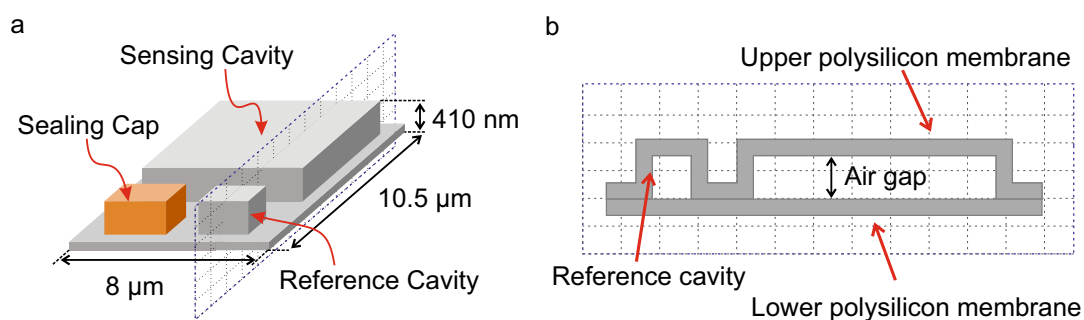


Figure 3.7. **Scheme of the second-generation designed devices.** a) Dimensions and 3D view of the scheme of the new design of the pressure sensor consisting in a sensing cavity and a reference cavity sealed by a polymeric sealing cap. b) Cross section schematic view of (a) showing the sensing and reference cavities with the same thickness for the air gap between the two polysilicon membranes.

The second-generation device design consists in two different cavities made of two parallel polysilicon membranes separated by an air gap plus a polymer sealing cap to achieve hermetic cavities (Figure 3.7). The large cavity is the sensing cavity, whose thickness changes when an external pressure is applied, and the small one is the reference cavity, whose dimensions are conceived so that the membranes do not deflect. This reference cavity

has been designed so that when it is subjected to an external pressure, in the range to be studied (<1 bar), the deflection of its membranes is not appreciable. Since the deflection of the membranes will be negligible, the reflected intensity is not dependent on the pressure change, only on the orientation of the device. In this way, it can be employed as a reference to calibrate the sensing cavity measurements affected by device tilt (Figure 3.7).

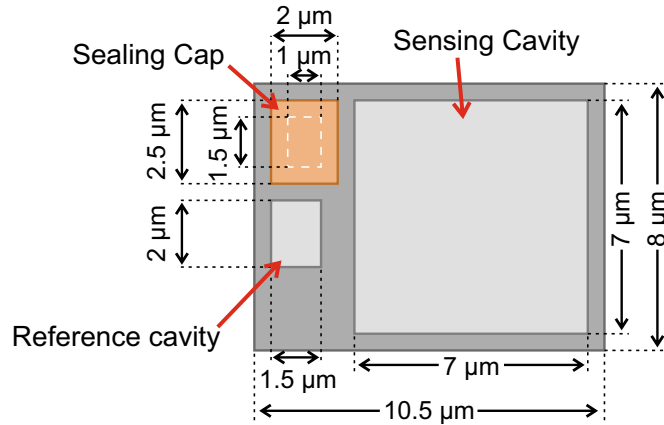


Figure 3.8. **Dimensions of the second-generation designed sensor.** Top view of the new design with the dimensions of the different parts of the sensor. White dotted rectangle represents the pinhole for the etching of the internal SiO_2 sacrificial layer.

To achieve the inner conditions of air at room temperature and atmospheric pressure, these cavities have to be sealed through fabrication techniques fulfilling these conditions. Thus, as photolithographic equipments operate at room conditions, to seal the devices we employed a polymer sealing cap defined through a photolithographic process. The device dimensions were fixed in the design values showed in Figure 3.8. This design was drawn in a layout editor and sent to the manufacturer for the reticle fabrication.

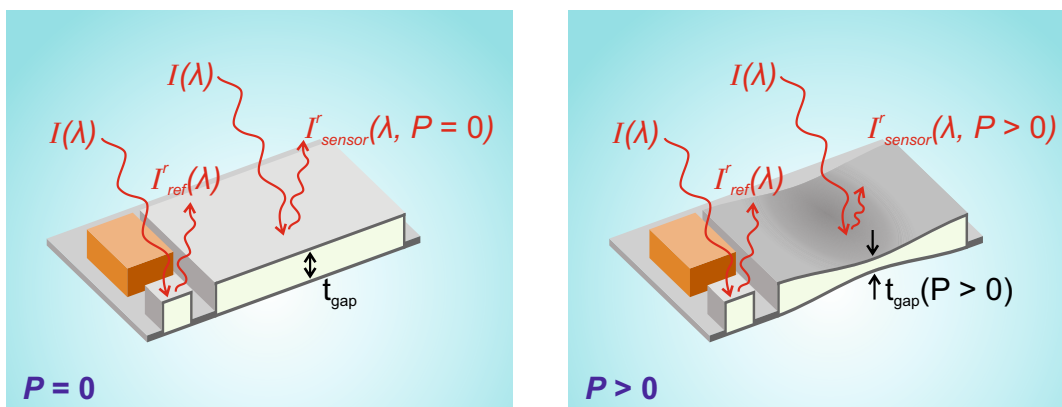


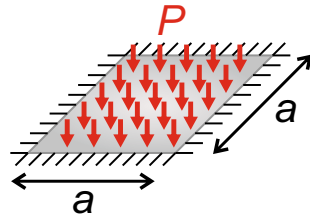
Figure 3.9. **Schematics of the operational mode of the second-generation sensor.** Working principle shows the incident light intensity, $I(\lambda)$, and the reflected light intensities from the reference cavity, $I^r_{ref}(\lambda)$, and from the centre of the sensing cavity, $I^r_{sensor}(\lambda, P)$. (Left) Initially ($P = 0$) the sensing cavity has their nominal t_{gap} . (Right) Membranes on the sensing cavity suffer a mechanical deformation when an external pressure, P , is applied. The reference cavity gap is not pressure dependent.

The operational mode of the sensor is based on the working principle of a Fabry-Perot interferometer (as the first generation of sensors), this means that the width of the sensing cavity is pressure-dependent. When an external pressure, P , is applied the polysilicon membranes of the sensing cavity deflect and the gap distance between them, t_{gap} , changes as shown in Figure 3.9.

On the contrary, the reference cavity will not undergo a significant deflection of its membranes, due to their low mechanical sensitivity. Hence, when the devices are observed under a light intensity at a certain wavelength, $I(\lambda)$, the intensity of the reflected light at the centre of the sensor membranes, I_{sensor}^r , is shaped by the applied external pressure, P . As this pressure modifies the distance between the parallel membranes of the sensing cavity, it is possible to derive its value from the value of the t_{gap} . Moreover, the reference cavity was conceived to compensate the device tilt. The reflected intensity on the center of the membrane of this cavity, I_{ref}^r , is not pressure dependent, $I_{ref}^r \neq I_{ref}^r(P)$ (Figure 3.9).

3.3 Mechanical analysis of the pressure sensor

For the mechanical analysis of the cavity, we studied the mechanical behaviour of a polysilicon membrane, both theoretical and simulated, under a uniform pressure load. The analytical solution for a rectangular plate subjected to a uniform pressure and clamped at its four edges (Figure 3.10) can be followed from [18]. Considering that our membrane is a square plate, the maximum bending at the centre of the membrane is expressed according to the equation 3.1:



$$\delta_{max} = 0.00126 \frac{a^4}{D} P \quad (3.1)$$

Figure 3.10. Applied pressure on a membrane. Schematic of a uniform pressure applied on a square membrane.

where D is the flexural rigidity, which depends on the Young's modulus, E , the thickness of the membrane, t_{memb} , and the Poisson ratio's, ν , as:

$$D = \frac{E}{12(1 - \nu^2)} t_{memb}^3 \quad (3.2)$$

Combining equations 3.1 and 3.2, it can be seeing the bending dependence with the geometrical and mechanical properties of the membrane and, certainly, with the applied pressure.

$$\delta_{max} = 0.01512 \frac{(1 - \nu^2)}{E} \frac{a^4}{t_{memb}^3} P \quad (3.3)$$

Hence, for the mechanical analysis of the sensors, we assumed the experimental tendency of the Young's modulus at the nanoscale obtained for ultrathin single-crystalline-silicon cantilever reported in the literature[19, 20], since for these sizes it can be considered that $E_{Si} \sim E_{poly}$. Thus, the size-effect of the Young's modulus for ultrathin layers, considering a second order polynomial fitting, leads to a value of $E = 76$ GPa ($\nu = 0.27$). On the other hand, for the geometrical dimensions involved in the bending, the nominal values ($a = 7 \mu m$ and $t_{memb} = 50$ nm) were taken for the analytical and the simulation calculations.

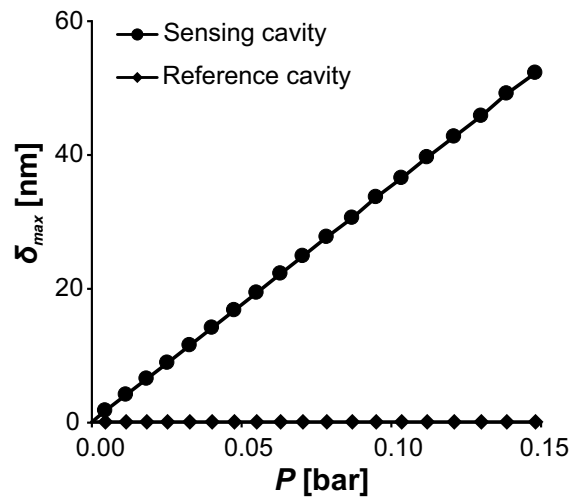


Figure 3.11. **Analytical mechanical study.** Theoretical analysis of the maximum displacement, δ_{max} , of a 50 nm-thick polysilicon membrane versus the applied pressure, P , on membranes of the size of the sensing and the reference cavities.

Analytically, the mechanical deformation of the polysilicon membranes (Figure 3.11) manifests the linear dependence between the applied pressure, P , and the maximum displacement at the center of the membrane, δ_{max} (equation 3.3). Moreover, Figure 3.11 shows negligible deflection values for the reference cavity in the range of pressures represented; even higher values of pressure (1 bar) presume low displacements for the reference cavity (~ 1.2 nm).

For the FEM (Finite Element Method) mechanical simulation study, ANSYS Multiphysics (Release 16.0, <http://www.ansys.com>) software were used, and the cavities were modelled using a 3D element, SOLID 95. The sensing and the reference cavities are isolated from each other by the sealing cap, so they were analysed separately for a simpler construction of the geometry of the model. Moreover, the reference cavity was simulated as a rectangular membrane, since the small displacements obtained from the analytical study demonstrated that second order effects on this membrane deflection can be neglected. Due to the non-linearity of the mechanical behaviour of the cavity,

the external pressure applied is an effective pressure, since, when applying pressure changes the volume of the gas (air) enclosed changes and, therefore, the internal pressure.

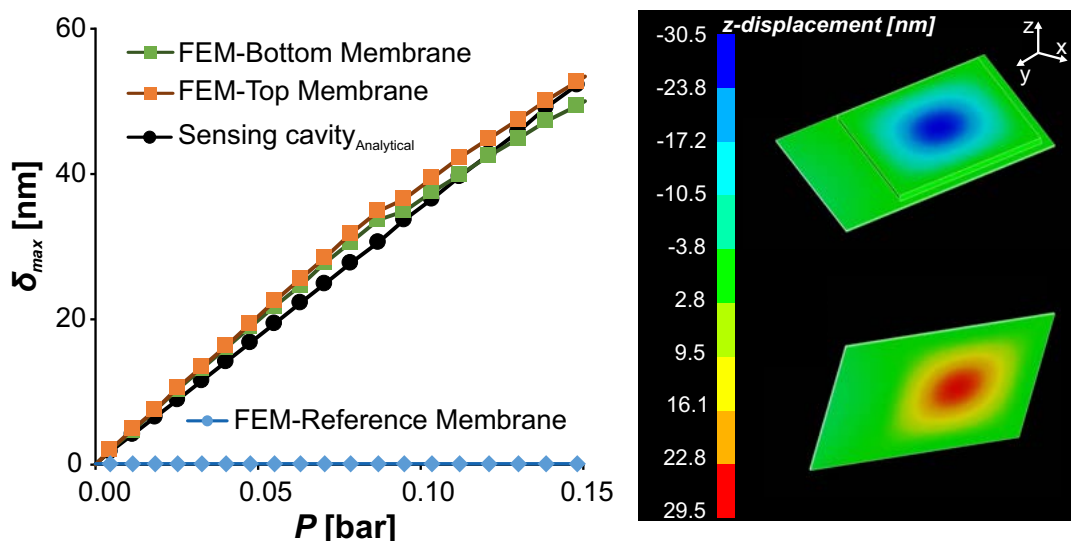


Figure 3.12. FEM simulation of the mechanical behaviour of the sensor. FEM simulation of maximum displacement at the center of the cavity, δ_{max} , versus applied external pressure, P , for the bottom and top membranes of the sensing cavity, and for the reference cavity. Moreover, analytical results have been included for a better comparison. (Right) Graphic images of the z-displacement simulated for the sensing cavity, displaying the maximum deflection at the center of the top and bottom membranes.

Maximum membrane deflection, δ_{max} , is shown in Figure 3.12 for a range of external pressure, P , applied on the surface of the membranes, both top and bottom membranes, of the sensing and reference cavities, together with a colour scale plot of the z-displacement at the membranes of the sensing cavity. A mechanical sensitivity of 0.36 nm per mbar is derived from the mechanical simulation analysis showed in Figure 3.12.

3.4 Optical analysis of the pressure sensor

Silicon is the most common material as structural layer for the fabrication of optomechanical systems[21–23], since its mechanical and optical properties have been widely studied. Thereby, polycrystalline silicon has a refractive index which confers an important spectral selectivity making it very suitable for optical sensors.

Our sensors act as a Fabry-Perot resonator, which can be schematized as an optical multilayer system (Figure 3.13). This optical system can be theoretically analysed with the transfer matrix (TM) method, which is based in the application of the Fresnel equations to analyse the propagation of the light

through a layered system by calculating the reflection and transmission coefficients of the light along it. The final TM of the multilayer system is the product of each of the TM of each layer, taking the product in the order in which the light passes along the stratified system[24].

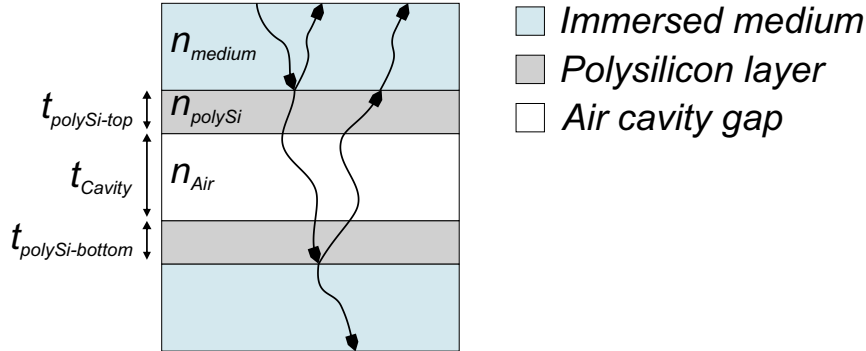


Figure 3.13. **Schematic of the multilayer optical system.** Multilayer consists in two polysilicon membranes separated by an air gap immersed in a medium. n and t refer to the refractive index and the thickness, respectively, of the subindexed layer.

Following Maxwell equations, the boundary conditions, at the interfaces a and b , for electric and magnetic fields of plane waves expressed that the magnitudes of the fields on both sides of the interface are equal.

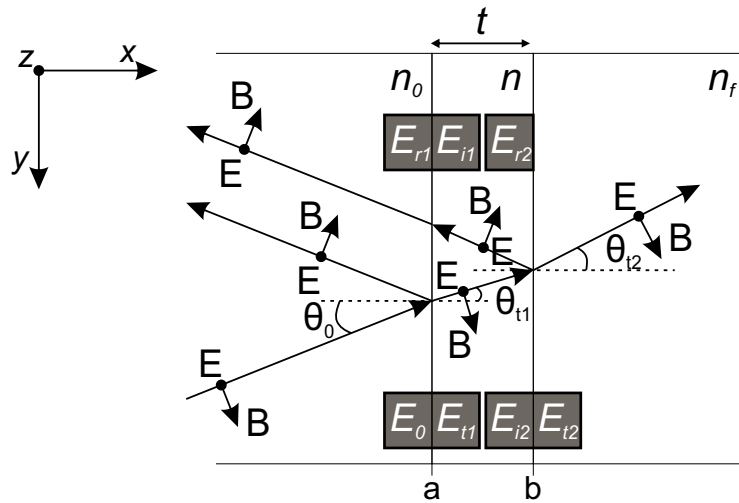


Figure 3.14. **Schematic of plane waves behaviour in a one-layer film optical system.** Black dots represent perpendicular direction to the plane of incidence. E and B represent the electric and magnetic fields, respectively; n refers to the refractive index; t indicates the thickness of the layer; and θ the angle at the interface[24].

Therefore, the electric and magnetic fields at the interfaces are:

$$E_a = E_0 + E_{r1} = E_{t1} + E_{i1} \quad (3.4a)$$

$$E_b = E_{i2} + E_{r2} = E_{t2} \quad (3.4b)$$

$$B_a = B_0 \cos \theta_0 - B_{r1} \cos \theta_0 = B_{t1} \cos \theta_{t1} - B_{i1} \cos \theta_{t1} \quad (3.4c)$$

$$B_b = B_{i2} \cos \theta_{t1} - B_{r2} \cos \theta_{t1} = B_{t2} \cos \theta_{t2} \quad (3.4d)$$

Taking into account that the magnitudes of electric and magnetic fields are related by:

$$B = \frac{1}{v}E = \frac{n}{c}E = n\sqrt{\epsilon_0\mu_0}E \quad (3.5)$$

Hence, equations 3.4c and 3.4d can be rewritten as

$$B_a = \gamma_0(E_0 - E_{r1}) = \gamma(E_{t1} - E_{i1}) \quad (3.6a)$$

$$B_b = \gamma(E_{i2} - E_{r2}) = \gamma_f E_{t2} \quad (3.6b)$$

by introducing the parameters defined as

$$\gamma_0 \equiv n_0\sqrt{\epsilon_0\mu_0}\cos\theta_0 \quad (3.7a)$$

$$\gamma \equiv n\sqrt{\epsilon_0\mu_0}\cos\theta_{t1} \quad (3.7b)$$

$$\gamma_f \equiv n_f\sqrt{\epsilon_0\mu_0}\cos\theta_{t2} \quad (3.7c)$$

Additionally, E_{i2} and E_{t1} , and E_{i1} and E_{r2} , differ in a phase, δ , due to one traversal of the film, which can be written in terms of the path length as $\delta = \Delta k_0 = \frac{2\pi}{\lambda_0}nt\cos\theta_{t1}$. Hence, the electric fields can be expressed as: $E_{i2} = E_{t1}e^{-i\delta}$ and $E_{i1} = E_{r2}e^{-i\delta}$.

Finally, substituting and grouping properly equations 3.4a, 3.4b, 3.6a and 3.6b, it can be obtained

$$E_a = E_b\cos\delta + B_b \left(\frac{i\sin\delta}{\gamma} \right) \quad (3.8a)$$

$$B_a = E_b(i\gamma\sin\delta) + B_b\cos\delta \quad (3.8b)$$

These equations give a relation between the magnitudes of the fields at the interfaces of a single layer system, and can be expressed in a matrix form as follows:

$$\begin{bmatrix} E_a \\ B_a \end{bmatrix} = \begin{bmatrix} \cos\delta & \frac{i\sin\delta}{\gamma} \\ i\gamma\sin\delta & \cos\delta \end{bmatrix} \begin{bmatrix} E_b \\ B_b \end{bmatrix} \quad (3.9)$$

where the 2×2 is the *transfer matrix* of the layer with the general representation as:

$$M = \begin{bmatrix} m_{11} & m_{12} \\ m_{21} & m_{22} \end{bmatrix} \quad (3.10)$$

The expression 3.9 can be generalized for a multilayer of N layers,

$$\begin{bmatrix} E_a \\ B_a \end{bmatrix} = M_1 M_2 M_3 \cdots M_N \begin{bmatrix} E_N \\ B_N \end{bmatrix} \quad (3.11)$$

Hence, using boundary conditions in equation 3.9, it can be obtained the transfer matrix in terms of the amplitude of the electric field

$$\begin{bmatrix} E_0 + E_{r1} \\ \gamma_0(E_0 - E_{r1}) \end{bmatrix} = \begin{bmatrix} m_{11} & m_{12} \\ m_{21} & m_{22} \end{bmatrix} \begin{bmatrix} E_{t2} \\ \gamma_f E_{t2} \end{bmatrix} \quad (3.12)$$

which define the reflection and transmission coefficients as

$$r \equiv \frac{E_{r1}}{E_0} = \frac{2\gamma_0}{\gamma_0 m_{11} + \gamma_0 \gamma_f m_{12} + m_{21} + \gamma_f m_{22}} \quad (3.13a)$$

$$t \equiv \frac{E_{t2}}{E_0} = \frac{\gamma_0 m_{11} + \gamma_0 \gamma_f m_{12} - m_{21} - \gamma_f m_{22}}{\gamma_0 m_{11} + \gamma_0 \gamma_f m_{12} + m_{21} + \gamma_f m_{22}} \quad (3.13b)$$

Expressions 3.13a and 3.13b are valid for a multilayer system, and these coefficients could be used to calculate the *Reflectance* and *Transmittance* at the system

$$R = |r|^2 \quad T = |t|^2 \quad (3.14)$$

Considering the representation of our system in Figure 3.13, we can then calculate the reflectance through the Fabry-Perot.

	$t_{\text{polySi-top}}[\text{nm}]$	$t_{\text{cavity}}[\text{nm}]$	$t_{\text{polySi-bottom}}[\text{nm}]$
Nominal	50	300	50
Experimental	43.7 ± 0.3	309.7 ± 2.5	50.5 ± 0.4

Table 3.1. **Thickness values of the fabricated polysilicon layers.** Nominal and experimental dimensions of the thickness of the polysilicon top, $t_{\text{polySi-top}}$, and bottom, $t_{\text{polySi-bottom}}$, membranes, and of the air cavity gap, t_{cavity} .

The reflectance at the center of the sensing cavity has been simulated regarding the nominal thickness and the experimental thickness of fabricated devices (Table 3.1).

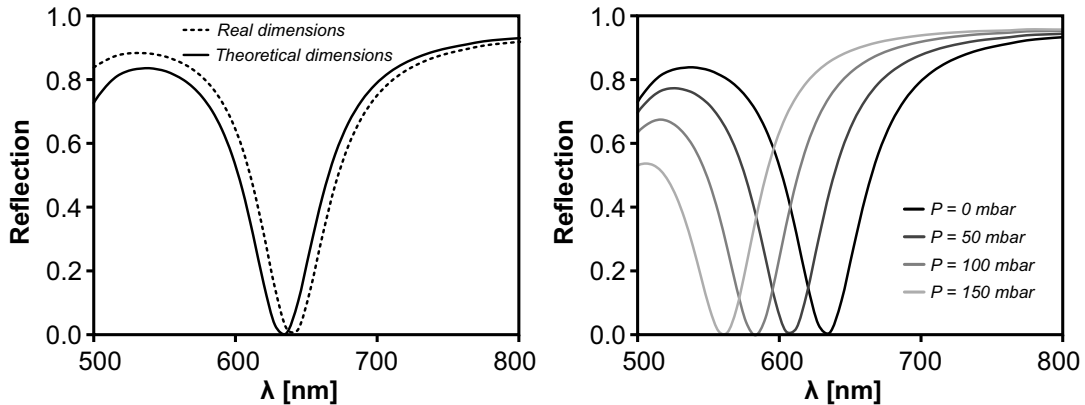


Figure 3.15. **Simulation of the reflection response through the cavity.** Theoretical analysis (left) comparing the reflectance response through the Fabry-Perot cavity with the designed dimensions and the ones obtained after the fabrication of the devices. (Right) Simulation results with the designed dimensions of the reflection for a sweep of pressures applied to the sensor (0 mbar, 50 mbar, 100 mbar and 150 mbar) that reduce the reflection values as consequence of the change in the thickness of the cavity.

The theoretical analysis of the Fabry-Perot resonator shows the relation between the reflection and the wavelength, which is slightly different for the nominal values and the obtained from a fabricated device (Figure 3.15, left). Hence, when an applied external pressure would be applied, t_{cavity} will change, producing a shift in the reflectance curve (Figure 3.15, right).

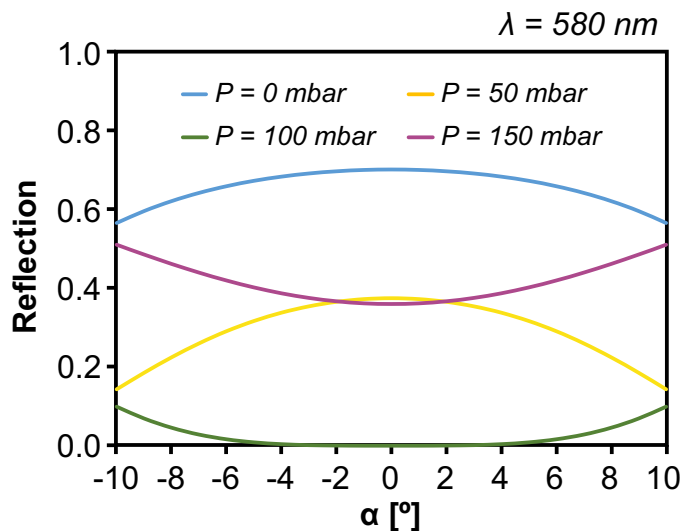


Figure 3.16. Simulation of the reflection dependence with the tilt angle of the device for $\lambda = 580$ nm. Results of the reflection at the center of the cavity for different applied pressure, P , for different angles of the incident light, α .

The reflection at the center of the devices was also analysed, for $\lambda = 580$ nm, for different angles of the incident beam, α , due to sensors may be tilted during their performance (Figure 3.16). When an external pressure, P , is applied on the system and the device is working at a tilted position, the reflection at the center of the cavity varies with the orientation angle and with the applied pressure as seen in Figure 3.16. It must be remembered that the reference cavity is not changing when pressure changes, hence, its profiles will always be as the represented for $P = 0$ in Figure 3.16.

3.5 Technological development for the fabrication of a sealed cavity

The most important challenge in the sensors fabrication is the technological development required to achieve them, as this work is framed at the limit of the microfabrication technology. On one hand, the polysilicon layers composing the detection membrane are very thin (50 nm) and, on the other hand, the cavities are needed to be hermetically closed. Hence, smooth functional layers and the appropriate sealing of the cavities are necessary for a correct measure detection.

3.5.1 Development of a thin-nongrainy polysilicon layer

Polysilicon has been used widely in microelectronic technology fabrication. In the case of transistors, polysilicon has been used as gate material for most of the microelectronics era, but following transistor miniaturization (related to Moore's law) a polysilicon gate thicknesses of 100 nm or less was required. Thus, controlling material properties on the nanometer scale becomes highly relevant in material science, making that the mechanical properties of the polysilicon layers need to be optimised according to the microsystem to be fabricated.

Intrinsic stress and stress gradients of deposited or grown layers are common problems in MEMS. In the case of the pressure sensor, the development of the polysilicon layer is a critical step as this layer composes the membrane through which the detection will be done. Commonly, in many research and industrial polysilicon-based mechanical devices, structural layers are in the range of microns containing surface irregularities of tens of nanometers, thus they do not affect the mechanical performance of the device. However, when the thickness of the layer is thinner, as in our case with a 50 nm polysilicon layer, surface defects of tens of nanometers may affect to the mechanical performance of the devices. This means that deposition conditions must also be optimized to achieve a smooth surface.

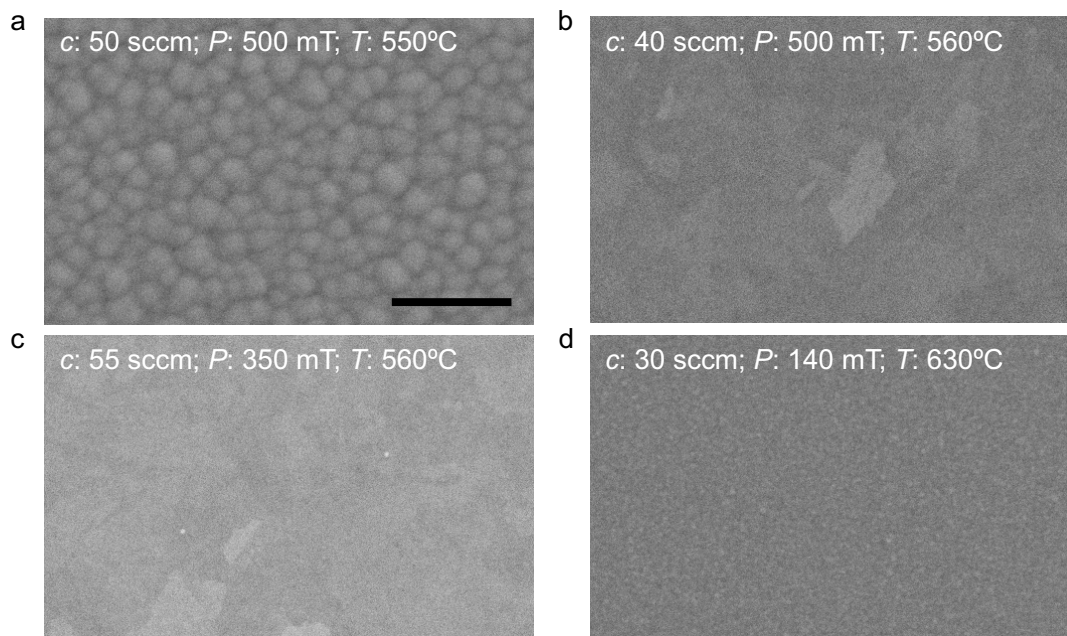


Figure 3.17. **Polysilicon deposit conditions.** SEM images of the surface of polysilicon layers deposited under different deposition conditions. c represents the gas flow, P and T are the pressure and the temperature in the chamber, respectively. Scale bar: $1 \mu\text{m}$. Conditions selected for the polysilicon layers on the pressure sensor fabrication are the represented in image d.

The deposition of the polysilicon layer for the fabrication of the sensor membranes is based on a Low Pressure Chemical Vapour Deposition (LPCVD)

process. The working substrate (a silicon wafer) is located in a high temperature chamber where one or more volatile precursors react and decompose on the wafer surface producing the layer deposit (here, the polysilicon layer). Deposit conditions make a major contribution to the smoothness of deposited polysilicon layer (Figure 3.17)[25].

In Figure 3.17, there are some SEM images representing different deposit conditions. It is clearly visible how the roughness of the layer is affected by the change on the parameters involved in the process. The selected conditions for the deposition process of the polysilicon for the pressure sensor devices were the ones of Figure 3.17d.

Additionally, the roughness of the layer with the selected conditions was measured by an AFM (Bruker) scanning (Figure 3.18). Two areas of $1 \times 1 \mu\text{m}^2$ at different positions on the wafer were scanned with roughness values less than 3 nm.

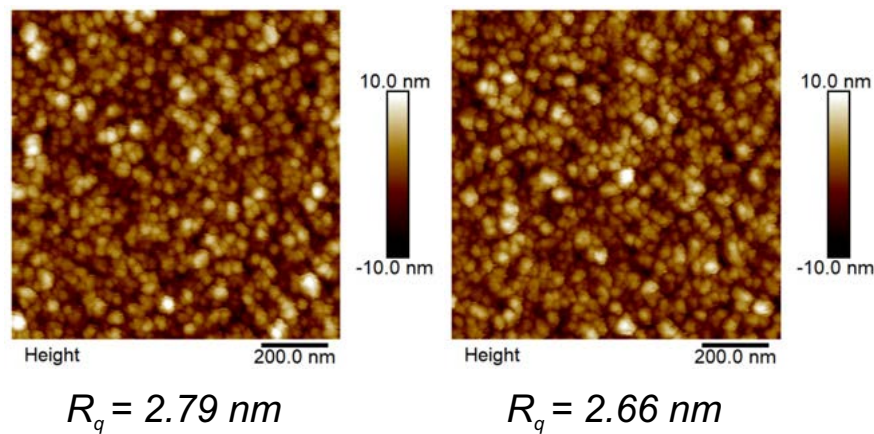


Figure 3.18. Polysilicon roughness. AFM scan of two areas of $1 \times 1 \mu\text{m}^2$ in the center (image on the left) and in a side (right image) of the wafer. Images show a roughness average less than 3 nm.

3.5.2 Fabrication of the pressure sensor devices

The intracellular pressure sensors were fabricated based on silicon micro-electronic techniques. For that, photolithographic processes were employed together with micromachining technologies through the etching of the sacrificial SiO_2 to shape the polysilicon layers of the sensor cavities. Following, the fabrication process is explained until this etching process.

Devices are fabricated over a four-inch p-type silicon wafer $\langle 100 \rangle$ (Okmetic) (Figure 3.19). –Ox1– Initially, a $1 \mu\text{m}$ -thick layer is grown by wet oxidation at $950 \text{ }^\circ\text{C}$. –Poly1– A 50 nm -thick polysilicon layer is deposited by a CVD (Chemical Vapour Deposition) process ($630 \text{ }^\circ\text{C}$, 140 mTorr). –Ox2– A 280 nm -thick silicon dioxide TEOS layer is deposited by a PECVD (Plasma-Enhanced Chemical Vapour Deposition). A $1.2 \mu\text{m}$ -thick of positive photoresist (ma-P 6512 MicroResist Technology) is spun onto the wafers. UV light

exposure (Stepper NSR 2205-i12D Nikon) is performed through the second quadrant of the reticule.

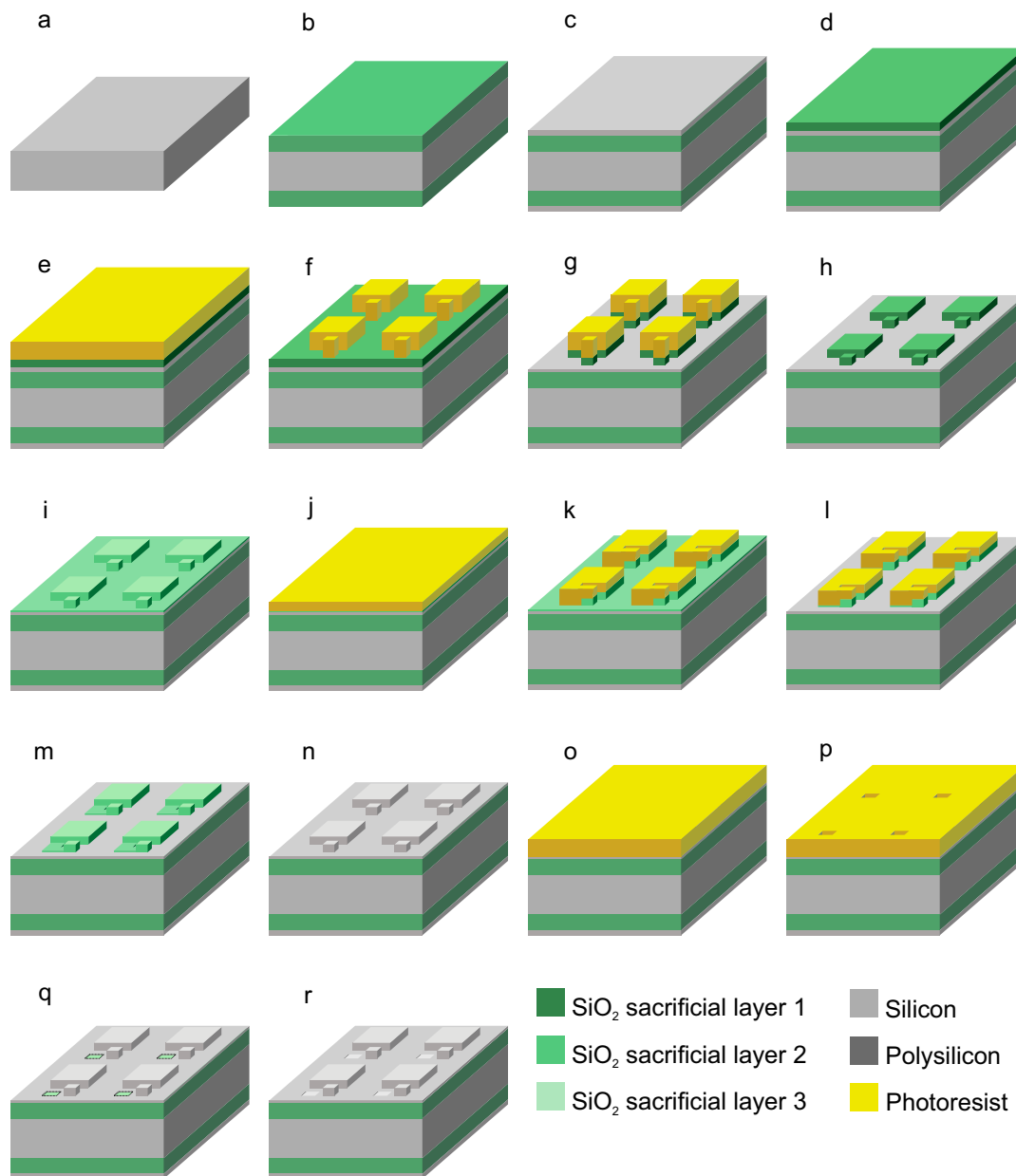


Figure 3.19. Detail of the pressure sensors fabrication steps before cavities etching. a) Silicon wafer as initial substrate. b) 1 μm -thick of grown SiO₂ as sacrificial layer for releasing the devices, *Ox1*. c) 50 nm-thick polysilicon deposition, *Poly1*. d) 280 nm-thick SiO₂ deposited, *Ox2*, to define the vertical dimension of the sensor cavity. e) 1.2 μm -thick of positive photoresist is spun. f) Photolithographic process followed by the resist developing and baking. g) 280 nm-thick SiO₂ layer is etched in a RIE process. h) Resist is removed. i) 30 nm-thick SiO₂ layer is deposited. j) 0.6 μm -thick of OiR photoresist is spun. k) Photolithographic process. l) 30 nm-thick SiO₂ layer is etched in a wet process. m) OiR resist is removed. n) 50 nm-thick polysilicon deposition, *Poly2*. o) 1.2 μm -thick of positive photoresist is spun. p) Photolithographic process. q) Resist is removed. r) SiO₂ internal sacrificial layers are wet-etched and a drying process is performed with a critical point dryer.

The resist is developed and baked during 30 min at 200 °C. Then the etching of the 280 nm-thick silicon dioxide layer is done with a C_2F_6 and CHF_3 RIE process (ALCATEL GIR 160). After that, the photoresist is stripped (TEPLA 300-E, Technics Plasma). Next, a 30 nm-thick silicon dioxide TEOS layer is deposited by a PECVD. A 0.6 μm -thick of positive photoresist (Fujifilm OiR 620-09) is spun onto the wafer. Then, the exposure of the photoresist is performed by UV light (Stepper NSR 2505-i12D Nikon) through the third quadrant of the reticle. The 30 nm-thick SiO_2 layer is etched by a wet buffered Hydrofluoric acid (HF)-based solution (SiO-etch MT 06/01 VLSI Selectipur, BASF). Lastly, the OiR photoresist is removed. –*Poly2*– A 50 nm-thick polysilicon layer is deposited. A 1.2 μm -thick of positive photoresist (ma-P 6512 MicroResist Technology) is spun onto the wafers. Then, the exposure of the photoresist is performed by UV light (Stepper NSR 2505-i12D Nikon) through the fourth quadrant of the reticle. The resist is developed and baked. The pinhole in the 50 nm-thick polysilicon layer is opened by a dry reactive ion etching with CF_4 and Cl_2 (AMI ETCH P-5000). Lastly, the photoresist is stripped. Next, the internal sacrificial layers of silicon dioxide are wet-etched with a HF-based solution. Drying process is performed with a critical point dryer of CO_2 (Supercritical Automegasamdri®-915B, Series C, Tousimis).

So far, two of the most critical step in the fabrication process are the etching of the 50 nm-thick polysilicon to open the pinhole and the following wet etching of SiO_2 inside the cavities (Figure 3.19p-r). Initially, the pinhole on the polysilicon layer was etched through a RIE (ALCATEL 601 E) based on a Bosch process, consisting in the combination of an ion bombardment by SF_6 with the deposition of a chemical etch resistant polymer (passivation layer) by $c-C_4F_8$. It resulted that when, the pinhole on the polysilicon layer was etched by this process, the subsequent wet etching of the SiO_2 failed.

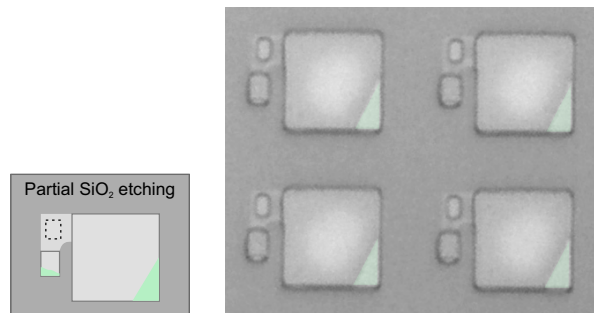


Figure 3.20. **Partial SiO_2 internal etching of the cavities.** (Left) Scheme of the (right) SEM image of the cavities with a non-correct etching due to the use of the $c-C_4F_8$ which promotes the formation of polymers walls.

As it can be observed in Figure 3.20, devices could not be completely etched. This failure was found to be originated in the passivation of the vertical walls of the pinhole during the polysilicon etching. The $c-C_4F_8$ passivation generates polymers that are deposited throughout the wafer. Those deposited on the surface are removed with the physical component of the etching. Otherwise, those that remain on the walls of the structures can not

be removed and hinder the subsequent wet etching, probably due to the hydrophobicity of the polymers promoted by the $c\text{-C}_4\text{F}_8$ etching, inhibits the entrance of the HF.

As the Bosch process is a deep RIE (DRIE), it is commonly used for large etching that require a highly anisotropic profile [26]. However, in our case it is not needed a high anisotropic profile, as the vertical depth is only of 50 nm and the motivation of this step is to etch the polysilicon layer in order to have accessible the SiO_2 from the interior of the cavities for its etching in the next step. Hence, this polysilicon etching was replaced by a dry etching with Cl_2 , HBr and He- O_2 (AMI-Etch P-5000 MXP; Applied Materials Inc.), with which the cavities were completely etched (Figure 3.21), as the He- O_2 passivates the substrate (in our case SiO_2) with oxygen but does not generate polymers on it. The resulting products from this passivation can be removed in aqueous media unlike those originated in the Bosch process.

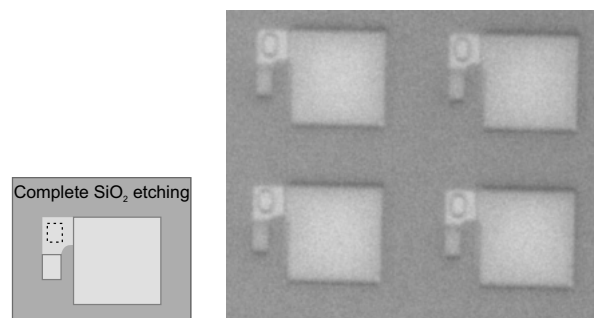


Figure 3.21. **Complete SiO_2 internal etching of the cavities.** (Left) Scheme of the (right) SEM image of the cavities with a correct etching through the process with Cl , HBr and He- O_2 gasses.

Now that the interior of the cavities has been released, sensors have to be sealed, so, we next investigated in the development of a correct sealing process for a tightness device.

3.5.3 Cavity sealing development for the tightness of the pressure sensors

To address air cavity sealing to gain sensitivity, the pair of conditions necessary to meet the requirements of atmospheric conditions of temperature and pressure inside the cavities must be considered. Most of the deposition processes involved on the microelectronic fabrication technology operate at high or low conditions of pressure or temperature. Also, it is necessary to choose a sealing material and process that ensures a hermetic seal of the cavity. These considerations led us to choose a polymer as the element to seal the cavity and photolithography as the process to define it. The nominal dimensions of the cap established in the photomask are $2.0 \times 2.5 \mu\text{m}^2$.

Firstly, we selected SU-8 polymer (SU-8 2000.5, MicroChem), which is a negative photoresist, that according to the datasheet of the product with the proper spin and bake conditions could reach a minimum thickness of $0.5 \mu\text{m}$.

It must be remembered that the maximum height of the sensor is 400 nm, so the sealing cap should not greatly exceed this figure.

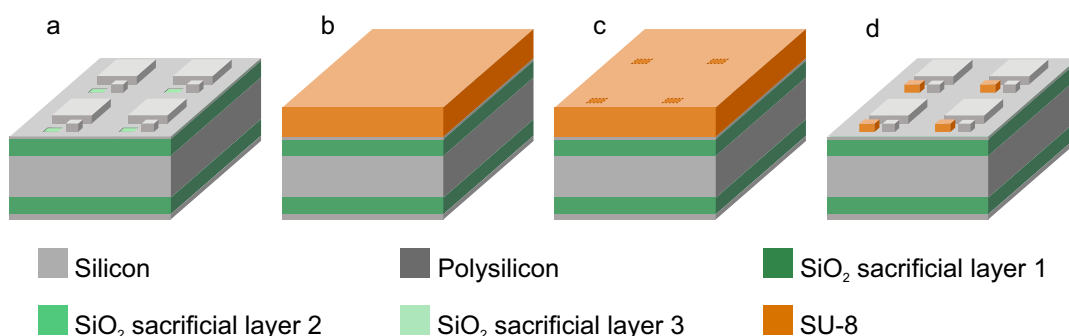


Figure 3.22. **SU-8 photolithographic process.** a) Sensors after the critical drying process following their internal SiO₂ etching. b) SU-8 resist is spun achieving a 0.5 μm-thick layer. c) Su-8 cap is structured by a UV photolithographic process and (d) is later developed and baked at 95 °C for 8 minutes.

In a photolithographic process there are two factors that can be controlled to fit the profile and dimensions of the design to be transferred to the resist. These factors are the Energy Dose (ED) and the Depth Of Focus (DOF). Therefore, we carried out a photolithography exposure test to establish the energy and focus settings for suitable cap dimensions.

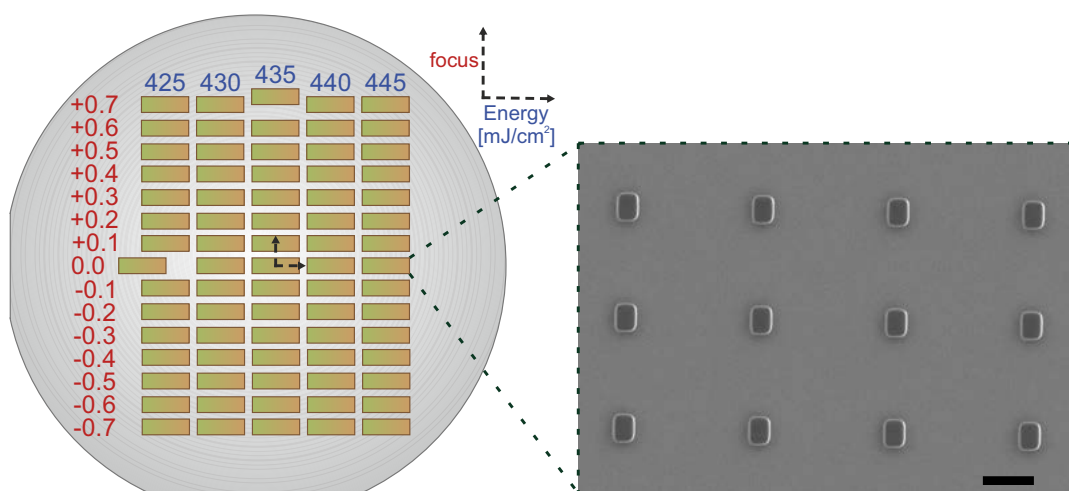


Figure 3.23. **Photolithography SU-8 test for the definition of the sealing cap dimensions.** (Left) Schematic of a wafer with photolithographed chip areas with different configurations of energy dose and depth of focus to achieve the proper dimensions of the SU-8 cap. (Right) SEM image shows some fabricated caps. Scale bars: 5 μm.

Hence, a silicon wafer with the structured polysilicon cavities before their internal SiO₂ releasing, is taken as initial substrate (Figure 3.22a). To perform the SU-8 exposure over sensors without etched cavities is based in the need to protect devices, as the cap photolithographic step is irreversible and sensors can not be recovered if cavities are damaged. Hence, the fabrication for the SU-8 cap is as follows. First, SU-8 resist is spun onto the substrate at 3000 rpm

to achieve a thickness of $0.5 \mu\text{m}$ (Figure 3.22b). Next, UV photolithographic exposition (Stepper NSR 2505-i12D Nikon) defines the physical dimensions of the cap through the photomask (Figure 3.22c). After the exposure, the resist is developed and baked during 8 minutes at 95°C (Figure 3.22d).

The SU-8 cap test exposure was done by varying the DOF in the vertical axis and the ED in the horizontal axis in each chip ($1.5 \times 0.5 \text{ cm}^2$) exposition, as schematized in Figure 3.23. Thereby, multiple combinations of DOF and ED were obtained and the one with the suitable dimensions was chosen. From the study, it was concluded that a DOF value of $+0.7$ and an ED level of $445 \text{ mJ}/\text{cm}^2$ were the best conditions to conform the sealing cap (Figure 3.24), with cap dimensions of $2.12 \times 2.61 \times 0.57 \mu\text{m}^3$.

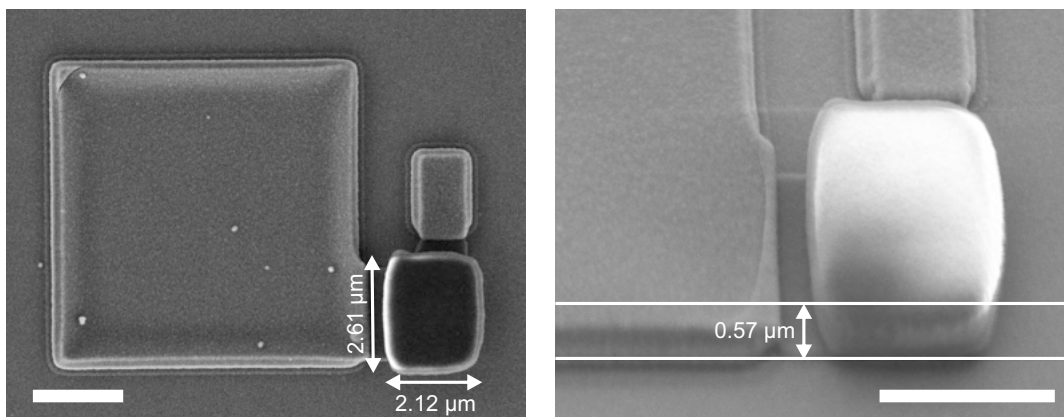


Figure 3.24. **SU-8 cap selected to fabricate the sensors.** SEM images of a sensor with the dimensions of the SU-8 cap from the best conditions of the photolithography test. Scale bars: $2 \mu\text{m}$.

Once the dimensions have successfully been attained, the resist resistance to acetone was evaluated (Figure 3.25). The need for this test lies in the subsequent exposure of the wafers to a resist stripping process (last step represented in Figure 3.26) that the polymer used as a cap will have to endure.

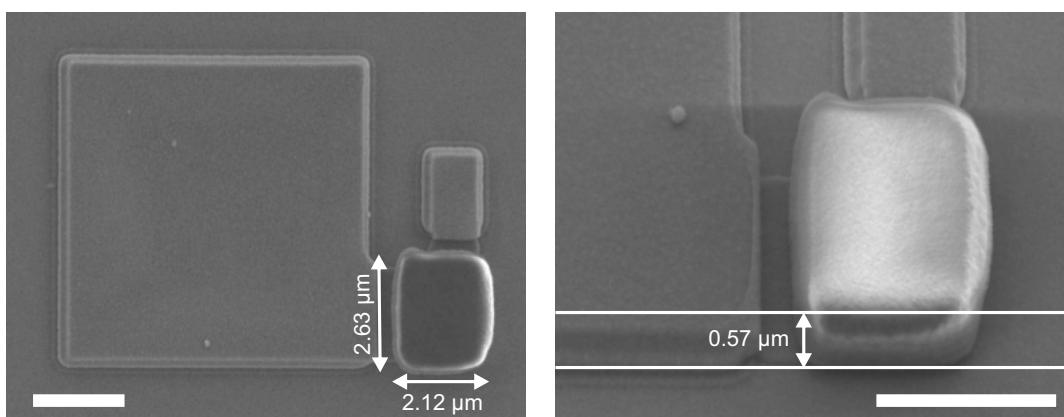


Figure 3.25. **Evaluation of the SU-8 resistance to acetone exposition.** SEM images of a sensor showing that the SU-8 cap maintained its dimensions after the immersion of the wafer in acetone during 5 minutes. Scale bars: $2 \mu\text{m}$.

Thus, the wafer was immersed during 5 min on a 140 mm glass crystalizer and later it was observed by SEM, confirming that the SU-8 cap conserved its defined dimensions (Figure 3.25). Finally, the SU-8 cap photolithographic steps were performed in real process wafers with sensors whose cavities have been etched (Figure 3.19r).

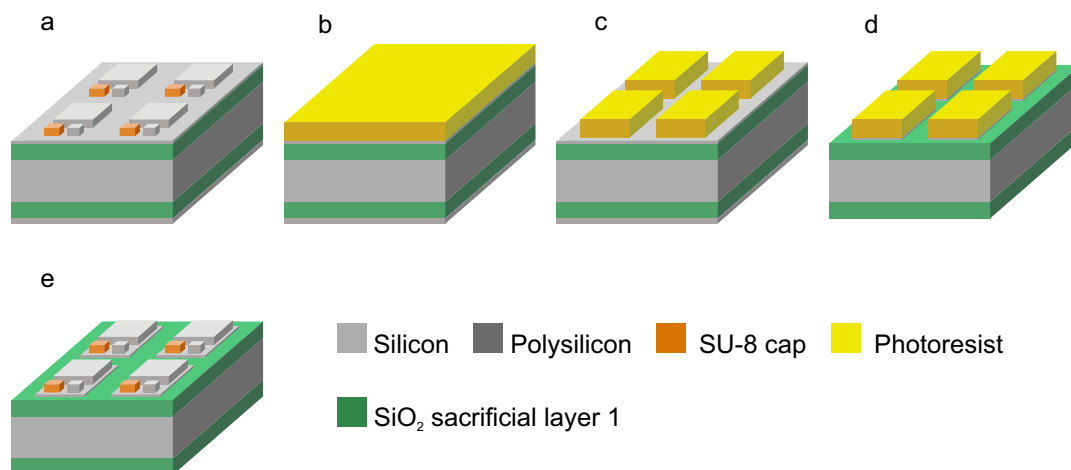


Figure 3.26. Last steps in the sensors fabrication with SU-8 cap. a) Sensors with SU-8 caps. b) 1.2 μm of positive resist is spun. c) Photoresist is developed. d) The 100 nm-thick polysilicon layer is etched in a RIE process. e) Photoresist is stripped.

Then, it follows a sequence of steps for the definition of the final dimensions of the sensors. As follows in Figure 3.26, starting from wafers with sealed cavities (Figure 3.26a) a 1.2 μm -thick layer of positive photoresist (ma-P 6512 MicroResist Technology) is spun onto the wafers (Figure 3.26b). Then, the exposure of the photoresist is performed by UV light (Stepper NSR 2505-i12D Nikon) through the fifth quadrant of the reticule and resist is developed (Figure 3.26c). The 100 nm-thick polysilicon layer is etched with SF_6 in a RIE process (GIR 160) (Figure 3.26d), and, after that, the photoresist is stripped (Figure 3.26e).

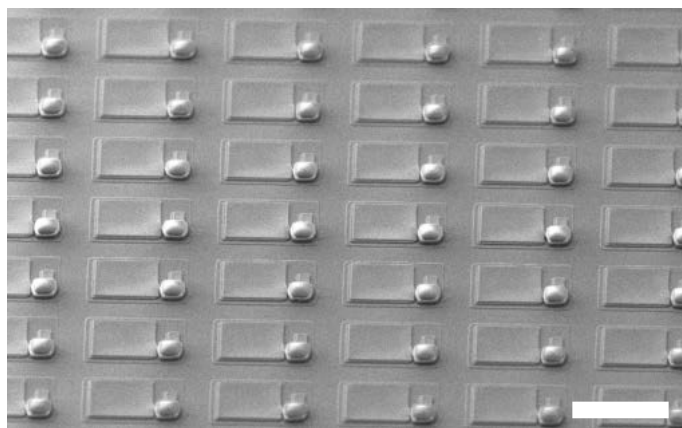


Figure 3.27. Fabricated sensors SEM image with SU-8 cap. SEM image shows that sensors have collapsed during the final steps of the fabrication process. Scale bar: 10 μm .

Devices were examined in SEM/FIB after the polysilicon etching, just before their releasing, to examine the reliability of the cavities. The wafer was located inside a FIB chamber (Zeiss 1560XB Cross Beam, Carl Zeiss) and a first scanning was done by the SEM column (Figure 3.27). Since SEM inspection (Figure 3.27) showed that sensors were collapsed, FIB nanomachining was used to section the devices to ascertain if the resist was entered inside the cavity. As shown in Figure 3.28, SEM images show that SU-8 resist appears to have entered the cavities, being the reason for its collapse.

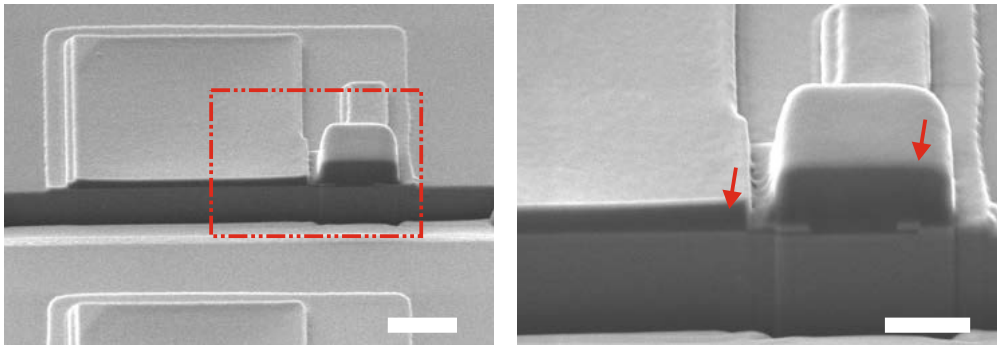


Figure 3.28. **Sensors with SU-8 cap after FIB milling.** SEM images of a sensor after the FIB nanomachining for the examination of the interior of the devices. Red arrows point the SU-8 within the cavity and the SU-8 in the cap. Devices are not functional as SU-8 has entered within the sensing cavity. Scale bar: 2 μm . Scale bar: 1 μm .

To further validate this assumption, the use of Energy-Dispersive X-ray Spectroscopy (EDXS, PentaFET-Precision attached to the SEM equipment, INCAx-act, Oxford Instruments) was done. Briefly, this technique consists of the surface analysis by the ionization of atoms of a sample. An electron beam hits the sample causing the ejection of an electron in an inner shell. Then, the excited atom can relax through the loss of energy by filling the hole (left behind by the ejected electron) with one of the outer shell. This energy loss outcomes in the emission of an X-ray, whose energy is the difference between the energy levels of the electron ejected and the electron shifted from the outer shell. As the energy of the emitted X-ray is exclusive for each element, it can be employed for chemical analysis with an energy dispersive detector[27].

Figure 3.29 shows the detected spectrum and the elements associated with the characteristic peaks obtained for different point positions of the sample. Spectrum 1 corresponds with the SU-8 cap (carbon, C, 0.277 keV and oxygen, O, 0.525 keV) and the characteristic peak of silicon (Si, 1.739 keV) is also detected. Spectrum 2 detects the elements which are presents at the interior of the sensing cavity (C, 0.277 keV; O, 0.525 keV and Si, 1.739 keV), and spectrum 3 is a detection of the silicon from the wafer substrate (Si, 1.739 keV). Therefore, it was probed that elements as C and O, specific of SU-8 resist, are present within the sensing cavity, and any kind of misconception or contamination of the sample was discarded by spectrum 3.

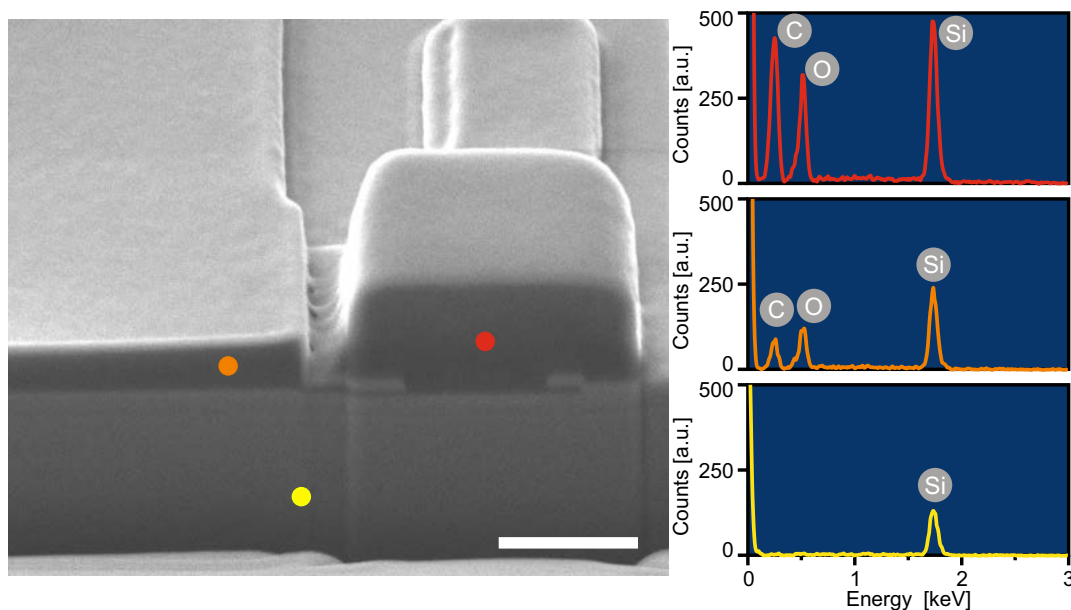


Figure 3.29. EDXS analysis of the interior of the devices. Cross section SEM image of the devices. Scale bar: 1 μm . Coloured dots mark the position where the EDXS has been performed. Profiles show the element in each of the corresponding colour dot, confirming SU-8 inside the cavity. The working voltage was 3 keV.

Thus, it was necessary to look for another polymer which allows us to perform a photolithography process to seal the cavities having the required dimensions without the resist enter into them. For that, we looked for a photoresist with a higher viscosity, since the SU-8 low viscosity (Table 3.2) probably stimulated its entry into the cavity. Among the commonly used resists, we selected an aqueous positive polyimide photoresist (HD-8820, MicroSystems), which has higher viscosity (Table 3.2) and it presents a thicknesses range between 4 to 10 μm (values have been extracted from the datasheet of the product).

	SU-8 2000.5	Polyimide HD-8820
Viscosity [St]	0.0249	18

Table 3.2. Viscosity of the resist. Viscosity values for SU-8 2000.5 and Polyimide HD-8820 resists.

Polyimide was tested in two ways, to tried to achieve the minimum height in the cap. One, based on the original polyimide and, the second based on the dissolution (1:1) of the polyimide with γ -Butyrolactone (GBL) solvent to reach a thinner layer. As in the case of the SU-8, a photolithographic test was done, with each polyimide configuration, to fit the dimensions of the cap, by varying the ED and the DOF.

Table 3.3 shows the selected factors for each one. For dissolved polyimide, the energy dose was ranged from 16 to 56 mJ/cm^2 in steps of 4 mJ/cm^2 , and the depth of focus from -0.2 to +0.2 in steps of 0.1.

	Energy Dose [mJ/cm^2]	Depth of focus
Polyimide	150	-0.25
Dissolved polyimide	36	+0.2

Table 3.3. ED and DOF for both polyimide configurations. Most suitable pairs for each one of the polyimide configurations.

The most suitable profile was achieved at the configuration of $36 mJ/cm^2$ in ED and a DOF of +0.2, with dimensions of $2.06 \times 2.59 \mu m^2$ in the plane of the wafer (Figure 3.30, left). The vertical profile was estimated to be lower than $0.5 \mu m$.

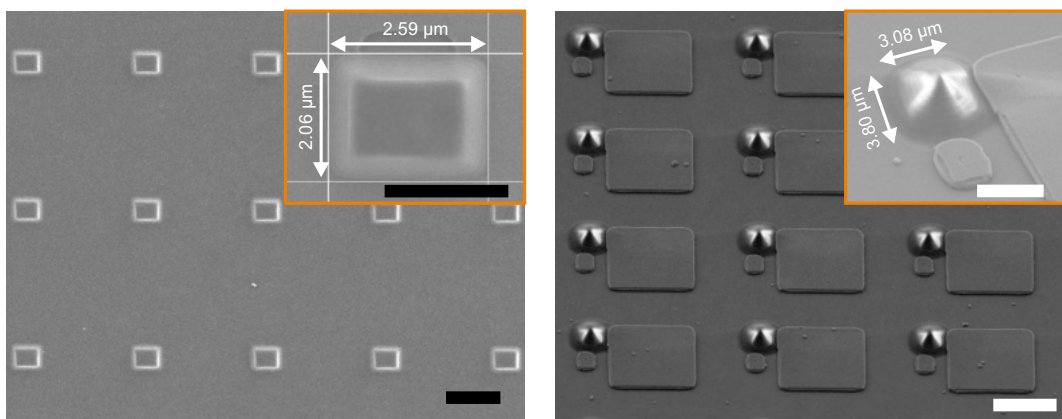


Figure 3.30. Selected polyimide cap with and without dissolve. SEM images with the dimensions of the polyimide (left) with and (right) without dissolving after the election of the best conditions from the photolithography test. Scale bars: $5 \mu m$. Inset scale bars: $2 \mu m$.

On the other hand, for the original polyimide, the best configuration was achieved for $150 mJ/cm^2$ in ED, for a range of values from 50 to $150 mJ/cm^2$, with step of $10 mJ/cm^2$, and a value of -0.25 for DOF, between the values -0.1 to -0.3, in steps of 0.05. With this configuration the obtained dimensions were $3.08 \times 3.8 \mu m^2$ in the plane of the wafer (Figure 3.30, right), and a vertical profile between 0.5 - $0.7 \mu m$, as its pyramidal shape, originated on the defocusing of the process, did not allow a better specification.

Returning to Figure 3.26, we followed the same last steps of the fabrication process of the sensors but with the polyimide configurations adopted above. First, it was processed the wafer with the dissolved polyimide, until the step prior to the etching of the SiO_2 sacrificial layer.

Devices were analysed by SEM, and it was found that cavities were collapsed (Figure 3.31), since polyimide entered inside them as corroborated by FIB nanomachining (Figure 3.31). This result forced us to completely dismiss the dissolved polyimide as an option for the cap.

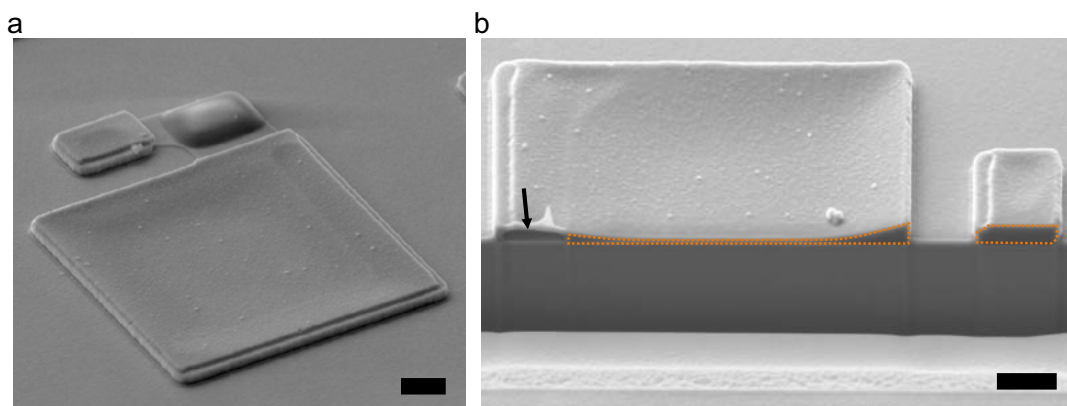


Figure 3.31. **Analysis of the collapsed sensors sealed with the dissolved polyimide.** a) SEM image shows a collapse sensor with the polyimide cap from the dissolved configuration. b) SEM image of a milled sensor by FIB showing that only the farthest zone to the pinhole is unfilled inside the sensing cavity (pointed by the arrow) and the rest is collapsed by the polyimide entry. The reference cavity is also filled with polyimide. Dotted orange areas show the space with polyimide. Scale bars: 1 μm .

On the other side, wafer with devices sealed with the ordinary polyimide were also processed following the steps described in Figure 3.26, with the difference that photoresist was annealed in step represented in Figure 3.26c.

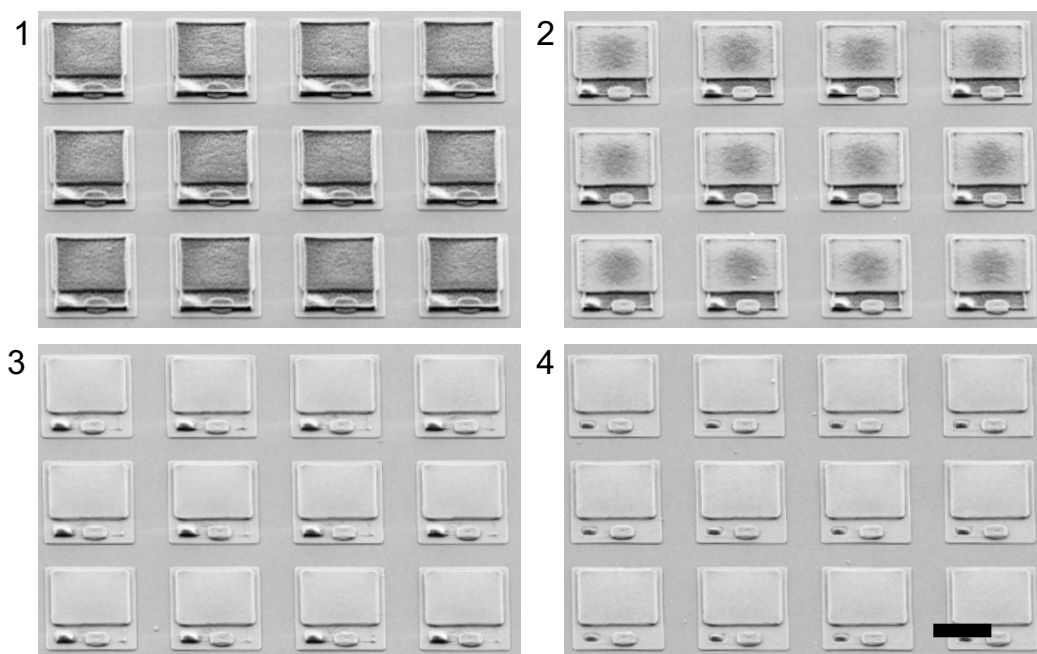


Figure 3.32. **Sensors with resist rests after the resist stripping.** SEM images of the resist rest showing the progression of the resist removal, from the center (1) to the border (4) by the plasma etching which also modifies the dimensions of the polyimide cap. Scale bar: 5 μm .

The annealing consists of a step where the photoresist is cured for 1 h with UV light and then the wafer is located in an oven for 20 minutes at

125 °C and then a ramp heating to 175 °C for 30 minutes. This hard baked was needed as the polysilicon etching were carried out in AMI ETCH P-5000 equipment, with CF_4 and Cl_2 gases. The hard baked of the photoresist on the previous step to the polysilicon etching, resulted in a over-hardened resist. Thus, the stripping of the resist was performed in TEPLA 300-E (Technics Plasma) by the use of oxygen (600 sccm) and CF_4 (15 sccm) gasses with a μ -wave-power of 500 W for 30 seconds. The CF_4 helps to remove the resist, but makes the process not homogeneous, causing a non-uniform etching of the resist along the wafer (Figure 3.32). The external parts are fully etched, even the polyimide cap has been completely stripped (Figure 3.33), while as we moved into the wafer the resist was less affected. Figure 3.32 shows the devices from a wafer examined by SEM, which still have photoresist traces on the internal areas, while in the border the polyimide cap and the resist has been completely removed.

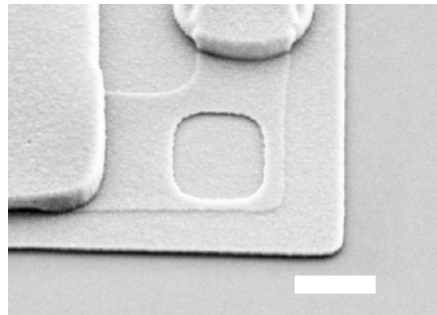


Figure 3.33. **Complete stripping of the resist and polyimide caps.** SEM image showing the polyimide cap has been totally stripped from a sensor. Scale bar: 1 μm .

Additionally, devices were milled by FIB for their internal inspection, checking that only the inner side that lengthen around the outline of the device shows an accumulative volume with polyimide extending less than 0.4 μm to cavity interior (Figure 3.34).

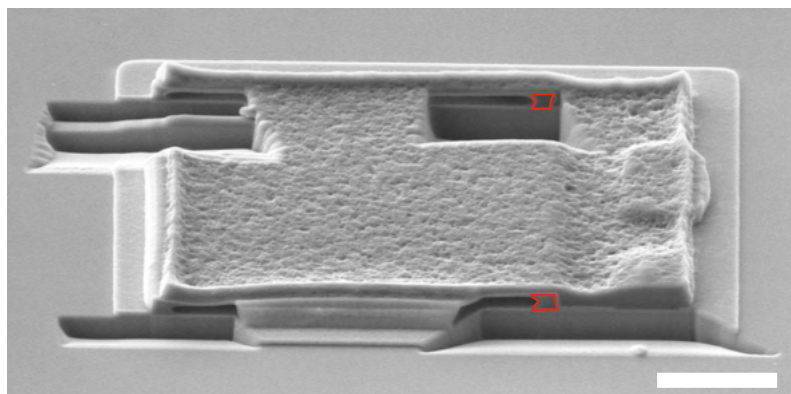


Figure 3.34. **FIB milling to probe sensors have not collapsed with the ordinary polyimide as sealing cap.** SEM image shows the internal part of the non-collapsed sensing cavity free of polyimide. Only the contour of the polyimide (red zones) has polyimide cumulus which can be consider as a loss in the device dimensions. Scale bar: 2 μm .

This internal polyimide accumulation could be considered as a small loss in the cavity dimensions, reducing its analytical sensibility a 15 % when the length of one side of the membrane changes to $a = 7 \mu\text{m}$ (nominal) to $a = 6.5 \mu\text{m}$. Nonetheless, this potential change in the size will not affect its mode of operation, since the devices are calibrated prior to their application in living cells.

To solve the problem of the cap stripping, we introduced a ramp baked of the polyimide to harden it (just following its photolithography) as a protective mode for subsequent stripping of the photoresist. The ramp baked consist in a program where the temperature of the oven is increasing from 100°C to 330°C for 1 hour, then the temperature continues for another hour at 330°C , and after that time a cooling steps is carried out for 2 hours. With this ramped process a gradual variation in temperature is guaranteed, protecting the devices from sudden alterations.

Therefore, the complete fabrication was carried out starting from a silicon wafer, as it was established before, with the original polyimide hardbaked after the photolithography, and without the UV recruit for the photoresist prior to the final etching of the 100 nm polysilicon layer (the entire fabrication process can be found in Subsection 3.5.4), obtaining a final fabrication yield of $\sim 3\%$ (around 800.000 devices). Optical images, in Figure 3.35, show sensors in the final step of the fabrication prior to their releasing. Depending on the position of the chips in wafer, devices looked collapse (periphery) or properly sealed (center).

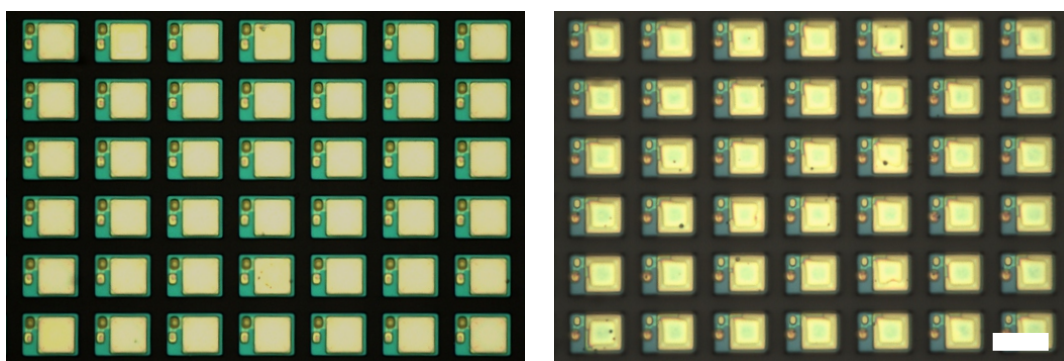


Figure 3.35. **Optical images of the fabricated sensors with polyimide cap.** Images show sensors on the step prior to their release, with (left) correct fabricated cavities in chips at the center of the wafer, and (right) collapsed cavities in chips at the periphery of the wafer. Scale bar: $10 \mu\text{m}$.

Thus, we will focus on the collection of sensors from chips in the center of the wafer to later try to perform their optical characterization.

3.5.4 Summary of the complete fabrication process of the pressure sensors with polyimide cap for sealing the cavities

Hence, to summarize the whole fabrication process of the intracellular pressure sensors were based on silicon microelectronic techniques; photolithographic processes were employed together with micromachining technologies by the etching of the SiO₂ layers to shape the polysilicon layers.

Devices are fabricated over a four-inch p-type silicon wafer <100> (Okmetic) (Figure 3.19). –*Ox1*– Initially, a 1 μm-thick layer is grown by wet oxidation at 950 °C. –*Poly1*– A 50 nm-thick polysilicon layer is deposited by a CVD (Chemical Vapour Deposition) process (630 °C, 140 mTorr). –*Ox2*– A 280 nm-thick silicon dioxide TEOS layer is deposited by a PECVD (Plasma-Enhanced Chemical Vapour Deposition). A 1.2 μm-thick of positive photoresist (ma-P 6512 MicroResist Technology) is spun onto the wafers. UV light exposure (Stepper NSR 2205-i12D Nikon) is performed through the second quadrant of the reticle. The resist is developed and baked during 30 min at 200 °C. Then the etching of the 280 nm-thick silicon dioxide layer is done with a C₂F₆ and CHF₃ RIE process (ALCATEL GIR 160). After that, the photoresist is stripped (TEPLA 300-E, Technics Plasma). Next, a 30 nm-thick silicon dioxide TEOS layer is deposited by a PECVD. A 0.6 μm-thick of positive photoresist (Fujifilm OiR 620-09) is spun onto the wafer. Then, the exposure of the photoresist is performed by UV light (Stepper NSR 2505-i12D Nikon) through the third quadrant of the reticle. The 30 nm-thick SiO₂ layer is etched by a wet buffered Hydrofluoric acid (HF)-based solution (SiO-etch MT 06/01 VLSI Selectipur, BASF). Lastly, the OiR photoresist is removed. –*Poly2*– A 50 nm-thick polysilicon layer is deposited. A 1.2 μm-thick of positive photoresist (ma-P 6512 MicroResist Technology) is spun onto the wafers. Then, the exposure of the photoresist is performed by UV light (Stepper NSR 2505-i12D Nikon) through the fourth quadrant of the reticle. The resist is developed and baked. The orifice in the 50 nm-thick polysilicon layer is opened by a dry reactive ion etching with CF₄ and Cl₂ (AMI ETCH P-5000). Lastly, the photoresist is stripped. Next, the internal sacrificial layers of silicon dioxide are wet-etched with a HF-based solution. Drying process is performed with a critical point dryer of CO₂ (Supercritical Automegasamdri®-915B, Series C, Tousimis). A 7 μm-thick of polyimide photoresist (HD-8820 MicroSystems) is spun onto the wafers. Then, the polyimide cap is performed by exposing the polyimide with UV light (Stepper NSR 2505-i12D Nikon) through the sixth quadrant of the reticle. The polyimide resist is developed and then hardbaked at 330 °C. A 1.2 μm-thick of positive photoresist (ma-P 6512 MicroResist Technology) is spun onto the wafers. Then, the exposure of the photoresist is performed by UV light (Stepper NSR 2505-i12D Nikon) through the fifth quadrant of the reticle. Here, we do not perform the annealing in order to avoid to damage the polyimide cap when stripping the photoresist after the etching. The 100 nm-thick polysilicon layer is etched with CF₄ and Cl₂ in a RIE process (AMI ETCH P-5000). The photoresist is stripped. Finally, the devices are released by HF vapours (49% HF; Honeywell) and collected in 96% ethanol.

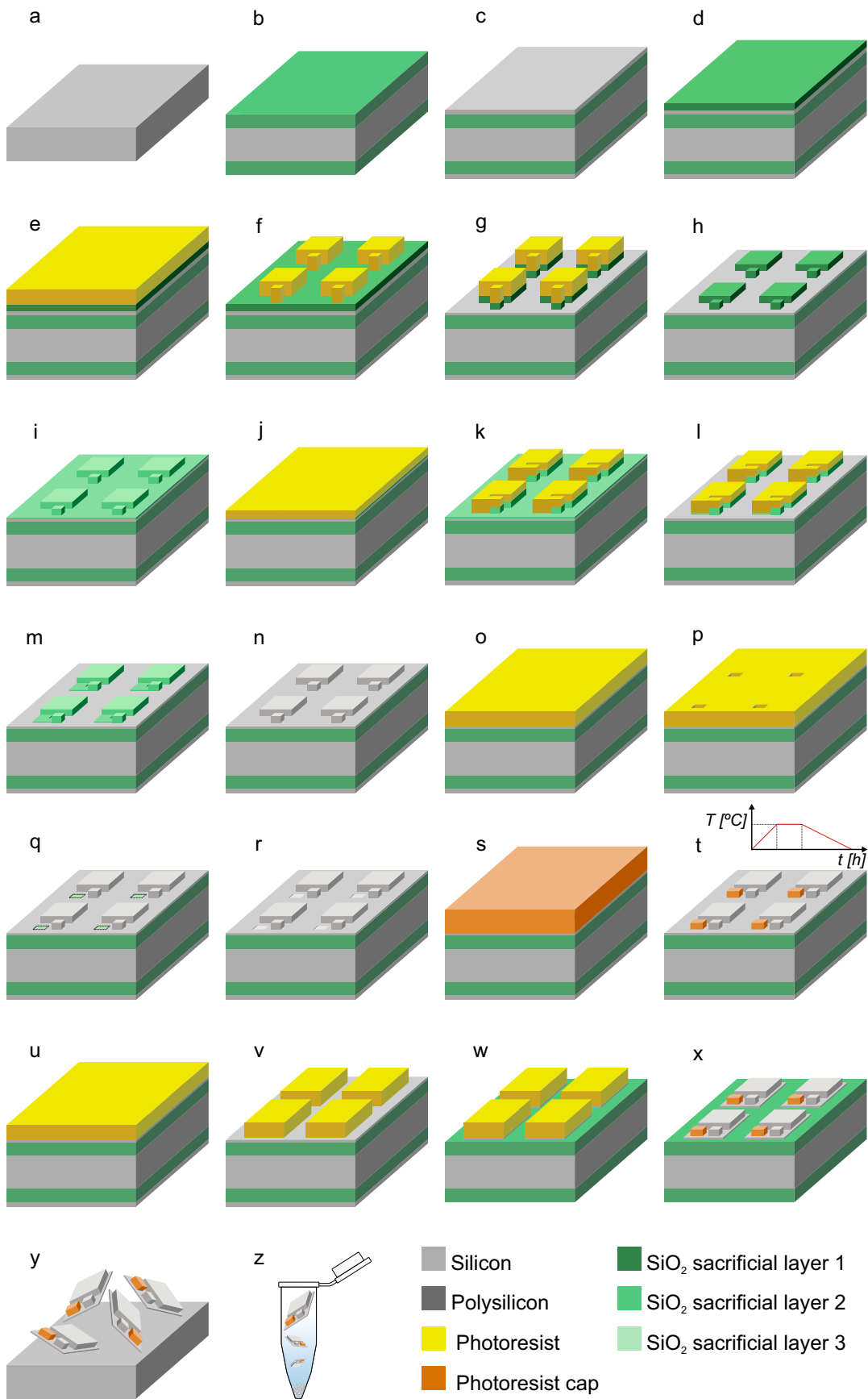


Figure 3.36. **Detail of the whole final fabrication of the pressure sensors.** a, Silicon wafer as initial substrate. b, 1 μm -thick of grown SiO_2 as sacrificial layer for releasing the devices, *Ox1*. c, 50 nm-thick polysilicon deposition, *Poly1*. d, 280 nm-thick SiO_2 deposited, *Ox2*, to define the vertical dimension of the sensor cavity. e, 1.2 μm -thick of positive photoresist is spun. f, Photolithographic process. After that the resist is developed and baked. g, 280 nm-thick SiO_2 layer is etched in a RIE process. h, Resist is removed. i, 30 nm-thick SiO_2 layer is deposited. j, 0.6 μm -thick of OiR photoresist is spun. k, Photolithographic process. l, 30 nm-thick SiO_2 layer is etched in a wet process. m, OiR resist is removed. n, 50 nm-thick polysilicon deposition, *Poly2*. o, 1.2 μm -thick of positive photoresist is spun. p, Photolithographic process to define the orifice dimensions and the 50-nm thick polysilicon etching to open the cavity on the layer. q, Resist is removed. r, SiO_2 internal sacrificial layers are wet-etched and a drying process is performed with a critical point dryer. s, 7 μm -thick of polyimide photoresist is spun. t, Polyimide cap is structured by a photolithographic process and is later developed and hardbaked at 330 °C. u, 1.2 μm of positive photoresist is spun. v, Photoresist is developed. w, The 100 nm-thick polysilicon layer is etched in a RIE process. x, Photoresist is removed. y, SiO_2 sacrificial layer is etched by HF vapours to release the devices. z, Finally, devices are collected in an Eppendorf with 96% ethanol.

3.5.5 Releasing of the pressure sensors

The final step in the fabrication of the sensors is their release from the substrate, in order to achieve them in suspension. For a better manipulation during the releasing process, the wafer is cut into chips (areas of 1 cm \times 0.5 cm) with a diamond tip; each chip contains 265,320 devices. Hence, the releasing process is as follow in Figure 3.37.

First, chips are place on a teflon holder and the SiO_2 sacrificial layer is etched by HF vapours (49% HF; Honeywell) four 40 minutes. Next, the etched chips are immersed in a plastic container with 96% ethanol inside, where they are initially obtained in suspension. Then, devices suspended in ethanol are collected in different Eppendorf tubes.

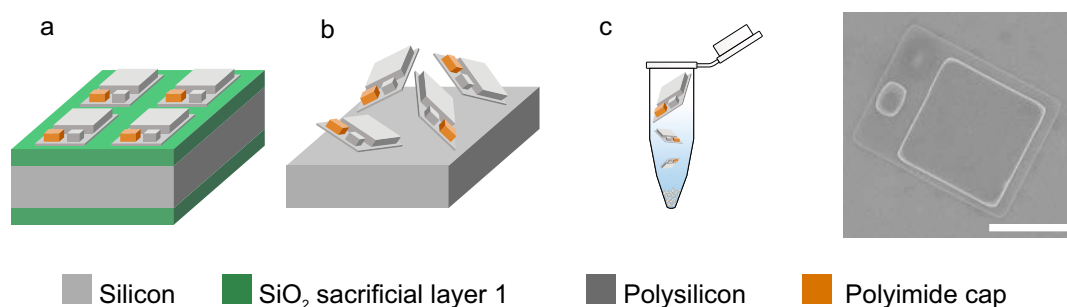


Figure 3.37. **Releasing process of the sensors from the wafer.** a) Starting from a silicon wafer with the fabricated devices on a SiO_2 , b) this SiO_2 sacrificial layer is etched by HF vapours to release the devices, and c) finally, devices are collected in an Eppendorf with 96% ethanol. SEM image shows a released fabricated sensor. Scale bar: 5 μm .

3.6 Preliminary characterization and validation of the first devices

Fabricated devices were characterized and validated, prior to their releasing and after that. Since the fabrication presented a low yield and only some devices were correctly sealed, further improvements have to be done in order to achieve faultless fabrication batches. However, properly fabricate devices were collected in suspension and a first measure, to characterize and validate their operational mode was done.

3.6.1 Morphological characterization of the fabricated devices

Fabricated devices were analysed using confocal microscopy (PLu neox, optical 3D surface profiler, Sensofar) to obtain a profile of the cavities to measure their dimensions.

Figure 3.38 shows the optical profile for a (left) collapsed cavity and for a (right) non-collapsed cavity. This method allows the characterization of the devices, which is important to validate sensors at critical steps during their fabrication. The measures show a z-profile of 85.85 ± 2.40 nm for the collapsed cavity and 325.89 ± 0.25 nm for the non-collapsed cavities.

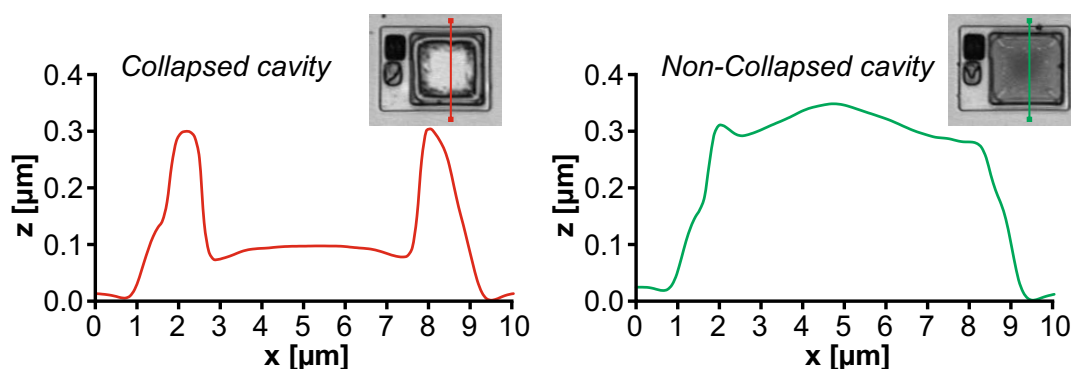


Figure 3.38. **Confocal characterization of the devices.** Confocal profiles of released devices (left) with a collapsed cavity and (right) with a non-collapsed cavity. Inset confocal images show the measured sensor with a coloured line defining the profile. The measured height of the center of the sensing cavity are 85.85 ± 2.94 nm for the collapsed and 325.89 ± 0.25 nm for the non-collapsed cavity.

Additionally, released devices were placed in a small piece of silicon to examine them in optical and electron microscopies. For that, collected devices were resuspended and a $2 \mu\text{l}$ -drop of ethanol was taken and placed within a SEM equipment or under an optical microscope in the piece of wafer. Figure 3.39 shows some released devices: at the left devices showing a correct fabrication on the sensing cavities and at the right devices with them collapsed. The analysis of the physical aspect of the fabrication also exhibits damages in the polysilicon top membrane of the reference cavity, which is caused by the resist reticulation by its baking (200°C during 30 min) for the first SiO_2 etching (Figure 3.19f).

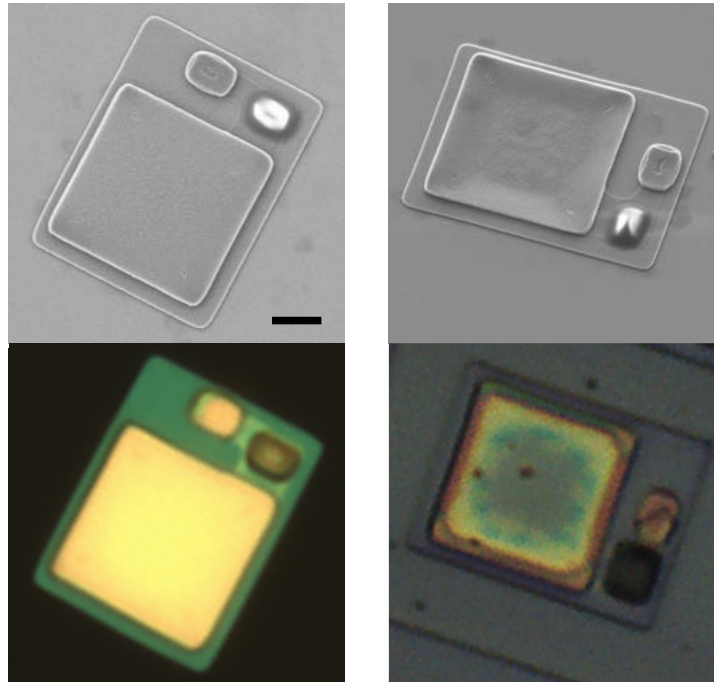


Figure 3.39. SEM and optical images of released devices. Images on the left show devices with a correct fabrication of the sensing cavity. On the right, images of devices with a non-correct fabrication present collapsed sensing cavities. Scale bar: 2 μm .

3.6.2 Validation of the pressure sensor operation principle by bright-field optical microscopy

Devices were validated under an optical microscope by sweeping the applied pressure and the wavelength. Particularly, image acquisition was performed in a bright-field optical microscope (Eclipse ME600 upright, Nikon) with a $\times 100$ magnification, 0.8 NA, long-distance objective LU Plan ELWD 3.5 (Nikon).

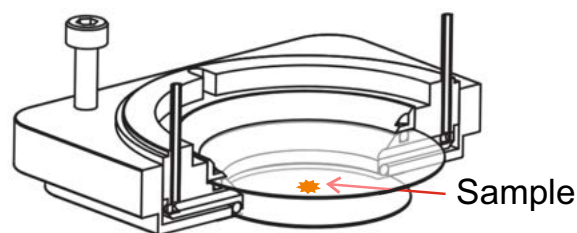


Figure 3.40. Scheme of the Ludin chamber. Cross section of the Ludin chamber where sensors are placed to be characterized during their exposition to different applied pressures. Orange star represents the position where the devices are placed.

Images were recorded using an 8-bit colour CCD (charge-coupled device) camera (DXM1200F, Nikon) using the advanced control software Nikon ACT-1 (Automatic Camera Tamer). Band-pass filters (Thorlabs) coupled with

a YM-NCB11 filter slider (Nikon) were used to sweep the wavelength of the incident light.

For the pressure application, a portable pressure calibration kit LPP-KIT-PD-05-9005 (Druck & Temperatur Leitenberger GmbH) and polytetrafluoroethylene (PTFE) tubing was used in the experiments. The LPP-KIT included a LPP 30 hand pump that can be used to generate pressures up to +35 bar and the electronic pressure calibration LR-Cal TLDMM with a range of -1 to +5 bar and an accuracy of $\pm 0.05\%$ FS. The experiment was carried out inside a hermetic live-imaging chamber for the microscope (Ludin Chamber Type 3; Life Imaging Services GmbH) (Figure 3.40). The steel body and the ($\Phi = 12$ mm) cover slip provided a high stiffness for the pressure experiments.

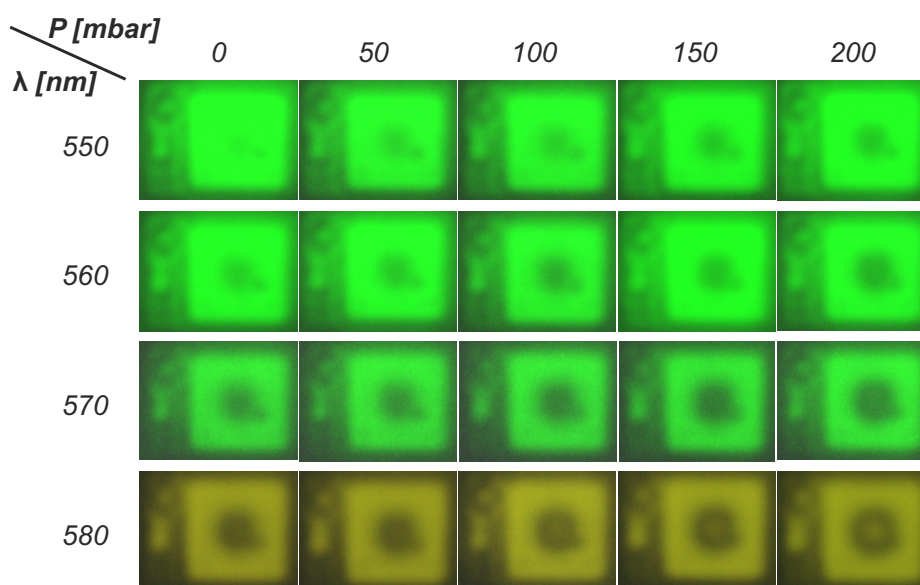


Figure 3.41. Pressure sensor validation subjected to a pressure sweep for different wavelengths. Optical bright field true-colour images of a sensor for different pressures, P , from 0 mbar to 200 mbar, for different wavelengths from 550 nm to 580 nm for the pressure sensor validation, λ .

To analyse the fabricated devices, we performed a pressure sweep, from 0 mbar to 200 mbar, in steps of 50 mbar, under the bright-field microscope. We hosted the devices in the hermetic chamber in an aqueous medium, and with the LPP 30 hand pump we produced changes in the external pressure. For the wavelength sweeping, filters from 540 nm to 580 nm, in steps of 10 nm, were used. Figure 3.41 shows optical changes in the reflection on the central area of the sensing cavities when the applied pressure changes.

This recorded images were analysed using the ImageJ software (<http://rsbweb.nih.gov/ij>). Two Regions Of Interest (ROI) were taken (Figure 3.42): ROI 1 is a line to measure the intensity profile along the sensing cavity and ROI 2 is a circular area in the reference sensor. A line instead a circular area was used in ROI 1 for a better determination of the center of the sensing cavity. ROI 2 will change when the device is tilted, but not due to a deflection

of the membranes, thus it will allow us to amend the tilt effect of the sensing cavity measurement.

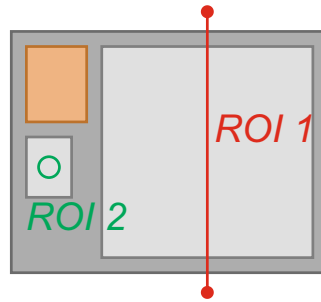


Figure 3.42. Scheme of the selected ROIs for the measure of the reflected intensity. Drawing of a sensor with a (red) line profile as ROI 1 for the sensing cavity and a (green) circle as ROI 2 for the reference cavity intensity measurements.

Therefore, the measured ROI 1 profile (I_{sensor}^r) was tilt-compensated by the factor of correction $\beta = I_{ref}^r(P = 0) / I_{ref}^r(P)$. Thus, the intensity reflected at the sensing cavity is normalized to $I_{sensor}^{norm} = \beta I_{sensor}^r$. The values for the intensities were established as the average value of the intensities measured in the ROI area for ROI 2, and the average value in a range of ± 10 pixels from the center of the line profile (total length 250 pixels) for ROI 1. In Figure 3.43 are presented the measured changes in the reflected intensity when pressure varies for different wavelengths. A clear trend downward and upward can be observed around $\lambda = 570$ nm, where a valley on the reflectance was found.

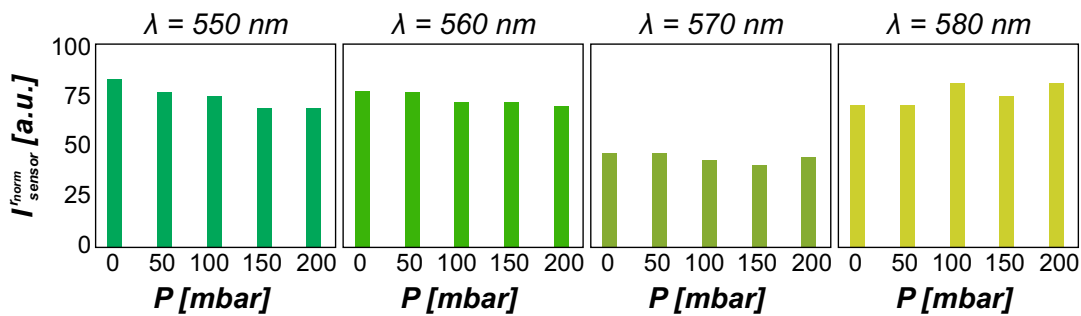


Figure 3.43. Reflection intensities for different values of λ in a sweep of pressures, P . Bright field optical measures of the reflected intensities at the sensing cavity normalized with the reference cavity measure, I_{sensor}^{norm} , for different wavelengths, λ , showing perceivable pressure changes with a valley shape around $\lambda = 570$ nm.

A surface plot to display a three-dimensional graph of the reflected intensities through the reference and sensing cavities in the areas shown in Figure 3.44 was performed for $\lambda = 580$ nm. Fulfilling the designed specifications, the intensity reflected at the reference cavity is invariable, due to the optical path does not change when the pressure varies. On the contrary, reflected light through the sensing cavity modifies its intensity values during the pressure sweep.

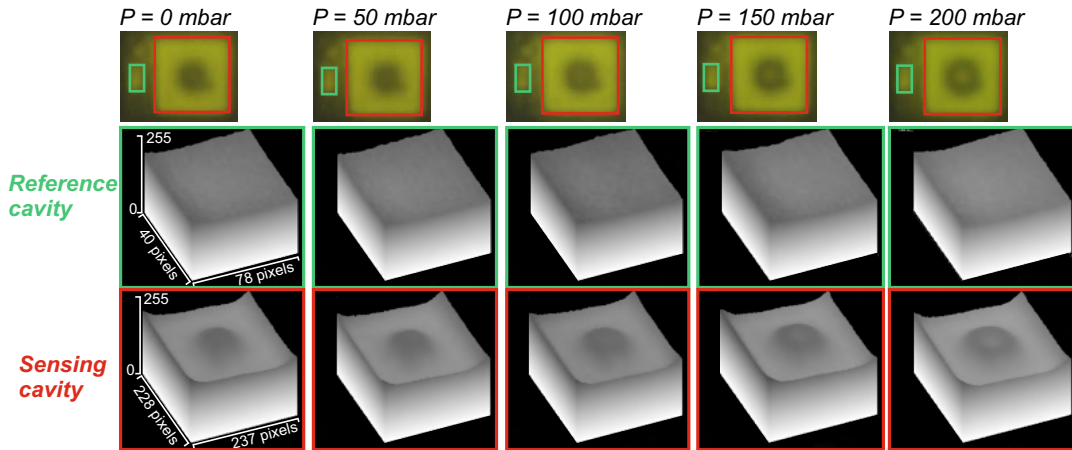


Figure 3.44. Surface plot of the reflected intensities of the sensor cavity. Three-dimensional surface plot of the (green frame) reference and (red frame) sensing cavities for the different values of pressure, P , at a fixed wavelength, $\lambda = 580$ nm.

Since changes up to 50 mbar have been measured, we wonder if lower variations of the applied pressure could be detected and measured with the sensors. Hence, a sweep from 0 mbar to 50 mbar, in steps of 25 mbar, was done for $\lambda = 580$ nm where it was found that 25 mbar pressure changes can be detected (Figure 3.45 and Figure 3.46).

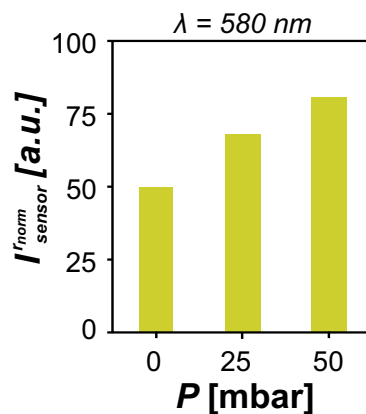


Figure 3.45. Normalized reflected intensities at the sensor cavity in a range of 0 to 50 mbar. Graph plot of the reflected intensities at the sensing cavity normalized with the reference cavity, $I_{\text{sensor}}^{\text{norm}}$, versus the applied pressure, P , for $\lambda = 580$ nm, showing detectable variations for 25 mbar increments.

To evaluate the deviation obtained from this measure we preformed the following calculations. First, the ROI 1 was traced and the average of the ± 10 pixels from the center was done to obtain the nominal value of the measure for each of the pressure values (as before). Next, four more measures were done by shifting the ROI 1 one pixel up, one down, one left and one right, and again averaging the central values of each one. In this manner, each measurements is affected by an average deviation of ± 1.58 a.u..

Additionally, it can be derived from the measure (Figure 3.45) that the sensibility of the devices obtained through a bright-field optical microscope

reached 1.59 mbar/a.u.. This remarkable result elucidate the high sensibility of the fabricated devices, which drives to an average deviation of 2.52 mbar in our measure system.

The surface plots on Figure 3.46 display the the cavity three-dimensional graphs detecting changes up to 25 mbar at the sensing cavity.

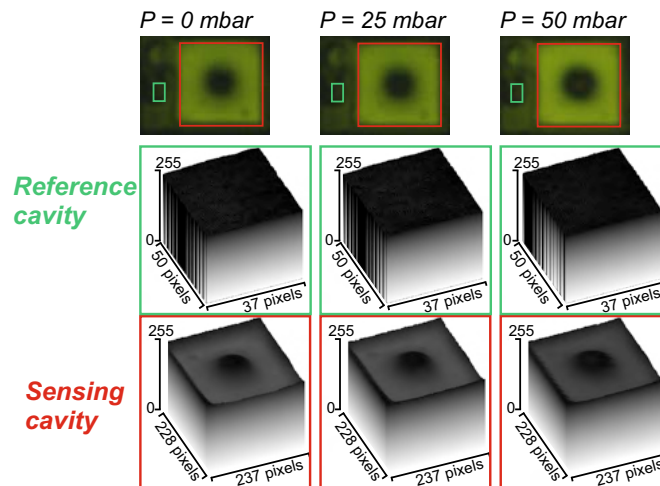


Figure 3.46. Surface plot of the reflected intensities in a range of 0 to 50 mbar. Three-dimensional surface plot of the (green frame) reference and (red frame) sensing cavities for pressure values in steps of 25 mbar.

The first generation of pressure sensors were designed to achieve theoretical mechanical sensitivities of 0.0055 nm per mbar (5.5 nm per bar) on the membranes. Our new proposal has been designed to reach 0.1683 nm per mbar ($E = 160$ GPa). This represents a 30-fold improvement in the mechanical sensitivity of the membranes. Also, this second generation of sensors can detect changes down to 25 mbar, which means (at least) a measured enhancement of 10-fold in the optical detection.

3.7 Discussion

In this chapter a more sensitive intracellular pressure sensor has been presented. Considering the previous pressure sensor developed by the group [13], a new device has been designed and the ground for a reliable fabrication has been developed.

The first generation of pressure sensors consisted in two parallel polysilicon membranes separated by a vacuum gap. Here, the design of the new device has been modified to improve its detection limit by devising larger membranes enclosing air between them. Hence, the sealing of the cavity had to be done at room temperature and atmospheric pressure, since major differences between the pressure inside and outside the cavity will damage or break the device. Therefore, we performed the sealing of the cavity by the photolithography of a polymer resist, since most processes of the microtechnology fabrication were discarded as they operate at high temperature and very low pressure. Moreover, a reference cavity was included in this device in order to amend the reflected intensity measured at the sensing cavity.

The analysis of the mechanical and optical performance of the designed cavity was also carried out. The deflection of the membranes was mechanically simulated by FEM and the analytical calculation of the deflection has been done to corroborate the simulation results. Furthermore, a theoretical study of the optical performance of the Fabry-Perot resonator proved their high reflectivity at the visible operational range.

Throughout the fabrication process various important steps were minutely analysed because of their relevance as critical procedure. First, polysilicon layers were correctly developed, achieving 50 nm-thick non grainy layers thanks to the fitting of the magnitudes involves on the deposition process. Later, it was also proved that the etching of the pinhole was needed to be performed without the presence of $c\text{-C}_4\text{F}_8$, as this passivation generates polymers that can not be removed from the vertical surfaces and hinder the SiO_2 etching from the interior of the cavities. Finally, the sealing of the cavity focused almost completely the fabrication development of the sensor. Different polymer resists were tested, concluding that a high viscosity polymer was needed in order to prevent the collapse of the cavities due to the entry of the resist. Polyimide was finally used to seal the sensors.

Final fabrication of the devices (prior to their released) have shown that not all the sensors along the wafer have been correctly sealed. Therefore, additional investigation on the sealing step must to be done in order to improve the fabrication yield, but also to obtain similar devices.

The devices were released from the wafer and we characterized some of the properly sealed. A sweep on the external pressure, P , for different wavelengths λ was performed under a bright-field optical microscope. The reflected intensity at the centre of the sensing cavity, I_{ref} , was detected to change when changing the pressure and the reference was used to compensate the measure, validating its working principle. Devices have shown to be

able to detect up to 25 mbar, with a sensibility of 1.59 ± 2.52 mbar/a.u.. These values pointed that these pressure sensors could help in the in the study of the dynamic pressure of vacuoles inside living cells.

An extraordinary improvement in the sensitivity of the devices, compared with the first generation of sensors[13], has been demonstrated, even the sensitivity could be higher when devices are scanned in a white light CLSM, where λ can be adjusted to set the most suitable for working with the one where the slope of the reflection spectrum is maximum. Moreover, the validation of the devices inside living cells remains to be performed, when the overall characterization of correct fabricated devices is completed.

This work is one more step in the search for a pressure sensor with a high sensitivity able to be internalized in living cells allowing a direct monitoring of the cell pressure changes in cytoplasm or even in vacuole.

Bibliography

- [1] Jiaxiang Tao, Yizeng Li, Dhruv K Vig, and Sean X Sun. Cell mechanics: a dialogue. *Reports on Progress in Physics*, 80(3):036601, 2017.
- [2] Hans Van Oosterwyck, Liesbet Geris, and José Manuel García Aznar. Cell mechanics and mechanobiology. *Editors: Manuel Doblare and Jose Merodio*, page 271, 2015.
- [3] Pragati Chengappa, Kimheak Sao, Tia M Jones, and Ryan J Petrie. Intracellular pressure: a driver of cell morphology and movement. *International review of cell and molecular biology*, 337:185–211, 2018.
- [4] AJ Steward, SD Thorpe, T Vinardell, CT Buckley, DR Wagner, and DJ Kelly. Cell–matrix interactions regulate mesenchymal stem cell response to hydrostatic pressure. *Acta Biomaterialia*, 8(6):2153–2159, 2012.
- [5] A Sousa, SC Neves, IC Gonçalves, and CC Barrias. In vitro interaction of polymeric biomaterials with cells. In *Characterization of Polymeric Biomaterials*, pages 285–315. Elsevier, 2017.
- [6] JL Arlett, EB Myers, and ML Roukes. Comparative advantages of mechanical biosensors. *Nature nanotechnology*, 6(4):203–215, 2011.
- [7] Martin P Stewart, Jonne Helenius, Yusuke Toyoda, Subramanian P Ramanathan, Daniel J Muller, and Anthony A Hyman. Hydrostatic pressure and the actomyosin cortex drive mitotic cell rounding. *Nature*, 469(7329):226–230, 2011.
- [8] Robert M Hochmuth. Micropipette aspiration of living cells. *Journal of biomechanics*, 33(1):15–22, 2000.
- [9] Jing Yang, Xing Duan, Andrew K Fraser, Mohammad Ikbal Choudhury, Andrew J Ewald, Rong Li, and Sean X Sun. Microscale pressure measurements based on an immiscible fluid / fluid interface. *Scientific reports*, 9(1):1–10, 2019.
- [10] SM Kelly and PT Macklem. Direct measurement of intracellular pressure. *American Journal of Physiology–Cell Physiology*, 260(3):C652–C657, 1991.
- [11] Ryan J Petrie and Hyun Koo. Direct measurement of intracellular pressure. *Current protocols in cell biology*, 63(1):12–9, 2014.
- [12] Manuel Gómez-González, Ernest Latorre, Marino Arroyo, and Xavier Trepap. Measuring mechanical stress in living tissues. *Nature Reviews Physics*, pages 1–18, 2020.
- [13] Rodrigo Gómez-Martínez, Alberto M Hernández-Pinto, Marta Duch, Patricia Vázquez, Kirill Zinoviev, J Enrique, Jaume Esteve, Teresa Suárez, and José A Plaza. Silicon chips detect intracellular pressure changes in living cells. *Nature Nanotechnology*, 8(7):517, 2013.

- [14] Rodrigo Gómez Martínez. *Intracellular silicon chips*. PhD thesis, Universitat Autònoma de Barcelona, 2016.
- [15] Eugene Hecht. *Optics, 5e*. Pearson Education India, 2002.
- [16] Rodrigo Gómez-Martínez, Patricia Vázquez, Marta Duch, Alejandro Muriano, Daniel Pinacho, Nuria Sanvicens, Francisco Sánchez-Baeza, Patricia Boya, Enrique J de la Rosa, Jaume Esteve, et al. Intracellular silicon chips in living cells. *Small*, 6(4):499–502, 2010.
- [17] Philip L Felgner, Thomas R Gadek, Marilyn Holm, Richard Roman, Hardy W Chan, Michael Wenz, Jeffrey P Northrop, Gordon M Ringold, and Mark Danielsen. Lipofection: a highly efficient, lipid-mediated dna-transfection procedure. *Proceedings of the National Academy of Sciences*, 84(21):7413–7417, 1987.
- [18] Stephen P Timoshenko and Sergius Woinowsky-Krieger. *Theory of plates and shells*. McGraw-hill, 1959.
- [19] Xinxin Li, Takahito Ono, Yuelin Wang, and Masayoshi Esashi. Study on ultra-thin nems cantilevers-high yield fabrication and size-effect on young's modulus of silicon. In *Technical Digest. MEMS 2002 IEEE International Conference. Fifteenth IEEE International Conference on Micro Electro Mechanical Systems (Cat. No. 02CH37266)*, pages 427–430. IEEE, 2002.
- [20] Xinxin Li, Takahito Ono, Yuelin Wang, and Masayoshi Esashi. Ultrathin single-crystalline-silicon cantilever resonators: Fabrication technology and significant specimen size effect on young's modulus. *Applied Physics Letters*, 83(15):3081–3083, 2003.
- [21] Ivan Favero and Khaled Karrai. Optomechanics of deformable optical cavities. *Nature Photonics*, 3(4):201–205, 2009.
- [22] Martin F Colombano, Guillermo Arregui, Nestor E Capuj, A Pianti, Jeremie Maire, Amadeu Griol, Blas Garrido, Alejandro Martínez, Clivia M Sotomayor-Torres, and Daniel Navarro-Urrios. Synchronization of optomechanical nanobeams by mechanical interaction. *Physical review letters*, 123(1):017402, 2019.
- [23] Kejie Fang, Matthew H Matheny, Xingsheng Luan, and Oskar Painter. Optical transduction and routing of microwave phonons in cavity-optomechanical circuits. *Nature Photonics*, 10(7):489–496, 2016.
- [24] Frank L Pedrotti, Leno M Pedrotti, and Leno S Pedrotti. *Introduction to optics*. Cambridge University Press, 2017.
- [25] M Ino, J Miyano, H Kurogi, H Tamura, Y Nagatomo, and M Yoshimaru. Rugged surface polycrystalline silicon film deposition and its application in a stacked dynamic random access memory capacitor electrode. *Journal of Vacuum Science & Technology B: Microelectronics and Nanometer Structures Processing, Measurement, and Phenomena*, 14(2):751–756, 1996.

-
- [26] R Gómez-Martínez, A Sánchez, M Duch, J Esteve, and JA Plaza. Drie based technology for 3d silicon barcodes fabrication. *Sensors and Actuators B: Chemical*, 154(2):181–184, 2011.
- [27] R David Holbrook, Anne A Galyean, Justin M Gorham, Andrew Herzog, and John Pettibone. Overview of nanomaterial characterization and metrology. In *Frontiers of Nanoscience*, volume 8, pages 47–87. Elsevier, 2015.

Chapter 4

H-comb polysilicon devices for tracking intracellular forces and mechanical property changes in mouse one-cell embryo development

In this chapter, the development of a polysilicon tool for intracellular mechanical characterization is detailed. Based on silicon technologies, a 25 nm-thick polysilicon device was designed and fabricated as a functional device for addressing fundamental biological questions at the initial phase of mouse embryo development. Nanodevices were microinjected into a mouse oocyte enabling us to monitor nanodevice displacement and bending in real-time movies during the embryo (containing nanodevices) development. Analytical processing of nanodevice displacement and bending yields fundamental information about how forces and cytoplasmic properties contribute to initial developmental steps in mouse embryos. Furthermore, the mouse one-cell embryo cytoplasm has been modelled in terms of viscous and elastic elements revealing a gradient of effective stiffness, which could facilitate the female and male pronuclei convergence. In particular, nanodevices revealed very low mechanical activity during chromosomes alignment. Additionally, nanodevices detected a reduction on the effective stiffness of the cytoplasm on embryos treated with an actomyosin inhibitor. This result allowed us to conclude that there is a program of intracellular force and mechanical property changes during the first stages of the embryo development, and that H-comb nanodevices allowed us to track and quantify it.

Note about my contribution to this work

This work began five years before I joined the group, thus I clarify here my contribution in the development of this investigation that involves several areas of the scientific knowledge, as it is a high multidisciplinary research. Hence, many researchers have contributed along the seven years of the work development. The contribution of each one has allowed these results to be achieved, thanks to the development of research that is at the limit of the knowledge of the involved fields.

Despite not to being part from the beginning of the work, I have contributed on the data analysis of the nanodevices inside the embryo, both treated and untreated embryos. For instance, data analysis of embryos with nanodevices was done prior to my incorporation, however, I joined to make the complete data analysis of treated embryos and also to accurate the method of data acquisition and re-analysed some of the previously examined nanodevices in untreated embryos.

On the simulation analysis, I have contributed on the research of the appropriate method to calculate the 25 nm-thick polysilicon Young's modulus. I have also taken part of the modelling of the cytoplasm organization by the analysis of the movement of organelles and vesicles.

Additionally, I have fully participated in the investigation about how much the device bending measures are affected by the diffraction limit, through the analysis of the injected H-comb devices, but also by the design, fabrication and characterization of new optical test structures.

Biological experiments such as nanodevice injection, embryo development, gene expression analysis or immunochemistry were entirely carried out by the biologist partners at the University of Bath led by Prof. Tony Perry (see *Collaborations and Stays in Research Entities*).

In spite of Prof. José Antonio Plaza and Prof. Tony Perry wrote most of the published manuscript, I have had the opportunity to contribute on the writing of the manuscript, as well as the responses to reviewers, during the publication process.

4.1 Introduction

Intracellular mechanics is a key determinant of cell biology. Each cell is mechanically stabilized by a filamentous cytoskeleton that controls relative stiffness[1]. Active mechanical behaviour generates intracellular pulling and pushing forces and drives stochastic force fluctuation to enable cytoplasmic remodelling[2]. Such dynamic mechanical intracellular behaviour provides a tier of regulation that may be as critical to developmental processes as regulation by gene expression[3, 4] and there is interplay between the two: force and stiffness changes control transcriptional programs involved in cell differentiation[5–7].

Successful and comprehensive models of cell mechanics will require information on different hierarchical levels to relate local interactions in the cytoskeleton to the aggregate mechanical behaviour of cells[1, 8, 9]. Broadly, there are two approaches to study cell mechanics: top-down (systems-level) and bottom-up (reductionist)[1, 10]. Top-down models are based on generic principles that are not obviously dependent on lower levels in the structure. These models are derived from extracellular devices[1, 9, 11–14]. By contrast, bottom-up methods derive system properties from those of their constituents (e.g. molecular assemblies including the cytoskeleton)[1, 8, 9, 11, 15].

Bottom-up approaches[16–18] can be based on local intracellular measurements but the descriptions of constituent functions cannot necessarily be extrapolated to higher-order structures (e.g. the cell) due to their complex heterogeneity[1]. Thus, improved models of cell mechanical behaviour will be required that meet the considerable challenges of devising top-down direct intracellular models. Tools to complete the internalized top-down picture were not available until recent advances in silicon-based nanodevices that can be reproducibly manufactured, are versatile, and have the potential to be placed completely inside cells[19, 20].

In the context of embryogenesis, externally-induced stiffness in mouse embryonic stem cells influences the expression of pluripotency factors such as Oct4 to drive differentiation[21, 22]. In addition, endogenous mechanical transitions play a critical role in preimplantation development of mouse embryos after several days[23], but almost nothing is known about whether similar processes are important for embryonic development immediately after fertilization.

We accordingly sought an intracellular top-down approach to study the cytoplasmic mechanics of mammalian one-cell embryos (to the first mitotic cell division), which are relatively large: ~ 170 pl compared to ~ 1 pl for other mammalian cells[24, 25]. Such large cellular volume likely affects chromatin remodeling, intracellular transport (including pronuclear convergence) and cell division[26]. Although this suggests that intracellular forces and changes to the mechanical properties of the cytoplasm play a crucial role, no mechanical model accounts for them.

Furthermore, measuring intracellular embryonic mechanics required the scalable, high-fidelity production of force-change-sensitive chips that can be entirely internalized within mouse metaphase II (mII) oocytes. Such devices needed to be large enough to average out random (local) molecular perturbations so that their intracellular behaviour would reflect force fluctuations and changes in cytoplasmic stiffness. For a top-down model, relatively large 2D devices are required ($22\ \mu\text{m}$, similar to the diameter of the pronucleus, pn). This precludes the use of spherical 3D tools of similar diameter, including some types of bead, or oil droplets[27], whose large volumes could perturb cytoplasmic dynamics. Device thickness also had to be on the nanometer scale, akin to cytoskeletal structures (Figure 4.1), giving them an extraordinarily small volume and a high mechanical sensitivity.



Figure 4.1. **Cytoskeletal structures.** Dimensional schematic of microtubules (mt) and actin microfilaments (mf).

In this work, we detail a direct mechanical readouts obtained following nanodevice injection and integrate them with molecular and gross morphological analyses. Results directly show an active program of forces and mechanical property changes that drive early embryo development.

4.2 Design and operational principle of the mechanical sensor

With the motivation to accomplish a mechanical portrait of the embryo cytoplasm, we contrived a 3D 'H-comb' polysilicon device (Figure 4.2). These polysilicon-based nanodevices comprised eight cantilever prongs, with a total width of $10.5\ \mu\text{m}$, and a length of the complete device of $22\ \mu\text{m}$ (Figure 4.2).

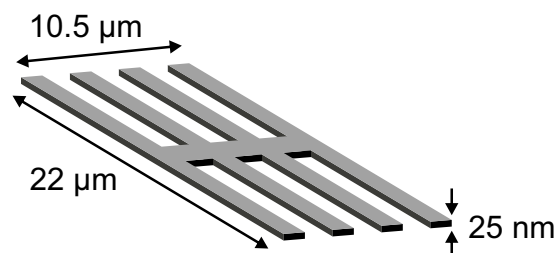


Figure 4.2. **H-comb device design dimensions.** Schematic representing the designed shape and dimensions of the H-comb device.

To achieve the dimensions of the H-comb device, we employed silicon chip technology. This technology permits a high degree of control and reproducibility over geometrical dimensions, as we will see in Section 4.3.2, allowing us to mass-produce complex structures.

In-plane dimensions of H-comb devices ($22\ \mu\text{m} \times 10.5\ \mu\text{m}$) were designed to be large enough to average random (local) molecular perturbations so that their intracellular behaviour would reflect mechanical load fluctuations and changes in cytoplasmic resistance due to cytoplasmic reorganization. Perpendicular dimensions were, by contrast, designed to be very small ($0.025\ \mu\text{m}$) to allow a high sensitivity and to minimize the impact of devices on embryo development.

The H-comb devices have free spaces between the eight cantilevers, further minimizing any impact on cytoplasmic organization and molecular diffusion compared with non-structured rectangular devices or spherical beads of similar micrometer-scale dimensions. The extraordinary aspect ratio of the nanodevices facilitates the measurement of their responsive rotation inside the embryo, revealing cytoplasmic dynamics and mechanical activity.

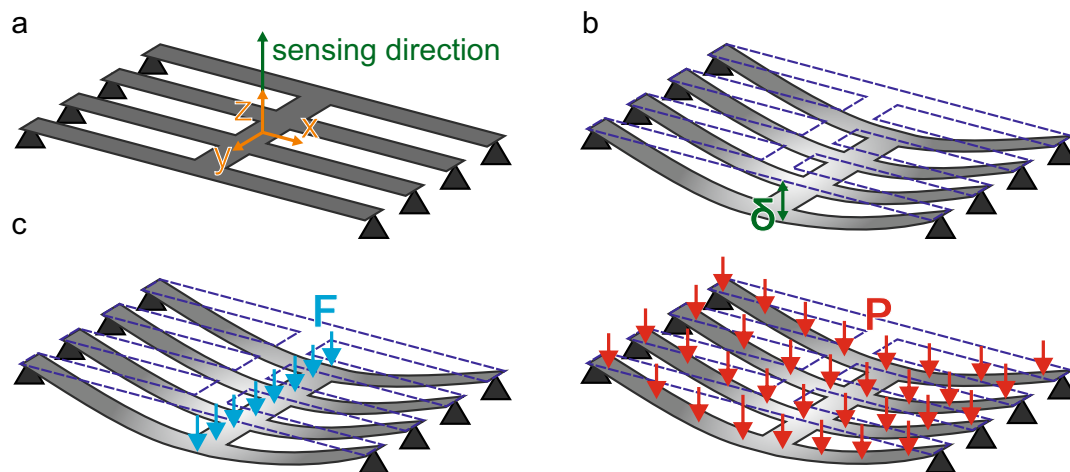


Figure 4.3. **Conceptualization of the operating principle.** a) Schematic view of the nanodevice sensing direction (nanodevice thickness, z-direction). b) Nanodevice bending, δ , by the action of (c) force loads, F , or a uniform distributed pressure load, P , (right).

Therefore, the nanodevices allow a readout of its bending and translate it into a measurement of force, F , or pressure, P (Figure 4.3). The eight-pronged H-comb nanodevice design avoids uncertainty in the determination of the maximum displacement, δ , that arises for narrow devices that are not coplanar to the image plane. A large device width solved the uncertainty of the maximum displacement, δ , determined by angular orientation, a problem that can arise with a beam design (Figure 4.4).

For the determination of the device bending, we firstly established three axes of rotation: $Rot(z)$, $Rot(w)$ and $Rot(l)$, from the point of view of the objective of the microscope, as outlined in Figure 4.5.

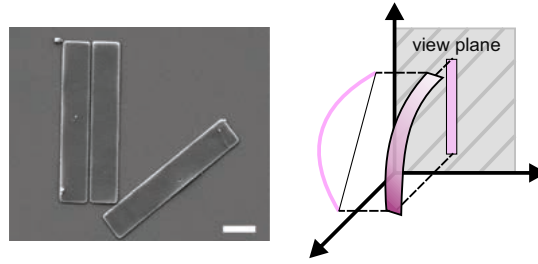


Figure 4.4. **Cantilever schematic of errors induced by the optical projection.** (Left) SEM images of $10.00 \times 2.00 \times 0.05 \mu\text{m}^3$ cantilevers which were initially fabricated for the first biological experiments. (Right) Optical projection of cantilever in the view plane illustrating that errors can be induced in the determination of its bending. Scale bar: $2 \mu\text{m}$.

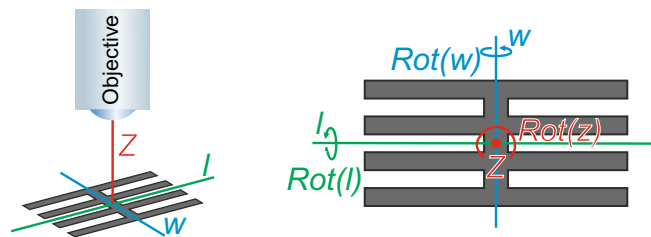


Figure 4.5. **Representation of the three axes of rotation.** Schematic representation shows the three axes of rotation: $Rot(z)$, $Rot(w)$ and $Rot(l)$.

Figures 4.5 and 4.6 help in the comprehension of these axes.

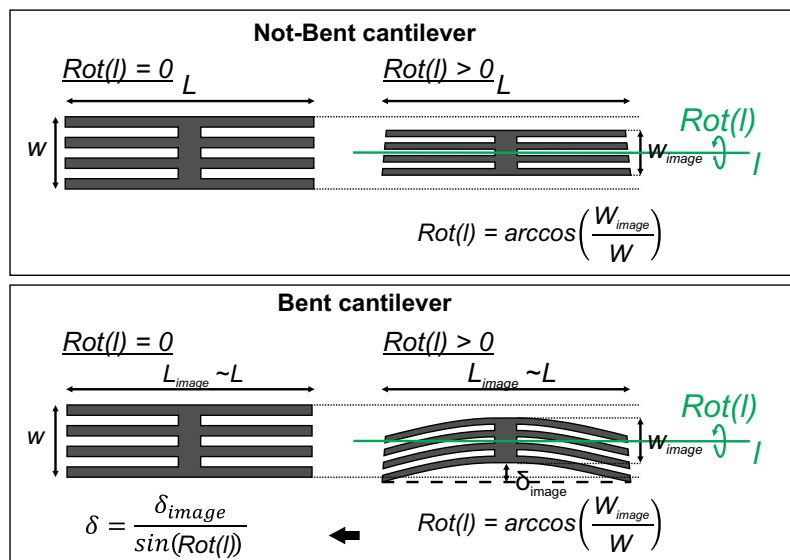


Figure 4.6. **Determination of the H-comb deflection.** Deflection calculation of (upper) a not-bent cantilever and (bottom) a bent cantilever, for the same configuration of the axes of rotation.

$Rot(z)$ rotations do not affect the determination of δ ; $Rot(w)$ rotations were not considered, as our experiments were restricted to analysis in which these rotations are small. Larger $Rot(w)$ rotations produce images in which part of

the device is out of focus, so these images were excluded. Finally, the precise determination of $Rot(l)$ rotations can be found by determining the projected width of the device in the image, W_{image} , compared to the one of the design, W . The angle of rotation determined in this way was used to correct the empirical δ_{image} , to give real bending of the device, δ .

4.3 Technological development for the fabrication process of the H-comb mechanical sensors

Following, it is detailed the whole fabrication process of the H-comb devices, from the silicon wafer as substrate to the released suspended devices. This fabrication process is based on the standard microelectronic techniques largely used in the microfabrication industry. It must be highlighted that the releasing and recollection steps are not standard processes from microelectronic industry, but they have been previously developed by the group and widely used in several works[19, 28, 29].

4.3.1 Fabrication steps of the H-comb mechanical sensors

H-comb devices were fabricated as illustrate in Figure 4.7.

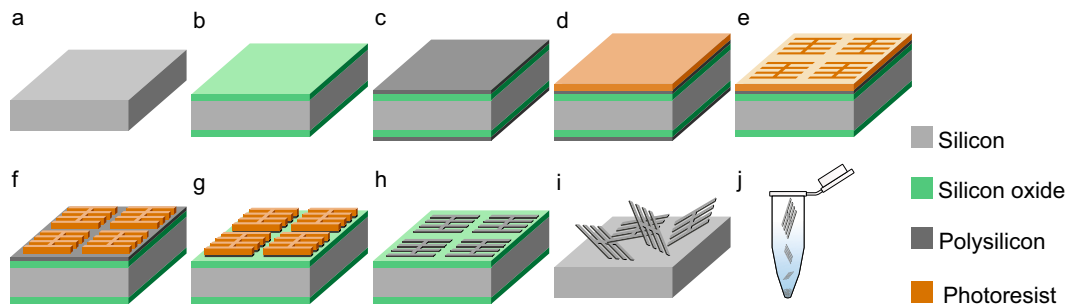


Figure 4.7. **Schematic of the fabrication process of the H-comb devices.** a) Silicon wafer as initial substrate. b) SiO_2 deposition as sacrificial layer. c) Polysilicon deposition as device layer. d) Photoresist spin-coating. e) Photolithographic exposure to UV and f) resist developed and baked. g) Polysilicon vertical etching. h) Photoresist removal. i) Etching of the SiO_2 layer for device releasing and j) devices collection in Eppendorf tubes.

100 mm p-type $\langle 100 \rangle$ silicon wafers (Si-Mat, Silicon Materials) of 500- μm -thick were used as substrate (Figure 4.7a). A 100 nm-thick SiO_2 TEOS tetraethylorthosilicate [$Si(OC_2H_5)_4$] layer was deposited by plasma-enhanced chemical vapour deposition (Figure 4.7b). Next, a polysilicon layer 25 nm-thick was deposited by chemical vapour deposition (630 °C, 120 mTorr) (Figure 4.7c) and a 1.2 μm -thick positive photoresist was spun onto the wafer (ma-P 6512 Micro Resist Technology) (Figure 4.7d). Then, the wafer was exposed to UV light (Stepper NSR1505-G7E; Nikon) to pattern the design through the reticule (Figure 4.7e). The resist was developed and baked (30

min, 200 °C) (Figure 4.7f), and the polysilicon layer was etched using SF₆ and c-C₄F₈ (ALCATEL 601E; Alcatel) (Figure 4.7g). After the etching process, the photoresist was stripped (TEPLA 300-E, Technics Plasma) (Figure 4.7h) and finally, chips were released by SiO₂ sacrificial etching in 49% (v/v) hydrogen fluoride (HF) vapours for 40 min and resuspended in 96% ethanol with short ultrasonic pulses (Figure 4.7i). Due to their fragility, centrifugation was impracticable and devices were collected by settling in Eppendorf tubes (Figure 4.7j).

Following this fabrication process, we are able to produce $> 1.5 \cdot 10^7$ device copies per 100 mm-diameter silicon wafer.

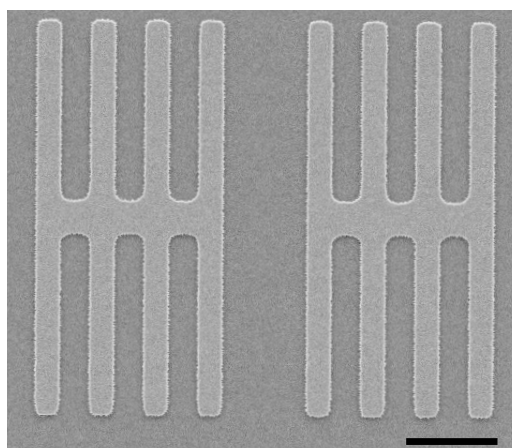


Figure 4.8. **Fabricated chips.** SEM image of fabricated chips on the silicon dioxide layer before their releasing. Scale bar: 5 μ m

Release of the devices cannot be achieved by ultrasound due to their fragility. Rather, we liberate devices from the substrate by immersion in ethanol and careful rinsing with recirculated ethanol using a micropipette. The released chips are washed thoroughly in ethanol to remove residual HF, which otherwise can affect embryo viability. Centrifugation of the chips was avoided, and devices were allowed to settle out of suspension or collected by filtering. After the final collection, devices were gently resuspended in sterile pure water.

Device manipulation is an extremely dainty step and it has to be performed carefully, always in liquid medium, to avoid device fracture and sticking to each other. H-comb nanodevices are very thin and soft that they can change their shape and adjust to their environment if they dry, as shown in Figure 4.9.

4.3.2 Reproducibility of nanodevice dimensions

The use of standard techniques in microelectronics for the fabrication of the H-comb nanodevices allows extraordinary control and reproducibility of geometrical dimensions during fabrication. To prove the reliability and reproducibility of the polysilicon devices, we performed a verification on the

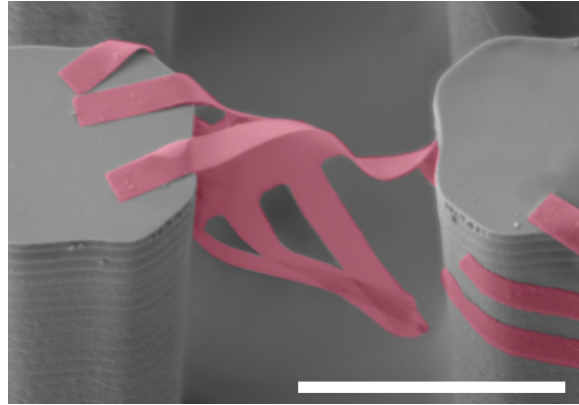


Figure 4.9. **Released chips.** Nanodevice immersed in ethanol and dropped onto a 3D microstructured substrate. The nanodevices are so soft that after drying they bend to adapt their shape to the 3D microstructures. Scale bar: 10 μm

thickness of the polysilicon layer and on the device dimensions after the photolithography and etching processes.

Our fabrication is carried out over a 4 inch silicon wafer, where the designed H-comb pattern is repeated in chip batches (1 cm x 1 cm) throughout the practical wafer area (Figure 4.10).

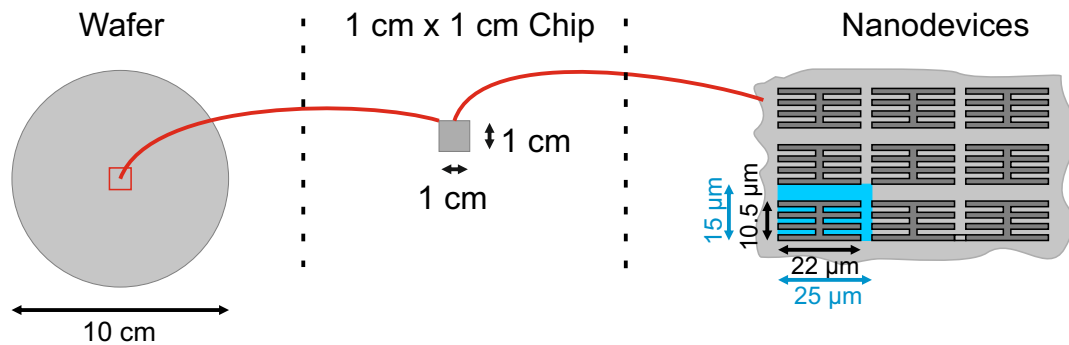


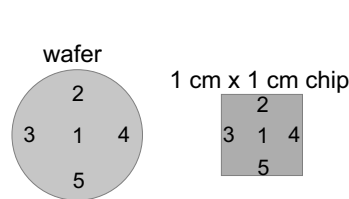
Figure 4.10. **Nanodevice area on a wafer.** Schematic of the dimensions (left) of a silicon wafer, (center) of the chip used for the experiments and (right) the total area occupied by a nanodevice (area of the H-comb plus the area between nanodevices).

The Table 4.1 presents values for the area and the number of fabricated devices per wafer and per chip. The used technology allows the fabrication of $>15 \times 10^6$ devices per wafer. A portion of the wafer is enough for the experimental applications, hence, the wafer is cut into chips of $1 \times 1 \text{ cm}^2$ containing $>2.6 \times 10^5$ devices. To verify if there are deep variations in the thickness of polysilicon all over the wafer, we performed a test consisting of measuring the thickness in five points at wafer and chip levels (Figure 4.11), by the use of Nanometric Nanospec 2011 equipment.

The polysilicon thickness was determined experimentally at these five points whose average values (\pm standard deviation, s.d.) are presented in the Table 4.2, resulting in very low ($< 2 \text{ \AA}$) values of standard deviation for both levels, wafer and chip.

	Substrate area [μm^2]	Number of nanodevices
Wafer	$>7 \cdot 10^9$	$>15 \cdot 10^6$
Chip	10^8	$>0.26 \cdot 10^6$
Nanodevice	375	1

Table 4.1. **Area and number of devices.** The left column of the table shows the area of the nanodevices compared with a wafer and a chip areas. The column on the right shows the number of the nanodevices contained in each of the previous areas.

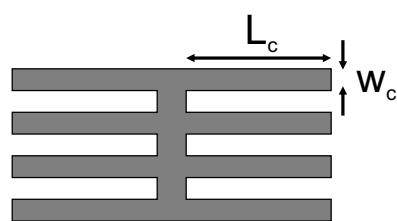


	Polysilicon thickness, $t[\text{\AA}]$					Av. [\AA]	1σ [\AA]
	1	2	3	4	5		
Wafer	294	294	295	294	298	295	<2
Chip	294	294	294	294	294	294	<1

Figure 4.11. **Wafer and chip points locations for polysilicon thickness measure.**

Table 4.2. **Polysilicon thickness variations.** Results of the measured thickness, $t[\text{\AA}]$, in the five points of the wafer and the chip, and the resulting average standard deviation values.

After the polysilicon deposition, a photolithographic process to transfer the pattern to the photoresist were executed. As this step is crucial (as it defines the dimensions of the devices), a Stepper NIKON Nsr 1505 G7e was employed allowing a high degree of lateral control over H-comb device fabrication. After that, the polysilicon layer was structured by an etching process in ALCATEL 601E using SF_6 and c-C $_4$ F $_8$.



	Wafer ($n=25$)			Chip ($n=5$)	
	Nominal [μm]	Av. [μm]	σ [μm]	Av. [μm]	σ [μm]
	L_c	10.00	9.93	0.03	9.90
w_c	1.50	1.58	0.03	1.58	<0.02

Figure 4.12. **Schematic of a nanodevice showing the lateral dimensions, L_c and w_c , of a cantilever.**

Table 4.3. **Measured dimensions of a cantilever of the nanodevice.** Nominal values of L_c and w_c , alongside their values determined experimentally and its corresponding errors over a wafer and a chip.

Therefore, for the verification of the dimensions of the devices across the entire wafer, we performed measures of the length and the width of the branches of the H-comb devices, L_c and w_c respectively (Figure 4.12). For that, we have measured these dimensions on five devices on each of the five regions of the wafer shown in Figure 4.11. Table 4.3 shows the average values of each dimension and its corresponding value of the standard deviation.

Results show low values on the standard deviation in the measures of L_c

and w_c over the wafer and even lower deviation over a chip, highlighting the control on the dimensions of the devices through the fabrication process and discarding it as a significantly source of error. Furthermore, for the experimental applications, we usually work with chips from the central area of the wafer as it is the best preserved area and chips from the wafer edges are avoided as they could have been damaged by the contact with the holder of the equipments or with wafer manipulation tools.

4.4 Theoretical and numerical analysis of the device through FEM simulations

4.4.1 Determination of the Young's modulus for the theoretical analysis

The nanodevices were fabricated using polysilicon deposition and patterning technologies that are highly refined in microelectronics processing, allowing a high degree of reproducibility. We empirically determined the errors in fabrication by directly measuring them (Section 4.3.2) and found that variations are not significant. However, the nanometric dimensions of the thickness of the polysilicon layer (29.4 nm) induced an uncertainty in the Young's modulus of the polysilicon layer.

For over three decades, and still today, size-dependent behaviour in physical properties of polysilicon and other microelectronic materials is under experimental and computational studies[30–32]. It has been reported that silicon or polysilicon layers of less than ~ 100 nm-thick possess an altered Young's modulus [31, 32]. For instance, in[32], *Li et al.* reported a reduction on the Young's modulus from ~ 170 GPa (when the layers were >100 nm-thick) to 68 GPa (38.5 nm) and 53 GPa (12 nm) for monocrystalline silicon layers. In the case of polysilicon, deposition parameters also influence the mechanical properties of the layer as they define the grain diameter.

Methods commonly used to characterize micro- and nanocantilevers and beams have limitations when it comes to determining mechanical sensitivity for the H-comb devices, as the stiffness of a given device depends on its geometry (shape and dimensions), the applied mechanical loads (i.e. Pressure (P), Force (F), ...), and the applied boundary conditions (type and localization) (Figure 4.13). These limitations include the difficulty (if it is possible at all) of reproducing the boundary conditions of free-floating cantilevers, and the difficulty (again, if it is even possible) of reproducing the applied load.

The small dimensions of the devices (whose cantilever components measure $10 \mu\text{m} \times 1.5 \mu\text{m} \times 0.025 \mu\text{m}$), their non-simple modal shapes, their small force constant ($\sim 10^{-3}$ N/m) and the fact that they are intended to be free-floating inside the cell, collectively dissuaded us from employing static

or dynamic deflection techniques to derive their mechanical sensitivity, but rather argued for a dimensional calculation[33].

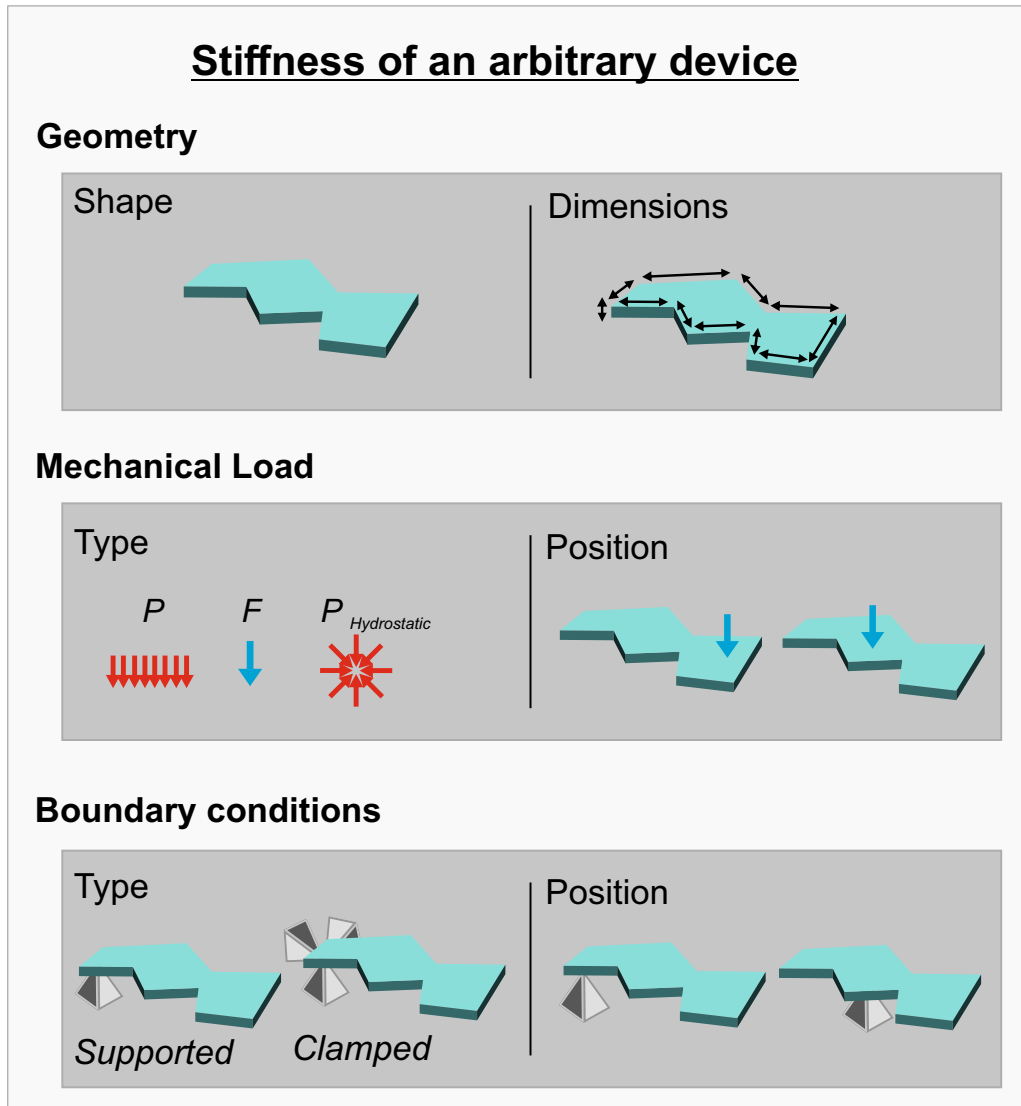


Figure 4.13. **Stiffness dependence of an arbitrary geometry.** Schematic of the parameters involved in the stiffness of an arbitrary device. Device geometry by its shape and dimensions, the type of the applied mechanical load and its position on the device, and the boundary conditions type and its position on the device.

Moreover, in the case of F , the exact force localization on the nanodevices is also a limitation due to the small size of the specimen, as a slight misalignment may introduce large variations of the momentum or undesired device torsions. These limitations mean that typical static and dynamic methods used for spring constant determination of cantilevers (AFM probes) do not provide a good solution for determining the mechanical sensitivity of H-comb nanodevices. It is important to appreciate that H-comb nanodevices are not simple rectangular cantilevers anchored at one end and operate at distinct boundary conditions, distinct applied loads and have a complex geometry (complex vibration modes).

Although these methods are unsuitable to provide a nanodevice precise spring constant, we tried to manipulate them to perform some tests. Firstly, free floating nanodevices immersed in ethanol were dropped onto a 3D microstructured substrate in order to evaluate whether any of the nanodevices lodged in such a way as to leave one of its cantilevers free-standing. The nanodevices are so soft that after drying they bend to adapt their shape to the 3D microstructures (Figure 4.14), making them useless for their characterization.

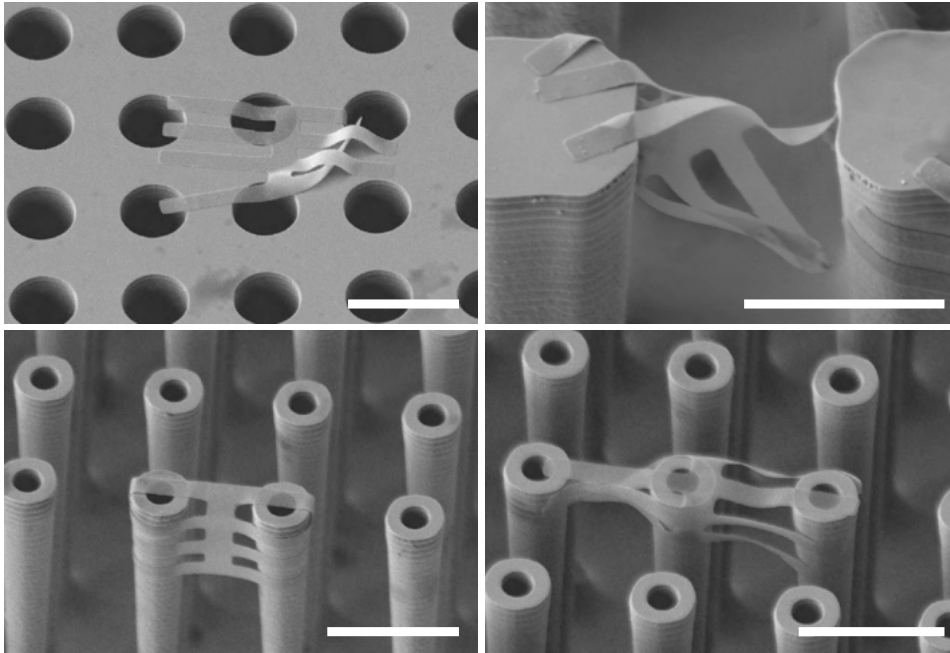


Figure 4.14. SEM images of the dropped devices for mechanical determination. Nanodevices immersed in ethanol and dropped onto a 3D microstructured substrate. The nanodevices are so soft that after drying they bend to adapt their shape to the 3D microstructures. Scale bars: 10 μm .

On the other hand, we attempted to manipulate nanodevices laying on a dry substrate (Figure 4.15) by Focused Ion Beam (FIB) micromachining. To this end, free floating H-comb devices immersed in ethanol were dropped onto a substrate and (after drying) introduced onto a SEM/FIB system. Within the SEM/FIB system, a sharpened micromanipulator tip was placed in contact with an H-comb device. Localized platinum deposition was then used to attach the micromanipulator tip to the nanodevice. The tip was then lifted, to detach the chip from its substrate, with the idea to re-attach it in a configuration suitable for a posterior mechanical characterization. However, as shown in Figure 4.15, the nanodevices did not detach. Again, this test proves how extraordinarily difficult is to manipulate the H-comb devices.

Given these difficulties, it was tried to characterise individual cantilevers at the wafer level. To attempt this, it would be necessary to alter the nanodevice fabrication process by performing a partial release etching of the devices in such a way that the eight cantilevers became released, but the central bar of the H-comb remained attached to the substrate. Although we used the

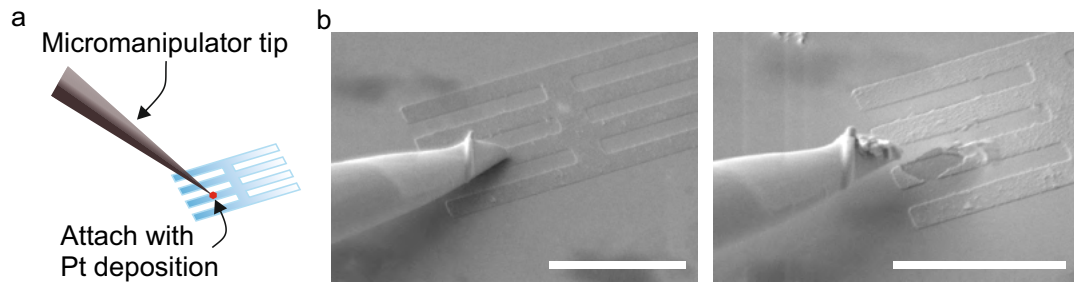


Figure 4.15. **FIB Lift-out with micromanipulator.** a) Representation of the FIB micromanipulator system. b) SEM images of a nanodevice on a dry substrate is attached by platinum deposition to a micromanipulator tip in a SEM/FIB system. Nanodevices laying on a substrate stick so hard that when the micromanipulator lifts, they break rather than detaching from the substrate. Scale bars: 10 μm .

Super Critical Dry etching technique (Supercritical Automegasamdri®-915B, Series C, Tousimis) to avoid sticking. However, the cantilevers are so soft that they stuck to the substrate (Figure 4.16).

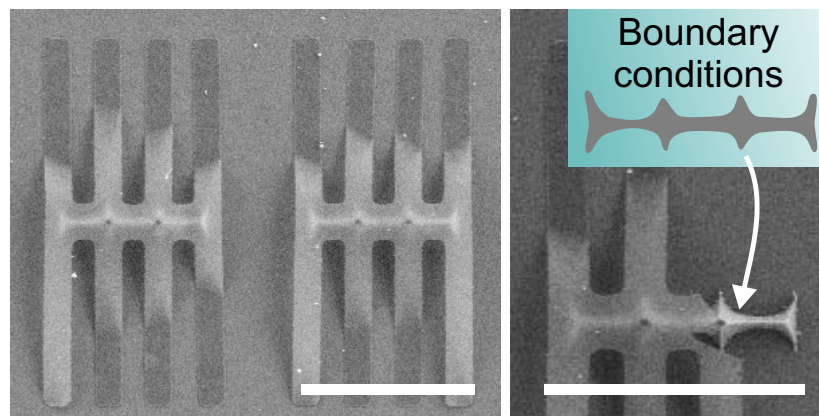


Figure 4.16. **H-comb nanodevices anchored at their centers.** SEM images of partial etching of the underlying sacrificial silicon oxide layer allows complete removal of the silicon oxide beneath the cantilever arms but not from the center of the H-comb devices. The attached zones are indicative of non-ideal boundary conditions. In addition the cantilevers stick to the substrate even though super-critical dry etching techniques were used. Scale bars: 10 μm .

Additionally, it can be seen, from Figure 4.16, that the boundary conditions defined by the areas that anchor the nanodevice to the substrate are irregular, which will prevent subsequent experiments to determine the mechanical performance of the device accurately or reliably.

These multiples difficulties prevent the use of static and dynamic methods in the determination of the Young modulus of the nanodevices. Nevertheless, another category of methods resulted appropriate for the mechanical performance of the H-comb: dimensional methods. Dimensional methods are based on theoretical or numerical calculations and on the material properties of the structures.

Therefore, we experimentally determined the Young's modulus of the 25 nm-thick polysilicon layer for the nanodevice fabrication using PeakForce Quantitative Nanomechanical Analysis (QNM-Brukker)[34] at the *Centros Científicos y Tecnológicos de la Universidad de Barcelona (CCiTUB)* by the aid of *Dr. Jordi Díaz*. This technique allows the determination of nanoscale mechanical properties by AFM nanoindentation. To this end, we employed portions of the same wafer from which the H-comb devices had been fabricated.

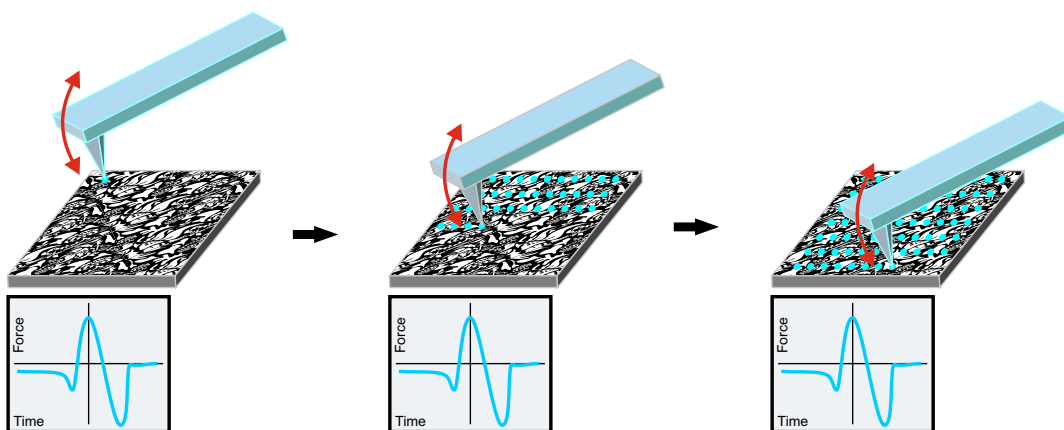


Figure 4.17. **Peak Force mapping scheme.** Special imaging mode for atomic force microscopy where the probe acquires a map of force-curves using PeakForce Quantitative Nanomechanical Analysis (QNM-Brukker).

Experiments were performed using an AFM Microscope Multimode 8 with electronic Nanoscope V (Bruker), Peak Force QNM Mode, and using a Tap525A model tip (Figure 4.17). The AFM probe scanned zones of $5 \times 5 \mu\text{m}^2$ area comprising 512×512 pixels (262144 force curves). The software, Nanoscope Analysis (Bruker), extracted the Young's modulus from each force curve and calculated the percentage of pixels with the same measured Young's modulus on the scanned area (Figure 4.18).

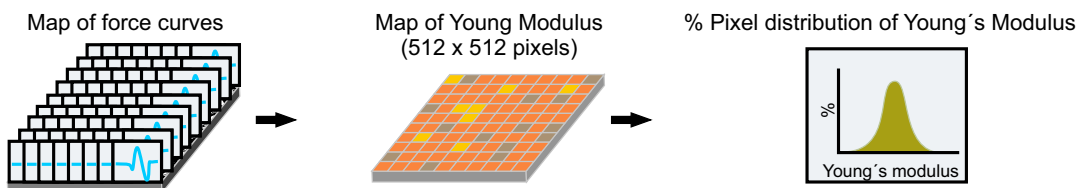


Figure 4.18. **Schematic of the Force map curves for Young Modulus calculation.** The AFM probe acquires a map of force-curves obtaining multiple mechanical properties, including a map of the Young's modulus of the nanolayer.

We performed ten different zones scanning across the surface of the wafer. Figure 4.19 shows each of the curves calculated on the ten measured areas. These plots are fitted by a Gaussian shape function, and the maximum of each of the plots represents the Young's modulus of the polysilicon layer of the sample. We determined the Young's modulus of ten different samples in this way (Table 4.4) and averaged them.

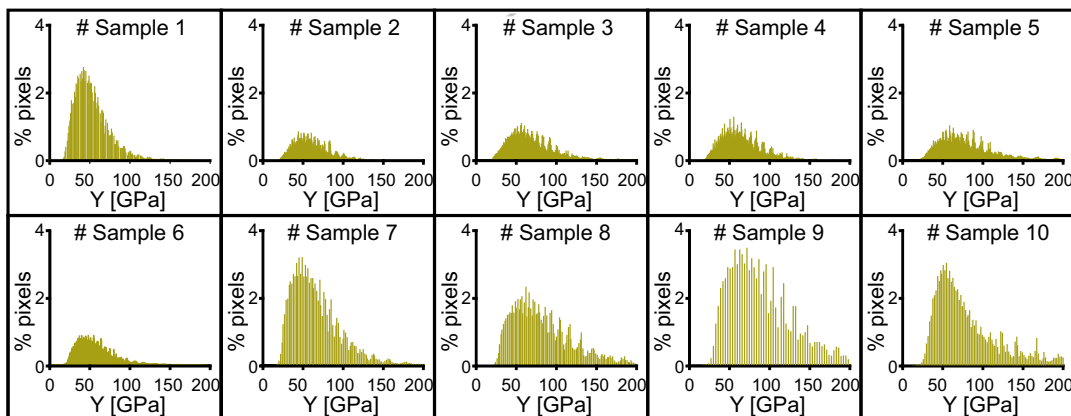


Figure 4.19. 25 nm-thick polysilicon layer Young's modulus estimation. Experimental values of the percentage of pixels with the same Young's modulus measured in 10 samples of polysilicon layers 25 nm-thick.

The experimental results revealed a Young's modulus of 54.4 ± 2.2 GPa for the nanodevice polysilicon layer, a value that is in good agreement with values obtained for monocrystalline silicon of similar thickness[31, 32], corroborating our approach and the obtained value. We accordingly adopted our experimental value for Young's modulus in the determination of nanodevice mechanical rigidity.


# Sample		1	2	3	4	5	6	7	8	9	10
Young's Modulus [GPa]		43.711	51.767	55.066	53.169	59.974	50.560	46.960	63.936	66.527	52.247

Table 4.4. Young's Modulus of the measured samples. Characteristic Young's modulus determined by Peak Force QNM Mode analysis (the maximum of the Gaussian-like adjusted curve) for the 10 samples.

4.4.2 Calculation of the devices sensitivity by Finite Element Method

Since H-comb nanodevices were conceived for a specific biological application (to detect the average of loads that drive cytoplasmic reorganization), we study, through FEM simulations, the mechanical behaviour of the devices with the constrictions of its operating environment: the cell interior. The cell interior has reduced inertial forces[35], and as a first approximation we modelled nanodevice bending based on two representative simulations: a pressure, P , applied to the device surface, or a force, F , applied at the center of the device (Figures 4.20). Our boundary conditions assume that nanodevice ends are free to rotate and translate and that constraints in the perpendicular plane acting at the ends of the H-comb cantilevers are required to cause nanodevice bending.

Thus, for the FEM simulation analysis we made use of the software ANSYS Multiphysics. Nanodevice quantitative modelling (Figures 4.20 and 4.21)

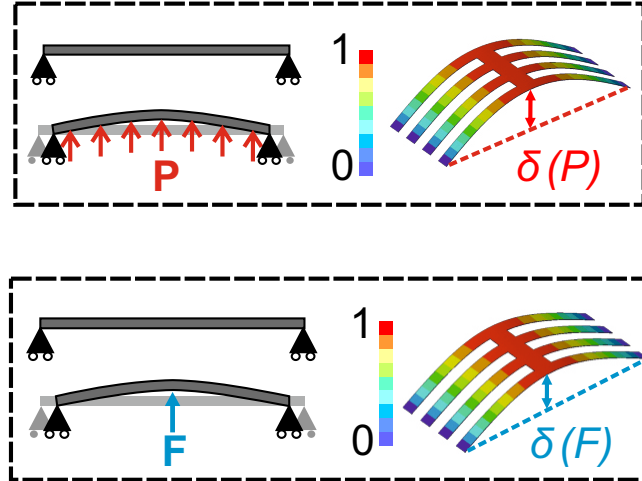


Figure 4.20. **Representation of the modelled device load state.** Scheme of the device load state and simulated normalized vertical displacement by the finite element method for uniform distributed pressure load (P , top) and force loads (F , bottom).

was performed using the 3D element, SOLID95. The nanodevices are large enough ($22.0 \times 10.5 \mu\text{m}$) compared to the embryo diameter ($\geq 70 \mu\text{m}$) that they can average random molecular perturbations and hence monitor cytoplasmic rearrangements.

We first studied bending based on applied loads but focusing on how the application location inferred in this bending. Thus, if the forces were applied closer to one border of the nanodevice (exactly mid-way along a cantilever), bending at the center would be $\sim 35\%$ of the deformation induced by the same force acting at the center of the device. To achieve a given deflection by acting nearer to the nanodevice center, the force responsible would need to be larger. With that, we modelled nanodevice bending based on a total force, $F_{total} = 8 \times F_{cant}$, applied at the center of the device, so that estimated forces represent the low limit of the possible range of intracellular forces.

Previous results on the contribution of the geometrical and material properties of the nanodevices lead to mechanical sensitivities of the nanodevices for the two proposed load conditions (Figures 4.20 and 4.21) of $0.029 \pm 0.001 \mu\text{m}/\text{Pa}$ and $0.30 \pm 0.01 \mu\text{m}/\text{nN}$ respectively. Furthermore, simulations predicted extremely low stiffness, with sensitivity to minute load states of $K_P = 35 \text{ Pa} \cdot \mu\text{m}^{-1}$ and $K_F = 3.39 \text{ nN} \cdot \mu\text{m}^{-1}$ (Figure 4.21).

4.4.3 Simulation analysis of an initial curvature of the nanodevices.

Another relevant characteristic to study is the possible initial curvature of our nanodevices after device releasing, as it can influence in the bending readout. Initial curvature due to stress has been widely proved in micro-machined cantilevers[36]. For instance, stress can affect mechanical sensitivities and resonance frequency changes on cantilevers, and stress gradients can

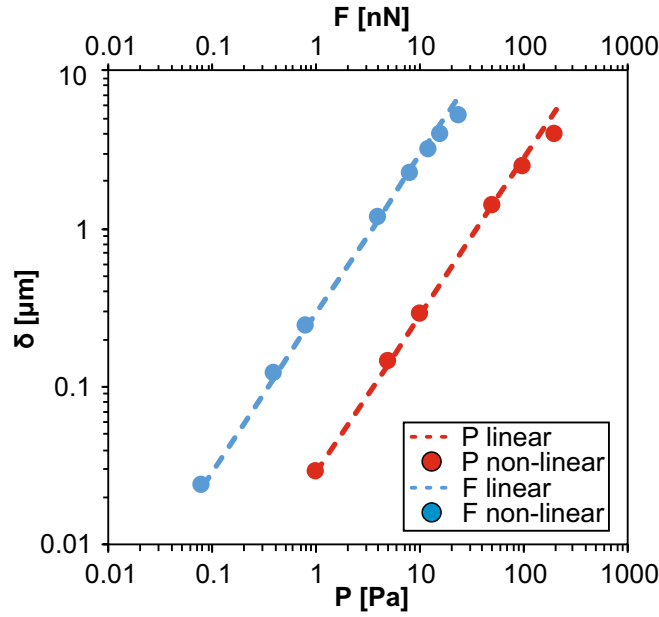


Figure 4.21. **Simulation results of applied pressure or force.** Simulated maximum vertical displacement versus applied pressure, P , and force, F .

bend cantilever beams. Because our nanodevices are freefloating, a gradient of stress has the potential to induce an initial curvature in them.

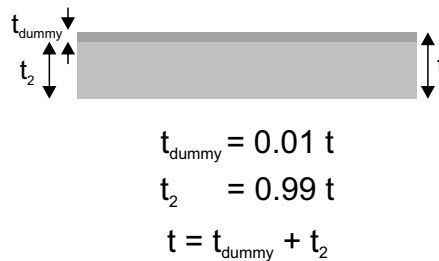


Figure 4.22. **Scheme of the layer modelling to simulate an initial curvature of the H-comb nanodevices.** Schematic of the model used to simulate initial nanodevice deflection due to an intrinsic stress gradient. The structure is simulated by considering two layers, the sum of whose thicknesses is the total thickness of the device.

Stress gradients can be modelled by applying a surface stress to one side (top or bottom) of the devices. Hence, we define a layer of thickness t (as the thickness of the device), composes by a dummy layer with a very small thickness, t_{dummy} , (representing the surface of the layer) and a second layer with a thickness of $t_2 = t - t_{dummy}$ (representing the remaining thickness) (Figure 4.22). Any imbalance of surface stresses between the top and bottom induces a vertical displacement (δ_{ini}) that is perpendicular to the plane of the device (Figure 4.23).

The study of an initial curvature by intrinsic stresses was simulated by ANSYS using the SOLID186 element. This is a 3D 20-Node Structural Solid element that allows modelling of layered structural solids (KEYOPT(3) = 1).

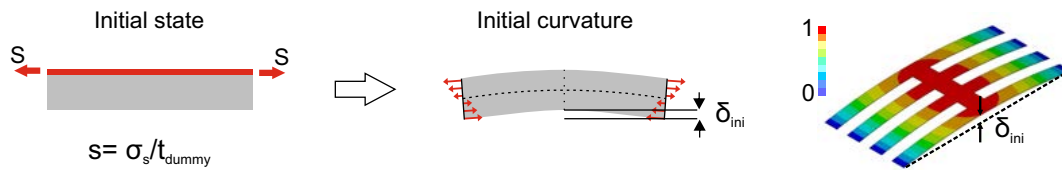


Figure 4.23. **Scheme of the imposed load conditions on the modelling of an initial curvature of the devices.** The upper layer (left, in red) is used as a dummy layer to apply a stress load (middle) that induces a stress gradient and bends the devices. (Right) Normalized vertical displacement of a nanodevice due to intrinsic surface stress.

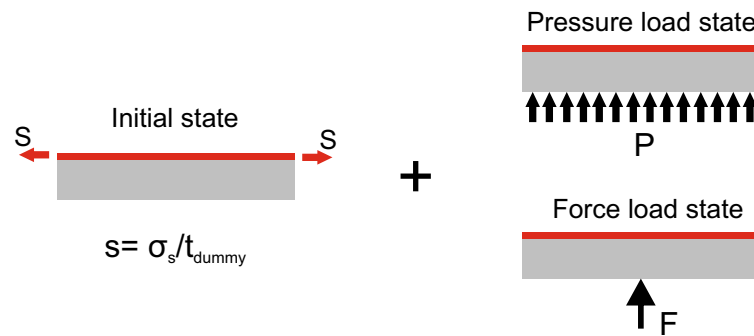


Figure 4.24. **Scheme of the initial state under F and P loads to be simulated.** Schematic of a model assuming an initial intrinsic curvature and an additional pressure load state, P , or a force load state, F .

Following the scheme of Figure 4.22, a dummy layer with a thickness of $1/100$ of the total thickness of the device was established to simulate the surface stress effects. The second layer therefore has a thickness of $99/100$ of the total thickness of the device. Both layers possess the Young's modulus for polysilicon, but an initial surface stress is applied to the dummy layer by using the INISTATE command in ANSYS to define initial states of structures. The applied surface stress in the dummy layer induces a stress gradient in the structure whose consequence is an initial offset in the displacement (δ_{ini}) (Figure 4.23). Subsequently, the load steps under evaluation (pressure or force load states) are applied and simulated (Figure 4.24).

These analyses show that the initial curvature induced by the fabrication generates an offset without altering the mechanical sensitivity, the slope of the curves (Figure 4.25).

4.4.4 Effects of geometrical and material property errors on device sensitivity

In previous sections, it has been proved the high reliability on the reproducibility of the device dimensions through the fabrication process, and it has been calculated the Young's modulus polysilicon layer. Thus, an analysis of how the geometry and the material properties could influence on the device sensitivity must be done.

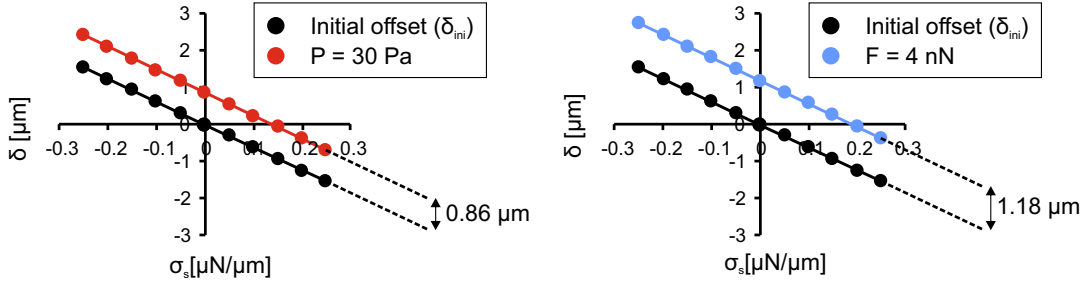


Figure 4.25. **Simulation results under F and P load states and considering an initial curvature on the devices.** Simulated displacement (δ) versus a representative surface stress for the case of an initial intrinsic curvature with a representative (left) $P = 30$ Pa, or a (right) $F = 4$ nN . Displacement (δ) curves, considering either the surface stress alone, or the surface stress plus pressure or force, are parallel, demonstrating that the initial curvature of the nanodevice does not affect its mechanical sensitivity.



Figure 4.26. **Representation of an applied pressure or force on a cantilever.** Schematic (left) of cantilever loaded with a uniform pressure, P , and a cantilever loaded with a force, F , at one end.

From a mechanical point of view, H-comb nanodevices could be analysed by considering each finger of the device as a cantilever. This consideration allowed us to evaluate the errors on device sensitivity by using simple equations. For that, we started from the analytical formula describing the maximum bending of a cantilever versus a pressure, P , applied uniformly along the cantilever length (L_c), or a force, F , applied at the end of it (Figure 4.26):

$$\delta_{max}(P) = \frac{3}{2} \frac{L_c^4}{Et^3} P \quad (4.1) \quad \delta_{max}(F) = \frac{4L_c^3}{Ew_c t^3} F \quad (4.2)$$

where w_c and t are the width and the thickness of the cantilever respectively, and E is the Young's modulus of the polysilicom. These equations are a good approximation to the mechanics of H-comb devices for symmetric load conditions.

Therefore, error on the calculation of the maximum bending, $\Delta\delta_{max}$, of the devices can be inferred from the propagation of dimensional errors and Young's modulus errors:

$$\frac{\Delta\delta_{max}(P)}{\delta_{max}(P)} = \sqrt{\left(4\frac{\Delta L_c}{L_c}\right)^2 + \left(3\frac{\Delta t}{t}\right)^2 + \left(\frac{\Delta E}{E}\right)^2} \quad (4.3a)$$

$$\frac{\Delta\delta_{max}(F)}{\delta_{max}(F)} = \sqrt{\left(3\frac{\Delta L_c}{L_c}\right)^2 + \left(\frac{\Delta w_c}{w_c}\right)^2 + \left(3\frac{\Delta t}{t}\right)^2 + \left(\frac{\Delta E}{E}\right)^2} \quad (4.3b)$$

Dimensional errors in the sensitivity of the nanodevices have been demonstrated to be very small and do not significantly affect the results (section 4.3.2). Hence, relative errors corresponding to the dimensional features of the devices contribute with a 1.3% and 1.7% on equations 4.3a and 4.3b, respectively.

On the other hand, experimental results have found a Young's modulus of 54.4 ± 2.2 GPa, whose relative error correspond to 4%, leading to a major contribution of the material properties in the sensitivity of devices. Actually, dimensional errors are negligible in the sensitivity of the nanodevices concluding that the main contribution come from the Young's modulus experimental calculation.

$$\frac{\Delta\delta_{max}(P)}{\delta_{max}(P)} = \frac{\Delta\delta_{max}(F)}{\delta_{max}(F)} \approx \left(\frac{\Delta E}{E} \right) \sim 4\% \quad (4.4)$$

4.5 H-comb deflection measure within mouse one-cell embryos for cytoplasm mechanical characterization

4.5.1 From device bending measurements to the mechanical description of the cytoplasm behaviour

Monitoring intracellular force dynamics and changes to the resistance to cytoplasmic reorganization along different phases of mouse one-cell embryo development after fertilization provide important new information about the role of cell mechanics at the onset of embryogenesis. Nanodevice rotation and translation (the displacement vector, d) describes cytoplasmic reorganization and is a consequence of changes in intracellular mechanical loads (the force vector, F). The level of intracellular forces can be determined by measuring the bending of the devices. How forces, F , affect cytoplasmic reorganization depends in part on the mechanical properties of the cytoplasm. This means that changes in the mechanical properties of the cytoplasm can be inferred by determining the level of mechanical loads (forces or pressures) and measuring nanodevice rotations or translations inside the embryo.

Hence, we investigated nanodevice behaviour in five nominal embryo phases: sperm decondensation, recondensation and pronucleus formation (SDR, corresponding to meiotic exit), pronuclear migration (PM, corresponding to G1- and S-phases), pronuclear envelope breakdown and chromosome mingling (PEB), embryo elongation just prior to division (EL, presumptively initiating in G2-phase) and the first (one- to two-cell) mitotic division (DIV) (Figure 4.27).

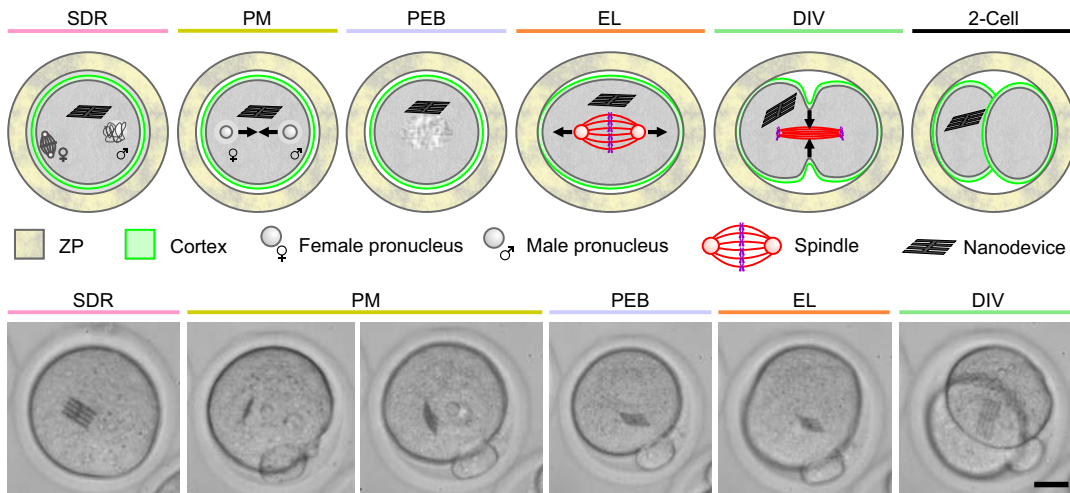


Figure 4.27. **Stages of the development of mouse one-cell embryo.** Schematic representation of the different stages in the mouse one-cell embryo (zygote) following fertilization, showing key structures in embryo mechanics and embryo stages. Optical images show mouse embryos at the different stages, each containing a microinjected nanodevice. Scale bar: 20 μm .

For that, H-comb nanodevices were co-injected inside a mouse oocyte with the sperm. Because injected nanodevices are free to move in the cytoplasm, it is not possible to dictate their localization apart from their approximate placement near the beginning of development in the SDR phase, soon after injection. Thus, the measured data for each phase represent different device positions inside a given embryo, reporting the overall cytoplasmic mechanics. It might be thought to mitigate this by the co-injection of multiple devices into a single oocyte, but this consideration was rejected as it is technically challenging and would result in the potentially toxic introduction of excessive volumes of injection medium.

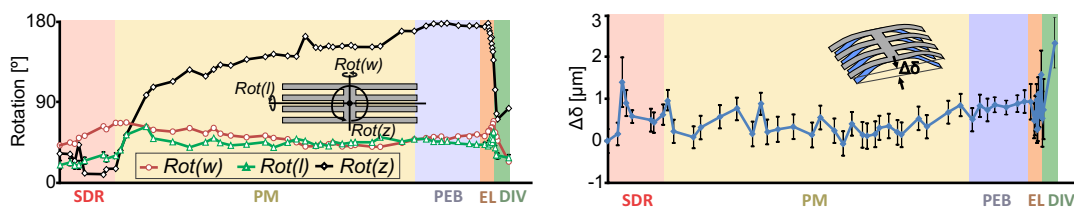


Figure 4.28. **Monitoring of H-comb during embryo development.** Representative plots showing rotations ($Rot(w)$, $Rot(l)$, $Rot(z)$, left) and nanodevice deformation ($\Delta\delta$, right). Each background colour corresponds to one of the different embryonic stages of Figure 4.27.

Once inside the embryo, nanodevices register intracellular mechanics of relatively large regions of cytoplasm (unlike small-scale measurements of individual random perturbations[2]): displacement, rotation and translation, contained information about the cytoplasmic reorganization, and nanodevice deformation revealed force magnitudes. In Figure 4.28, it is shown the tracking of one embryo during the complete development cycle up to the first mitotic division.

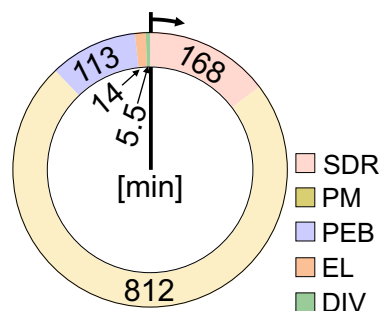


Figure 4.29. **Phase duration.** Average duration of each nominal stage of one-cell embryo development.

To interpret this information, we propose two ad hoc theoretical parameters: $\zeta_k = F_{max}/Rot_{max}$, related to resistance to cytoplasmic reorganization (F_{max} and Rot_{max} are, respectively, maximum force and rotation detected by the nanodevice), and $\zeta_{mact} = (\Delta\delta_{av} \times Rot_{av})/time$, related to transitions in time-averaged mechanical activity (where time is the phase duration and $\Delta\delta_{av}$ and Rot_{av} are respectively averages of measured nanodevice bending and rotation during that time) (Figure 4.29).

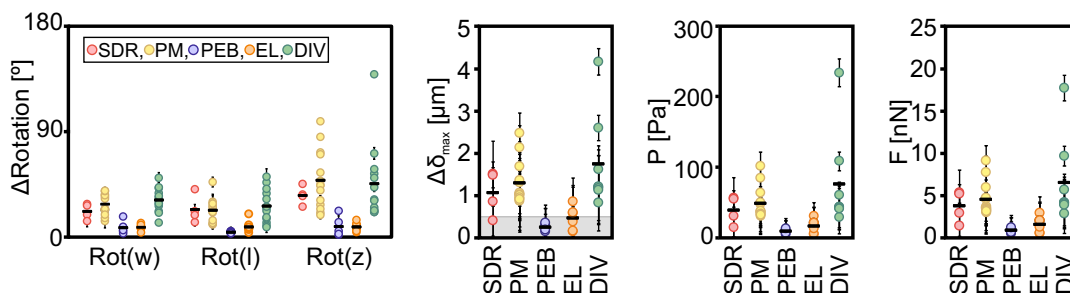


Figure 4.30. **Experimental results in control embryos.** Maximum rotations, $Rot(w)$, $Rot(l)$, $Rot(z)$, maximum nanodevice deformation, $\Delta\delta_{max}$, for each stage with the range of lower confidence indicated in grey, and simulation of the pressure or force on the nanodevice necessary to obtain given values of $\Delta\delta_{max}$. Error bars depict measurement uncertainty. Black horizontal lines show mean values.

To carefully carry out the analysis of the forces and mechanical changes of the cytoplasm, we examined the H-comb behaviour inside the cytoplasm in several embryos by measuring the rotation and the bending changes of the nanodevices in each of the established stages (Figure 4.30). Moreover, as previously investigated, nanodevices may have an initial curvature which induces an offset in their deflection. To avoid uncertainty due to any potential initial offset, we confined our calculations to considering variations of deflection, $\Delta\delta$.

In Figure 4.30, it is plotted the obtained values of rotations ($n = 41$ for $Rot(w)$, $n = 43$ for $Rot(l)$, $n = 46$ for $Rot(z)$) and the maximum change on the bending of the devices ($n = 36$ for $\Delta\delta_{max}$) along the embryo stages, and its corresponding P and F value.

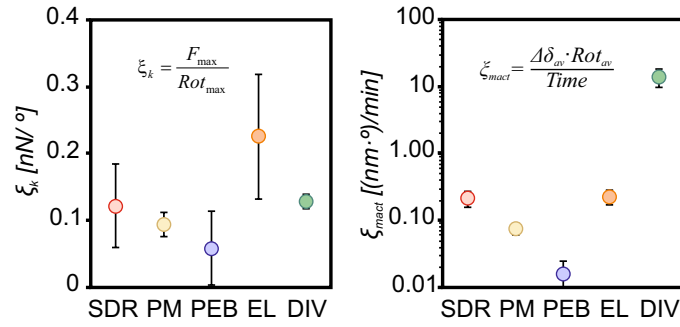


Figure 4.31. **Experimental ad hoc parameters.** Transitions of ζ_k and ζ_{mact} along embryo stages.

From the obtained values represented in Figure 4.30, the theoretical parameters defined previously (ζ_k and ζ_{mact}), are found to mechanically characterise the embryo cytoplasm as shown in Figure 4.31. These parameters revealed that mouse embryos exhibited programmed transitions in intracellular ζ_k and a range of several orders of magnitude in ζ_{mact} (Figure 4.31) during the first stages of the embryonic development.

A deeper analysis of the obtained results in each embryo stage is examined separately on the section 4.7. First, an analysis over the limitation of the measure method of the device bending shall be done.

4.5.2 Device bending limitation under experimental conditions

Once proved that fabricated nanodevices are useful tools to characterise the cytoplasm mechanics from its bending, we wonder how much our measurements are affected by the limitations of the optical microscopes. Thus, we investigated if the diffraction limit has a relevant contribution in our measurements errors under the conditions established for the experiments.

Firstly, it is necessary to detail the measurement protocol. After the injection of the nanodevices in the cytoplasm, embryos are recorded in a time-lapse videomicroscope (DO/LUCPLFLN60X PH/ NA 0.7, Universal C-plan Fluorite) capturing images at 1 min to 2 min intervals and each frame was scanned in 7-10 z-slices, each 2 μm-thick. With that conditions, we restricted the measures to the best-focused images (Figure 4.32).

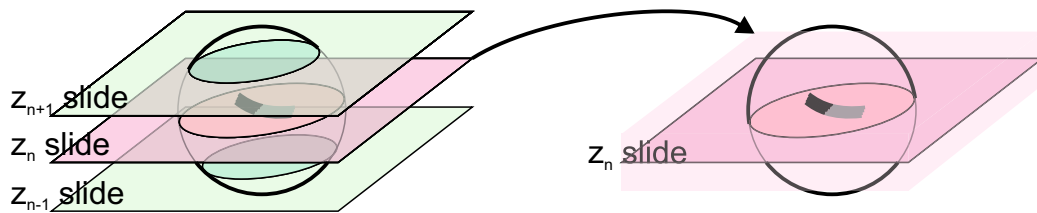


Figure 4.32. **Scheme of the z-stack images acquisition.** a, Representations of z-stack images (left) corresponding to those taken for videos. The best-focused images (right) are used for processing.

For the calculation of the device deflection, δ_{image} , we drew an imaginary line (red) on the image, from one end of the H-comb to the other, as shown in Figure 4.33.

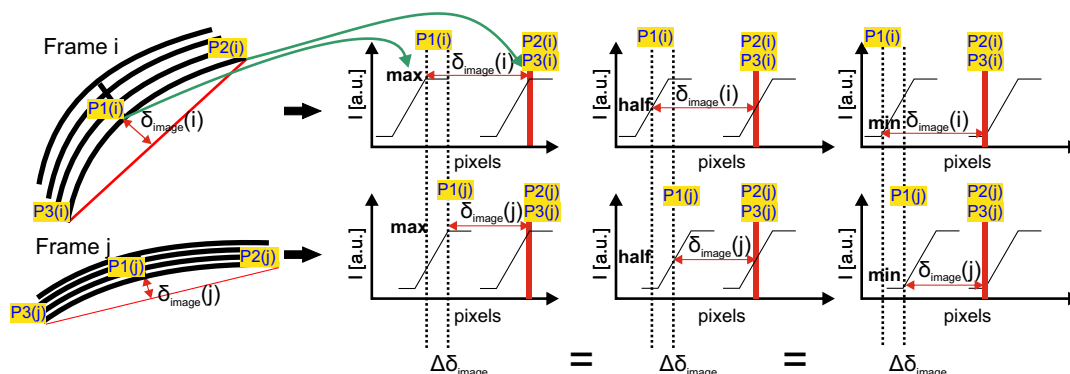


Figure 4.33. **Detail of the calculation method of the device deflection.** Location of $P1$, $P2$, $P3$, pixel point positions needed to calculate δ_{image} at each frame (i, j) by always following the same criteria (max, half, or min intensity).

δ_{image} length is the smallest that is determined, but we took advantage of the fact that it is not necessary here to resolve features and that all devices have an offset bending. Hence, for its determination we established different point positions, $P1$, $P2$, $P3$ (Figure 4.33), required for the measurements, and, as devices can be tilted, we selected the best-focused z-slide for each one, which is not necessarily on the same focal plane. With all, the same criteria are always used to calculate δ_{image} (max, half, or min intensity; see Figure 4.33), namely, to localize pixels $P1$, $P2$ and $P3$ at the borders of the nanodevice.

Therefore, as the resolution of an optical microscope is constrained by light diffraction, we investigated how it affects to the method described above. Considering a point source of light, or light passing through a minute space (Figure 4.34, left), a small pattern, so-called *Airy pattern*, appears in the images instead of a point, because of the interference between the light and the small space. Thus, the optical resolution of a microscope (Figure 4.34, center) is defined as the smallest distance between two points on a specimen that can still be distinguished as two separate entities. Without computational fitting algorithms, this limits the smallest distance between two points that can be distinguished to a few hundred nanometers. However, if the two image points are far enough apart, they can be recognized as separate objects and their separation can be calculated even though they cannot be individually resolved. When there are non-point sources (Figure 4.34, right), as in the case of light passing near to the nanodevices, it follows from the Huygens-Fresnel Principle that each point on a wavefront is itself a source of spherical wavelets. The sum of these spherical wavelets forms the wavefront, which can be viewed as the origin of the diffraction effects on their borders[37].

Since adjacent optical slices were separated by $2 \mu\text{m}$ (z -step) (Figure 4.35, left), we calculated errors in the determination of distances between adjacent slices using a flat dummy device as a test specimen, deliberately out of focus

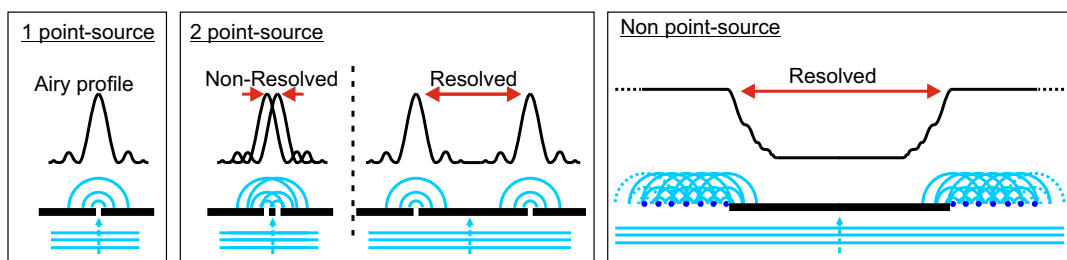


Figure 4.34. Scheme of the resolving distances of different interference profiles. Interference profile between the light and (left) a small space, and (center) two small spaces situated very close and far from each other. (Right) The interference profile of non-point sources widely separated.

in $+1$ and -1 z-planes. To achieve this, devices immersed in ethanol were deposited onto glass such that after the ethanol had evaporated, the chip adhered to the glass slide, assuring its flatness and avoiding device rotation before the z-slices were acquired.

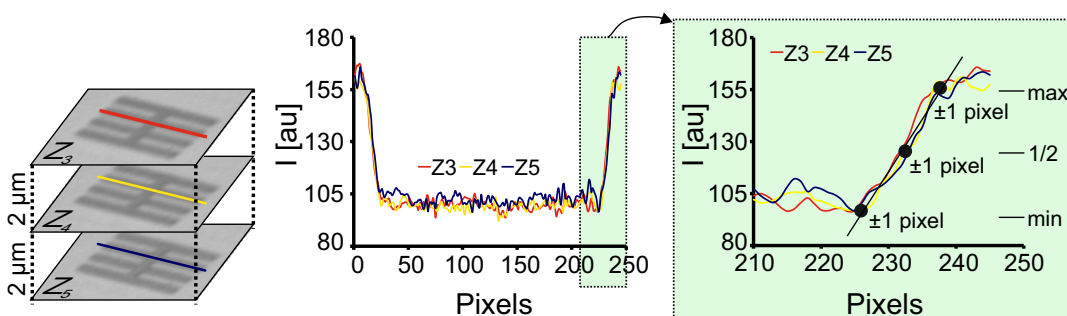


Figure 4.35. Nanodevice intensity profile over a z-stack. Three z-images of a nanodevice. Z_4 is focused and Z_3 and Z_5 are out of focus (yellow, red and blue lines-ROI, respectively). (Center) Intensity profile of the line-ROI (Region Of Interest) of the device length on each three z-images. Detail (right) of the same profile taken from the border of the chip, where diffraction and noise effects are observed as a gradual intensity transition in spite of the step transition. Black dots indicate the pixel ratio ± 1 .

Figure 4.35 represents three z-slices with a $2 \mu\text{m}$ -step between each one of them. It is shown high contrast of a nanodevice, whether the device is in focus (Z_4) or out of focus (Z_3 and Z_5). Coloured lines depict the line-ROI for the three intensity profile plots. These profiles show that, even when the devices are out of focus (± 1 optical slice), the dimensions extracted from their intensity profiles are similar. Although best-focused z-stack images are used for dimension processing, points not exactly in the focal plane can also be measured accurately. The main contribution of defocusing (blurring) occurs when there is a lack of contrast, but as silicon is opaque, the contrast of the nanodevices in the images is very high, facilitating image processing.

For instance, we performed the measure of a similar profile in a nanodevice injected in a mouse embryo. Hence, two frames were taken from a videomicroscopy, to determine the nanodevice edge position (Figure 4.36).

We precisely localize the minimum of intensity in the diffraction profile in an effort to minimize the error (pink rectangle in Figure 4.36). In addition, we do not calculate absolute distances, as explained before (Figure 4.33); we calculate the increment of distances, further reducing invariant errors between frames.

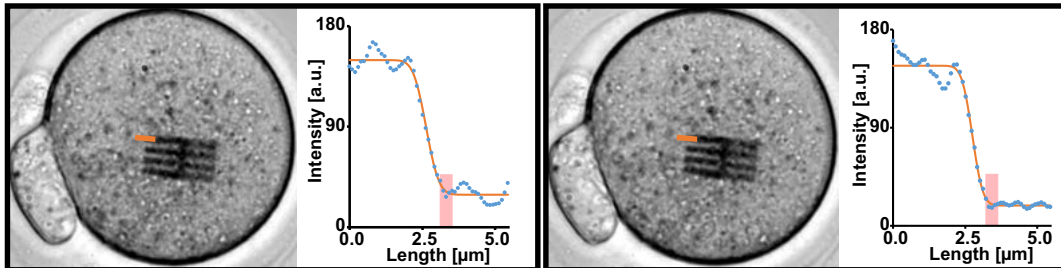


Figure 4.36. Nanodevice intensity profile inside an embryo. Optical images of mouse embryo containing a nanodevice and the intensity profiles (orange) along one edge in two consecutive frames.

Figure 4.36 shows optical images of a mouse embryo containing a microinjected H-comb nanodevice (left in each pair), showing the optical profile along the path indicated by orange lines in each micrograph, at the edge of the nanodevice (right in each pair), at two time consecutive points during videomicroscopy. Clearly, it can be identified the typical diffraction profile from the edge of a structure found in usual optical books[37].

Therefore, diffraction is not the main limitation for the determination of δ_{image} , as long as the same criteria are always used to calculate it (max, half or min intensity; see Figure 4.33) by localizing pixels $P1$, $P2$ and $P3$ at the borders of the nanodevice, and they present high contrast even inside embryos.

4.5.3 Development of optical structures for the calculation of the device bending limitation

To further clarify the contribution solely by diffraction to our measurements, we designed and fabricated optical structures. A series of specific test structures, similar to the H-comb cantilevers of the manuscript, was developed. Each of the designed test structures has a pre-determined bend in the range of the value of the bending, δ , that is measured in H-comb devices inside embryos (Figure 4.37a).

Later, test structures will be used to calibrate our optical images. The bending of the different test devices were determined by the same optical method used to determine H-comb nanodevice bending inside embryos and employing the same microscope settings.

For the fabrication of the test structures, we started from a 800 μm -thick Fused Silica wafer (Si-Mat) as substrate. Next, an aluminium layer (100 nm-thick) was deposited by sputtering (Leybold Z550) on top of the wafer. The

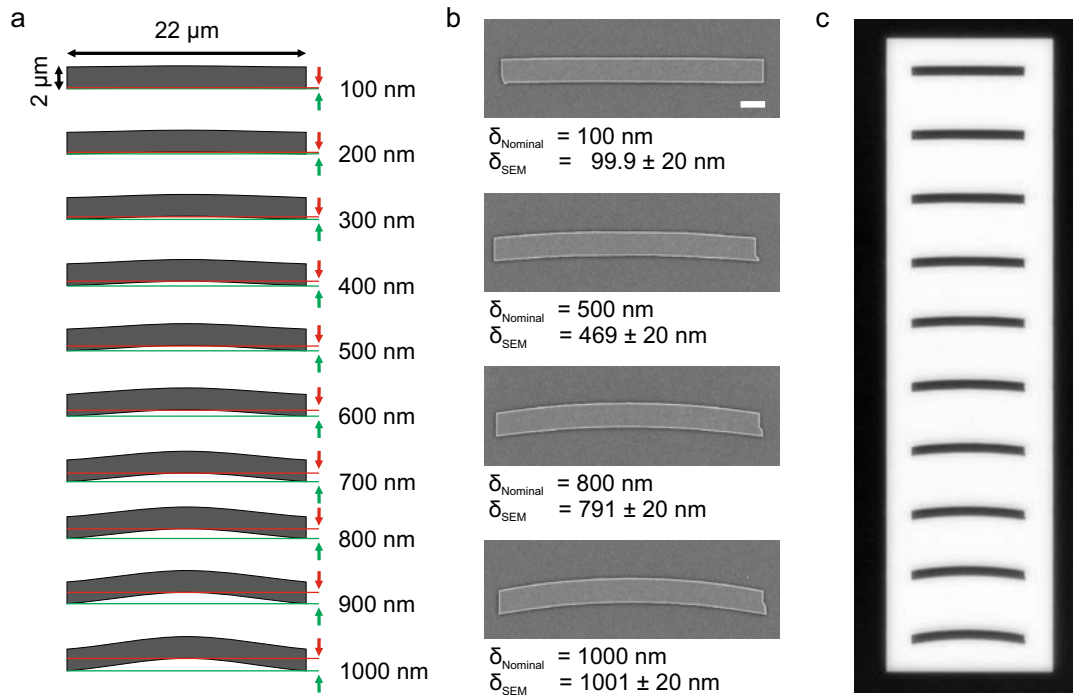


Figure 4.37. **Optical test structures fabricated by EBL to determine the minimum curvature that can be solved.** a, Scheme of the designed structures dimensions. Bending ranges from 100 nm to 1000 nm in steps of 100 nm; they are arranged in order, with the smallest bending at the top. b, SEM images of the fabricated devices showing their intended bending ($\delta_{nominal}$) and the bending determined empirically by SEM (δ_{SEM}). Scale bar: 2 μm . c, Optical image of test structures recapitulating cantilever bending. Black areas are aluminium and bright areas are fused silica.

wafer was then diced to form 1 cm x 1 cm chips. Then, CSAR62 (ALLRESIT) resist was spun onto the chips as a previous step of an electron beam lithography (EBL) process (RAITH 150 (two)), which permitted the definition of structures with nanometer precision. The resist was developed by ARS600-546 (ALLRESIT). After that, a dry etching process was used to pattern the aluminium layer using SENTEC equipment and the resist removed by PVA TEPLA 300SA. Finally, the resulting structures were calibrated in a SEM (LEO 1530) at a resolution of <20 nm (Figure 4.37b). The test structure bending were determined optically (Figure 4.37c), $\delta_{Optical}$, under our standard experimental conditions, so they could be compared to the high precision determination obtained by SEM, δ_{SEM} .

Moreover, the measuring of $\delta_{Optical}$ was done in blind experiment conditions, in order to reduce or eliminate the bias of the experimenter who recorded the device bending. The resulting comparison is presented in the table of the Table 4.5, confirming the fidelity on the determination of the bending by optical microscopy.

As can be seen in Table 4.5, the optically-determined measurements were in good agreement with the actual bending values: all confirmed that the error in the determination is not limited by the diffraction limit. $\delta_{Optical}$ errors were below the 2 pixel error that we considered for our calculations. The

δ_{SEM} [nm]	100	141	258	398	469	586	656	791	908	1001
$\delta_{Optical}$ [nm]	103	132	210	315	406	511	609	702	850	1022
$\delta_{SEM} - \delta_{Optical}$ [nm]	-3	9	48	83	63	75	47	89	58	-21

Table 4.5. **Calibration values of the optical test structures.** Bending determined by SEM δ_{SEM} and optically $\delta_{Optical}$ for each test structure, showing the $\delta_{Optical}$ errors assuming the δ_{SEM} as calibrated values.

main source of errors in our method to determine δ is due to the optical noise inside the embryo and is not limited by diffraction.

4.5.4 Measure limitation inside embryos due to optical noise

All the previous analysis have shown that the determination of the device bending is not mainly limited by the diffraction of the light, as its contribution is minimized. On the other hand, a second error source than the diffraction could impact on the calculation of optical errors in our measurements: the optical noise.

Therefore, the determination of the optical noise contribution to the measurement errors of injected devices in mouse embryos have to be done under the same conditions of real experiments. One method to determine its contribution could be to account the device deflection in fixed cells recorded under the same optical conditions than the usual experimental ones. Clearly, as the cells have been fixed, the nanodevices should not change its curvature and have a constant value along the recorded video.

25 μm -thick nanodevices were injected in embryos and, after ± 6 h post-fertilization (PM-phase), were fixed in 4% (w/v) paraformaldehyde and recorded immediately after. Figure 4.38 shows five frames from the recorded embryo containing a nanodevice. Measurements of the device bending were carried out following the described method in Figure 4.33 in images taken each 2 min. As observed in Figure 4.38 the measures present a variance of $\pm 0.21 \mu\text{m}$.

However, measuring fixed embryos presents technical and biological drawbacks. For example, fixation induced device bending (av. measured initial offset bending = $2.41 \pm 0.21 \mu\text{m}$) and it might alter the optical properties of the experiment.

Although the detected variations of the measure with the fixed samples were very small, we performed an additional experiment to further analyse the effects of the optical noise. For that, we injected oocytes with sperm plus a 100 nm-thick device and recorded the resulting embryos ($n = 2$) during PM phase. These devices are $\sim 4^3$ (~ 64) times stiffer than those handled in the main investigation (25 nm-thick) and are not predicted to exhibit observable change in bending during PM-phase. The 100 nm-thick devices should

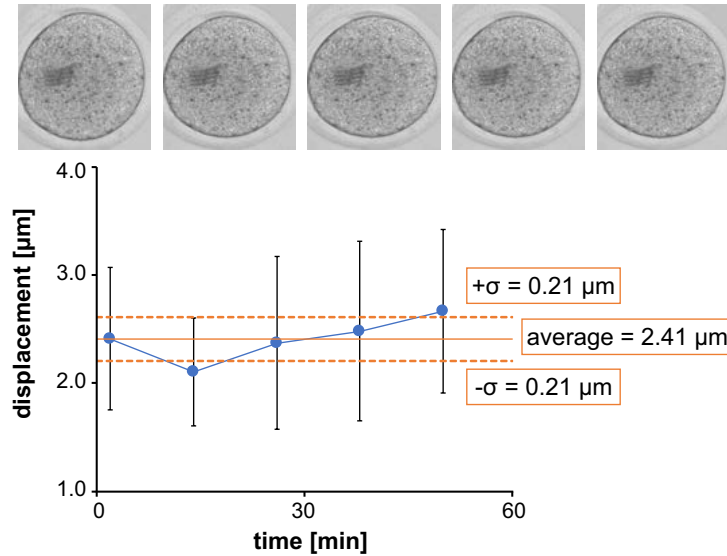


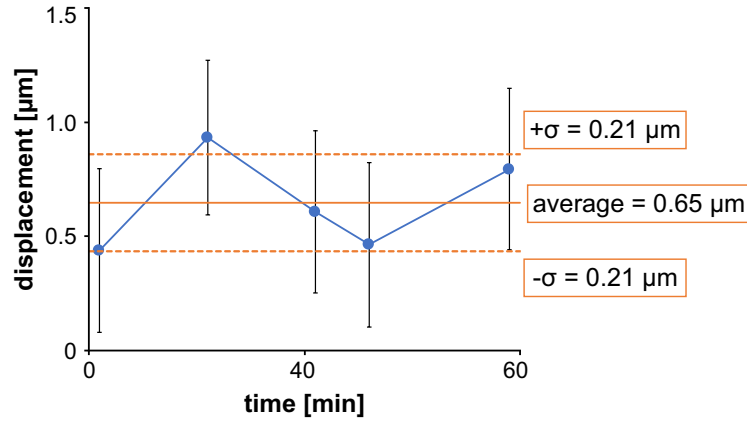
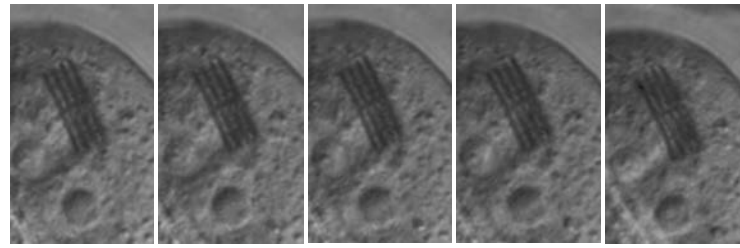
Figure 4.38. **Fixed embryo with nanodevice for optical noise determination.** Optical images of a fixed embryo in five frames of a videomicroscopy containing a nanodevice. Displacement values of the nanodevice within the embryo and its corresponding deviation for each frame. Orange line depicts the average value and its deviation (dashed).

thus serve as test structures to reveal optical errors independently of bending within living embryos.

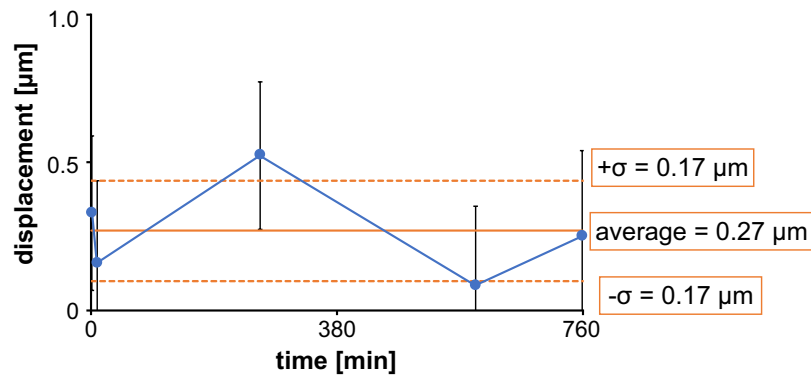
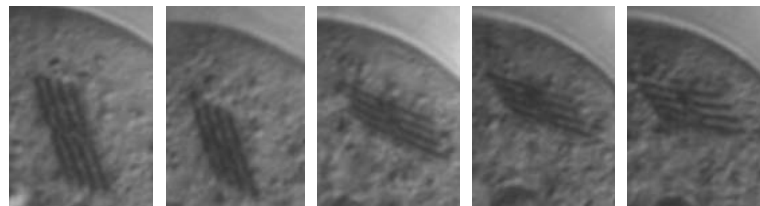
For the analysis, we took five images covering a period of 40 min for the first embryo and 700 min for the second one. As for 25 nm-thick devices, we selected frames with a clear image of the device. Experiments with the 100 nm-thick nanodevice inside the embryo have all of the features of those with the 25 nm one, including displacement, rotation, diffraction effects, optical noise of the camera and errors due to vesicles/particles moving over the chip; the images were collected under the same optical conditions. Figure 4.39 show five frames (each) for analysis of 100 nm devices with negligible physical bending.

Values of the bending of the device for the five images of embryo 1 and 2 show that the initial offset bending (due to fabrication) was $0.65 \mu\text{m}$ and $0.27 \mu\text{m}$, for each device, with a standard deviation about this mean of $\pm 0.21 \mu\text{m}$ and $0.17 \mu\text{m}$, respectively, throughout the analysed time course.

These experiments empirically suggest that errors introduced by optical noise inside embryos are the main limitation for the deflection calculation. This led us to present a confidence level $< 0.5 \mu\text{m}$ as a grey area in the calculation of $\Delta\delta_{max}$, Figure 4.30.



(a). Embryo 1



(b). Embryo 2

Figure 4.39. Embryos within a 100 nm-thick device for optical noise determination. a, and b, Optical images of two different embryos in five frames of a videomicroscopy containing a 100 nm-thick H-comb device. Displacement values of the nanodevice within each embryo and its corresponding deviation for each frame. Orange lines depict the average value and its deviation (dashed).

4.6 Normal embryo development injected with H-comb nanodevices

There are few, if any, reports of cells harbouring entirely internal exogenous artefacts of $>10 \mu\text{m}$ and it was unclear whether mII oocytes would survive injection or tolerate the presence of such large (if extremely thin) structures. Thus, it is necessary to assure the normal healthy development of embryos containing H-comb nanodevices after the microinjection which precisely delivered fully internalized nanodevices into the cytoplasm of mII oocytes by membrane puncture. Nanodevice volume was small compared to the volume of mII oocytes (with a volume ratio of $\leq 1.4 \times 10^{-4}$); oocytes could survive injection with devices.

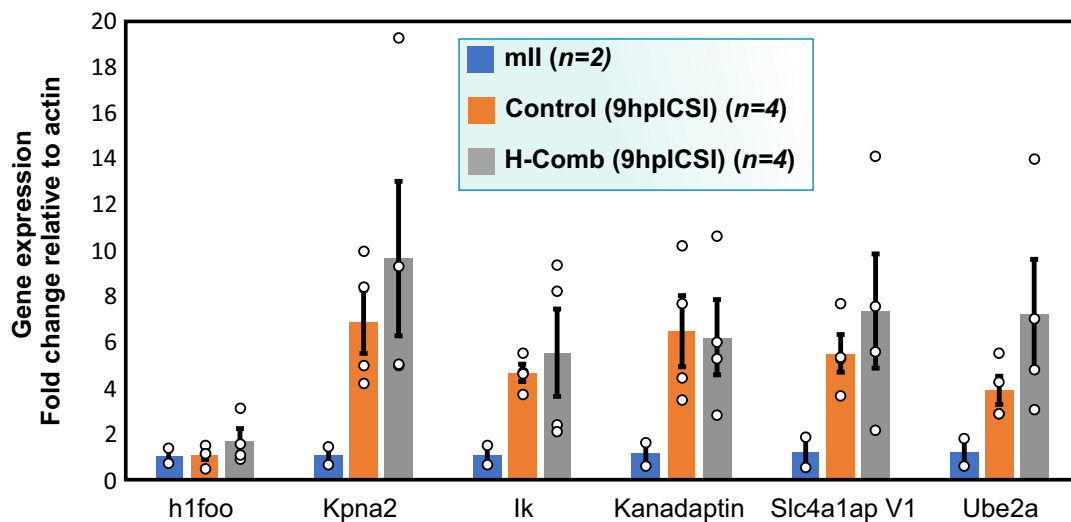


Figure 4.40. Histogram levels in one-cell embryos of transcripts upregulated following embryonic genome activation determined by ratiometric, semiquantitative PCR (qPCR). Wild type metaphase II (mII) oocytes ($n=2$) were injected with a sperm alone (Control (9hpICSI), $n=4$) or a sperm plus an H-comb device (H-comb (9hpICSI), $n=4$) and resulting embryos collected 8 h later. Transcript levels were normalized against levels of the house-keeping gene, H1foo and shown (\pm s.e.m.) relative to a value set at ~ 1.00 for mII oocytes. Unpaired two sided t-test $p \geq 0.25$ for all control vs corresponding H-comb embryo levels (*H1foo*, $p=0.321$; *Kpna2*, $p=0.488$; *Ik*, $p=0.683$; *Kanadapatin*, $p=0.907$; *Slc4a1apV1*, $p=0.416$; *Ube2a*, $p=0.261$).

Coinjecting mII oocytes with $22.0 \times 10.5 \times 0.025 \mu\text{m}^3$ H-comb nanodevices and sperm heads permitted nanodevice delivery and fertilization in the same procedure so that force changes could be captured from the earliest moments of development in the resulting embryo. One-cell embryos containing H-comb nanodevices expressed genes at control levels (Figure 4.40), consistent with normal development. Oocytes coinjected with sperm plus nanodevices produced embryos that developed at high rates ($90.0 \pm 10.0\%$) to form expanded blastocysts (Figure 4.41) indicative of healthy development after nanodevice injection.

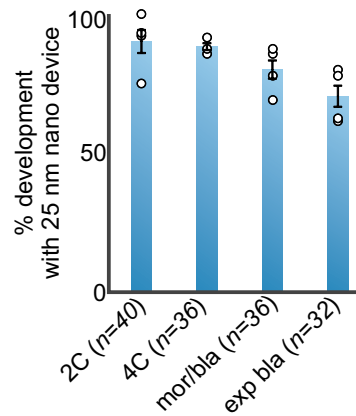


Figure 4.41. **Development of 25 nm nanodevice-injected embryos.** Development rates plotted at two-cell (2C, $n=40$), four-cell (4C, $n=36$), morula-blastocyst (mor/bla, $n=36$) and expanded blastocyst (exp bla, E5.0, $n=32$) stages (\pm s.e.m.). Dot plots indicate percentages from $n=4$ biologically independent experiments.

4.7 Detailed analysis of the mouse one-cell embryo development stages

H-comb nanodevices have been successfully proved as a tool for the cytoplasm mechanics characterization without interfering in the normal embryo maturing. Hence, it is possible to analyse each of the early stages of the embryo development, specified in Section 4.5.1: SDR, PM, PEB, EL and DIV.

4.7.1 SDR-phase. Major mechanical activity during paternal genome reprogramming

Within 20 min of injection into mII oocytes, sperm heads started decondensing and increased ~ 7 -fold in length (Figure 4.42) before recondensing and forming a visible pronuclear envelope [38, 39], corresponding to the SDR-phase, lasting 168 ± 27 min (Figure 4.29).

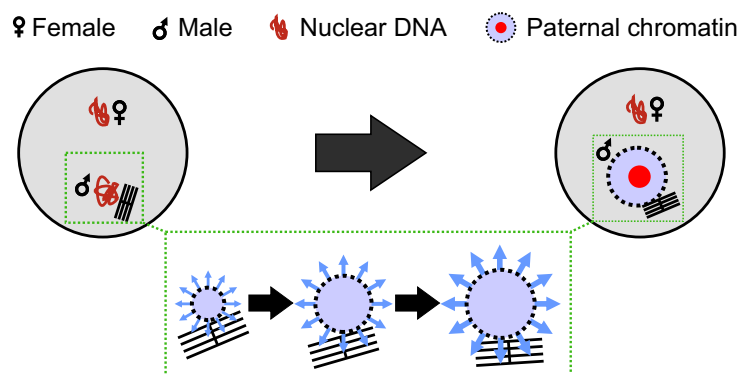


Figure 4.42. **Rearrangement close to the sperm.** Schematic showing the displacement of the devices associated with paternal (sperm-derived) genome remodelling.

Nanodevices were typically near the sperm head ($9.5 \pm 4.5 \mu\text{m}$) and rotated up to $44 \pm 1^\circ$, with elastic deformations of $1.5 \pm 0.8 \mu\text{m}$ (Figure 4.30).

Maximal nanodevice deformation corresponded to $P = 56.2 \pm 28.7$ Pa ($1 \text{ Pa} = 1 \text{ pN} \cdot \mu\text{m}^{-2}$) and $F = 5.3 \pm 2.7$ nN (Figure 4.30). These results reveal major ξ_{mact} and thus cytoplasmic reorganization near the paternal genome during chromatin remodelling (Figure 4.31). Although direct force comparisons between studies are difficult, forces near to the sperm head were ~ 50 times larger than those inside aortic muscle cells measured with silicon nanowires (with peaks of 116 pN)[17] and three orders of magnitude greater than forces exerted by single cytoskeletal motors (< 10 pN)[40].

4.7.2 PM-phase. Membrane ruffling detected close to the embryo center

Pronuclei appeared 4.0~4.5 h after fertilization and during pronuclear migration (PM) converged on the embryo center until membrane breakdown (Figure 4.27), 812 \pm 195 min after sperm injection (Figure 4.29)[39, 41].

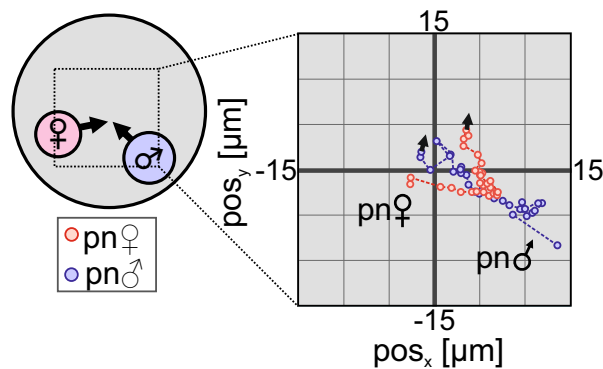


Figure 4.43. **PM movement towards embryo center.** Two-dimensional pronuclear translations around the embryo center. pos_x , represents position in x ; and pos_y , represents position in y .

On small spatio-temporal scales, pronuclear migration was directionally stochastic (Figure 4.43). This translation was accompanied by random ruffling of up to $2 \mu\text{m}$ at the embryo surface, which our nanodevices were able to detect even when close to the center (Figure 4.44). Pronuclear and nanodevice random displacements reflected random kinetic activity and were concurrent with centralizing directional displacements.

Nanodevices deformed by $1.3 \pm 0.1 \mu\text{m}$, corresponding to loads of 47.9 ± 6.1 Pa and 4.5 ± 0.5 nN and rotated $47.0 \pm 6.7^\circ$ (Figure 4.30), evidencing a program of gradual (over several hours) long-range cytoplasmic reorganization required for pronuclear convergence at the center.

The mechanical properties of mouse one-cell embryo cytoplasm were modelled in terms of elastic and viscous elements using a combination of springs and dashpots[42], and it was found these simulations supported a model in which the embryo cytoplasm exhibits a gradient of effective stiffness (GES)[43] (Figure 4.45).

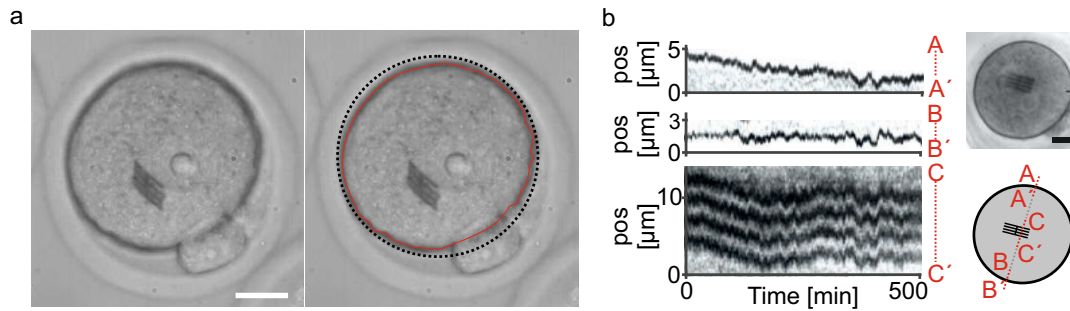


Figure 4.44. **Membrane ruffling during pronuclear migration.** a, Optical images of an embryo during PM-phase showing membrane ruffling, and (left) a red line indicating the membrane profile and a dashed black circle representing the embryo diameter. b, Membrane topography changes at two opposite points and movement of the nanodevice (near the center) with time. *pos* indicates the scan position along AA', BB' and CC' versus time.

In the GES model, the effective elastic constant and viscosity are increased by the relatively stiff cortical system in a manner that is also a function of the internal particle size. In agreement with this, the random migration of endogenous cytoplasmic particles is typically smaller the closer the particles are to the cortex (Figure 4.46).

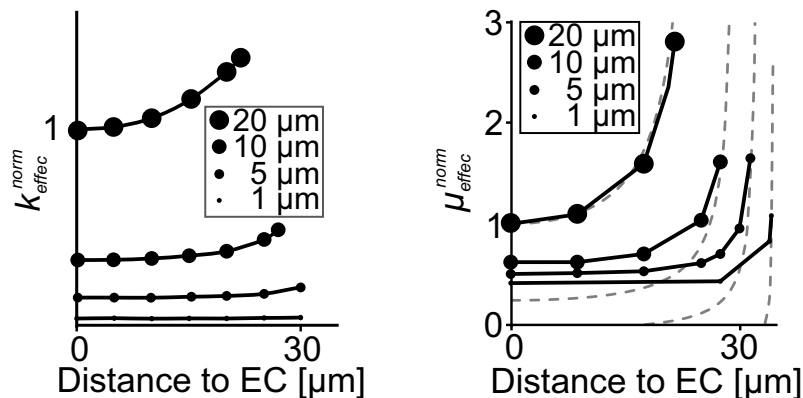


Figure 4.45. **Simulated normalized effective elastic and viscous constant.** Qualitative simulated normalized effective elastic constant (k_{eff}^{norm} , left) and viscosity (μ_{eff}^{norm} , right) for the displacement of spherical objects of different diameters versus the object position relative to the embryo center. Dotted lines show theoretical values (valid for objects near the border).

To probe this, an empirical analysis of endogenous embryonic behaviour was done. Empirical analysis of real time movies (Figure 4.46, center) allowed optical tracking of particles (1.9-6.9 μm diameter; average 2.8 μm) within living embryos ($n=3$ biologically independent samples (embryos); ~ 2 h post-fertilization) so that their respective maximum distances could be plotted from the starting position, $dist_{max}$, (normalized to 100 seconds) versus the particle distance from the EP. Figure 4.46, right, shows distances from the respective starting positions of particles over a given time, relative to their starting positions from the EP.

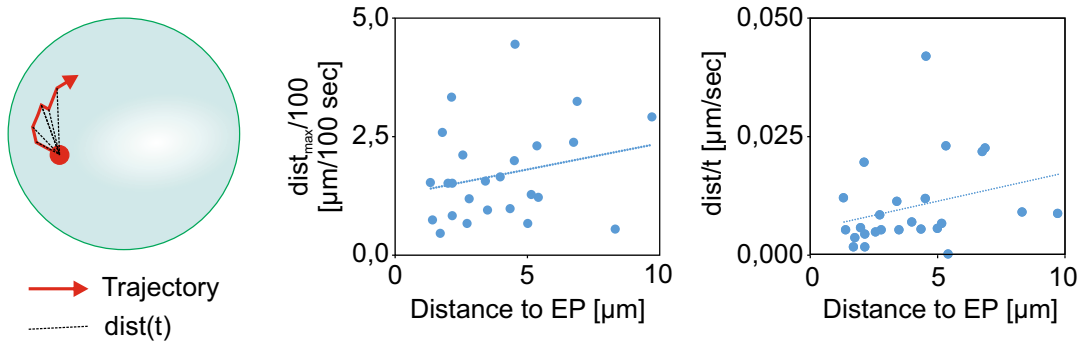


Figure 4.46. **Endogenous embryonic particle trajectories analysis.** Schematic (left) representing the trajectory (red) of an endogenous particle within a one-cell mouse embryo, and the distance ($dist$) from its starting position (black line). (Centre) Maximum distances from the starting position, $dist_{max}$, (normalized to 100 seconds) versus the particle distance from the embryo periphery (EP) and (right) distances, $dist$, from the respective starting positions of particles over a given time, relative to their starting positions from the EP. Linear fitting with straight lines was included to approximate tendencies.

Particles within $\sim 10 \mu\text{m}$ of the membrane border were analysed, as this is the region in which GES is relevant for particles with diameters in the $1.9\text{-}6.9 \mu\text{m}$ range (Figure 4.45). Thus, particles close to EP exhibited relatively small maximum displacements, in agreement with GES model.

Although limited by inherent intraembryonic heterogeneity, the GES model predicts that an increase in pronuclear size during the PM-phase would favor movement towards the embryo center, where the effective stiffness is smaller. This prediction was validated by real-time videomicroscopy revealing pronuclear expansion in mouse (Figure 4.47). In addition, GES explains the increment of mechanical loads detected by nanodevices during this phase (Figure 4.30), which could also contribute to pronuclear centring.

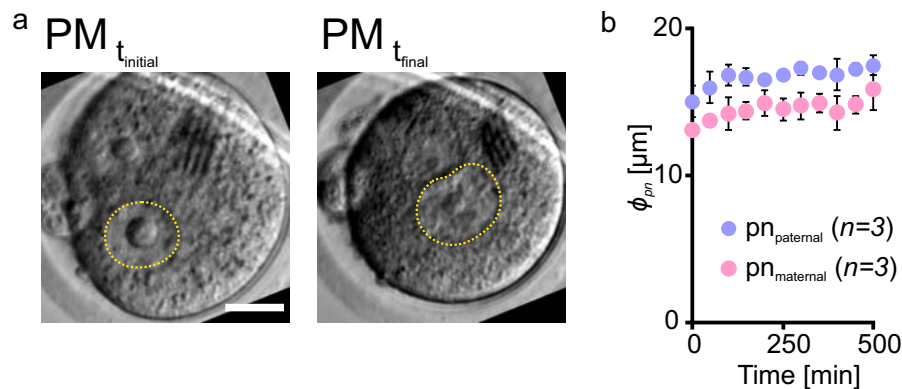


Figure 4.47. **Embryo pronuclear growth.** a, Optical images of an embryo at an initial moment ($PM_{t_{initial}}$) and at the end ($PM_{t_{final}}$) of the PM-phase. Dashed yellow lines indicate the area of the pronuclei. b, Measured pronuclear diameter (ϕ_{pn} , mean \pm s.e.m.) determined by videomicroscopy analysis ($n = 3$).

4.7.3 PEB-phase. Low cytoplasmic mechanical activity during spindle formation

The pronuclear envelope breakdown (PEB) phase (lasting 113.0 ± 30.8 min) (Figure 4.29) included spindle formation and chromosome alignment prior to the onset of embryo elongation. During the PEB-phase, nanodevices reported cytoplasmic mechanical load changes at the lower threshold of detection and the smallest of the entire embryo one-cell stage (8.6 ± 1.7 Pa, 0.8 ± 0.2 nN) (Figure 4.30). Embryo surface membrane ruffling stopped simultaneously and abruptly with PEB, in agreement with the minimal ζ_{mact} reported by the nanodevices (Figure 4.31). This coincided with a marked increment of cortical F-actin (Figure 4.48), reflecting actin redistribution from the embryo interior to cortex. A reduction of cytoplasmic forces during the PEB-phase could facilitate spindle assembly and chromosome alignment.

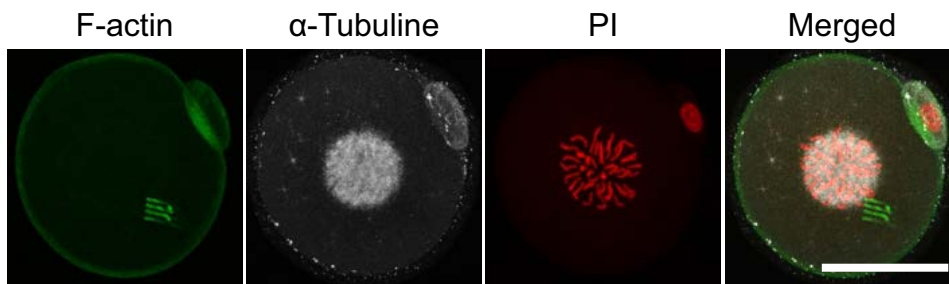


Figure 4.48. Fluorescence confocal images of injected embryos during PEB. Embryos were stained with phalloidin to label F-actin (green), anti- α -Tubulin antibodies to label α -Tubulin (gray) and propidium iodide (PI) to label nuclear DNA (red). Scale bar: $70 \mu\text{m}$.

The minute changes on the curvature of the nanodevices along this phase allow us to experimentally determine their average initial curvature. As PEB-phase reported the smallest forces (PEB), we use devices during this phase to obtain a range of initial curvatures ($\sim 1.3 \pm 0.3 \mu\text{m}$) due to the intrinsic deflections of them. From that, it was simulated the effect of this curvature on the mechanical sensitivity of the devices as explained in the Section 4.4.3, concluding that they do not change the mechanical sensitivity. This supports our analysis of deflection differences rather than absolute deflection values to produce conclusions from the resulting trends and averages.

4.7.4 EL-phase. Cytoplasmic stiffening governs embryo elongation

The embryo elongation phase, EL, lasted 14 ± 2 min (Figure 4.29) and was characterized by spindle separation and embryonic axial elongation of $\sim 10\%$ ($\sim 8 \mu\text{m}$). After the embryo poles contacted the zona pellucida (ZP), embryo elongation continued at the same rate, $\sim 1.25 \mu\text{m} \cdot \text{min}^{-1}$ (Figure 4.49). This plot incorporated changes that reflected mechanical transitions that we designated (in temporal order): EL1, EL2 and DIV.

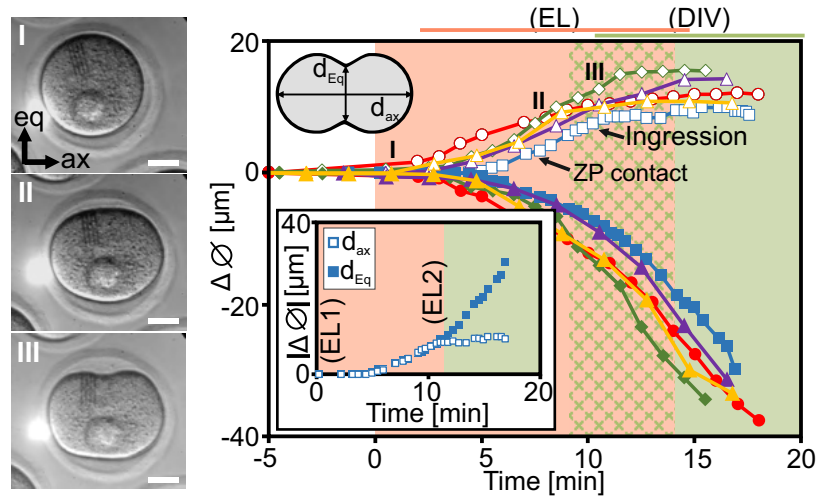


Figure 4.49. **Morphological changes during elongation and division.** Representative images (left) of EL, showing an initial stage before the onset of elongation (I), elongation in which zero axial cortical curvature is achieved in the equatorial region (II) and EL after cleavage plane instatement (III). Increment, $\Delta\phi$, of axial (d_{ax}) and equatorial (d_{eq}) diameters of five mouse embryos (right), showing absolute values of d_{ax} and d_{eq} diameter increments, $\Delta\phi$ (inset). Scale bar: 20 μm .

Immunofluorescence images of embryos revealed changes in microtubule organization coinciding with EL1, EL2 and DIV (Figure 4.50).

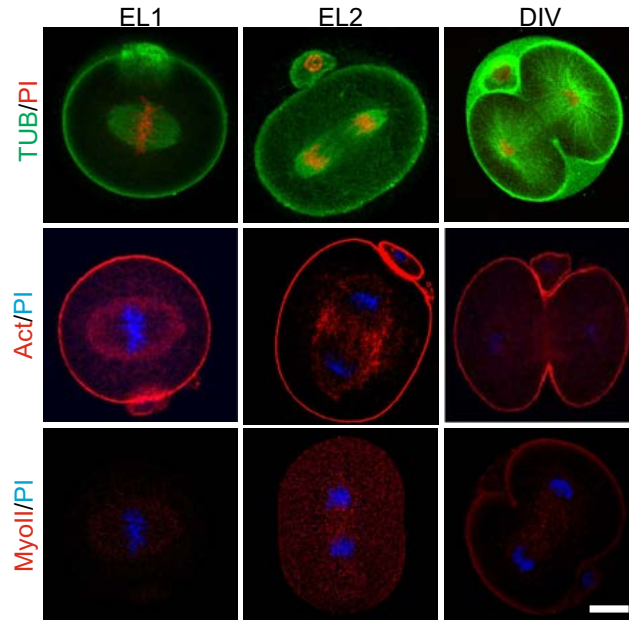
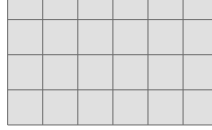


Figure 4.50. **Immunofluorescence images of embryo elongation and division.** Immunofluorescence images (top) of α -tubulin (TUB) showing microtubules in mouse embryos during initial spindle elongation (EL1), equatorial tubulin meshwork appearance (EL2) and after the appearance of radial microtubules and invagination (DIV). Immunofluorescence images (center) of F-actin (Act) and myosin II (MyoII, bottom) showing a myosin II increase after EL1 and a decrease after EL2. Genomic DNA is stained with propidium iodide (PI) in all the images. Scale bar: 20 μm .



4.7. Detailed analysis of the mouse one-cell embryo development stages 119

EL1 microtubules shape the spindle and localize cortically with F-actin, augmenting cortical stiffness. At EL2 (just before cleavage furrow formation at the embryo center), a tubulin meshwork[44] appeared in the equatorial region (Figure 4.50). Radial microtubules then increasingly emanated from spindle poles, first towards their proximal overlying equatorial cortex and subsequently (during DIV), towards polar cortical regions (Figure 4.50), when elongation practically stopped.

Overall, EL-phase embryos experienced the largest global deformation, but nanodevices counter-intuitively reported the smallest rotations (Figure 4.30), indicating minimal cytoplasmic reorganization. Consistent with their decreased rotation, nanodevices detected the greatest ζ_k at EL (Figure 4.31). The fact that the embryo normally elongated, even though radial microtubules were absent, suggests that the mechanical load generated by the elongating spindle is transmitted through the bulk cytoplasm to the axial cortex.

An increment of myosin II from EL1 to EL2 is shown in Figure 4.50, in agreement with previously suggested myosin-mediated cytoplasmic stiffening. This directly demonstrates that the cytoplasmic stiffness of mouse embryos increases during the EL-phase, accompanied by an increase in myosin II activity.

4.7.5 DIV-phase. Cytoplasmic softening and the largest forces during division

During the brief division (DIV) phase (lasting 5.5 ± 1.6 min) (Figure 4.29), nanodevices near the cleavage plane underwent rotations of up to $137 \pm 2^\circ$ and deformations of $4.2 \pm 0.3 \mu\text{m}$, corresponding to $P = 233 \pm 20$ Pa (17.7 ± 1.5 nN) (Figure 4.30).

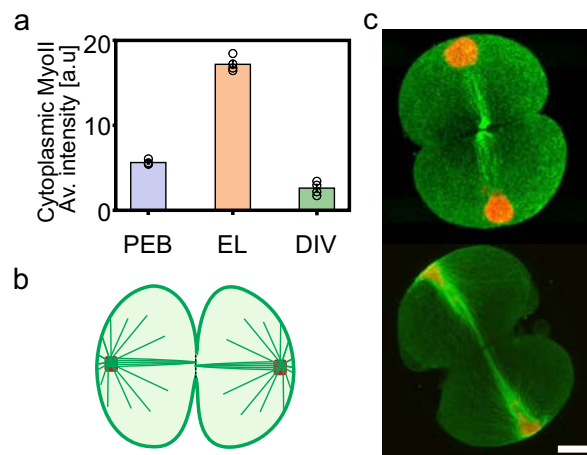


Figure 4.51. **Embryo DIV-phase analysis.** a, Average cytoplasmic myosin II intensity (determined by quantitative immunofluorescence \pm s.e.m.) at PEB, EL and DIV stages ($n = 4$ each), showing an increase during the EL and a posterior decrease during the DIV. b, Schematic of microtubule distribution. c, Representative immunofluorescence micrographs ($n = 2$) of α -tubulin showing microtubule (green) and nuclear DNA (red) distributions near the end of the DIV-phase. Scale bar: $10 \mu\text{m}$.

Nanodevices reported maximal ζ_{mact} approximately two orders higher than at any other time in the embryo (Figure 4.31). This, combined with the rapidity of nanodevice bending and relaxation, suggested a decrease in ζ_k during DIV, indicating active softening of the cytoplasm.

Furthermore, it was probed that changes in cytoplasmic stiffness correlated with cytoplasmic myosin II dynamics (Figure 4.51a). Close to DIV completion, spindle and radial microtubules underwent a collective motion similar to an umbrella folding as each of the two chromosome sets moved towards their respective cortical pole (Figure 4.51b,c). Therefore, the fact that nanodevices reported a large ζ_{mact} and that chromosome sets are located close the embryo poles, this suggest that chromosomes moved further from the division plane, where cytoplasmic reorganization is greater, guaranteeing the chromosome segregation to respective daughter cells.

4.8 Experimental perturbation of the mouse cytoplasm mechanical program

This work predicts a program of mechanical and force changes within embryos through the changes detected in the bending of H-comb nanodevices. Thus, we thought about the evaluation of this program via perturbation experiments. We reasoned that this might be achieved by the actomyosin (myosin II) motor inhibitor, blebbistatin, to reduce force generation[45] and cytoplasmic stiffness[46] within the embryo.

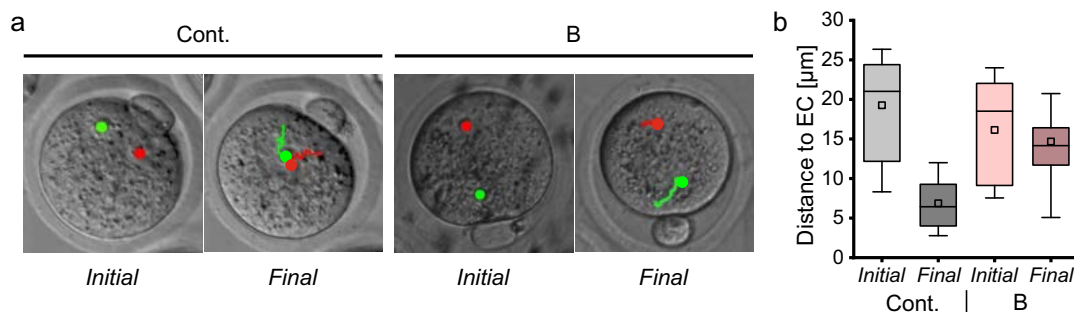


Figure 4.52. **Blebbistatin treated embryos during PM-phase.** a, Time-lapse images of embryo ($n = 2$ each) cultured without (control, Cont.) or with blebbistatin (B; $200 \mu\text{M}$) just after pronuclear formation (Initial) and at PEB (Final), showing starting and final positions (dots) and trajectories of female (green) and male (red) pronuclei. b, Box-and-whiskers plots showing distances between pronuclei and embryo centres at initial (pronucleus formation) and final (PEB) positions ($n \geq 5$). Whiskers, 0 to 99th percentile; box, 25th to 75th percentile; line within box, median. Values (maximum, mean, minimum): Cont. (initial) 26.34, 19.25, 8.32; (final) 12.00, 6.87 and 2.78; B (initial) 24.00, 16.14, 7.55; (final) 20.74, 14.68, 5.08.

Accordingly, embryos incubated in the presence of blebbistatin underwent a reduction in cortical ruffling and pronuclear convergence during the PM-phase compared to untreated controls (Figure 4.52a,b).

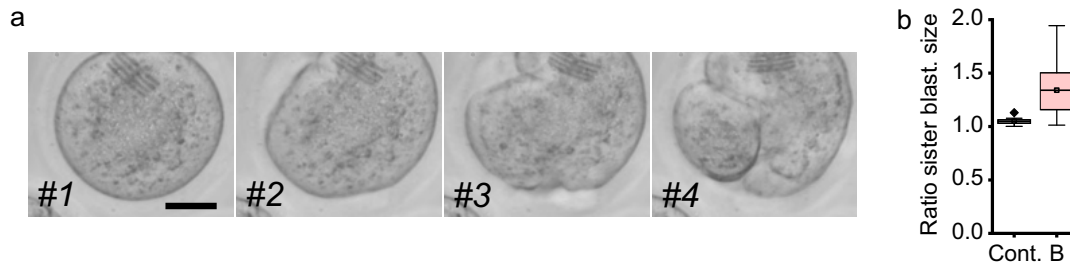


Figure 4.53. **Blebbistatin treated embryo underwent asymmetric division.** a, Optical images of different frames from embryo elongation to division. Scale bar: 20 μm . b, Percentages of control (Cont.; $n = 10$) or in 200 μM - blebbistatin (B; $n = 22$) cultured embryo undergoing asymmetric division. Data are box-and-whiskers plots (whiskers, 0 to 99th percentile; box, 25th to 75th percentile; line within box, median). Values (maximum, mean, minimum): Cont., 1.08, 1.05, 1.00; B, 1.94, 1.34 1.01.

Moreover, exposure to blebbistatin did not prevent embryo division but it occurs asymmetrically as shown in Figure 4.53.

Compared to unexposed controls (Figure 4.30), nanodevices within blebbistatin-treated embryos exhibited a marked reduction in rotation (related to cytoplasmic reorganization) and mechanical loads throughout much of the one-cell stage (Figure 4.54), further evidencing a functional role for the actomyosin complex in force generation. In addition, the reduced forces and increased random pronuclear movement in blebbistatin-treated embryos provided evidence for a reduction in effective stiffness caused by myosin inhibition[46].

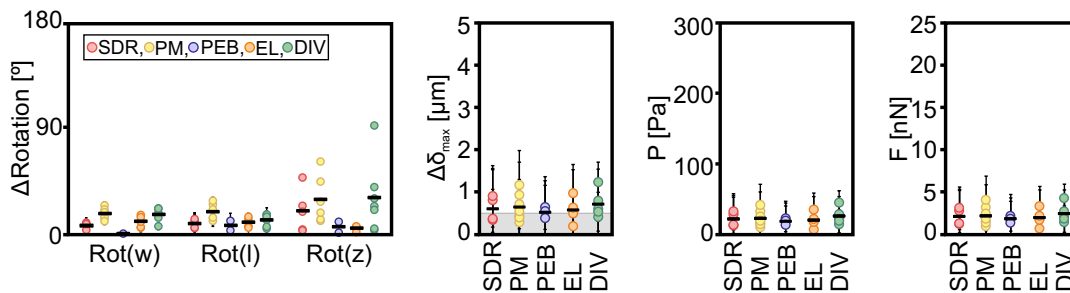


Figure 4.54. **Experimental measures with several devices on treated embryos.** Maximum intracellular device rotations $\text{Rot}(w)$ ($n = 21$), $\text{Rot}(l)$ ($n = 24$) and $\text{Rot}(z)$ ($n = 25$), $\Delta\delta_{\text{max}}$ during embryo stages ($n = 23$). Grey area indicates a range of lower confidence, and simulated pressure (P) and force (F) acting on the nanodevice necessary to obtain given values of $\Delta\delta_{\text{max}}$. Data are for embryos cultured in blebbistatin, with bars depicting error propagation.

Although blebbistatin-treated PM-phase embryos experienced a two-fold cytoplasmic mechanical load reduction (Figure 4.30 and Figure 4.54), pronuclear centring was reduced ~ 10 -fold, suggesting that cytoplasmic forces alone are not sufficient to account for pronuclear centring (Figure 4.52b). The reduction in cytoplasmic stiffness caused by blebbistatin would also reduce spindle force transmission to the cortex, leading to aberrant spindle centring

followed by asymmetric division (Figure 4.53b).

4.9 Suspended intracellular devices developed for mechanical actuation inside eukaryotic living cells

Mouse embryos ($\theta \sim 70 \mu\text{m}$) are large in terms of size of cells. For instance, the diameters of HeLa cells are approximately $20 \mu\text{m}$. Pursuing in the pivotal task of this thesis, we devised new suspended star-shaped devices to measure intracellular forces in cells with smaller sizes ($\sim 20 \mu\text{m}$ in diameter). Cell interior is a dynamic organization of microtubules, intermediate and actin filaments which pull and push generating intracellular forces. Therefore, to internally measure these forces we designed and fabricated these new set of polysilicon devices (Figure 4.55).

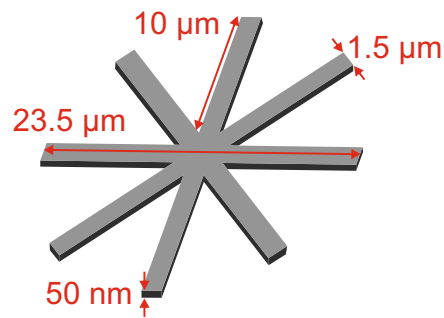


Figure 4.55. **Star-shaped device design dimensions.** Scheme representation of the star-shaped structures with designed dimensions.

Here, the basis of the development of these new intracellular tools will be briefly presented, which are currently being tested at the Dr. Suárez laboratory (see *Collaborations and Stays in Research Entities*) using HeLa cells. Next, the design, fabrication and simulation of the mechanical behaviour will be shown.

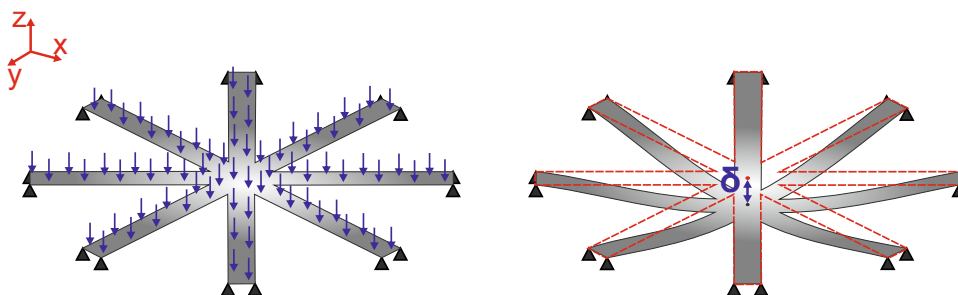


Figure 4.56. **Simplified working principle of star-shaped devices.** Scheme of the device with physical constrains at the end of the cantilevers subjected to a load (a force, F , or a uniform distributed pressure load, P) that causes the its bending in z -direction, δ .

The design consists in an eight cantilevers in a star-shaped distribution. Each cantilever has a length of $10\ \mu\text{m}$ and a width of $1.5\ \mu\text{m}$, while the total length of the device was established to $23.5\ \mu\text{m}$ (Figure 4.55). As we previously designed in the case of the H-comb, the device has free zones between cantilevers to reduce the impact on the cytoplasm organization. Furthermore, the sensing principle of the devices will be again based on the bending (δ) readout of the cantilevers and its conversion into a force (F) or a pressure (P) (Figure 4.56).

The fabrication process is the same than for the H-comb nanodevices (Figure 4.57). 100 mm p-type $\langle 100 \rangle$ silicon wafers (Si-Mat, Silicon Materials) of $500\text{-}\mu\text{m}$ -thick are used as substrate (Figure 4.57a). A $100\ \text{nm}$ -thick SiO_2 layer is grown by wet oxidation at $950\ ^\circ\text{C}$ (Figure 4.57b). Next, a $50\ \text{nm}$ -thick polysilicon layer is deposited by chemical vapour deposition (Figure 4.57c).

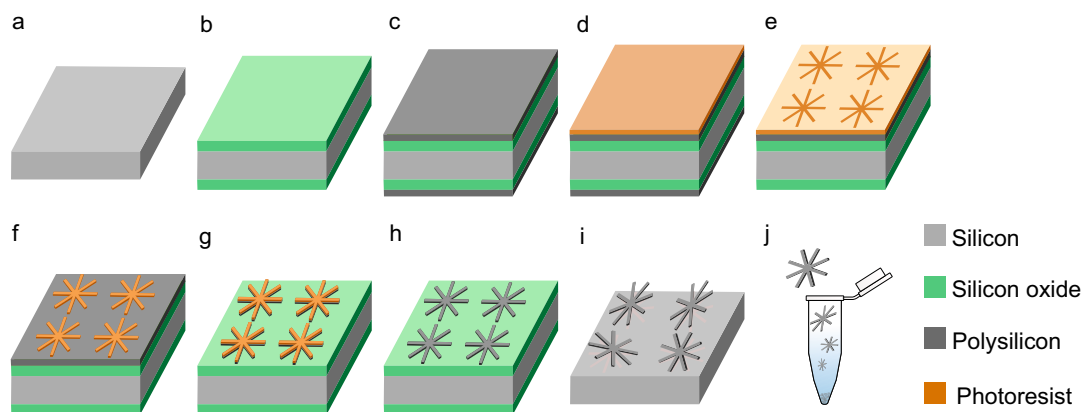


Figure 4.57. **Schematic of the fabrication process of the star-shaped devices.** a) Silicon wafer as initial substrate. b) SiO_2 as sacrificial layer. c) Polysilicon deposition as device layer. d) Photoresist spin-coating. e) Photolithographic exposure to UV and f) resist developed and baked. g) Polysilicon vertical dry etching. h) Photoresist removal. i) Etching of the SiO_2 layer for device releasing and j) devices collection in Eppendorf tubes.

$1.2\ \mu\text{m}$ -thick positive photoresist is spun onto the wafer (ma-P 6512 Micro Resist Technology) (Figure 4.57d) and later the wafer is exposed to UV light (Stepper NSR1505-G7E; Nikon) patterning the design across the reticule (Figure 4.57e). Then, the resist is developed and baked (30 min, $200\ ^\circ\text{C}$) (Figure 4.57f), and the polysilicon layer is etched using SF_6 and $\text{c-C}_4\text{F}_8$ (ALCATEL 601E; Alcatel) (Figure 4.57g). Next, the photoresist is stripped (TEPLA 300-E, Technics Plasma) (Figure 4.57h) and finally, chips are released by etching the SiO_2 sacrificial layer in 49% (v/v) hydrogen fluoride (HF) vapours for 40 min and resuspended in 96% ethanol with short ultrasonic pulses (Figure 4.57i). Devices are collected by settling in Eppendorf tubes (Figure 4.57j).

Then, a $2\ \mu\text{l}$ -drop of 96% ethanol with immersed recollected chips is taken from the tube and placed in a small piece of silicon, as a substrate, to evaluate the fabricated devices by SEM inspection (Figure 4.58). Devices show

the correct dimensions and polysilicon presents a smooth aspect with a non-grainy layer thanks to the optimization of the deposit conditions carried out in the previous chapter (section 3.5.1).

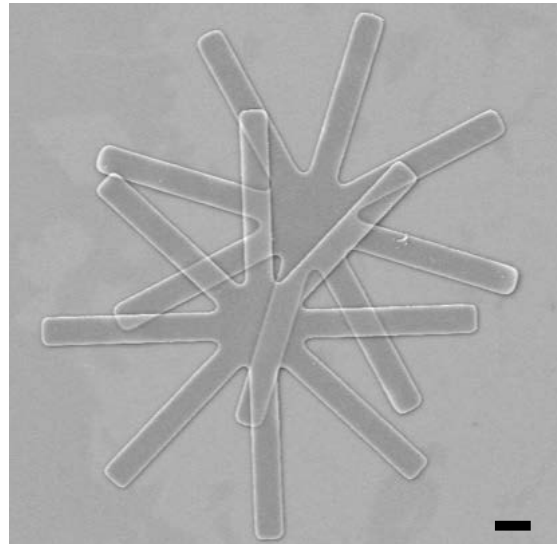


Figure 4.58. SEM image of the star-shaped fabricated devices. Released devices dropped on a piece of silicon are partially transparent evidencing their thin thickness. Scale bar: 2 μm .

Finally, the mechanical behaviour of the structures was analysed by FEM simulation with the use of the software ANSYS Multiphysics. Star-shaped devices were modelled using SOLID95 as a 3D element.

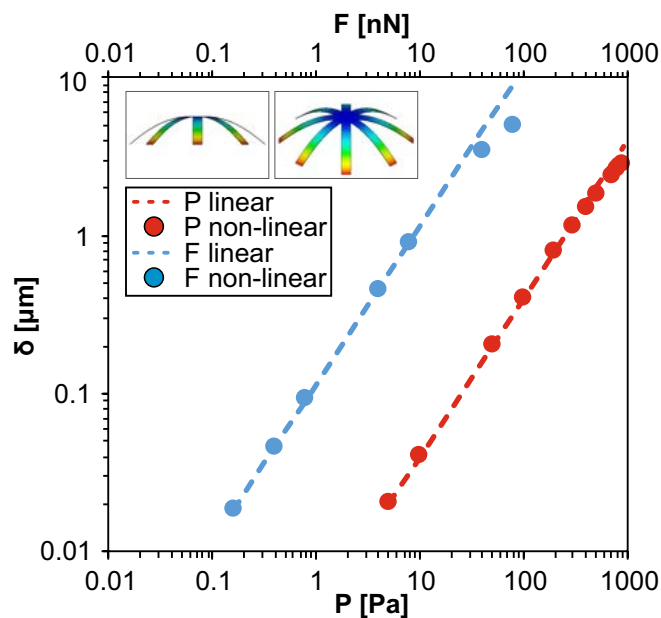


Figure 4.59. Simulation of the vertical displacement] versus a pressure or force. Maximum vertical displacement of star-shaped devices under applied pressure, P , and force, F .

Simulation results in elastic constant of $K_P = 251 \text{ Pa}\cdot\mu\text{m}^{-1}$ and $K_F = 8.8 \text{ nN}\cdot\mu\text{m}^{-1}$ (Figure 4.59), which are larger than those of the H-comb nanodevices, as the star-devices are thicker than them.

4.10 Discussion

This interdisciplinary work adopts a top-down intracellular approach that identifies a program of intracellular force and mechanical property changes during mouse one-cell embryo development. Intracellular nanodevices revealed a program of cytoplasmic force and stiffness changes that map to developmental progression.

H-comb devices, with a nanometer dimension, has successfully been fabricated and collected, allowing, for the first time, a direct measure from the interior of mouse embryos of the forces generated in the cytoplasm during the first stage of the mouse one-cell embryos development.

Nanodevice deflections during the SDR-phase revealed major mechanical activity that coincided with dynamic paternal chromatin remodeling[38]. This is possibly the first direct force measurement associated with any intracellular genome reprogramming, with relevance to chromatin remodeling[47, 48]. The GES model[43] considers the effects on cytoplasmic effective mechanical properties due to boundary conditions. Although it is descriptive in nature, given the molecular nature of some of the force generators and the unknown role played by cytoplasmic heterogeneity, it explains why pronuclear displacement is larger in the direction of center of the embryo during the PM-phase, predicts the contribution of pronuclear growth to centring and is compatible with force gradient models.

Spindle alignment throughout the PEB-phase is facilitated by reducing cytoplasmic mechanical activity and could act as a mechanism to avoid chromosome mis-sorting during cell division. During the EL-phase, nanodevices reported high cytoplasmic resistance to reorganization which counterintuitively occurred in the absence of radial microtubules. Such cytoplasmic stiffening would enhance spindle centering and the transmission to the cortex of mechanical loads exerted by spindle elongation. Acute softening of the cytoplasm would be required for rapid cleavage plane progression and extensive cytoplasmic reorganization[49] during cell scission. Cytoplasmic forces larger than 10 nN were detected that may indeed be necessary during completion of the first cell cycle in mouse embryonic development, and it is notable that our devices measure average forces driving cytoplasmic reorganization rather than intracellular point forces. For example, the devices tracked large average reductions in cytoplasmic mechanical loads and cytoplasmic redistribution after blebbistatin perturbation (Figure 4.60), in agreement with consequential reduction in pronuclear centring and increased asymmetric division.

Collectively, these findings are consistent with fundamental roles for intracellular forces and cytoplasmic mechanical dynamics in early mammalian development (Figure 4.49). Thus, this work will open a window onto intracellular physics and will provide complementary information to existing techniques for mechanobiology. Consequently, we have already begun to develop a new intracellular device with a star-shape design, to carry out a

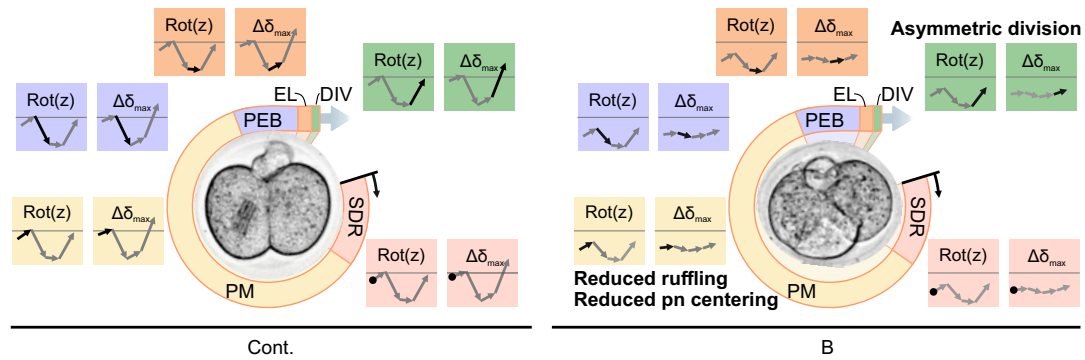


Figure 4.60. **Outline of the mechanical program of mouse embryo.** Models of the mechanical program for controls (Cont.) and embryos perturbed by blebbistatin treatment (B).

mechanical sensing inside eukaryotic living cells. These devices have been fabricated based on silicon microtechnologies with a high-aspect ratio, $23.50 \mu\text{m}$ in length and $0.05 \mu\text{m}$ in thick. Moreover their mechanical behaviour has been analysed by the use of FEM simulations and the biological experimentation is a future task.

Bibliography

- [1] Philip Kollmannsberger and Ben Fabry. Linear and nonlinear rheology of living cells. *Annual review of materials research*, 41:75–97, 2011.
- [2] Ming Guo, Allen J Ehrlicher, Mikkel H Jensen, Malte Renz, Jeffrey R Moore, Robert D Goldman, Jennifer Lippincott-Schwartz, Frederick C Mackintosh, and David A Weitz. Probing the stochastic, motor-driven properties of the cytoplasm using force spectrum microscopy. *Cell*, 158(4):822–832, 2014.
- [3] Lance Davidson, Michelangelo von Dassow, and Jian Zhou. Multi-scale mechanics from molecules to morphogenesis. *The international journal of biochemistry & cell biology*, 41(11):2147–2162, 2009.
- [4] Thierry Savin, Natasza A Kurpios, Amy E Shyer, Patricia Florescu, Haiyi Liang, L Mahadevan, and Clifford J Tabin. On the growth and form of the gut. *Nature*, 476(7358):57–62, 2011.
- [5] Emmanuel Farge. Mechanical induction of twist in the drosophila foregut/stomodaeal primordium. *Current biology*, 13(16):1365–1377, 2003.
- [6] Joy Kahn, Yulia Shwartz, Einat Blitz, Sharon Krief, Amnon Sharir, Dario A Breitel, Revital Rattenbach, Frederic Relaix, Pascal Maire, Ryan B Rountree, et al. Muscle contraction is necessary to maintain joint progenitor cell fate. *Developmental cell*, 16(5):734–743, 2009.
- [7] Akiko Mammoto, Tadanori Mammoto, and Donald E Ingber. Mechanosensitive mechanisms in transcriptional regulation. *Journal of cell science*, 125(13):3061–3073, 2012.
- [8] Daniel TN Chen, Qi Wen, Paul A Janmey, John C Crocker, and Arjun G Yodh. Rheology of soft materials. *Annu. Rev. Condens. Matter Phys.*, 1(1):301–322, 2010.
- [9] Emad Moeendarbary, Léo Valon, Marco Fritzsche, Andrew R Harris, Dale A Moulding, Adrian J Thrasher, Eleanor Stride, L Mahadevan, and Guillaume T Charras. The cytoplasm of living cells behaves as a poroelastic material. *Nature materials*, 12(3):253–261, 2013.
- [10] Pere Roca-Cusachs, Vito Conte, and Xavier Trepats. Quantifying forces in cell biology. *Nature cell biology*, 19(7):742–751, 2017.
- [11] Gang Bao and Subra Suresh. Cell and molecular mechanics of biological materials. *Nature materials*, 2(11):715–725, 2003.
- [12] CT Lim, EH Zhou, and ST Quek. Mechanical models for living cells—a review. *Journal of biomechanics*, 39(2):195–216, 2006.
- [13] Xavier Trepats, Linhong Deng, Steven S An, Daniel Navajas, Daniel J Tschumperlin, William T Gerthoffer, James P Butler, and Jeffrey J Fredberg. Universal physical responses to stretch in the living cell. *Nature*, 447(7144):592–595, 2007.

- [14] William J Polacheck and Christopher S Chen. Measuring cell-generated forces: a guide to the available tools. *Nature methods*, 13(5):415, 2016.
- [15] Xavier Trepat, Guillaume Lenormand, and Jeffrey J Fredberg. Universality in cell mechanics. *Soft Matter*, 4(9):1750–1759, 2008.
- [16] Kinneret Keren, Patricia T Yam, Anika Kinkhabwala, Alex Mogilner, and Julie A Theriot. Intracellular fluid flow in rapidly moving cells. *Nature cell biology*, 11(10):1219–1224, 2009.
- [17] John F Zimmerman, Graeme F Murray, Yucai Wang, John M Jumper, Jotham R Austin, and Bozhi Tian. Free-standing kinked silicon nanowires for probing inter-and intracellular force dynamics. *Nano letters*, 15(8):5492–5498, 2015.
- [18] Adam G Hendricks and Yale E Goldman. Measuring molecular forces using calibrated optical tweezers in living cells. In *Optical Tweezers*, pages 537–552. Springer, 2017.
- [19] Rodrigo Gómez-Martínez, Alberto M Hernández-Pinto, Marta Duch, Patricia Vázquez, Kirill Zinoviev, J Enrique, Jaume Esteve, Teresa Suárez, and José A Plaza. Silicon chips detect intracellular pressure changes in living cells. *Nature nanotechnology*, 8(7):517, 2013.
- [20] Núria Torras, Juan Pablo Aguil, Patricia Vázquez, Marta Duch, Alberto M Hernández-Pinto, Josep Samitier, Enrique J de la Rosa, Jaume Esteve, Teresa Suárez, Lluïsa Pérez-García, et al. Suspended planar-array chips for molecular multiplexing at the microscale. *Advanced Materials*, 28(7):1449–1454, 2016.
- [21] Dennis E Discher, David J Mooney, and Peter W Zandstra. Growth factors, matrices, and forces combine and control stem cells. *Science*, 324(5935):1673–1677, 2009.
- [22] Matthias P Lutolf, Penney M Gilbert, and Helen M Blau. Designing materials to direct stem-cell fate. *Nature*, 462(7272):433–441, 2009.
- [23] Jean-Léon Maître, Ritsuya Niwayama, Hervé Turlier, François Nédélec, and Takashi Hiragi. Pulsatile cell-autonomous contractility drives compaction in the mouse embryo. *Nature cell biology*, 17(7):849–855, 2015.
- [24] E Lehtonen. Changes in cell dimensions and intercellular contacts during cleavage-stage cycles in mouse embryonic cells. *Development*, 58(1):231–249, 1980.
- [25] Amit Tzur, Ran Kafri, Valerie S LeBleu, Galit Lahav, and Marc W Kirschner. Cell growth and size homeostasis in proliferating animal cells. *Science*, 325(5937):167–171, 2009.
- [26] Li-quan Zhou and Jurrien Dean. Reprogramming the genome to totipotency in mouse embryos. *Trends in cell biology*, 25(2):82–91, 2015.

- [27] Otger Campàs, Tadanori Mammoto, Sean Hasso, Ralph A Sperling, Daniel O'connell, Ashley G Bischof, Richard Maas, David A Weitz, Lakshminarayanan Mahadevan, and Donald E Ingber. Quantifying cell-generated mechanical forces within living embryonic tissues. *Nature methods*, 11(2):183, 2014.
- [28] Rodrigo Gómez-Martínez, Patricia Vázquez, Marta Duch, Alejandro Muriano, Daniel Pinacho, Nuria Sanvicens, Francisco Sánchez-Baeza, Patricia Boya, Enrique J de la Rosa, Jaume Esteve, et al. Intracellular silicon chips in living cells. *Small*, 6(4):499–502, 2010.
- [29] Elisabet Fernandez-Rosas, Rodrigo Gomez, Elena Ibanez, Leonardo Barrios, Marta Duch, Jaume Esteve, Carme Nogués, and José Antonio Plaza. Intracellular polysilicon barcodes for cell tracking. *Small*, 5(21):2433–2439, 2009.
- [30] Mohammad Nasr Esfahani and Burhanettin Erdem Alaca. A review on size-dependent mechanical properties of nanowires. *Advanced Engineering Materials*, 21(8):1900192, 2019.
- [31] H Sadeghian, CK Yang, JFL Goosen, E Van Der Drift, A Bossche, PJ French, and F Van Keulen. Characterizing size-dependent effective elastic modulus of silicon nanocantilevers using electrostatic pull-in instability. *Applied Physics Letters*, 94(22):221903, 2009.
- [32] Xinxin Li, Takahito Ono, Yuelin Wang, and Masayoshi Esashi. Ultrathin single-crystalline-silicon cantilever resonators: fabrication technology and significant specimen size effect on young's modulus. *Applied Physics Letters*, 83(15):3081–3083, 2003.
- [33] Ben Ohler. Veeco instruments inc. *Practical Advice on the Determination of Cantilever Spring Constants*, pages 1–11, 2007.
- [34] Bede Pittenger, Natalia Erina, and Chanmin Su. Quantitative mechanical property mapping at the nanoscale with peakforce qnm. *Application Note Veeco Instruments Inc*, pages 1–12, 2010.
- [35] Anthony A Hyman, Christoph A Weber, and Frank Jülicher. Liquid-liquid phase separation in biology. *Annual review of cell and developmental biology*, 30:39–58, 2014.
- [36] Weileun Fang and JA Wickert. Determining mean and gradient residual stresses in thin films using micromachined cantilevers. *Journal of Micromechanics and Microengineering*, 6(3):301, 1996.
- [37] Eugene Hecht. *Optics, 5e*. Pearson Education India, 2002.
- [38] Naoko Yoshida, Manjula Brahmajosyula, Shisako Shoji, Manami Amanai, and Anthony CF Perry. Epigenetic discrimination by mouse metaphase II oocytes mediates asymmetric chromatin remodeling independently of meiotic exit. *Developmental biology*, 301(2):464–477, 2007.

- [39] Toru Suzuki, Maki Asami, Martin Hoffmann, Xin Lu, Miodrag Gužvić, Christoph A Klein, and Anthony CF Perry. Mice produced by mitotic reprogramming of sperm injected into haploid parthenogenotes. *Nature communications*, 7(1):1–15, 2016.
- [40] Arpan K Rai, Ashim Rai, Avin J Ramaiya, Rupam Jha, and Roop Mallik. Molecular adaptations allow dynein to generate large collective forces inside cells. *Cell*, 152(1-2):172–182, 2013.
- [41] Christopher Payne, Vanesa Rawe, João Ramalho-Santos, Calvin Simerly, and Gerald Schatten. Preferentially localized dynein and perinuclear dynactin associate with nuclear pore complex proteins to mediate genomic union during mammalian fertilization. *Journal of Cell Science*, 116(23):4727–4738, 2003.
- [42] Basarab G Hosu, Steven F Mullen, John K Critser, and Gabor Forgacs. Reversible disassembly of the actin cytoskeleton improves the survival rate and developmental competence of cryopreserved mouse oocytes. *PLoS One*, 3(7), 2008.
- [43] Marta Duch, Núria Torras, Maki Asami, Toru Suzuki, María Isabel Arjona, Rodrigo Gómez-Martínez, Matthew D VerMilyea, Robert Castilla, José Antonio Plaza, and Anthony CF Perry. Tracking intracellular forces and mechanical property changes in mouse one-cell embryo development. *Nature Materials*, pages 1–10, 2020.
- [44] Gerald Schatten, Calvin Simerly, and Heide Schatten. Microtubule configurations during fertilization, mitosis, and early development in the mouse and the requirement for egg microtubule-mediated motility during mammalian fertilization. *Proceedings of the National Academy of Sciences*, 82(12):4152–4156, 1985.
- [45] Anna Ajduk, Tagbo Ilozue, Shane Windsor, Yuansong Yu, K Bianka Seres, Richard J Bomphrey, Brian D Tom, Karl Swann, Adrian Thomas, Chris Graham, et al. Rhythmic actomyosin-driven contractions induced by sperm entry predict mammalian embryo viability. *Nature communications*, 2:417, 2011.
- [46] Arne Schäfer and Manfred Radmacher. Influence of myosin II activity on stiffness of fibroblast cells. *Acta Biomaterialia*, 1(3):273–280, 2005.
- [47] Amy R Strom, Alexander V Emelyanov, Mustafa Mir, Dmitry V Fyodorov, Xavier Darzacq, and Gary H Karpen. Phase separation drives heterochromatin domain formation. *Nature*, 547(7662):241–245, 2017.
- [48] Adam G Larson, Daniel Elnatan, Madeline M Keenen, Michael J Trnka, Jonathan B Johnston, Alma L Burlingame, David A Agard, Sy Redding, and Geeta J Narlikar. Liquid droplet formation by hp1 α suggests a role for phase separation in heterochromatin. *Nature*, 547(7662):236–240, 2017.

- [49] Jennifer Zenker, Melanie D White, RM Templin, RG Parton, O Thorn-Seshold, S Bissiere, and N Plachta. A microtubule-organizing center directing intracellular transport in the early mouse embryo. *Science*, 357 (6354):925–928, 2017.

Chapter 5

Anchored silicon chips for cell traction forces determination

Cell traction forces are a main factor of cellular development, motion, shape and extracellular matrix remodelling. Hence, there exists a huge interest in the development of tools able to measure traction forces to understand cell behaviour behind them. Here, we explore different fabrication technologies to develop traction force devices. We started by fabricating a traction force microscope consisting of a periodically-spaced Quantum Dots substrate from a PDMS stamp obtained by electron beam lithography silicon master fabrication. Since the stamping process to obtain nanometric dots with a nanometric pitch was unattainable with the technology at our disposal, we switch to a novel standing silicon chips anchored by nanopillars whose rupture is used for the determination of the ultimate cell traction forces. Fabrication of the nanopillar system was carried out through silicon-based microtechnologies, where the sharpening of the pillar anchors was approached by different etching processes. This sharpening process was the challenge of the fabrication development, since standing pillars reach dimensions less than 25 nm at the anchor. Successfully, the fabrication of the samples was reached and pillars were mechanically studied to characterize their fracture force. Finally, HeLa cells were seeded on a chip demonstrating their interaction with the pillars, through which cell traction forces could be measured.

5.1 Introduction

The determination of cell traction forces is a key issue in cell mechanobiology[1–3]. Cells mechanically interact with their environment and these interactions regulate many cell functions as cell proliferation, differentiation and migration[1, 2].

Despite the relevant role of the mechanical traction processes of the cell, there is a limited number of tools to study cell mechanics compared to the larger number of molecular genetic techniques to study cells[1]. This arises from the difficulty of measuring directly the cell traction forces as they are very small (pN to nN) and occur in small length scales (nm- μ m)[1].

Quantification methods of cell traction forces are mainly based on microscope imaging of the displacement field induced by the cells in a substrate, whose mechanical properties are known. The displacement field is later used as input in a mechanical model system to simulate the exerted forces. Two main methods are used for this purpose: (1) traction force microscopes (TFM) on soft elastic substrates and micro-pillars (μ P); and (2) TFM on soft elastic substrates with embedded particles[1, 3] or Quantum Dots (QD) nanodisc printing on elastic silicone substrates[4, 5]. These second methods require the optical measurement of the displacement of the particles, the reconstruction of the displacement field and the numerical solution based on a substrate material model[4–6]. Conversely, arrays of elastic μ P are also routinely used to calculate the exerted forces by cells using the bending of the pillars as an input, and the beam theory to translate the pillar bending in an applied force[2, 7–9].

However, these techniques are subjected to some limitations, since they require to measure the initial or a reference state, and they share the challenge of measuring the nanometre displacements in a noisy environment, which requires techniques and equipments that might not be available on a standard laboratories[1]. Moreover, some of them are inverse methods, in the sense that the measured displacement field must be numerically post-processed to determine the forces, which can also be difficult for laboratories that want to implement this technique[1, 3]. In this sense, a great effort has been done to improve the postprocessing techniques in order to reduce errors due to ignorance of the out-of-plane displacement components and of the mechanical properties inherent to non-linearities of soft materials, to reduce noise effects and selecting the best interpolation methods for an ill-posed problem[3, 6].

Additionally, these systems suffer from mechanical coupling effects between adjacent particles or pillars, and stresses are transmitted through the soft substrate. In these sense, in order to increase sensitivity, avoid the cross-sensitivities between pillars made of soft-materials and, at the same time, increase the pillars density, hard materials for nanopillars, as GaAs and GaP, have been proposed[2, 10, 11].

Despite the fact that both, the soft elastic substrate and the μ pillars measure traction forces, they present an important difference between them: one

is two-dimensional and the other three-dimensional. Thereby, the cellular behaviour (and, thus, the measured forces) can differ as, in the first, cells lie on a 2D substrate to which they can attach meanwhile cells experienced a 3D environment in the case of μ pillars. Although being reductionist approaches, 2D systems have facilitated the understanding of cell behaviour[12]. Conversely, some studies have shown 3D environments reflect more accurately the cellular microenvironment[13, 14], since cell proliferation, differentiation, mechano-responses, and cell survival have been proved to be affected by the dimensionality of the extracellular matrix (ECM) surrounding cells[12, 15, 16]. Consequently, the adoption of 3D systems aims to be more appropriate as it mimics physiological processes in vivo more realistically.

Different challenges can be distinguished in the determination of cell traction forces. Many studies are interested in solving the fundamental biological problem of the origin of the cellular traction forces, for instance, the molecular complexes that generate the forces, the cytoskeletal components and molecular motors involved or the role of the focal adhesions. In many of these experiments, the challenge is to detect small forces, for what, the important parameter is to improve the low detection limit of the techniques. This can be approached by improving imaging resolution[4, 5, 17] and/or by improving the algorithms for force calculation[17, 18]. In other cases, spatial resolution is the important parameter in order to accurately obtain a force map with resolution below the cell size[4, 5, 17–19].

However, in many other experiments the Ultimate Traction Force (UTF), which can be defined as the maximum traction force exerted by a cell, can be of enormous interest to determine the condition of the cell. In this sense, traction forces have been demonstrated to be a biomarker of malignant cells and a way to investigate the effects of anticancer drugs[10, 11]. For instance, UTF have been used to distinguish between MCF7 breast cancer cells and MCF10A normal-like breast epithelial cells, and even to monitor traction forces to investigate the effects of anticancer drugs by using the bending of nanopillars[11]. Hence, there is a lack of simple, fast and direct 3D techniques for the UTF calculation.

Here, we initially started our research on the development of a new 2D TFM with improved capabilities as we devised a TFM with a forthwith printing method of a periodically spaced QD pattern combining EBL with printing techniques to reduce the pitch between the spots. In that sense, the fabrication process is faster, as the printing of the pattern is done in one go rather than point by point as found in the literature. However, as discussed below, this system was dismissed since the fabrication difficulties were tougher than the advantages that this tool presents. We then moved to a more sophisticated design and we fabricated a silicon chip with standing nanopillars to contribute in the study of cell UTF. This silicon chip comprises an array of mechanical test specimens (nanopillars) with catalogued minimum forces for their structural integrity. In this way, cells cultured on them can fracture some specimens up to a certain one in which the required force to fracture

will define the maximum force applied by the cells.

5.2 Electron Beam lithography patterning for a PDMS-based cell TFM

Our first proposal for the determination of the cell forces exerted on a substrate, was the development of a TFM. Inspired by previous works consisting of embedded beads[4, 5], we thought on the fabrication of a substrate patterned with QD, which allows the quantification of the cell migration forces by the change on the position of these dots.

5.2.1 Design of a patterned substrate as a TFM

The design of the TFM is based on an array of periodically-spaced dots printed on a cellular substrate. Seeded adherent cells attach and spread over the substrate where they exert *traction forces* when modifying its shape or migrate. These cell-generated forces provoke changes in the substrate which translate in changes in the position of the printed dots. Hence, by an optical read-out we can measure the position of the printed spots that will be laterally displaced. The deformation of the substrate can be correlated to the exerted forces. Moreover, due to the periodicity of the pattern, it is easy to notice this change, and from this shift, we are able to calculate the applied force by the cell (Figure 5.1).

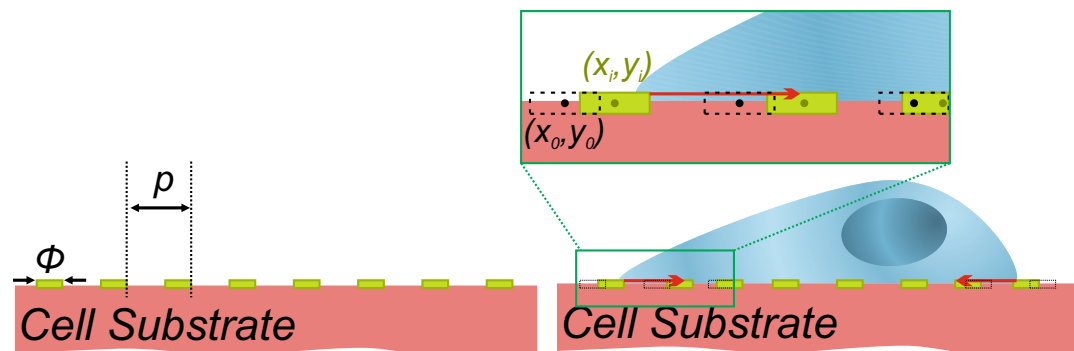


Figure 5.1. **Schematic of the working principle of the TFM for cell force measurements.** Periodically distributed QD stamped on a cell substrate with a pitch p and a diameter ϕ . When cells are cultured and adhered on the substrate they exert forces on it making the position of the dots changes, so the applied force can be derivated from the change in dots location.

The designed conception for the fabrication of the TFM (Figure 5.2) was to print QD on the cellular substrate with a polydimethylsiloxane (PDMS) stamp ((Figure 5.2c). The PDMS stamp consists in vertical nanopillars of 200 nm of height and 160 nm of diameter. The top surface of the nanopillars will be initially inked with a QD solution and then will be stamped on a substrate in which living cells will grow. The PDMS stamp will be replicated from a

silicon master (Figure 5.2b), which is previously fabricated with the Electron Beam Lithography (EBL) technique (Figure 5.2a). Lithography techniques (electron and ion beam and photolithography) are commonly used to obtain a master for the fabrication of PDMS micropillar membranes [7, 20, 21].

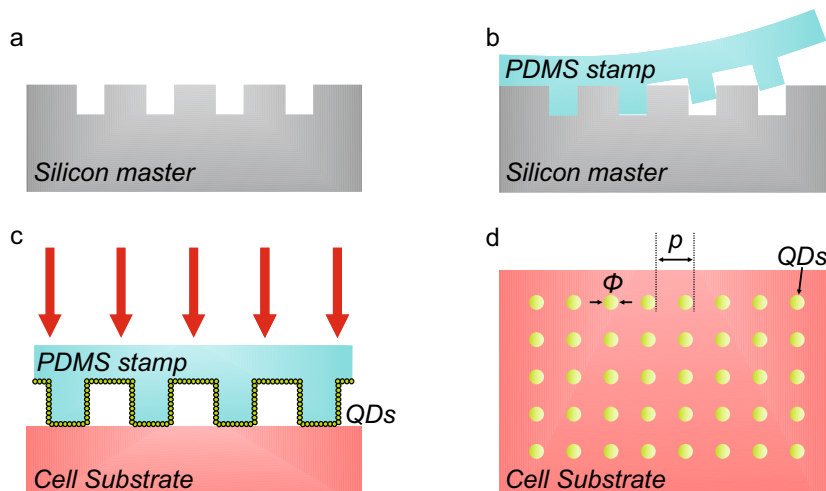


Figure 5.2. **Designed steps for the fabrication of the TFM.** a) Silicon master has to be fabricated in order to create a (b) PDMS nanopillars stamp which (c) will be coated with a QD solution to stamp the pattern on a cell substrate (d) to finally obtain the TFM with periodically spaced (p) dots (ϕ).

The pattern is written with EBL by importing a previously drawn file with a matrix of $5 \times 5 \mu\text{m}^2$ with 500 nm-pitch between dots. This small matrix is later replicated with the EBL software settings to define the final layout for filling an area of $500 \times 500 \mu\text{m}^2$.

5.2.2 Technological development for the fabrication of a periodically-spaced dots substrate

As summarized in the previous section, the technological development to fabricate a periodically-distributed dot pattern can be approached in two steps: first, the PDMS stamp is obtained from a silicon master fabricated by EBL (Figure 5.2a,b), and second, the PDMS is inked with a QD solution to stamp the pattern on the substrate (Figure 5.2c,d).



Figure 5.3. **PMMA-Copolymer profile after EBL exposure.** A thinner sidewall profile is obtained with a polymer-copolymer configuration.

The silicon master fabrication was performed by electron beam lithography (EBL Raith 150 Two, Raith) over a 100 nm-thick PMMA 950K A2 and a 200 nm-thick Copolymer EL6 layers. With that polymer-copolymer configuration a thinner sidewall profile is achieved, due to the different dissolution rates of the layers are different at the developing step (Figure 5.3).

For sample preparation, a four-inch p-type silicon wafer <100> (Okmetic) is diced in $1.5 \times 1.5 \text{ cm}^2$ chips, on which the exposure will be done. The selected chip is cleaned by a piranha etching (H_2SO_4 and H_2O_2 solution) to remove organic residues, and is activated by oxygen plasma (TEPLA 300-E, Technics Plasma) to generate $-\text{OH}$ moieties on the surface for a better adhesion of the polymer (Figure 5.4a). Next, the chip is placed on a hot plate for 90 s at 180°C to evaporate aqueous rests. Then, a layer of 100 nm-thick PMMA 950K A2 is spun at 1500 rpm and after 1 min the sample is post-baked on the hot plate during 1 min at 180°C (Figure 5.4b). After that, 200 nm-thick copolymer EL6 is spun for 1 min at 1500 rpm. The sample is then post-baked on the hot plate for 1 min at 180°C and ready for the EBL exposure (Figure 5.4c).

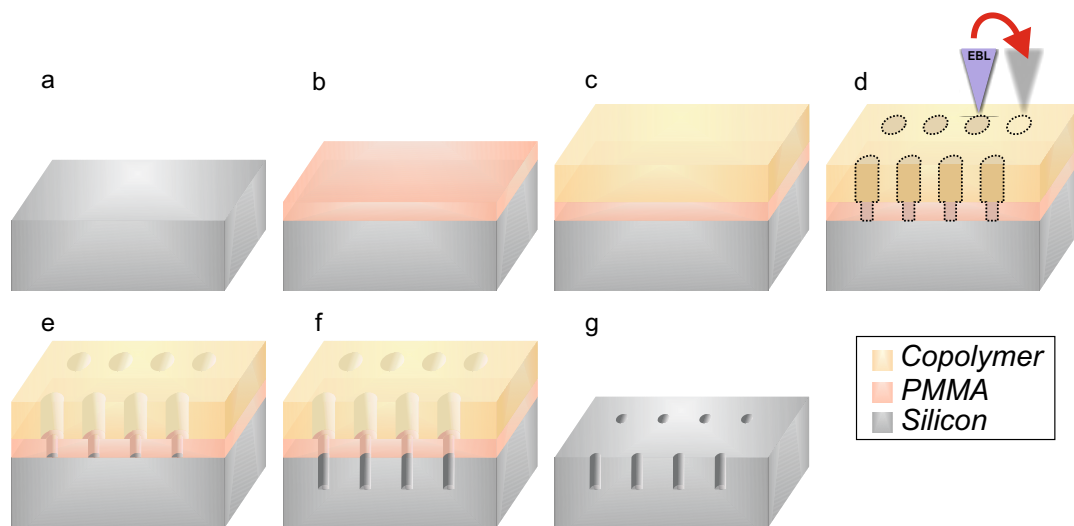


Figure 5.4. **EBL process for the silicon master fabrication.** a) A cleaned diced piece of a silicon wafer. b) 100 nm-thick PMMA 950K A2 is spun. c) 200 nm-thick copolymer EL6 is later spun. d) EBL exposure is performed. e) Resists are developed. f) Silicon substrate is etched by anisotropic RIE. g) Finally, resist is stripped to obtain the silicon master.

EBL exposure (Figure 5.4d) is performed by replicating a matrix of $5 \times 5 \mu\text{m}^2$, with dots periodically spaced 500 nm, up to a final area of $500 \times 500 \mu\text{m}^2$. The beam column parameters are fitted to a voltage of 20 kV and an aperture of $30 \mu\text{m}$ with a beam current, I_{beam} , of 312.3 pA. Since the designed layout is comprised by dots, to achieve the exposure of a 160 nm diameter area for the wells of the silicon master, it is needed to establish a time for the beam to remain in each spot delivering the correct dose, T_{Dwell} . This time is fixed in $T_{Dwell} = 0.25 \text{ ms}$. Hence, the dot dose, defined by equation 5.1, is $0.078 \text{ pA}\cdot\text{s}$.

$$DD = I_{beam} T_{Dwell} \quad (5.1)$$

After the exposure, the resist is developed (Figure 5.4e) by the chip immersion in a Methyl isobutyl ketone (MIBK) : Isopropyl alcohol (IPA) (1:3) solution for 30 s then a 30 s rinse in IPA, and, finally, dried with N₂.

Once the resist is developed, the pattern is transferred to the silicon substrate by anisotropic RIE (Alcatel AMS-110DE P10) with SF₆, C₄F₈, O₂ gases (Figure 5.4f). Finally, resist is tripped to get the silicon master (Figure 5.4g).

Following, the PDMS stamp is fabricated in a two-step procedure: first the silicon master is silanized by exposure to a fluorinated alkyl silane (1H, 1H, 2H, 2H–Perfluorooctyltriethoxysilane, PFOTCS, Fluka) vapours rendering its surface hydrophobic to avoid it sticking to the PDMS (Figure 5.5). The PDMS mixture is then prepared and poured over the master (Figure 5.6).

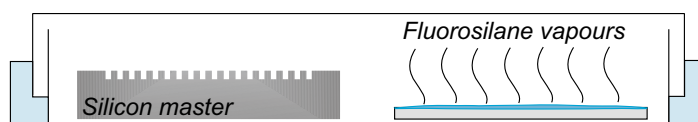


Figure 5.5. **Silicon master surface preparation.** The surface of the silicon master was treated under a fluorinated alkyl silane ambient to avoid sticking between the PDMS stamp and the silicon master surface. Silicon master is located inside a Petri dish next to a coverglass with some drops of fluorinated alkyl silane which evaporate after introducing the whole system inside a vacuum desiccator.

To accomplish the silanization, the silicon mould is sonicated in ethanol for 1 min to clean it and then activated in oxygen plasma (TEPLA 300-E, Technics Plasma) for 1 min at 500 W. Immediately thereafter, the chip is placed inside a Petri dish next to a coverglass with a few drops of the fluorinated alkyl silane (Figure 5.5). The whole setup is later introduced in a vacuum desiccator and the vacuum is activated for 1 min. The silane evaporates and it is left to deposit over the master during 1 h. Then, we introduced the chip in an oven at 80°C for 30 min and finally we rinsed it with ethanol and dried with N₂ prior to the PDMS casting.

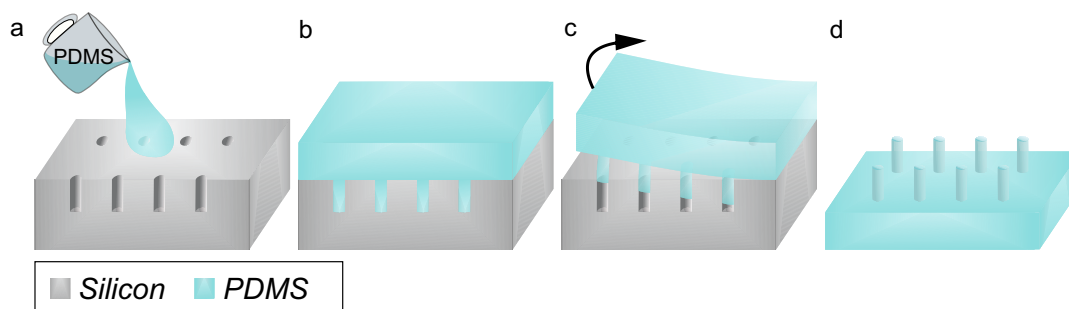


Figure 5.6. **PDMS stamp fabrication.** a) PDMS prepolymer is cast on the silicon master. b) PDMS is cured for 2 h in an oven at 80°C. c) After cooling, the PDMS stamp is peeled-off (d) obtaining the replicated PDMS stamp.

For the PDMS stamp fabrication, initially the base polymer and the curing agent (Sylgard 184 PDMS elastomer, Dow Corning) are mixed by weight at a ratio 10:1 in a plastic container. Next, the plastic container is placed in a desiccator for 30 min to degas the mixture under vacuum. Once the bubbles have been removed, the PDMS polymer mix is poured over the silicon master (Figure 5.6a). Then, the sample is cured for 2 h inside an oven at 80°C (Figure 5.6b). After cooling it is peeled-off (Figure 5.6c) to obtain the final PDMS stamp (Figure 5.6d).

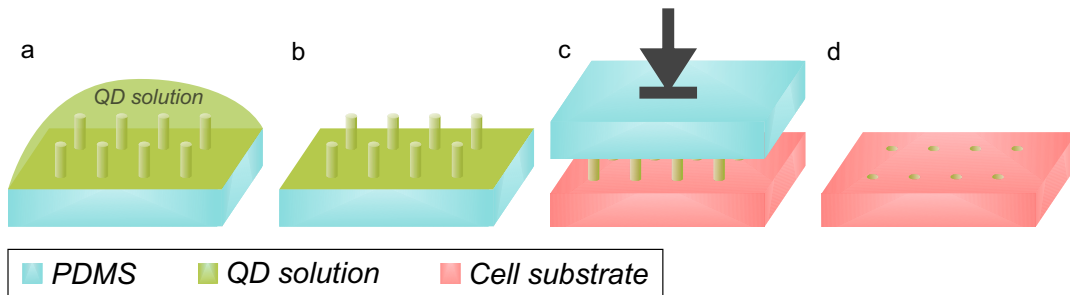


Figure 5.7. **PDMS stamp on cell substrate.** a) PDMS stamp is inked with a QD solution. b) The inked PDMS stamp is washed to remove extra ink. c) The pattern is transferred to a cell substrate by stamping the PDMS pillars. d) Finally, the TFM is achieved.

The top surface of the PDMS nanopillars is incubated with an 1:20 v/v aqueous:QD solution (Qdot 585 or Qdot 655 ITK amino (PEG) Thermo Fisher Scientific) (Figure 5.7a). The inked PDMS stamp is washed to remove excess ink (Figure 5.7b) and the adsorbed QDs are transferred by stamping the PDMS into the substrate (Figure 5.7c) to get the final TFM where living cells will grow (Figure 5.7d).

The silicon master can be reused in forthcoming stamps fabrication. Thus, the chip has to be cleaned in a 0.2 M Tetra-n-butylammonium fluoride (TBAF, Sigma) solution in Dimethyl Sulfoxide (DMSO, Sigma) overnight. Then, the chip is sonicated (immersed in the solution TBAF:DMSO) in an ultrasonic bath (Ultrasonicator - Selecta 3000683) to release possible stuck PDMS rests. Finally, the silicon master is cleaned with DI water and dried with N₂.

5.2.3 Characterization of the TFM

The whole fabrication process was characterized in order to verify the perfect completion of each fabrication stage.

As the silicon master dots features were fixed at 160 nm-diameter (ϕ), 500 nm-pith (p) and depth of 200 nm (h), the stability and the non-collapse to the ground of the PDMS nanopillars is guaranteed, as the aspect ratio (ratio between h and ϕ) was lower than the critical one (between 2 and 4)[20]. It was confirmed when a deeper ($h \sim 600$ nm) silicon master was fabricated (Figure 5.8, left), leading us to a PDMS stamp with collapsed nanopillars (Figure 5.8, right), since the aspect ratio was comprised between the critical values.

Hence, the fabricated silicon master with the proper dimensions was analysed by SEM (LEO 1530) and it was milled by FIB (Zeiss 1560XB Cross Beam, Carl Zeiss) to measure its depth (Figure 5.9), verifying its correct dimensions.

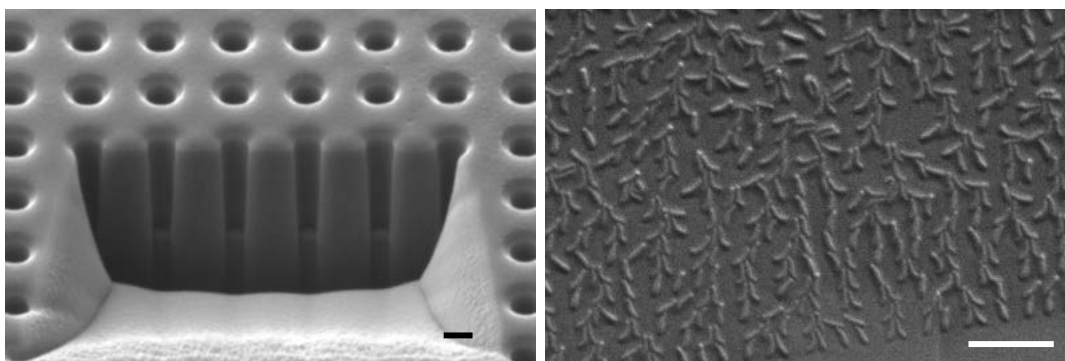


Figure 5.8. **Characterization of high aspect ratio fabrication structures.** SEM images of (left) 600 nm-deep silicon master nanomilled by FIB and (right) collapsed PDMS high aspect ratio nanopillars. Scale bar: (black) 200 nm and (white) 2 μm .

Later, the PDMS stamp was examined by SEM (Figure 5.10, left) and nanopillars height was measured by AFM (Bruker) showing a height of 126.93 nm (Figure 5.10, right). The height of the PDMS nanopillars resulted smaller than the 160 nm deep of the holes on the silicon master, probably originated by the incomplete filling of the grooves.

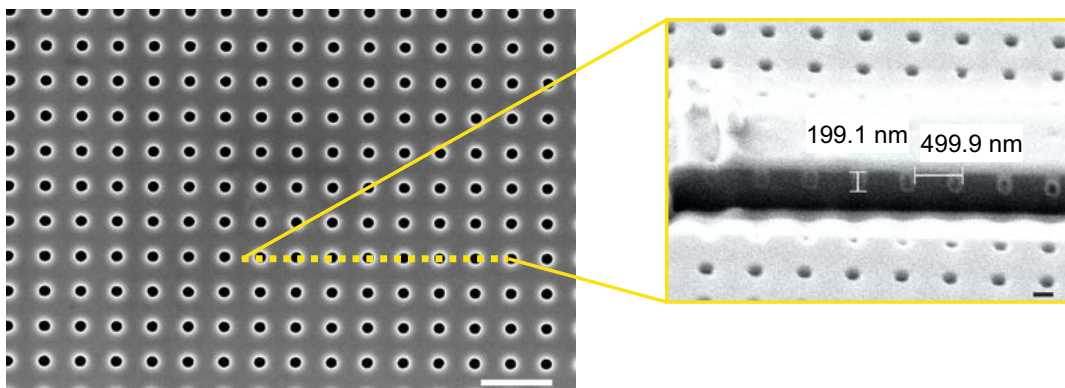


Figure 5.9. **Silicon master characterization.** SEM images of (left) a top view of the silicon mater showing the periodically spaced holes and (right) the result of FIB nanomilling of the master to measure the depth of the holes after the dry etching. Scale bar: 1 μm . Scale bar: 200 nm.

The inked nanopillars were initially stamped in a clean piece of a silicon wafer in order to check the printing of the QD. Eclipse 80i microscope (Nikon, Japan) was used to collect the fluorescence images with a Nikon Camera DXM1200F.

Printed dots with emission at $\lambda=585$ nm was observed to be correctly transferred but only in a small rectangle area of the entire matrix (Figure 5.11), even with a measurable profile of the periodicity of the pattern. Conversely, the rest of the printed matrix showed a homogeneous distribution

on the reflected intensity as seen in the margins around the rectangle of the optical image on Figure 5.11.

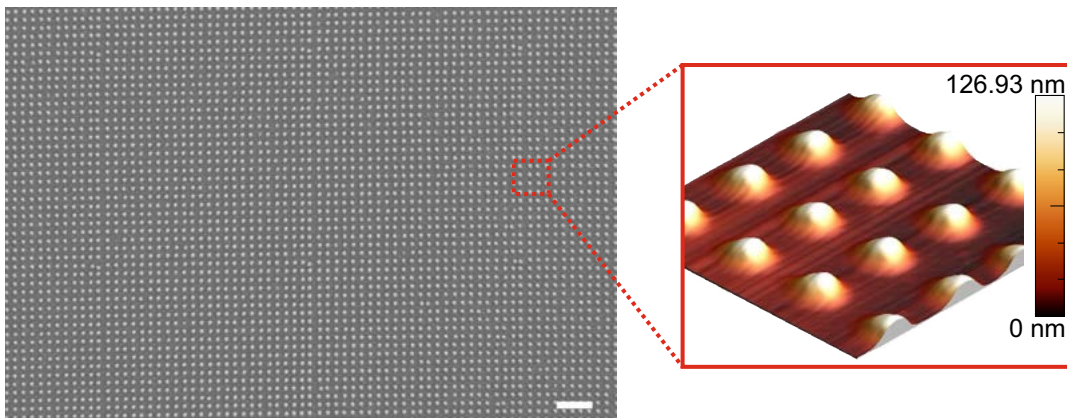


Figure 5.10. **PDMS stamp characterization.** Top SEM image of the PDMS nanopillars stamp and a zoom with an AFM measure to analyse the final vertical dimension of the pillars. Scale bar: 2 μm .

This sample was later examined by SEM, in order to analyse the aspect of the printed QD (Figure 5.12). Notably, the QD presented the periodicity raised on the fabrication however their shape did not have the expected circular geometry. On the other hand, areas with a wrong transference of the pattern presented a dirty-like stain under SEM inspection (Figure 5.13).

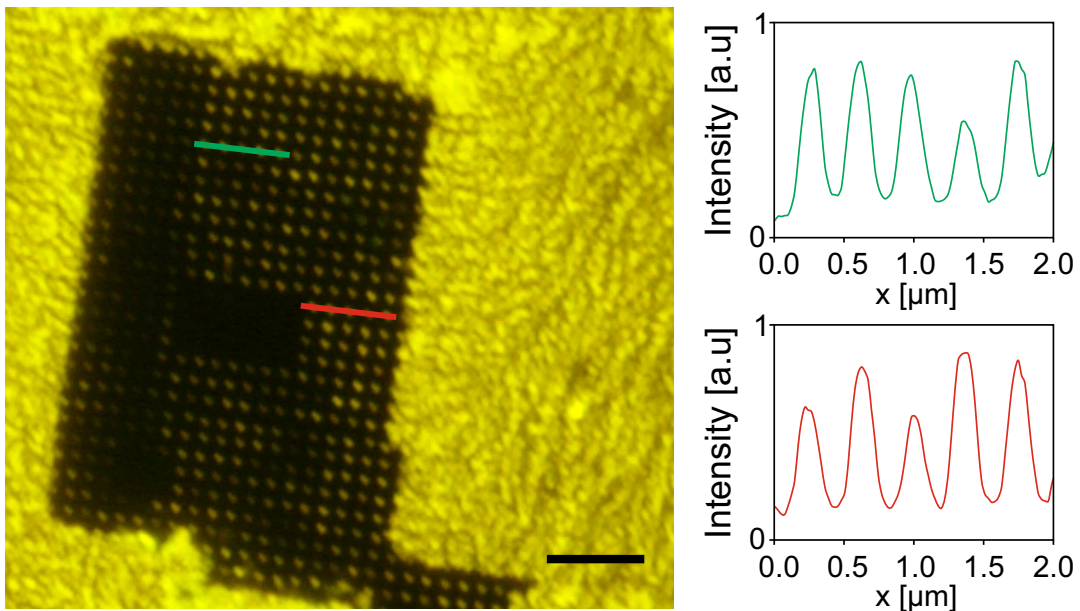


Figure 5.11. **Printed QD characterization by fluorescence microscopy.** Fluorescence optical image of the transferred pattern to a piece of silicon wafer as a substrate. Coloured marks represent the lines along the intensity profiles of the right graphs have been measured. Scale bar: 2 μm .

A second PDMS stamp fabricated and inked with QD of $\lambda=655$ nm was examined under the fluorescence microscope. In the Figure 5.14 (left), there

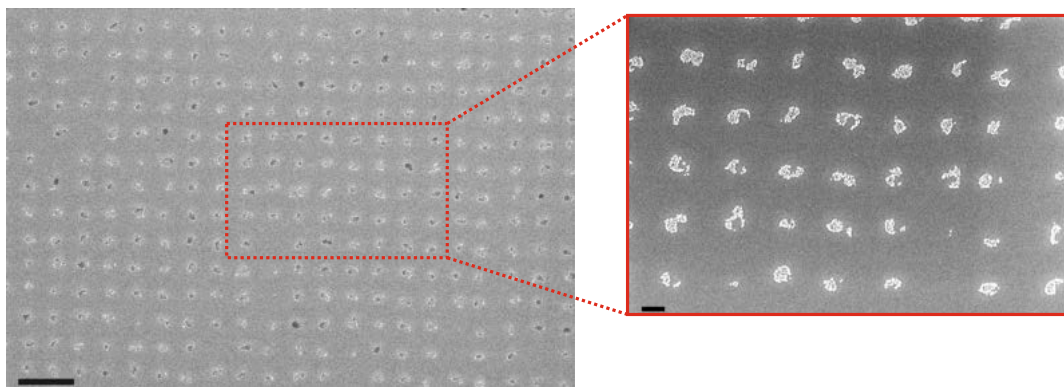


Figure 5.12. **Printed QD characterization by SEM.** SEM images of an area of the silicon substrate with transferred QD showing the periodicity of the pattern but with a non-circular shape on the spots. Scale bar: $2 \mu\text{m}$. Scale bar: 200 nm.

are cues of a pattern but it is difficult to determine the position of the dots, which does not make this stamp transference good either. Also, comparing the optical image with a SEM image of the stamp (Figure 5.14), both presented the same defect coming from a defect on the fabrication when the small matrix design is replicated.

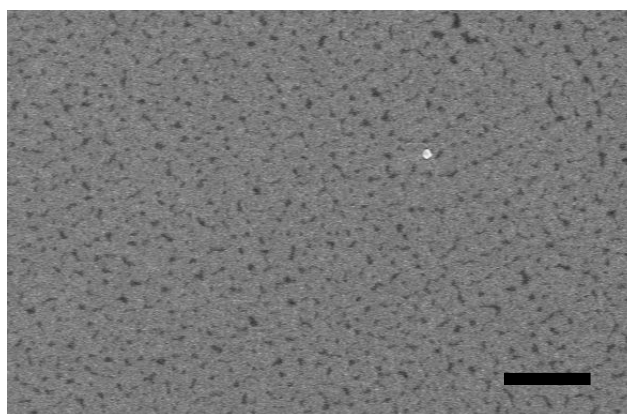


Figure 5.13. **Wrong printed QD zone characterization by SEM.** SEM image of a non-correct transference area of the periodically-spaced dots pattern. Scale bar: $2 \mu\text{m}$.

Hence, this method results technologically complex on the transference of the pattern to the substrate, since it was not possible to reproduce a large dotted area which enable its use as a TFM. Current developed tools, even if time-consuming in the fabrication of the TFM, present greater improvements as reference-free acquisition and high-resolution quantification of force fields[22]. Our TFM could be instantaneously fabricated but the development of a correct printed pattern is more a drawback than the potential advantages on the final tool compared with the state of the art. Thereby, we move to a more sophisticated 3D tool in which the highest forces that a cellular type could achieve can be quantified.

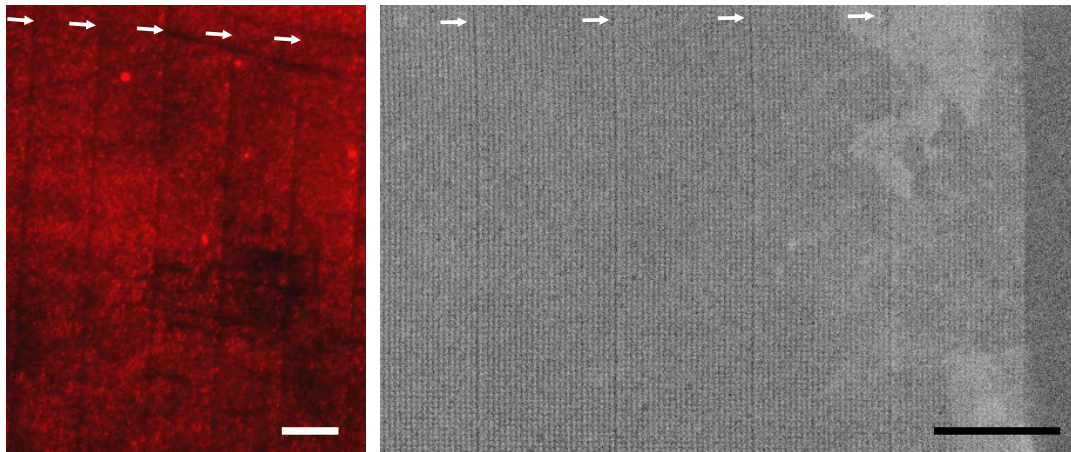


Figure 5.14. **Printed QD characterization with inked QD655.** Fluorescence image of the transferred pattern showing a non discernible profile of the dots. (Right) SEM image showing the defect on the PDMS stamp originated in the matrix replication during the EBL fabrication. Both images present this defect which is pointed with whit arrows. Scale bar: $10\ \mu\text{m}$.

5.3 Design of the silicon-pillars platforms

With the aim of quantifying cellular forces, we devised a platform with structured mushroom-shaped silicon pillars whose stalks diameter, θ , range from $25\ \text{nm}$ to $1.575\ \mu\text{m}$ in order to establish a correspondence between the stalks and the applied force, F , to shatter them (Figure 5.15). Hence, we develop an *Ultimate Traction Force* (UTF) as a direct method to determine ultimate forces based on the fracture of these nanomechanical test specimens.

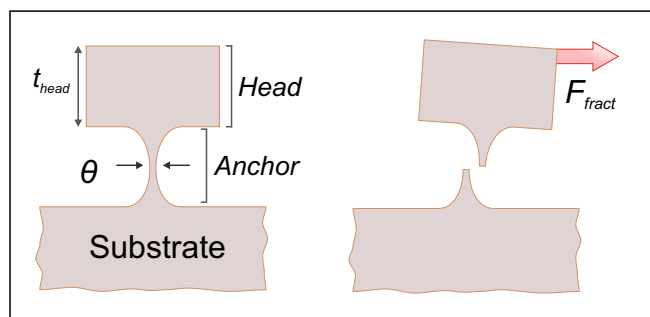


Figure 5.15. **Scheme of the designed silicon pillars relating the anchor diameter and the applied force.** Schematic of a mushroom-shaped silicon-based pillar specimen rooted on the substrate with a minimum diameter on the anchor, θ , a head with a thickness t_{head} , and the applied force needed to fracture the pillar, F_{fract} .

Compare to the previous 2D method, this new proposal is faster and simpler allowing a direct *in-situ* measurement which avoids the obtaining of the displacement field induced by the cell on a substrate and the subsequent obtaining of the force map.

The proposed test specimen consists of a two parts: a head and an anchor (stalks) (Figure 5.15). The anchor has a non-uniform cross section to control

the mechanical failure location. A transversal force, F , applied at the head of the specimen will produce the lateral bending of the structure or its fracture, when the exerted force exceeds the fracture force, F_{fract} (Figure 5.16).

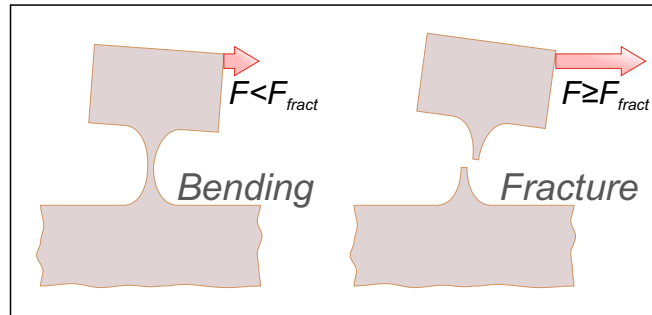


Figure 5.16. **Specimen behaviour with the magnitude of the applied force.** A lateral force, F , (left) below the force limit to fracture the specimen will bend the device and (right) over the force limit will fracture it.

During bending, the narrowest part of the anchor concentrates the maximum deformation and, hence, the maximum stress. The localization of the maximum stress defines the initial position of the fracture in the case that the value exceeds the fracture strength of the material. The control of the failure position is an important point as it reduces the dispersion of the yield strength of specimens with the same dimensions.

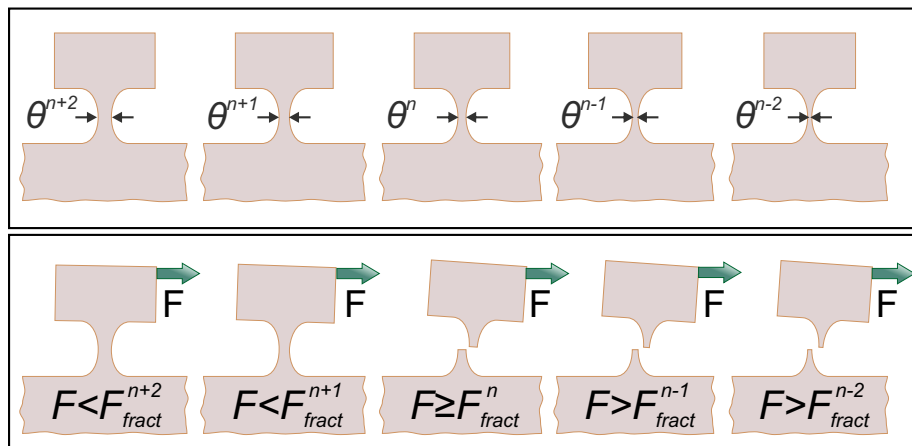


Figure 5.17. **Schematic of the pillar behaviour dependence between an applied force and the anchor size.** Specimens (top) with different θ size (bottom) bend or fracture if a given applied force, F , exceeds the fracture force limit, F_{fract} . The fractured specimen with the larger diameter, θ_n , stipulates the ultimate traction force. Specimens with larger diameter, $\theta > n$ will not fracture, and those with smaller diameter, $\theta < n$, will fracture.

For a given F , structures that differ on the size of the minimum diameter of the anchor will show different level of the maximum concentrated stresses, being larger the narrower is the diameter (Figure 5.17). In the case that concentrated stresses are larger than the fracture strength, the specimen mechanically fails. Thus, there will be a critical diameter, θ_n , so that, for the

same F , specimens with narrow diameter, $\theta \leq \theta_{n-1}$, fail and specimens with larger diameter, $\theta \leq \theta_{n+1}$, at most, will bend (Figure 5.17). The idea of this work is to design a chip consisting of a library of specimen arrays with the same θ inside each one, but with different θ among the different arrays (Figure 5.18).

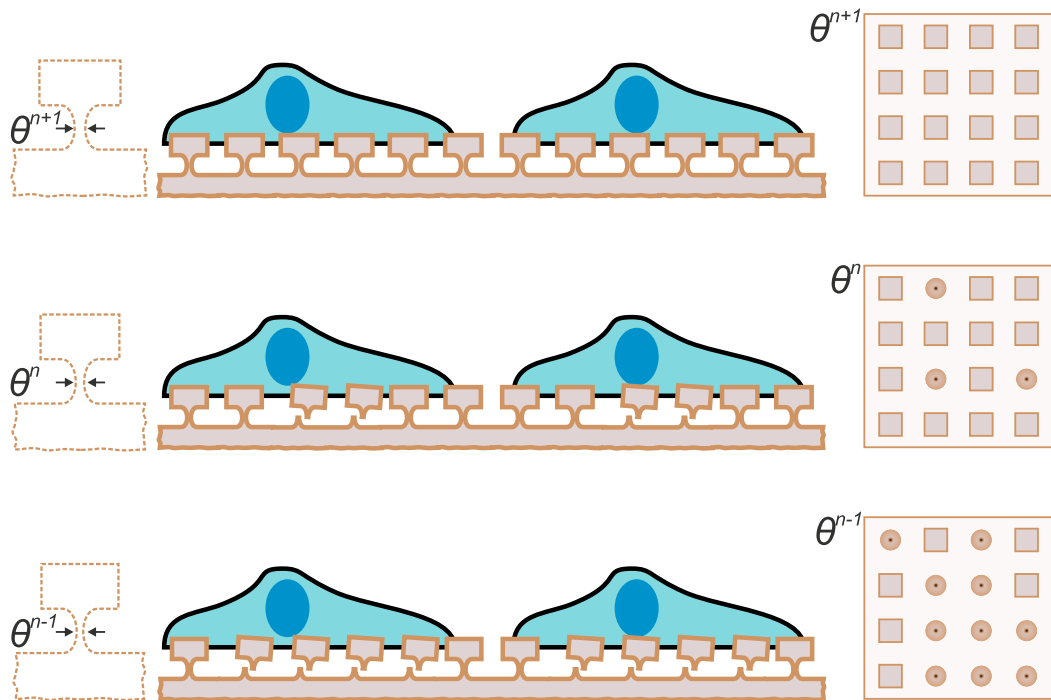


Figure 5.18. **Cell culture interaction with nanopillar chips.** Cells cultured on a matrix of identical test specimens exerting forces on the substrate. Specimens in arrays with $\theta > n$ will remain standing, in those with $\theta \leq n$ few specimens will be fractured, and in arrays with thinner diameters, $\theta < n$, many specimens will fracture, more broken structures the thinner they are.

Cells cultured on the chip exert traction forces that, if they exceed the forces that induce stresses over the fracture strength, they are able to fracture the specimen. Thus, the array with the larger θ showing fractured specimens informs about the maxim traction forces that exhibit the cultured cells (Figure 5.18).

The chip design was set up on a chessboard-like configuration (Figure 5.19a) with 8×8 quadrants in which each quadrant (Q) has pillars with different sizes at its narrowest diameter, θ . Hence, each Q was defined in the layout of the reticle as an array of squares, separated $5 \mu\text{m}$ side to side, with equal dimensions, ranging from $2.425 \mu\text{m}$ in $Q64$ to $4.000 \mu\text{m}$ in $Q1$ (Figure 5.19b). Thereby, as it will be explained later in section 5.4, the squares will act as a mask for the subsequent definition of the anchor size. A quasi-isotropic dry etching will be applied to create the anchor of the mushroom-shaped silicon pillar beneath a silicon head[23–25].

Until now, we have only discussed the influence of the diameter of the anchor of the pillars in the value of the force required for their rupture. However, there is another dimension that we can control during the fabrication that directly influences the mechanical behaviour of the specimen according to the position (r) of the applied force (F): the thickness of the head, t_{head} .

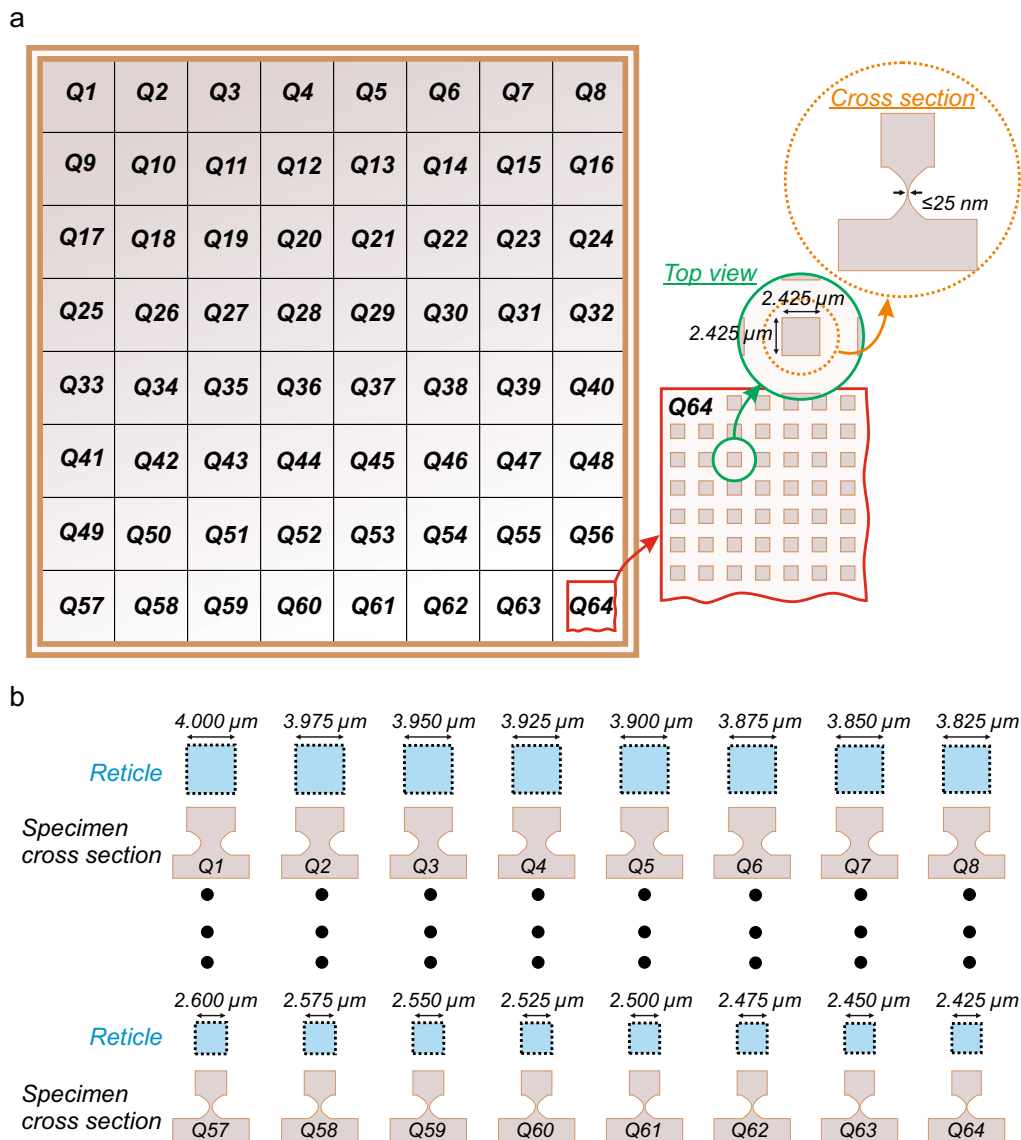


Figure 5.19. Design conception for the fabrication of an UTF with silicon chips anchored to the substrate. a) Schematic of the chip design in an 8×8 quadrant (Q) configuration, where each Q is labelled with its number in the upper left corner and has its own size for the head pillar and an anchor diameter. b) Schematic correspondence between the designed square on the layout reticle and the dimension of the specimens. Reticle squares sizes range from $2.425 \mu\text{m}$ to $4.000 \mu\text{m}$, establishing a relation with the width of the anchor.

Thus, through the use of the concept of torque or moment of force (τ), it is clear to see that larger values of t_{head} , for a given force value, always applied in the highest part of the pillar head, will facilitate the breakage of the pillar

(Figure 5.20). Therefore, it will be possible to fabricate a chip with a force catalogue where we can adjust t_{head} and θ in order to get the appropriate system.

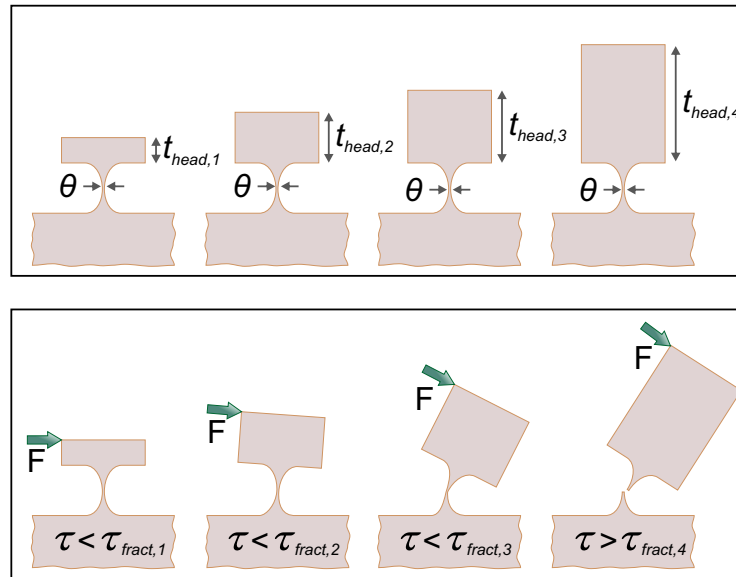


Figure 5.20. Schematic of the pillar behaviour dependence between an applied force and the size of the pillar head. For different fabricated chips, specimens (top) with different thickness of the pillar head, τ , (bottom) bend or fracture if the applied force, F , exceeds the fracture torque limit, τ_{fract} .

5.4 Technological development of a narrow anchor for the fabrication of high sensitive mechanical silicon-based platforms

Chips were fabricated using silicon-based technologies, derived from the microelectronics techniques, which offer unique capabilities in terms of the batch fabrication of millions of identical structures with submicron dimensions. Silicon presents important advantages being use as structural material, due to its excellent mechanical properties for the fabrication of mechanical sensors and actuators[26].

The first fabrication steps were designed as explained below. The initial substrates are 100-mm-diameter p-type $\langle 100 \rangle$ 500 μm -thick silicon wafers (Okmetic) (Figure 5.21a). Wafers are oxidized at 1100 $^{\circ}\text{C}$ in a wet oxygen atmosphere to grow a 1 μm -thick silicon dioxide (Figure 5.21b). A 1.2 μm -thick positive photoresist is spun onto the wafers (ma-P 6512 Micro Resist Technology) (Figure 5.21c). Then, exposure to UV light (Stepper NSR1505-G7E, Nikon) is performed through a reticule and the resist is developed and baked (30 min, 200 $^{\circ}\text{C}$) (Figure 5.21d). Next, the 1 μm -thick silicon dioxide is etched with CHF_3 (AMI etch P-5000) (Figure 5.21e). The silicon wafer is vertically etched (1-10 μm) by an anisotropic DRIE process with SF_6 and C_4F_8

gases (A-601E, Alcatel) (Figure 5.21f). After that, the photoresist is stripped by oxygen plasma (TEPLA 300 SemiAuto). Subsequently, an ozone rinse is performed (Sirius HydrOzone, Semitool), since the photoresist was previously hardened and some rests could remain on the wafer (Figure 5.21g). A 30 nm-thick silicon dioxide layer is grown (SM Furnaces LB45) to protect the walls of the head of specimens for the next silicon etching (Figure 5.21h).

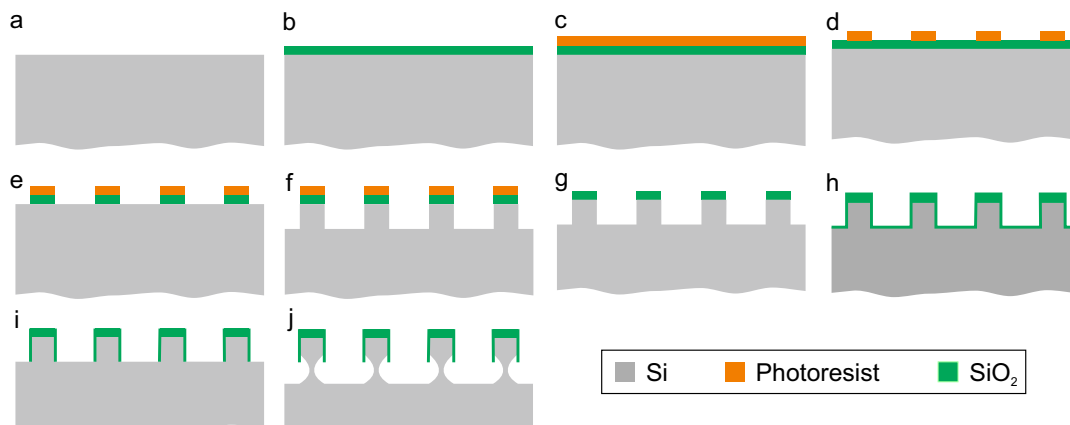


Figure 5.21. **Fabrication steps of the nanopillar chips.** a) Silicon wafer as initial substrate. b) 1 μm -thick SiO_2 wet oxidation. c) A 1.2 μm -thick photoresist is spun. d) UV photolithographic exposure is done to define the structures, and later the resist is developed and baked for 30 min at 200 $^\circ\text{C}$. e) SiO_2 layer is etched by RIE. f) Silicon is vertically etched (1-10 μm) by an anisotropic DRIE process. g) Resist is stripped. h) Silicon vertical walls are protected with a 30 nm-thick SiO_2 . i) a 30 nm-thick SiO_2 dry etching is performed. j) Silicon quasi-isotropic etching to define the underneath silicon anchors.

A 30 nm-thick silicon dioxide layer is vertically etched with CHF_3 (AMI etch P-5000) (Figure 5.21i and Figure 5.22, left). Next, silicon is partially etched with SF_6 and C_4F_8 gases (A-601E, Alcatel) using a quasi-isotropic (anisotropy ~ 0.6) process to define the anchors with a non-uniform section underneath each silicon chip (Figure 5.21j and Figure 5.22, right).

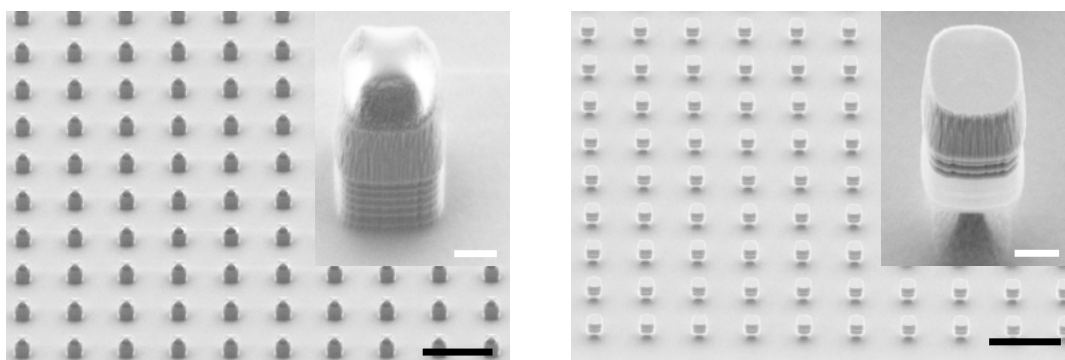


Figure 5.22. **SEM images at some steps of the fabrication.** Fabrication SEM images at wafer level of the pillars (left) after the *f*-step and (right) after the *j*-step schematized in Figure 5.21. Scale bars: (black) 10 μm and (white) 1 μm .

Now, starting from pillars as found in Figure 5.22, right, the diameter of the narrowest part of the silicon anchors is measured, in order to proceed with a sharpening of the anchors of the silicon pillars.

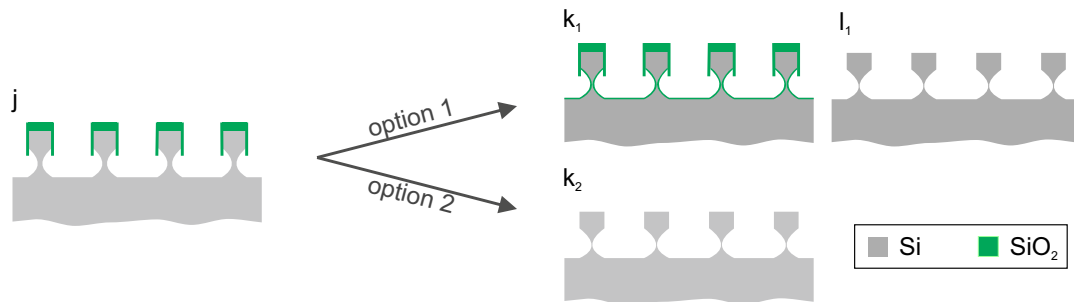


Figure 5.23. **Fabrication step options of the nanopillar sharpening.** Starting from the step Figure 5.21j, silicon pillars were sharpened by following to different fabrication options. From j), Silicon quasi-isotropic etching to define the underneath silicon anchors, two options of the sharpen step are represented. *Option 1*: k₁) dry oxidation for a first sharpening of the pillar anchors, and l₁) SiO₂ etching by HF vapours. *Option 2*: k₂) an accurate fine controlled process consisting of the use the physical component of a RIE process based in CHF₃ with a low silicon etching rate.

Initially, the sharpening process was addressed by two different options (Figure 5.23). *Option 1* consists in performing a dry oxidation of the silicon in order to reduce the silicon thickness to reach a 25 nm-diameter in the thinner one.

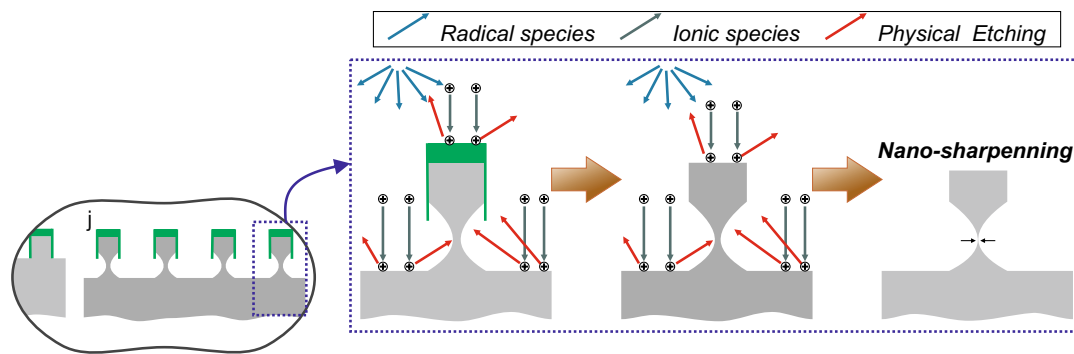


Figure 5.24. **Detail of the nano-sharpening process of the nanopillars through Option 2.** Starting from the step Figure 5.21j, silicon pillars are *nano-sharpened* with an accurate fine controlled process consisting of the use the physical component of a RIE process based in CHF₃. Moreover, the chemical component reacts with the SiO₂ layer to etch it.

Hence, considering that the 44% of the oxidation thickness is lying below the initial silicon surface and the 56% above it[27, 28], if the measured diameter of the anchored part of the smallest quadrant is θ_{Si} , then, to achieve an anchor diameter of 25 nm in this quadrant, the oxidation thickness can be established as $0.44 \cdot t_{SiO_2} = \frac{\theta_{Si}}{2} - \frac{25}{2} \text{ nm}$. Accordingly, a non-chlorinated dry oxidation with a t_{SiO_2} thickness is done (Figure 5.23k₁). Next, the wafer is diced to get the individual chips and the silicon dioxide layer is completely wet

etched by using a buffered HF-based solution (SiO-etch 6:1 SYgma Aldrich) and chip are dried with critical point dryer of CO₂ (Supercritical Automegasamdri®-915B, Series C, Tousimis) to prevent the collapse of the pillars (Figure 5.23₁).

The development of the sharpening in *Option 2* is based on an accurate mechanism of silicon etching from the physical contribution of a RIE process. The selected approach for the nano-sharpening was initially designed to etch silicon dioxide with a high selectivity versus silicon (CHF₃ gas, AMI etch P-5000), and has an extraordinary small etch-rate to silicon (40 nm/min). This small etch-rate enables a high control of the nano-sharpening with diameters of the narrow part of the anchor, θ , below 20 nm, by controlling the etching time. The process uses the ability to etch from the ions striking (physical contribution of the etching) the upper surface of the silicon wafer[29] combined with the etching of the SiO₂ (from the chemical reactions) (Figure 5.24).

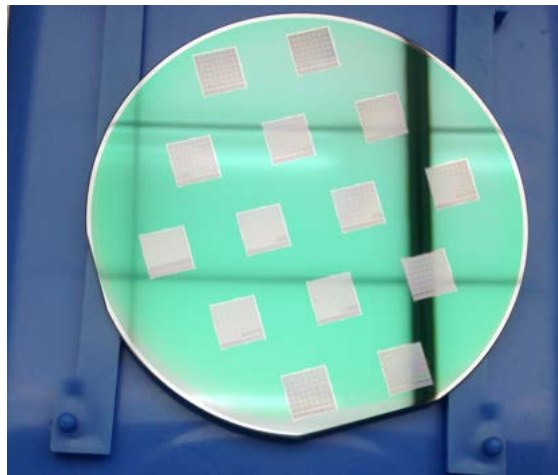


Figure 5.25. **Wafer before cutting into chips.** Image of a wafer with the squares defining the chips. Chip dimensions are 1 cm \times 1 cm.

Before this second option was implemented, the wafer was diced in chips, on one side in order to have a better control of the etching in the resulting pillar dimensions, but also to avoid cutting the wafer once pillars have already been sharpened, which is when the chips are already more fragile to handle. The appearance of the wafers before cutting them is as shown in the Figure 5.25.

5.5 Physical characterization of the silicon standing nanopillar chips

Along the fabrication process, some checkpoints were done in order to guarantee a correct fabrication of the pillars.

The fabricated devices have to be physically characterized in order to measure and assort the mean narrowest diameter of pillar anchors within

each Q . Hence, before the application of the chip to cellular forces experiments, we need to know the pillar dimensions in order to establish a force correspondence. A mean value for each Q was determined by SEM measurement of five pillars distributed in each Q (Figure 5.26). Moreover, the t_{head} was measured in various Q without significant changes along the chip. It should be noted that it is not necessary to measure the mean anchor value at all quadrants, since they are designed to have a variation of 25 nm in diameter each quadrant skip.

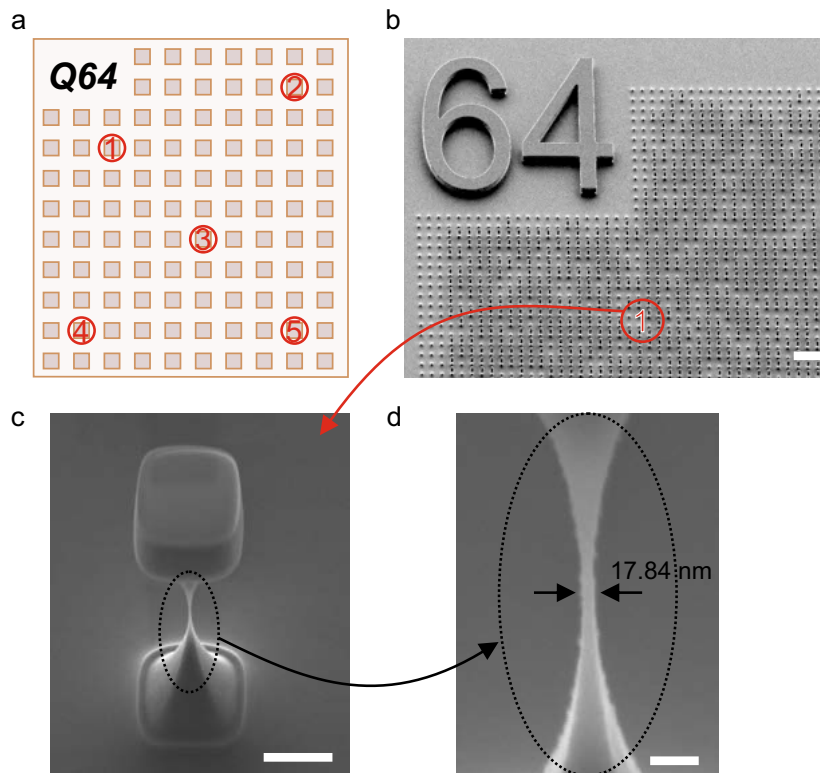


Figure 5.26. **Process to determine the mean value of the anchor diameter for every Q and chip.** a) Schematic of the complete area of the quadrant 64 and, in red, the five dispersed points where the thickness of the anchors were measured. b) SEM image of the left-upper corner of the quadrant 64 with a red circle of the zone 1 to select (c) a pillar for measuring (d) its anchor size. Scale bars: (b) 20 μm , (c) 1 μm and (d) 100 nm.

Therefore, only quadrants from the last row (from Q_{64} to Q_{57}) were measured, since the largest one will have a theoretical thickness of 200 nm at the thinnest part of the anchor. Otherwise, it could happen that the narrowest anchor does not match the last quadrant (Q_{64}) due to the fabrication process collapses this Q . Thus, the smallest diameter would be in the Q immediately above the last collapsed. This is viable because the design, and also the fabrication process, allow to always obtain a 25 nm in anchor diameter (or less) but shifted in the “chessboard”. Since the largest critical variations will occur in the largest quadrants (those having the narrowest thickness), once can consider that smallest Q (larger anchor diameter) will allow us to extrapolate in the dimensions of the successive ones adding jumps of 25 nm as designed.

We are not interested in the Q – number, but in the dimensions of the pillars. Moreover, as we will see later experimentally, and supported by the simulations, cellular forces are limited to anchor diameters not higher than 400 nm (for the range of t_{head} of the tested pillars).

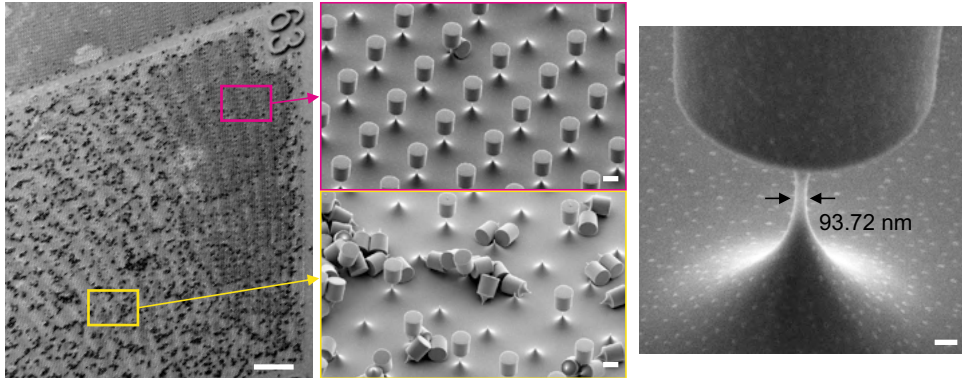
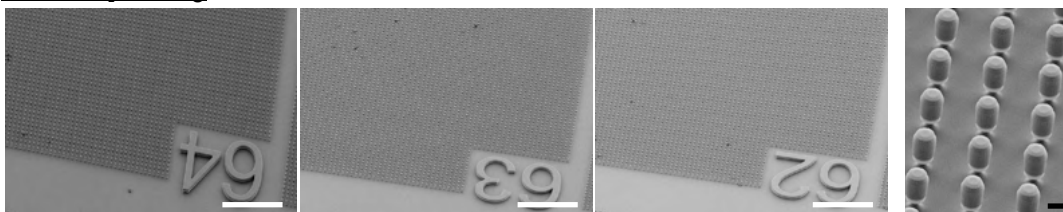


Figure 5.27. Fabricated chip through the sharpening *Option 1* method. SEM images of one fabricated chip, following the sharpening process through the silicon oxidation, after the wet etching of the SiO_2 . (Left) Q63 pillars are mostly overthrown after the wet etching (center, down) which causes the fallen pillars to form clumps. Otherwise, (center, top) the area where pillars are still standing presents (right) anchor sizes with a mean value of 93.72 nm with a deviation of 3.44 nm. Scale bars: (right) 100 μm , (center) 2 μm and (left) 200 nm.

Considering the sharpening methods explained before, SEM characterization of the devices fabricated through the *Option 1*, showed a minimum mean attainable value of 93.72 nm, with a standard deviation of 3.44 nm, for Q63, where a large part of the pillars was down during the SiO_2 wet etching process (Figure 5.27). The cap thickness was measured to have a value of 1.7 μm at this chip.

Prior SiO₂ etching



After SiO₂ etching

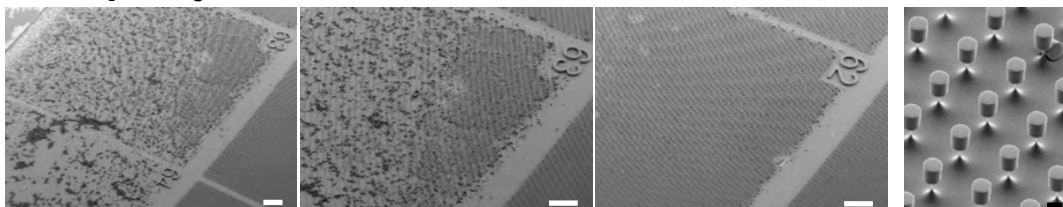


Figure 5.28. Analysis of the chip condition prior and after the SiO_2 wet etching. SEM images showing the status of the last three quadrants and a zoom of the pillars (top) before and (bottom) after SiO_2 wet etching. Scale bars: (top-white) 20 μm , (bottom-white) 100 μm and (black) 100 nm.

A comparison between the status of the chip prior and after the SiO₂ etching reflects how delicate the pillars are (Figure 5.28): Q64 resulted completely shattered, Q63 was mostly and Q62 remained standing, where pillars have a mean diameter of 122.62 nm with a deviation of 4.98 nm.

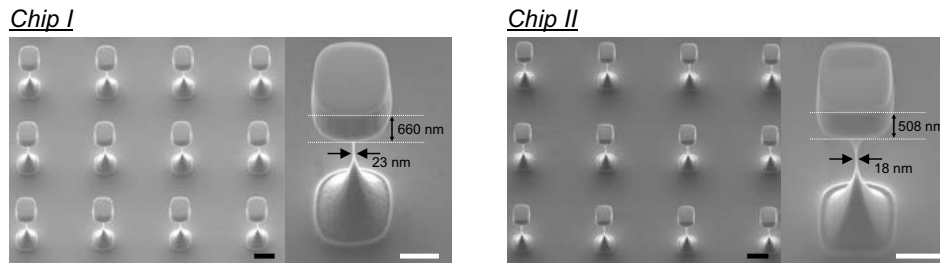


Figure 5.29. Analysis of the fabricated chips following the *Option 2*. SEM images of two fabricated chips showing the remarkable narrow diameter achieved for pillar anchors. Scale bars: (black) 2 μm and (white) 1 μm .

Moreover, even being able to reach nanometric dimensions, this sharpening method is hazardous, not only because it compromises the stability of the pillars, but also because it is not a clean method and it makes all the pillars that have fallen mess the whole chip. Otherwise, vertical walls of the pillars, which showed typical scalloping profiles of a Bosch process, presented smoother surfaces after the etching since the oxidation of the silicon soften them.

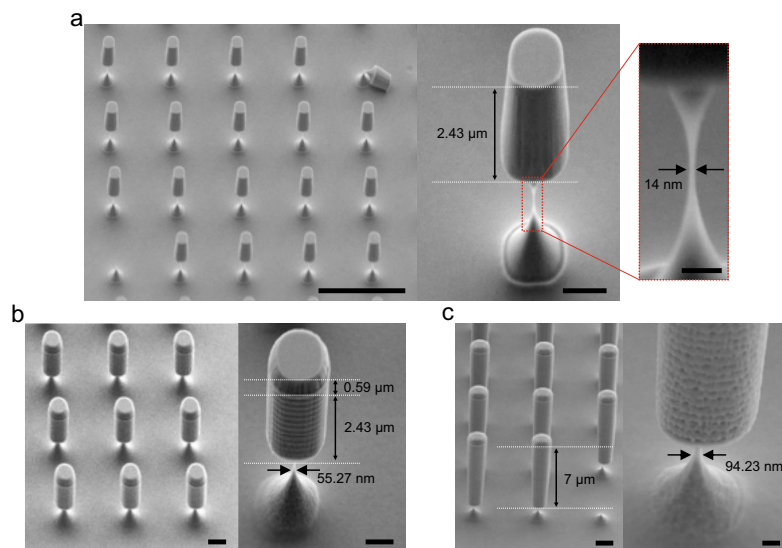


Figure 5.30. Fabricated chips with different t_{head} values following *Option 2*. a, SEM images of a chip with standing nanopillars up to 14 nm-size at the narrowest diameter of their anchors, with a t_{head} of 2.43 μm . Scale bars (from left to right): 10 μm , 1 μm and 200 nm. b, Still SEM images showing a chip where the fabricated pillars have reached a thickness value of 55.27 nm and the SiO₂ layer was not completely etched during the nano-sharpening process. The total thickness of the head is $t_{head} = t_{ox} + t_{Si} = 0.59 \mu\text{m} + 2.43 \mu\text{m} = 3.02 \mu\text{m}$. Scale bars (from left to right): 2 μm and 1 μm . c, Finally SEM images of the highest fabricated pillars with a t_{head} of 7 μm . Scale bars (from left to right): 2 μm and 300 nm

On the other hand, the physical analysis of the structures fabricated following the *Option 2* evidenced that extraordinary thin anchors could be obtained by the nano-sharpening process (Figure 5.29).

Hence, different chips with various head thicknesses were fabricated by this method, in order to produce an UTF capable to detect small fracture forces by controlling two parameters, t_{head} and θ (Figures 5.29 and 5.30). It may occur that during the nano-sharpening process the SiO_2 layer is not fully etched, as the desired diameter can be achieved before the oxide is completely consumed. This situation does not introduce a difficulty, but the SiO_2 thickness must be considered in the total thickness of the head of the pillars (Figure 5.30b). Additionally, when the nano-sharpening etching is needed to be longer in time in order to achieve a narrow anchor, the lateral dimensions of the pillar heads are also being reduced from the physical etching, as can be clearly observed in Figure 5.30a.

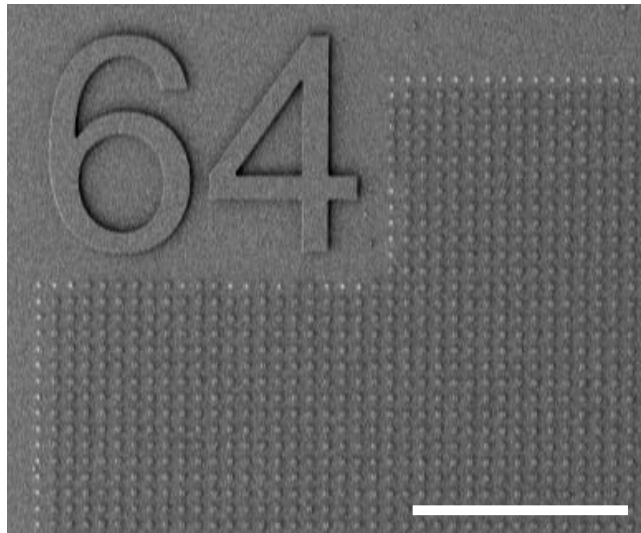


Figure 5.31. **Q64 with fallen pillars on the edges.** SEM image of a chip where Q64 presents fallen pillars on its perimeter. These pillars act as a checkpoint of the limit of the pillars stability during the nano-sharpening process. Scale bar: 100 μm .

As seen in Figure 5.31, pillars on the perimeter of the quadrants act as checkpoints of their stability limit, where white dots represent positions where a pillar broke. Thus, this method is more delicate allowing a better and more accurate control on the size of the pillar anchors preventing whole quadrants from falling.

5.6 Mechanical experimental characterization and simulation analysis for the determination of the fracture force of the nanopillars

Following, we are describing the mechanical performance through nanoindentation equipments for the determination of the necessary forces to the

breakage of the pillars. Then, we will balance these measurements with the simulation results obtained by FEM analysis.

5.6.1 Preliminary nano-indentation analysis of pillars fracture

The experimental mechanical characterization of the specimens was performed in the *IMDEA Materials Institute* by Dr. Miguel Monclús and Dr. Jon M. Molina-Aldareguia, who lead the Micro and Nanomechanics group, specialized in the study of the mechanical behaviour of advanced structural materials from the nanoscale to the macroscale (see *Collaborations and Stays in Research Entities*).

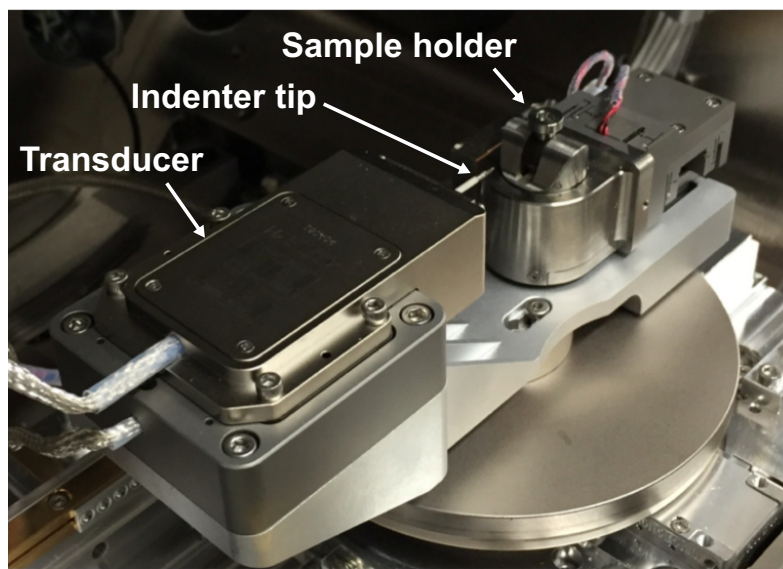


Figure 5.32. Set-up of the PI87 Picoindenter module inside the SEM chamber. The sample will be placed in the holder and the indenter tip will be approached to the pillar for the measurements.

In situ tests on the Si pillars were carried out inside the FEI Helios Nano-Lab 600i FIB FEG-SEM dual beam microscope using a PI87 Picoindenter (Hysitron Inc.). This nanoindentation system is a miniaturised test platform designed to perform quantitative micromechanical testing while simultaneously imaging with the SEM (Figure 5.32). In this system, a force is applied electrostatically, and the displacement is measured capacitively. The vacuum compatible transducer has a maximum force of 10 mN with a force resolution smaller than 1 nN and a displacement resolution below 0.05 nm. Tips with different geometries can be fitted to the instruments depending on the type of testing.

To carry out the measurements, we first cut the chip in order to have a direct access to a line of pillars to be measured (Figure 5.33). In preparation for the mechanical test, the sample with the nanopillars was placed on a holder (using silver pain) facing the indenter tip, with the indenter axis normal to the vertical wall of the pillars (Figure 5.34).

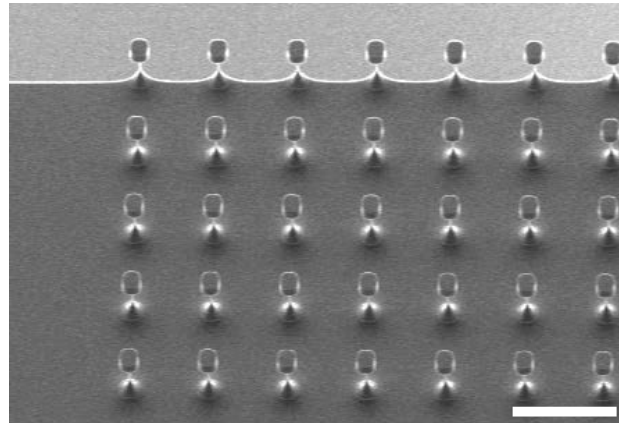


Figure 5.33. **Chip cut with a line of pillars accessible.** SEM image of the edge of a cut chip with pillars at this edge available for the mechanical study. Scale bar: 10 μm .

This initial alignment was done using the tilting and rotation movements of the sample holder. The indenter tip used for the tests was a flat punch diamond tip with a diameter of 5 μm . The tip was then manually aligned to the side of the pillar head using the X, Y and Z motion of the sample holder.

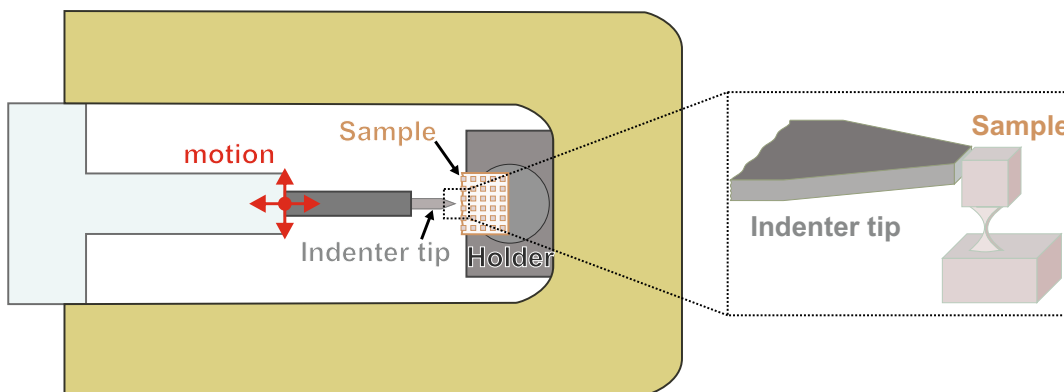


Figure 5.34. **Schematic representation of the experimental set-up using the PI-87 SEM PicoIndenter.** Representation of the set-up for the mechanics characterization where the sample is placed in the holder to induce pillars displacement through an indenter tip.

The micromechanical tests performed on the Si pillars consisted in the application of a force to the side of the pillar until its failure (Figure 5.35). As the pillars are pushed, the load-displacement curves are acquired simultaneously with the SEM imaging recording throughout the performance until the pillar fractures (Figure 5.36). The force-displacement curve measurements were carried out by the displacement control test type. First, the tip was brought into contact with the sample, and next, it was withdrawn to an adequate distance ensuring the tip was free from contact with the specimen (Figure 5.36). The transducer was then actuated under displacement control with displacement rates of 15 nm/s.

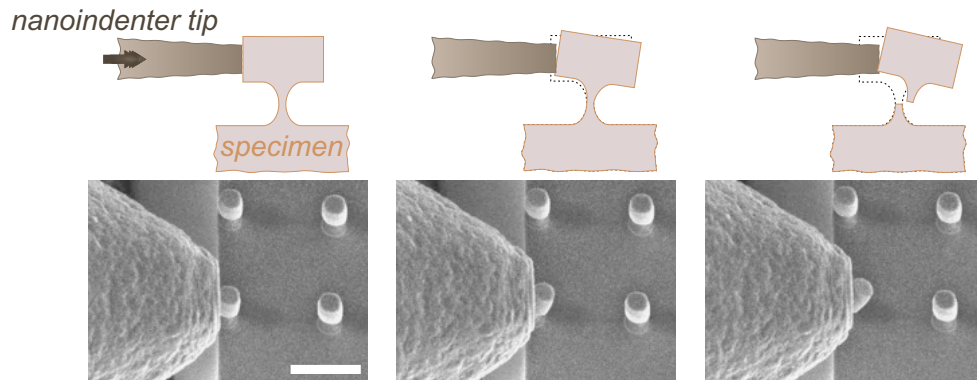


Figure 5.35. **Schematic and SEM images of the operational mode of the nanoindenter measurements.** Initially the tip is brought to the pillars head, then the probe promotes a displacement on the pillars as the force is applied, until the final breakage of the specimen. Scale bar: 5 μm .

The curve represented in Figure 5.36 shows the characteristic shape of a force-displacement curve of a pillar with $\theta \sim 100 \text{ nm}$: the loading and the unloading curves.

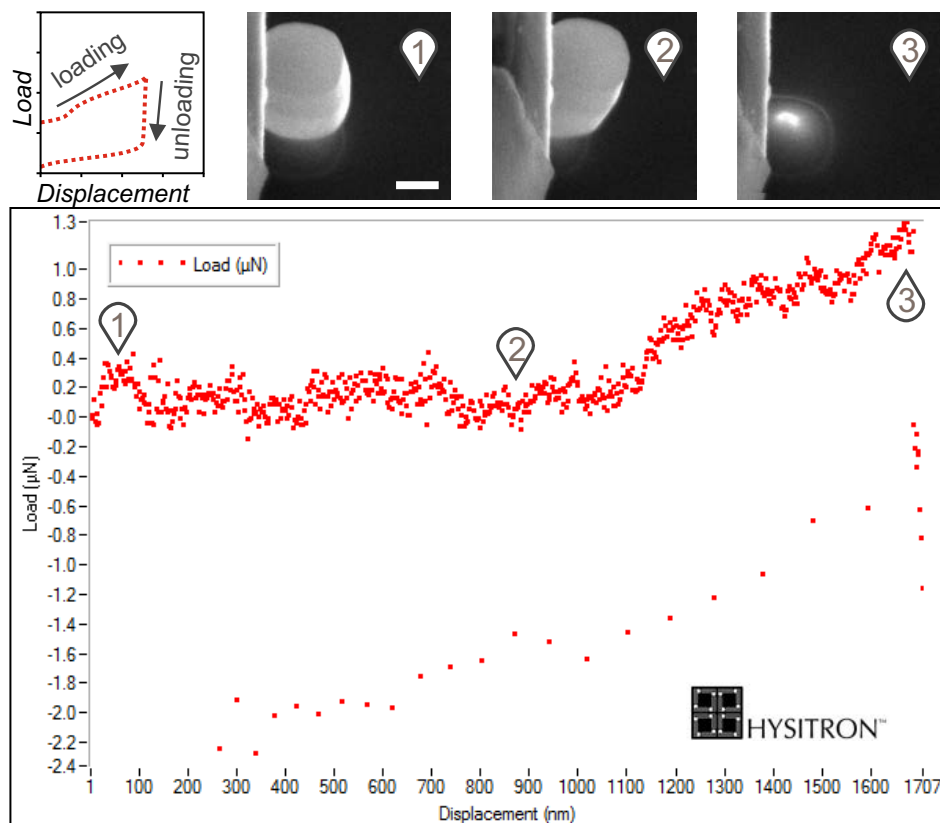


Figure 5.36. **Load-displacement curve of a tested pillar from Q62.** (Top) Scheme of a load-displacement curves and SEM images of the behaviour of the pillar at different displacement positions during (bottom) the characteristic result of the nanoindentation test where a load curve is first recorded until the breakage of the pillar when the unload curve occurs. Scale bar: 1 μm .

Initially, there is a flat lift segment which indicates the tip is out of contact with the specimen, then, the force begins to increase its values as the probe has made contact with the specimen until its failure. Finally, the tip moves back through the unloading curve (Figure 5.36).

Specimens with anchors of different diameters were tested to acquire the load-displacement curves with the aim of determining their fracture forces. Mostly, recorded curves were very noisy making highly complicated to obtain information from the measurements, mainly for thicknesses less than 100 nm, where we work on the force detection limit of the equipment (force noise floor < 400nN). Exceptional deflections of the pillars have been observed during the measurements prior to their failure, evidencing the high flexibility of silicon high-aspect-ratio nanostructures.

A clear trend between the necessary force to promote the failure of the specimens and their thicknesses is observed in Figure 5.37 where it is represented the F_{fract} for some specimens with diameters from 50 nm to 210 nm.

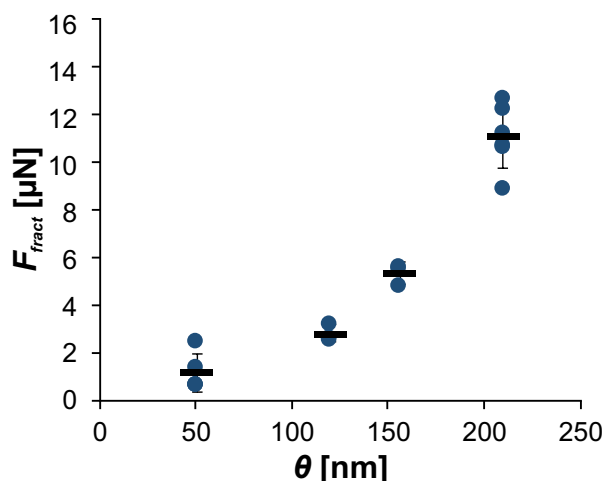


Figure 5.37. **Fracture force versus the diameter of the nanopillars.** F_{fract} obtained for different thickness of the anchor of the pillars from the load-displacement curve of the nanoindentation test. Black horizontal lines represent mean values. Error bars depict measurement standard deviation.

Despite working at the limit of the equipment for some of the test samples, fracture forces could be obtained without a large deviations. Thus, this study confirms that the design of our structure is adequate to concentrate the efforts in a specific area.

5.6.2 Theoretical analysis of the mechanical performance through FEM simulations

The pillars comprising the UTF have a very particular shape, which makes its theoretical mechanical study highly complicated, otherwise, they are designed to concentrate the maximum deformations and stresses in a specific position, the narrowest diameter of the anchors. Hence, we made use of FEM

simulation analysis to determine their deformation and to ascertain the necessary force that causes their breakage.

We addressed the mechanical analysis by simulating pillars whose anchor diameters and cap lengths correspond to those tested with the nanoindenter system. That mechanical experimental performance has revealed the extraordinary bending of the pillars prior to their failure. The theoretical ultimate silicon strength limit has been previously estimated in 21 GPa[30]. As this value is theoretical, several studies have investigated about the experimental ultimate strength of silicon specimens reporting a maximum strength from 12-18 GPa for silicon nanowires of 40-120 nm-thick[31] or 16.5 GPa for silicon nanowires of 40-140 nm-thick[32]. Thus, we will try to frame the fracture force of each tested specimen obtained experimentally with the equivalent stress (σ_{eqv}) results from the simulation.

Therefore, ANSYS Multiphysics software was used to model the specimen shapes using the 3D element, SOLID95. Physical constraints were fixed on the bottom of the substrate and the enforcement of the load was applied at the mid nodes of the lateral lines of the vertical length of the cap to mimic the nanoindenter operation (Figure 5.38).

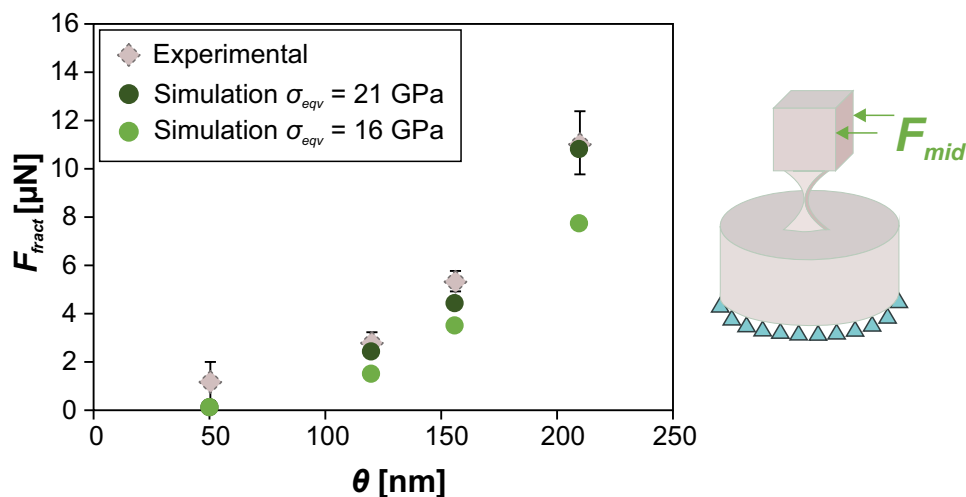


Figure 5.38. **Simulation results of the fracture force versus the diameter depending on the ultimate strength limit.** (Left) FEM simulation results of the fracture force, F_{fract} , versus the diameter of the pillar, θ , for 21 GPa and 16 GPa as equivalent stress. The experimental mean values of each pillar diameter are also represented for a better comparison. (Right) Scheme of the applied forces at the middle nodes of the vertical edges of the pillar head, and the physical constraints at the bottom of the substrate.

We carried out a simulation study of the F_{fract} , depending on the anchor size (θ), necessary to achieve the ideal ultimate silicon strength limit, namely, 21 GPa. Moreover, as we know that this value is theoretical, the forces obtained for each anchor size will represent an upper limit of the real exerted forces. Hence, we included in the study the same analysis by looking for the

forces to reach 16 GPa for the ultimate strength limit as a more realistic experimental limit. Figure 5.38 shows the simulation results of F_{fract} versus the size of the anchor, for the two different values of σ_{eqv} established.

The results obtained by the simulation show that the experimental data of the fracture force are slightly higher than the simulation predicts for an ultimate strength of 21 GPa. The differences between the results of the measurements and those of the simulations are justified from different aspects. On the one hand, the complexity in the shape of the specimens makes difficult to replicate their experimental geometry strictly for simulation. Moreover, second order effects, as the surface defects or the dependence of the size with the Young's Modulus, have not been considered. Thereby, there may exist differences between the experimental and the simulated specimen. On the other hand, the experimental measurement of force by the nanoindenter system undergo some conditions that cannot be precisely controlled, such as the positioning of the tip to apply the force in a specific position, and that this position remains throughout the measurement until the breakage. In this sense, we considered three different force application points (top, middle and bottom of the cap of the specimen), and we simulate the fracture of the specimens to find the necessary force to reach the experimental ultimate strength limit (16 GPa) (Figure 5.39).

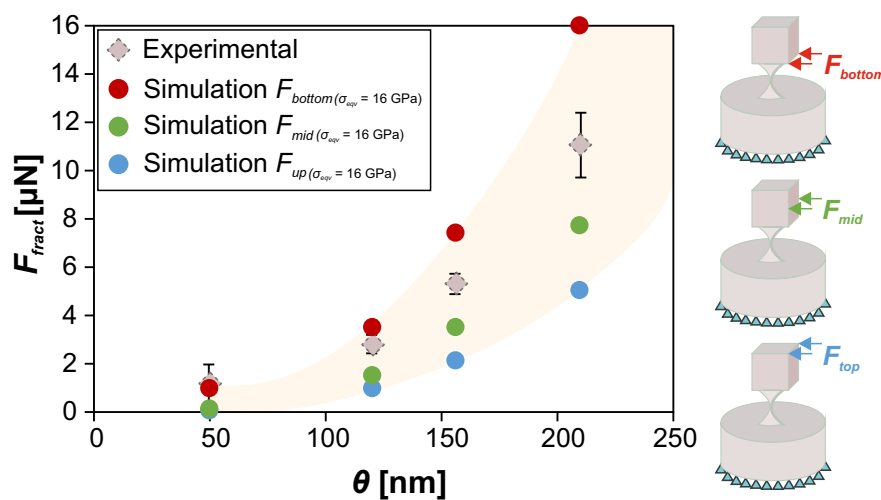


Figure 5.39. **Simulation results of the fracture force versus the diameter for multiple force application positions.** (Left) FEM simulation results of the fracture force, F_{fract} , versus the diameter of the pillar, θ , for $\sigma_{eqv} = 16$ GPa and different force application positions. The experimental mean values of each pillar diameter are also represented for a better comparison, and a confident area (in shadow). (Right) Scheme of the position of applied forces (top, middle and bottom of the cap of the specimen) and physical constrains at the bottom of the substrate.

It is remarkable the dependence between F_{fract} and the point of application of this force. Thus, we have built a confidence area enclosing the applied force (shadow area in Figure 5.39), where higher differences occur for thicker anchors. Despite the uncertainties in the mechanical characterization

of the fracture forces through the nanoindentation test, the simulation results showed that these measures are properly framed.

5.7 Biological application: preliminary results of the cell force measurements

Here we show the applicability of the UTF as a tool for cell force measurements, with the future purpose of discriminating different cell lines according to the force they are able to exert.

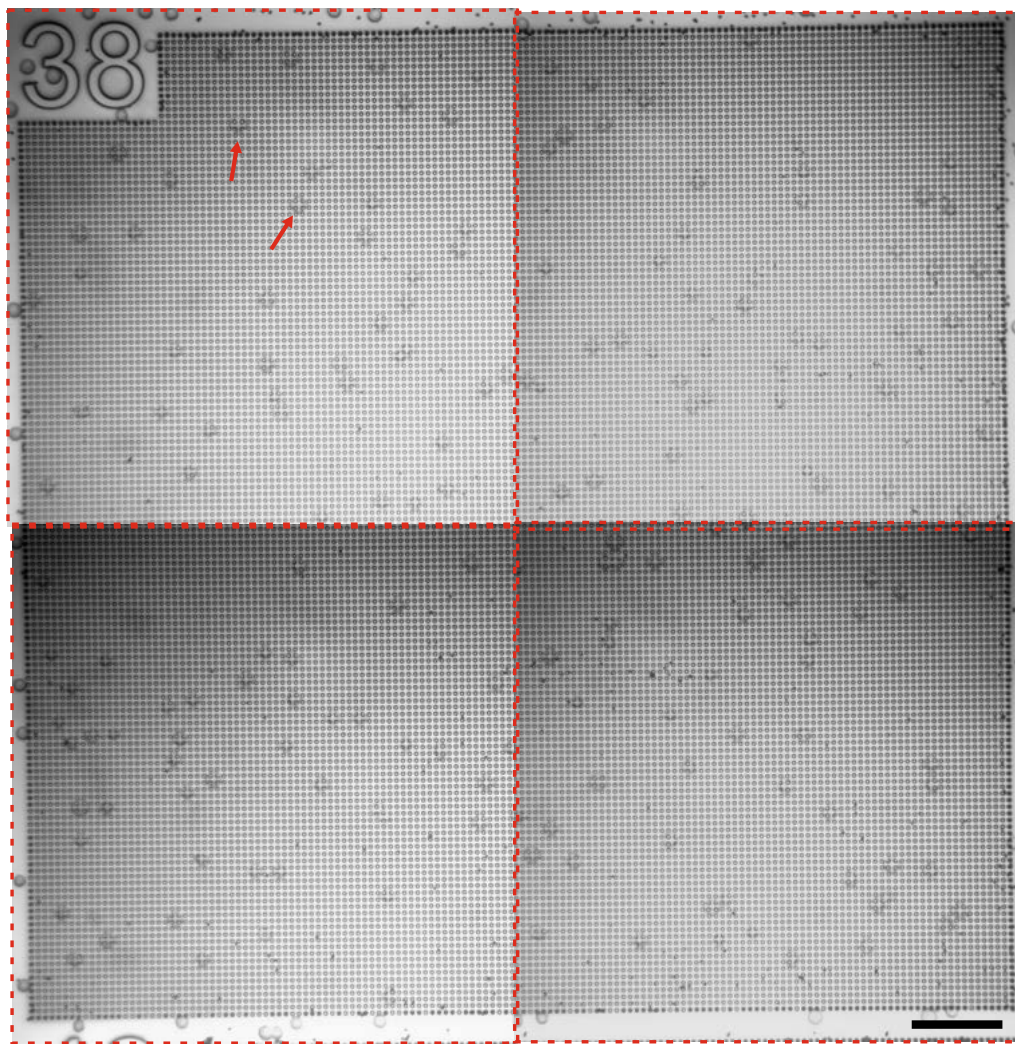


Figure 5.40. **Optical images conforming a quadrant after cells seeding.** State of the quadrant Q38 following cells seeding on a chip. Four images were taken to build the whole quadrant at $t = 0$ to ensure comparison with later times. Bright circles are standing pillars while the dark ones are the anchors after pillars breakage. Red arrows point to two examples of round cells. Scale bar: $100 \mu\text{m}$.

All the biological experiments were carried out in partnership with the group headed by Dr. Teresa Suarez from 3D LAB Development, Differentiation & Degeneration group at the *Centro de Investigaciones Biológicas Margarita*

Salas (CIB, CSIC) (see *Collaborations and Stays in Research Entities*). As it has been strongly tested along this thesis and in other reported works, silicon is a biocompatible material. Hence, we directly started by exploring the behaviour of HeLa cells when they are seeded on our silicon chips.

For that, we first sterilized the chip inside a chamber with a flow hood using flux by ultraviolet lamps for 30 minutes. Then, the chip was placed in a 35 mm-Petri dish and cells were seeded over it very delicately, as this process is critical for the stability of the structures. Immediately afterwards, the chip was inspected under a Zeiss Axioplan microscope to establish the reference at $t = 0$ of the state of the pillars, focusing the observation of the state on the pillars in the quadrants with the narrowest anchors (since these are the most fragile and could be damaged after cell seeding). Thus, several images were taken, by sweeping the quadrants of interest, with a CCD Leica DFC350 FX camera connected to the microscope using a x20 objective (Figure 5.40). It should be noted that large magnifications are not needed for the experimental performance, facilitating its implementation in any laboratory where ordinary simple microscopes are sufficient.

t [h]	0	24	48	72	96	120	144	168
$Total n_{cells}^o$	120,000	240,000	480,000	960,000	1,920,000	3,840,000	7,680,000	15,360,000
$n_{cells}^o / chip$	18,000	36,000	72,000	144,000	288,000	3,840,000	576,000	1,152,000

Table 5.1. Estimation of the number of cells in the experiment versus time.

To evaluate the interaction between cells and pillars, HeLa cells were cultured for long periods (up to 168 h) and observed under the microscope every 24 h. For that reason, to avoid the cellular crowding in the last days, the initial number of cells was fitted for the experiment, and an amount of $\sim 120,000$ HeLa cells were seeded in the 35 mm-Petri dish. Hence, considering the dimensions of the chip at ~ 12 mm per side, we can estimate that there will initially be about 18,000 cells on the chip (Table 5.1). HeLa cells population have a characteristic doubling time (dt) of 18-20 h.

The following presented results were obtained from the examination of some quadrants in the same chip, taken images every 24 h after cell seeding. In this experiment, quadrant Q42, with most of its pillars standing at $t = 0$ h (Figure 5.41), was established as the one with the narrowest anchors, since the adjacent quadrant, Q43, presented all its pillars collapsed at $t = 0$ h. The dimensions of the pillar anchors in Q42 were previously measured having a mean value of 90.39 nm (Table 5.2). During the fabrication narrower diameters were achieved in the anchors of the pillars. However, such small dimensions in the anchors of the specimens are not necessary for the cell type we analyse here, as HeLa cells exerts forces capable of fracture thicker anchors. Instead, anchors whose fracture forces are lower, namely, narrower diameters, may be required when other cell types will be tested.

In Figure 5.41 are presented some SEM images of the experimental results of the HeLa cells interaction with the quadrant Q42. Initially, Q42 presented

some broken pillars, originated in the manipulation of the chip for cell seeding. After 24 h, there were no clear differences in the standing pillars. This period of time seems to be the necessary for cells to adhere to the substrate (here, the silicon pillars), thus, they can properly spread and interact with pillars. After $t = 48$ h, Q42 exhibited more pillars breakage, and at $t = 72$ h pillars are broken throughout the entire quadrant.

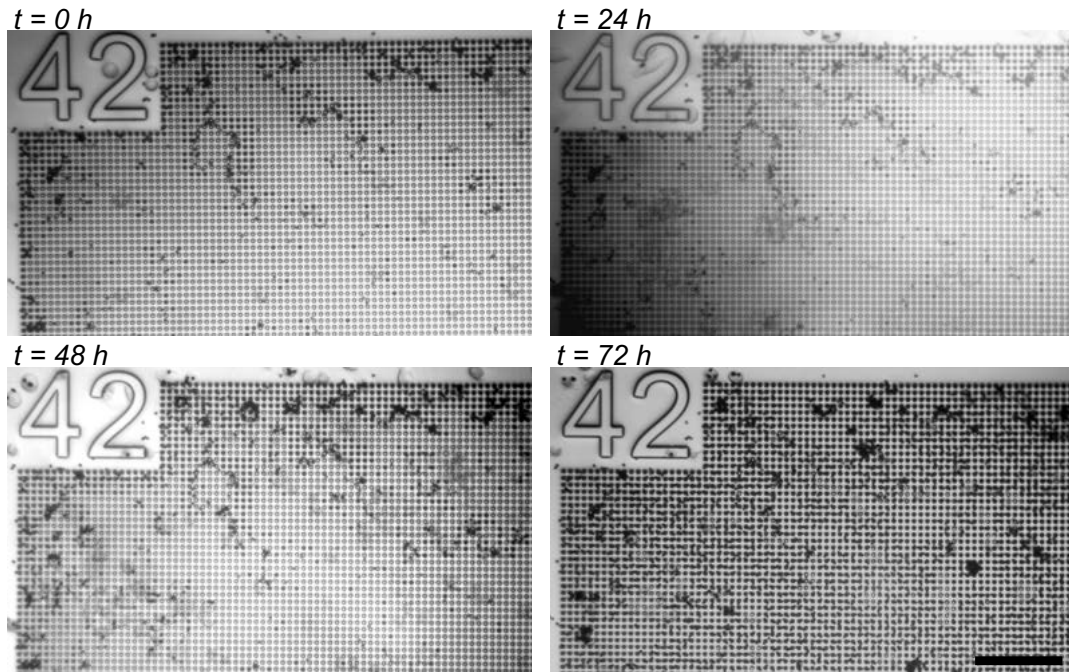


Figure 5.41. **Optical images of the quadrant Q42 over the time.** The quadrant status at $t = 0$ h with some broken pillars caused by cell seeding since the fragility of their narrow anchors. During successive days ($t = 24$ h, $t = 48$ h and $t = 72$ h), it is notorious how cells fracture the pillars, and more dark areas appeared. Scale bar: $100 \mu\text{m}$.

These results show a strong time-dependent interaction between HeLa cells and pillars with the consequence of an increase in the breakage of the pillars with time evolution and, consequently, with the number of cells (Table 5.1).

	Q42	Q41	Q40	Q39	Q38	Q37	Q36	Q35
θ [nm]	90.39	115.39	140.39	165.39	190.39	215.39	240.39	265.39
F_{fract} [μN]	0.44	0.85	1.60	2.60	3.86	5.36	7.40	10.00

Table 5.2. **Anchor size and fracture force in quadrants Q42 to Q35.**

For the determination of the F_{fract} we carried out a FEM simulation analysis as explained in the previous subsection 5.6.2. Due to the uncertainty in determining the exact point of force application, the simulation of the F_{fract} of the specimen was based on the assumption that cells will stretch from the higher part of the cap of the pillars (Figure 5.42). In this way, we are not

overestimating the exerted forces as these will be the ones with the higher momentum.

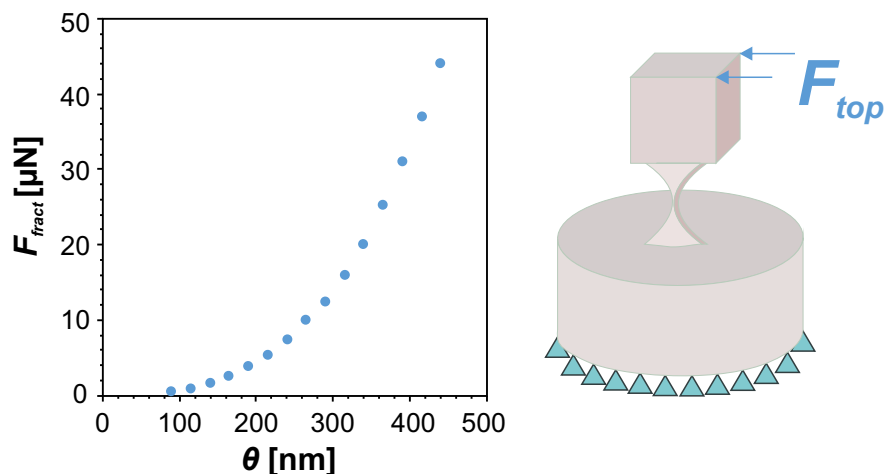


Figure 5.42. Simulated F_{fract} related to the anchor size of the pillar. (Left) FEM simulation results of the fracture force, F_{fract} , versus the diameter of the pillar, θ , for $\sigma_{eqv} = 16$ GPa, (right) considering cells over the pillars, and the force applied at the upper part of the pillar head and physical constrains at the bottom of the substrate.

Moving on to following quadrants, we can see similar results. For instance, Figure 5.43 shows images from Q35, where after 48 h, the interaction begins to translate into the failure of the pillars, as time goes by, as we saw earlier in Q42. In this case, pillars have a mean value of the anchor size of 115.39 nm (Table 5.2). Again, in this quadrant we found that cells need between 24 h and 48 h to attach properly to the substrate to attain a good contact for the interaction.

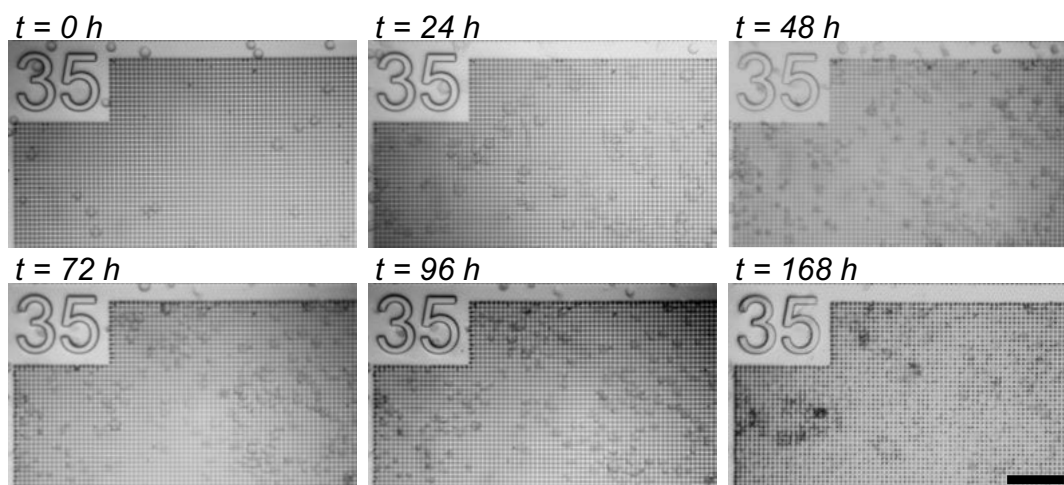


Figure 5.43. Optical images of Q35 status from $t=0$ h to $t=168$ h. Cell-pillar interactions causing the rupture of the pillars begin after 48 h, becoming more remarkable after 96 h with an evolution in the number of cells as estimated in Table 5.1. Scale bar: 100 μm .

From Table 5.2 and the results showed in Figure 5.43, it can be deduced that HeLa cells reached a maximum applied force of 10 μN , which is a higher

value than those found in the literature of pillar bending experiments, where it is reported that individual HeLa cells exert forces of up to $\sim 4 \mu\text{N}$ [10, 33].

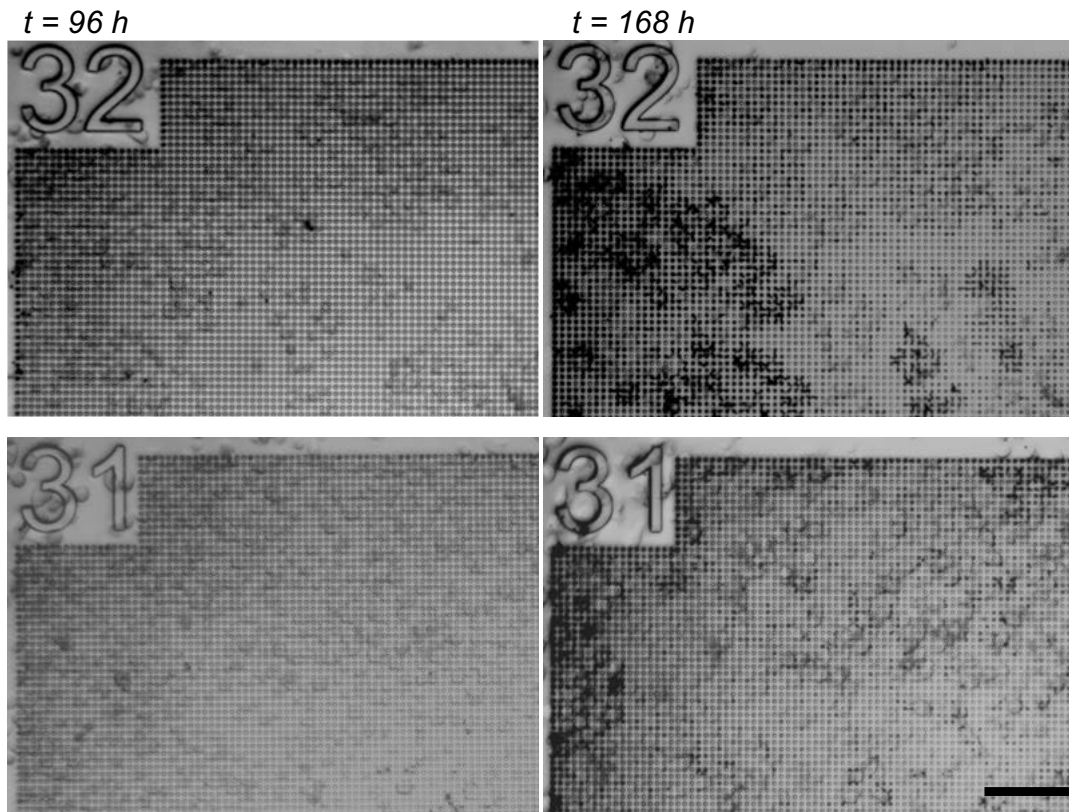


Figure 5.44. **Optical images of quadrants with thicker anchor sizes at $t=96 \text{ h}$ and $t=168 \text{ h}$.** Images shows the state of the quadrants Q32 and Q31 after at $t = 96 \text{ h}$, with all pillar standing, and at the time $t = 168 \text{ h}$, where pillars are broken, after HeLa cells interaction. Scale bar: $100 \mu\text{m}$.

To explore if higher values of forces can be reached, quadrants with pillars with thicker anchors were also examined. Quadrants Q32 and Q31 presented broken pillars between 96 h and 168 h around its perimeter and within the quadrant (Figure 5.44). The dimensions of the pillars from the quadrants Q32 and Q31 are tabulated in Table 5.3 together with the required fracture force (F_{fract}).

	Q34	Q33	Q32	Q31
θ [nm]	290.39	315.39	340.39	365.39
F_{fract} [μN]	12.30	16.00	20.00	25.20

Table 5.3. **Anchor size and fracture force in quadrants Q34 to Q31.**

Forces up to $25.20 \mu\text{N}$ are needed to fracture these pillars which is a really high value compared with the reported one[10, 33]. This leads us to consider that the forces generated after a certain time may not be originated by the interaction of a single cell, but rather are somehow cooperative or coincident forces, where several cells exert it. Thereby, these broken pillars might be the

result of the activity of many cells grouped together exerting forces on the pillars, as observed at $t = 168$ in Figure 5.43 and Figure 5.44.

Additionally, we performed a silicon stability test to prove that pillars do not break as a consequence of the silicon decomposition when the chips are immersed within the cell culture medium at 37°C. Thereby, a chip was immersed in a saline buffer medium (Dulbecco's phosphate buffered saline, Sigma) and images of the initial status of the chip quadrants were acquired by a Moticam 10+ camera connected to a Leica DM 2700M microscope with a x20/0.40 objective (Leica) (Figure 5.45).

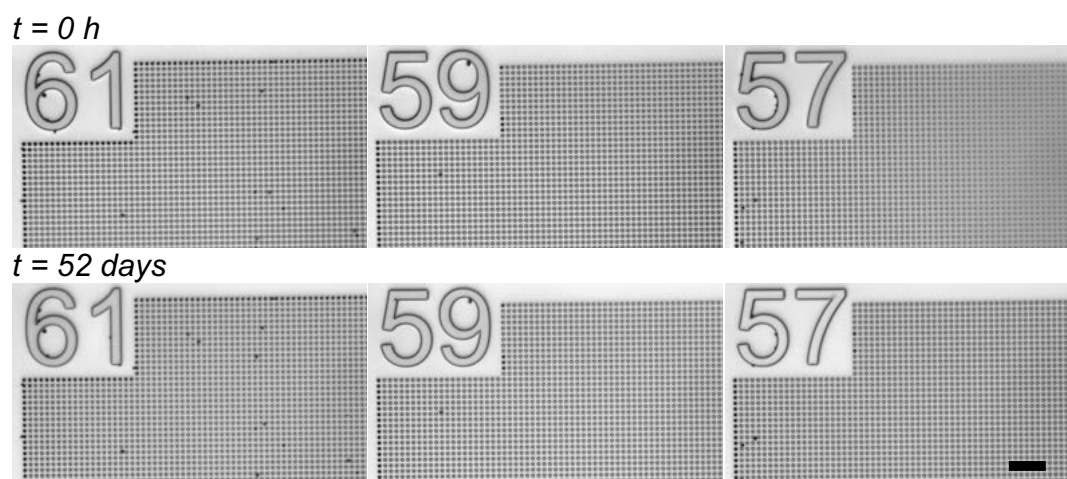


Figure 5.45. **Silicon stability test.** Optical images, at $t = 0\text{ h}$ and $t = 52\text{ days}$, of some quadrants of the chip immersed in a saline buffer medium (Dulbecco's phosphate buffered saline, Sigma) for the silicon stability test concluding that there is not effect caused by the cell culture medium on the breakage of the silicon nanopillars. Scale bar: 50 μm .

The chip was re-inspected under the optical microscope after 52 days, which is ~ 7 -fold the time-length of a cellular experiment, being possible to verify that there is no degradation of the silicon pillars causing their breakage originated by the cell culture medium during this long period (Figure 5.45).

Finally, cell-pillar interaction was examined by fixing HeLa cells with 4% PFA (Paraformaldehyde, Sigma-Aldrich). Cells were stained with anti-beta tubulin (Sigma-Aldrich), phalloidine (Thermofisher), DAPI (Sigma-Aldrich) and CD98 (Abcam) for microtubules filaments, actin filaments, nuclei and cell membrane dyeing, respectively, to observe under a Confocal Laser Microscope (CLSM, LEICA TCS SP8 STED 3X) (Figure 5.46).

Figure 5.46 shows how HeLa cells nuclei (dark blue) mould their shape according to the surrounding pillars, microtubules (green) and F-actin filaments (red) organize the cytoskeleton, and together with the cell membrane (clear blue) present larger accumulations around and over pillars in a clear sign of cell-pillar interaction.

Later, this chip was examined under a SEM. Figure 5.47 exhibits the interaction between HeLa cells and the surrounding pillars. The images show

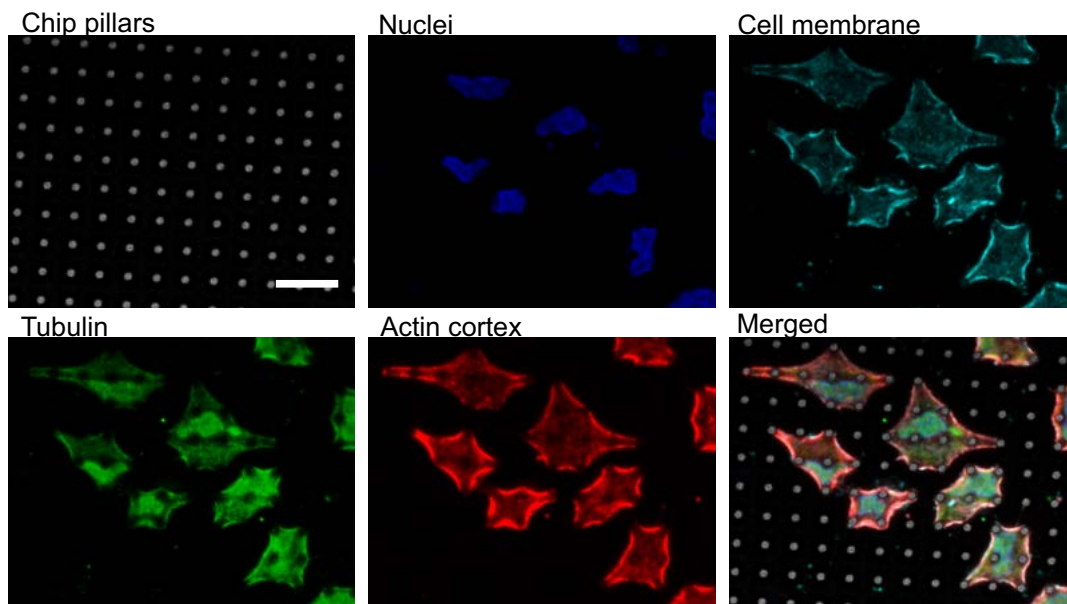


Figure 5.46. CLSM images of HeLa cells adhered to the pillars of a silicon chip. Pillars image in reflection mode and HeLa cells images in different channels showing nuclei (blue) stained with DAPI, cell membrane (clear blue) with CD98, microtubules (green) with anti-beta tubulin, and F-actin (red) with phalloidine. Finally, merged images. Scale bar: 20 μm .

how the cells envelop the pillars from below, as we already saw in the immunofluorescence images, but also how the filopodia extend to the nearest pillars gripping them from the top.

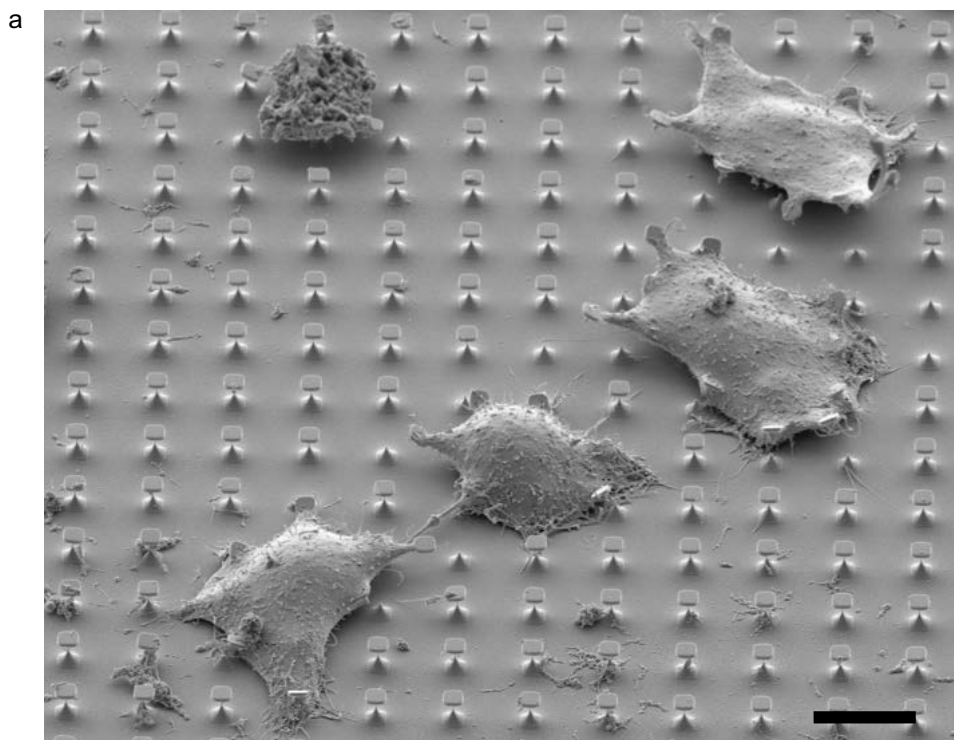


Figure 5.47

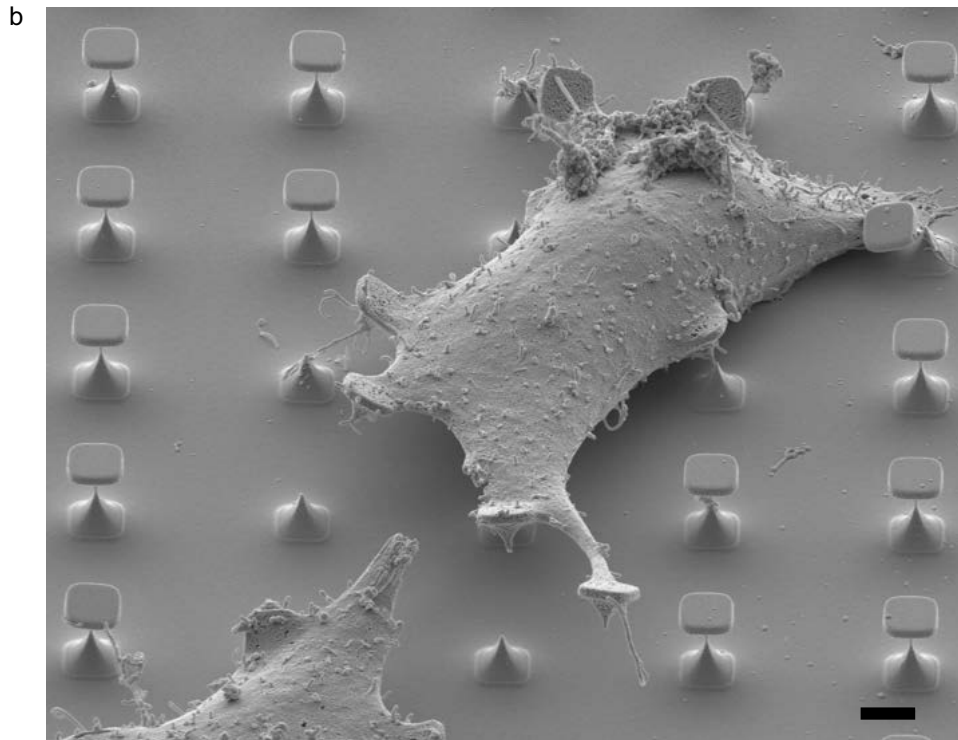


Figure 5.47. **SEM images of HeLa cells adhered to the pillars of a silicon chip.** Fixed HeLa cells interact with the pillars enveloping them completely during their migration and also by spreading the filopodia to the nearest pillars. Scale bars: (top) $10\ \mu\text{m}$ and (bottom) $2\ \mu\text{m}$.

5.8 Discussion

The investigation on the development of new methods to sense cellular forces has been the main key on this chapter. Here, we initially reported the design and fabrication of a TFM consisting of a periodically-distributed QD pattern on a soft substrate. This new system was fabricated integrating multiple laboratories techniques in order to increase the spatial resolution by decreasing the QD spot pitch. EBL was used for the fabrication of the silicon master, and stamping methods were employed to obtain the final pattern on the substrate. The operational mode of the TFM was based on the methodology of the conventional systems, where the forces exerted by living cells were calculated after measuring displacement fields[4–6]. This TFM was thought in order to represent an improvement over the fabrication process of the existing ones. However, we were technologically limited and the final QD pattern could not be obtained satisfactorily with the developed technology, since, during the printing step, the pattern could not be transferred. Then, we decided to develop a new cell force sensing system.

From the motivation to develop systems enabling cellular interaction for cell mechanics study, we developed the UTF chip. This highly sophisticated device was designed to sense the ultimate force exerted by living cells, enabling the elaboration of a force catalogue for different cell lines. The fabrication was carried out through top-down microelectronic techniques. The system consists in a silicon device with chips anchored to the substrate by nanosharpened stalk that will break to detect cellular traction forces. To achieve a very thin anchor, two different processes were addressed, where the nano-sharpening method, combining chemical and physical dry etching, promotes the desired dimensions through an accurate controlled process. Very delicate structures were obtained; nanometric dimensions were achieved, down to 15 nm, in the anchor size while the head of the nanopillars, and its total length, were in the range of the microns. The chessboard-like configuration can be optimized by adjusting in the design the number of the quadrants and the initial size of the squares to reach the size of the pillars to be in the range of the exerted forces of the cells to be tested.

Furthermore, a preliminary mechanical characterization of the system was performed by in situ nanoindentation tests. This analysis was highly sensitive to the position of application of the force, with a non-accurate control of this feature during the mechanical performance. Despite the system worked at the limit of its operational mode for the fracture force of pillars with the smallest anchors, a suitable relation between the experimental measurements and the simulations analysis have could be done, assuming that the ultimate strength of the pillars is close to 16 GPa.

In the study of their applicability to the force cell measurements, HeLa cells were found to be able to interact for long periods with the pillars. The HeLa cell seeding protocol was fine-tuned to achieve the appropriate conditions for cell growth during the experiments. Immunostaining after HeLa cells fixation revealed that they were firmly attached to the pillars as we

could also be observed by SEM inspection. Cells, including their nucleus, would change their shape by mimicking the devices by surrounding completely the pillars. The formability of HeLa cells complicates the analysis and, consequently, the choice of the load point for the simulation study of the failure of the pillars. Nonetheless, during FEM analysis we assumed that the forces were applied at the top of the pillars head, since at this point we are not overestimating the forces. The simulation results suggested that HeLa cells are able to achieve forces up to $10.00 \mu\text{N}$ after 48 h, and up to $25.20 \mu\text{N}$ between 96 h and 168 h after they were seeded on the chip. Partially, our results are in the range of those reported previously [10, 33]. However, the range of forces obtained at the end of the experiments, when cell crowding is high, are extremely higher, reaching $25 \mu\text{N}$, which could demonstrate that we are detecting ultimate forces. Thus, we stand that a deeper investigation on the origin of such high forces is required. Hence, whether they were forces exerted by individual cells or, conversely, they were the result from cellular collaboration must be evaluated. Besides, we have demonstrated the reliability of the chip as a tool for cell forces detection.

To evaluate the exerted forces in order to try to discriminate between the different cellular lines, other cells will be tested as MCF7, NIH-3T3 or *Dictyostelium discoideum* (Dicty). Cellular seeding conditions must be adjusted for each cellular line, and the chips to be tested will be those with pillars whose dimensions correspond to F_{fract} similar to the forces exerted by the cell line to be examined reported in the literature.

Micro- and nanofabrication technology represents an important tool for the development of new systems that allow us to study and understand the cellular response to the environment that surrounds them. Thus, topographical surfaces capable of better mimicking the natural extracellular matrix and their impact on cell behaviour are the focus of scientific research [34]. We envision that the development of ultimate force test devices will have a range of applications in fundamental cell mechanic studies, even with the potential applicability to diagnosis. Further investigation in the ultimate force of other cellular types has to be done with the target to identify different cell types and even differentiate among normal-like and cancer cells by their generated ultimate force.

Bibliography

- [1] William J Polacheck and Christopher S Chen. Measuring cell-generated forces: a guide to the available tools. *Nature methods*, 13(5):415–423, 2016.
- [2] Philipp Paulitschke, F Keber, Andrej Lebedev, Jürgen Stephan, Heribert Lorenz, Sebastian Hasselmann, Doris Heinrich, and Eva M Weig. Ultraflexible nanowire array for label-and distortion-free cellular force tracking. *Nano letters*, 19(4):2207–2214, 2018.
- [3] Ulrich S Schwarz and Jérôme RD Soiné. Traction force microscopy on soft elastic substrates: A guide to recent computational advances. *Biochimica et Biophysica Acta (BBA)-Molecular Cell Research*, 1853(11):3095–3104, 2015.
- [4] Huw Colin-York, Dilip Shrestha, James H Felce, Dominic Waithe, Emad Moeendarbary, Simon J Davis, Christian Eggeling, and Marco Fritzsche. Super-resolved traction force microscopy (stfm). *Nano letters*, 16(4):2633–2638, 2016.
- [5] Huw Colin-York, Yousef Javanmardi, Liliana Barbieri, Di Li, Kseniya Korobchevskaya, Yuting Guo, Chloe Hall, Aaron Taylor, Satya Khuon, Graham K Sheridan, et al. Spatiotemporally super-resolved volumetric traction force microscopy. *Nano letters*, 19(7):4427–4434, 2019.
- [6] Manuel Zündel, Alexander E Ehret, and Edoardo Mazza. Factors influencing the determination of cell traction forces. *PLoS One*, 12(2):e0172927, 2017.
- [7] John L Tan, Joe Tien, Dana M Pirone, Darren S Gray, Kiran Bhadriraju, and Christopher S Chen. Cells lying on a bed of microneedles: an approach to isolate mechanical force. *Proceedings of the National Academy of Sciences*, 100(4):1484–1489, 2003.
- [8] Sujin Lee, Juhee Hong, and Junghoon Lee. Cell motility regulation on a stepped micro pillar array device (smpad) with a discrete stiffness gradient. *Soft Matter*, 12(8):2325–2333, 2016.
- [9] Stuart G Higgins, Michele Becce, Alexis Belessiotis-Richards, Hyejeong Seong, Julia E Sero, and Molly M Stevens. High-aspect-ratio nanostructured surfaces as biological metamaterials. *Advanced Materials*, 32(9):1903862, 2020.
- [10] Zhou Li, Jinhui Song, Giulia Mantini, Ming-Yen Lu, Hao Fang, Christian Falconi, Lih-Juann Chen, and Zhong Lin Wang. Quantifying the traction force of a single cell by aligned silicon nanowire array. *Nano letters*, 9(10):3575–3580, 2009.
- [11] Zhen Li, Henrik Persson, Karl Adolfsson, Laura Abariute, Magnus T Borgström, Dan Hessman, Kalle Åström, Stina Oredsson, and Christelle N Prinz. Cellular traction forces: a useful parameter in cancer research. *Nanoscale*, 9(48):19039–19044, 2017.

- [12] Brendon M Baker and Christopher S Chen. Deconstructing the third dimension—how 3d culture microenvironments alter cellular cues. *Journal of cell science*, 125(13):3015–3024, 2012.
- [13] Alexander B Bloom and Muhammad H Zaman. Influence of the microenvironment on cell fate determination and migration. *Physiological genomics*, 46(9):309–314, 2014.
- [14] Kayla Duval, Hannah Grover, Li-Hsin Han, Yongchao Mou, Adrian F Pegoraro, Jeffery Fredberg, and Zi Chen. Modeling physiological events in 2d vs. 3d cell culture. *Physiology*, 32(4):266–277, 2017.
- [15] Franck Bonnier, ME Keating, Tomasz P Wrobel, Katarsyna Majzner, Malgorzata Baranska, Amaya Garcia-Munoz, Alfonso Blanco, and Hugh J Byrne. Cell viability assessment using the alamar blue assay: a comparison of 2d and 3d cell culture models. *Toxicology in vitro*, 29(1):124–131, 2015.
- [16] Robert Gauvin, Ying-Chieh Chen, Jin Woo Lee, Pranav Soman, Pinar Zorlutuna, Jason W Nichol, Hojae Bae, Shaochen Chen, and Ali Khademhosseini. Microfabrication of complex porous tissue engineering scaffolds using 3d projection stereolithography. *Biomaterials*, 33(15):3824–3834, 2012.
- [17] Huw Colin-York, Christian Eggeling, and Marco Fritzsche. Dissection of mechanical force in living cells by super-resolved traction force microscopy. *Nature protocols*, 12(4):783–796, 2017.
- [18] Benedikt Sabass, Margaret L Gardel, Clare M Waterman, and Ulrich S Schwarz. High resolution traction force microscopy based on experimental and computational advances. *Biophysical journal*, 94(1):207–220, 2008.
- [19] Bin Li, Luke Xie, Zane C Starr, Zhaochun Yang, Jeen-Shang Lin, and James H-C Wang. Development of micropost force sensor array with culture experiments for determination of cell traction forces. *Cell motility and the cytoskeleton*, 64(7):509–518, 2007.
- [20] Pere Roca-Cusachs, Félix Rico, Elena Martinez, Jordi Toret, Ramon Farré, and Daniel Navajas. Stability of microfabricated high aspect ratio structures in poly (dimethylsiloxane). *Langmuir*, 21(12):5542–5548, 2005.
- [21] Yo Tanaka, Keisuke Morishima, Tatsuya Shimizu, Akihiko Kikuchi, Masayuki Yamato, Teruo Okano, and Takehiko Kitamori. Demonstration of a pdms-based bio-microactuator using cultured cardiomyocytes to drive polymer micropillars. *Lab on a Chip*, 6(2):230–235, 2006.
- [22] Martin Bergert, Tobias Lendenmann, Manuel Zündel, Alexander E Ehret, Daniele Panozzo, Patrizia Richner, David K Kim, Stephan JP Kress, David J Norris, Olga Sorkine-Hornung, et al. Confocal reference free traction force microscopy. *Nature communications*, 7(1):1–10, 2016.

- [23] Núria Torras, Juan Pablo Agusil, Patricia Vázquez, Marta Duch, Alberto M Hernández-Pinto, Josep Samitier, Enrique J de la Rosa, Jaume Esteve, Teresa Suárez, Lluïsa Pérez-García, et al. Suspended planar-array chips for molecular multiplexing at the microscale. *Advanced Materials*, 28(7):1449–1454, 2016.
- [24] Juan Pablo Agusil, Núria Torras, Marta Duch, Jaume Esteve, Lluïsa Pérez-García, Josep Samitier, and José A Plaza. Highly anisotropic suspended planar-array chips with multidimensional sub-micrometric biomolecular patterns. *Advanced Functional Materials*, 27(13):1605912, 2017.
- [25] Carolina Vargas-Estevez, Marta Duch, Marcos Duque, Francisco Javier Del Campo, Lilian Enriquez-Barreto, Gonzalo Murillo, Núria Torras, José A Plaza, Carlos A Saura, and Jaume Esteve. Suspended silicon microphotodiodes for electrochemical and biological applications. *Small*, 13(41):1701920, 2017.
- [26] Kurt E Petersen. Silicon as a mechanical material. *Proceedings of the IEEE*, 70(5):420–457, 1982.
- [27] RYS Huang and RW Dutton. Experimental investigation and modeling of the role of extended defects during thermal oxidation. *Journal of applied physics*, 74(9):5821–5827, 1993.
- [28] Darius Andriukaitis and Romualdas Anilionis. Oxidation process and different crystallographic plane orientation dependence simulation in micro and nano scale structures. In *2007 29th International Conference on Information Technology Interfaces*, pages 573–578. IEEE, 2007.
- [29] S-B Wang and AE Wendt. Ion bombardment energy and sio₂/si fluorocarbon plasma etch selectivity. *Journal of Vacuum Science & Technology A: Vacuum, Surfaces, and Films*, 19(5):2425–2432, 2001.
- [30] SM-M Dubois, G-M Rignanese, Thomas Pardoen, and J-C Charlier. Ideal strength of silicon: An ab initio study. *Physical Review B*, 74(23):235203, 2006.
- [31] Gheorghe Stan, Sergiy Krylyuk, Albert V Davydov, and Robert F Cook. Bending manipulation and measurements of fracture strength of silicon and oxidized silicon nanowires by atomic force microscopy. *Journal of Materials Research*, 27(3):562, 2012.
- [32] S Durán, Sergi Novo, M Duch, R Gómez-Martínez, M Fernández-Regúlez, A San Paulo, C Nogués, J Esteve, E Ibañez, and JA Plaza. Silicon-nanowire based attachment of silicon chips for mouse embryo labelling. *Lab on a Chip*, 15(6):1508–1514, 2015.
- [33] Magdalini Panagiotakopoulou, Tobias Lendenmann, Francesca Michela Pramotton, Costanza Giampietro, Georgios Stefopoulos, Dimos Poulikakos, and Aldo Ferrari. Cell cycle-dependent force transmission in cancer cells. *Molecular biology of the cell*, 29(21):2528–2539, 2018.

- [34] Marziye Mirbagheri, Vahid Adibnia, Bethany R Hughes, Stephen D Waldman, Xavier Banquy, and Dae Kun Hwang. Advanced cell culture platforms: a growing quest for emulating natural tissues. *Materials Horizons*, 6(1):45–71, 2019.

Chapter 6

General conclusions and perspectives

This thesis reports on the development of different extra- or intracellular tools that act as mechanical sensors. Along this thesis, the conclusions of the developed work have been addressed at the end of each chapter. Following, I summarize the main conclusions and discuss the relevance of the obtained results within the field of the mechanical manipulation of cells and cell mechanics.

In Chapter 2, we have presented the technological development to integrate magnetic manipulation capabilities into intracellular barcode chips. CoNi barcodes were co-cultured with HeLa cells, showing that they are not compatible with cell viability. Two different technological processes for encapsulating the CoNi barcodes by a gold layer were tested. Nonetheless, these coatings were not a barrier to prevent the toxicity of the devices to HeLa cells. The continuous search for tools capable of integrating magnetic capabilities, with the quality of being biocompatible in their application in living cells, led us to look for a new material. Ni devices were successfully fabricated with electroplating techniques and later were demonstrated not to affect HeLa cells viability. Beyond the viability test, it was possible to demonstrate the performance of Ni magnetic barcodes in HeLa cell cultures for the separation of those cells that had internalized the Ni barcodes from those that had not. This proof of concept is a further step in the development of multifunctional chips which integrate multiple capabilities as a key element in field of intracellular devices. These Ni magnetic barcodes contribute to the technology development of tools that enables the mechanical manipulation of living cells, which is a requirement to better understood mechanobiology[1].

To improve the detection limit of intracellular pressure sensors previously developed by the MNTL group[2], in Chapter 3, the proposal of a new design with the challenge of the technological development of the sealing process was shown. The dare posed was to achieve a device of less than $0.5 \mu\text{m}$ -thick with an air gap in the sensing cavity and a reference cavity to correct the tilt of the device. The mechanical behaviour of the polysilicon membranes was performed with FEM simulations and compared with the analytical deformation results of the membranes. Since the cavity behaves as a Fabry-Perot resonator, the optical analysis of the reflectivity was also performed. During the fabrication processes, a great effort has been done in order to achieve the correct execution of several critical fabrication step. First, non-grainy polysilicon layers were manufactured by fitting the deposit condition of a LPCVD process. Secondly, the fabrication technology of the critical process to open the pinhole was successfully addressed by a dry etching without passivation, which cannot be removed initially and hindered the subsequent silicon oxide etching. Finally, an in-depth investigation was conducted on a hermetic sealing cap by using polymers of different viscosities. This step is crucial for the integrity of the devices, since the entry of the resist into the cavities jeopardizes the correct functioning of the sensors. In fact, the fabrication yield must be improved; a small amount of devices within a wafer were fabricated and characterized, so large batch productions remain as a future task.

Notwithstanding, the operation mode of the device was proved and some devices could be tested with a portable pressure calibration kit, by sweeping the external applied pressure, under a bright-field optical microscope. It was demonstrated that a high-sensitive cavity was obtained and measurements of pressure changes down to 25 mbar could be registered. Their application to living cells pressure change measures will be the next step, when the fabrication of the devices is reproducible and solely one sensor calibration has to be performed.

In Chapter 4, we have contributed to the characterization of the mouse embryo mechanical behaviour by the development of an intracellular nanotool capable of measure a program of mechanical changes and forces within the cytoplasm of a mouse embryo. The H-comb shape design, unlike a simple cantilever, prevents ambiguity when the device is projected in 2D, and it can be distinguished between its bending and tilt or rotation. Large batch production was successfully achieved through the fabrication techniques of the microelectronic systems. The nanodevices, after being carefully microinjected into mouse one-cell embryo, enable the study of the cytoplasm mechanical properties by tracking and measuring the changes in its deflection. H-com nanodevices measured an active program of intracellular forces and changes in cytoplasmic mechanical properties during the different stages of mouse one-cell embryo early development, suggesting that these intracellular forces and changes in cytoplasmic mechanical properties are required to complete the sequential stages of early development. This premise was proved when embryos were treated by an actomyosin inhibitor, blebbistatin, and the mechanical program of embryos was altered since nanodevices reported a reduction of the cytoplasm basal force level. Additionally, two mechanical theoretical parameters could be derived to explain the stiffness of the cytoplasm: ζ_k , to inform about the resistance to cytoplasm reorganization, and ζ_{mact} , which reports transitions in time-averaged mechanical activity.

On the other hand, the GES model, based on a gradient of effective stiffness of the embryo cytoplasm, demonstrated that universal physical laws are entirely sufficient to explain what drives some parts of one-cell development. For instance, GES model explained the pronuclear convergence during the migration phase, and for the first time it was able to predict pronuclei centering and expansion during this phase, and also the relation between intracellular particle velocity and its size.

Globally, this work presents highly relevant results for the objectives of mechanobiology[3], which are related to how physical forces and mechanical properties affect cell behaviour, development and disease. The novelty of the device in the direct measurement of the mechanical properties reveals the importance of the findings in the field compared to traditional indirect techniques. Therefore, H-comb devices motivate us in the development of tools smaller than a cell to measure intracellular forces. Thus, star-shaped devices arose as a new tool to be tested within living eukaryotic cells. These new devices were fabricated and a preliminary study on their mechanical behaviour was also conducted by FEM simulations. Star-shaped devices will explore

the idea of a silicon chip, as small as a typical eukaryotic cell, which enables the sensing of intracellular forces and mechanical changes. Hence, based on silicon micro- or nanoelectronic technologies, these devices will contribute as a new approach, within mechanobiology, from a mechanical action instead of a chemical one, and on a single cell.

In addition to the intracellular tools previously presented, we complemented cell mechanics study with the development of an extracellular tool based on intracellular anchored silicon chips. In Chapter 5, a system to determine the ultimate traction forces exerted by living cells was developed. The initial exploration was addressed by the fabrication of a system consisting of a periodically-distributed QD pattern on a soft substrate which enables to calculate the forces applied by living cells on their extracellular environment by measuring the changes on the dot positions. However, the final obtaining of the QD pattern could not be achievable as the technology limit the correct fabrication of this device. Thereby, high-aspect-ratio nanostructured silicon pillars were designed and the technological development for their fabrication was reached by investigating two different methods to sharpen the anchor of the pillars. These methods endure the fabrication of pillar anchors with nanometric dimensions, which facilitates the obtaining of structures whose fracture forces ranged from nN to μN . The mechanical characterization of the pillars was carried out by in situ nanoindentation tests. This mechanical performance was a preliminary study where to control the position of the probe was a critical feature during the test. In order to ascertain the forces needed for the pillars breakage, the nanoindentation tests were complemented with FEM simulations. The device operation mode was validated in its application to force cell measurement. 48 h after the seeding of HeLa cells on the device, forces of up to $10 \mu N$ were revealed due to the breaking of the pillars whose diameters correspond to these loads, assuming the traction is exerted in the highest part of the pillar head. Moreover, between 96 h and 168 h, forces up to $25.20 \mu N$ were registered. These unprecedented results evidence extremely high forces, which is a great contribution to the field for the characterization of cell mechanical behaviour. The main uncertainties that have to be analysed is whether the forces are exerted individually or collectively by the cells. Nevertheless, we have demonstrated the application of this original device for the measurement of cellular forces. The application of the device to test other cell lines, and even to differentiate between normal-like cells and cancer cells, is a remaining task.

Broadly, the main contribution of this thesis, from silicon micro- and nanotechnologies, has been the development of the fabrication technology to obtain new tools to face the cell mechanics study with easier or more innovative approaches. Since biology is not just chemistry, the physic of a cellular life is crucial due to, for instance, the mechanical forces has been shown to be decisive in the fate of disseminated metastatic cell[4]. Hence, the importance of determining the mechanical properties of the cell nucleus, the cytoskeleton or the cell membrane, but also to elucidate which are the mechanical cues that regulate, mediate or affect to cellular behaviour, requires the development of

biocompatible tools[5]. In this way, this work contributes to the enrichment of knowledge in the field of mechanobiology, always from a physical and technological framework, and continues opening a new application field for chips.

Bibliography

- [1] Carlos Matellan and Armando E del Río Hernández. Where no hand has gone before: probing mechanobiology at the cellular level. *ACS Biomaterials Science & Engineering*, 5(8):3703–3719, 2018.
- [2] Rodrigo Gómez-Martínez, Alberto M Hernández-Pinto, Marta Duch, Patricia Vázquez, Kirill Zinoviev, J Enrique, Jaume Esteve, Teresa Suárez, and José A Plaza. Silicon chips detect intracellular pressure changes in living cells. *Nature Nanotechnology*, 8(7):517, 2013.
- [3] Jeroen Eyckmans, Thomas Boudou, Xiang Yu, and Christopher S Chen. A hitchhiker’s guide to mechanobiology. *Developmental cell*, 21(1):35–47, 2011.
- [4] Marco Montagner and Sirio Dupont. Mechanical forces as determinants of disseminated metastatic cell fate. *Cells*, 9(1):250, 2020.
- [5] Mustafa Unal, Yunus Alapan, Hao Jia, Adrienn G Varga, Keith Angelino, Mahmut Aslan, Ismail Sayin, Chanjuan Han, Yanxia Jiang, Zhehao Zhang, et al. Micro and nano-scale technologies for cell mechanics. *Nanobiomedicine*, 1(Godište 2014):1–5, 2014.

Chapter 7

Resumen en Español

7.1 Introducción

Una célula se define como la unidad estructural y funcional de vida y establece la base para la formación de tejidos, órganos y organismos. Dado que los procesos más relevantes ocurren en su interior, existe una alta demanda en la innovación de herramientas intracelulares para aplicaciones biomédicas, bioeléctricas y/o biomecánicas.

Típicamente, el análisis celular se ha llevado a cabo a través de técnicas basadas en el análisis de poblaciones celulares, de modo que, las medidas asociadas a una célula individual se corresponden con valores promedio del conjunto de la población. Sin embargo, a lo largo de las últimas décadas se ha demostrado que las células son elementos heterogéneos dentro una misma población, es decir, células con fenotipos similares pueden reaccionar y comportarse de manera diferente ante un mismo estímulo. Por tanto, el desarrollo de nuevas herramientas para monitorizar, analizar y estudiar células individuales ha generado un gran esfuerzo en la mejora de la tecnología[1].

Dentro del campo de la microelectrónica, científicos e investigadores apuntaron que las herramientas necesarias para resolver algunos de estos interrogantes pertenecen a aplicaciones típicas del campo de los microchips. Así pues, los MEMS y NEMS (del inglés, *Microelectromechanical Systems* y *Nanoelectromechanical Systems*) abrieron un abanico de nuevas oportunidades para el control espacial y temporal del comportamiento celular, y revelaron nuevas rutas con las que afrontar la investigación biomédica y farmacéutica. Por ejemplo, la microscopía por sonda de barrido emergió como una herramienta muy interesante para la biología que permitía el escaneo de células a muy alta resolución[2–4].

A pesar de su potencial, estas herramientas presentan dimensiones mayores que el tamaño de las células y, por tanto, solo pueden estudiar el comportamiento celular desde fuera o, algunas herramientas, pueden llevar a cabo medidas intracelulares a través de métodos de punción de la membrana celular, lo que puede comprometer la viabilidad de las células. En este sentido, el grupo *Micro- and NanoTools* (MNTL) del IMB-CNM, CSIC, fue pionero a nivel mundial en el desarrollo de chips más pequeños que la escala celular. El diseño y la fabricación de nuevos dispositivos para aplicaciones relacionadas con el estudio de células individuales ha centrado el foco de trabajo del grupo permitiéndoles cimentar una base sólida, incluso acuñando dos nuevos términos en el campo: *chip-in-a-cell*[5] y *chip-on-a-cell*[6, 7].

Por consiguiente, se demostró el uso de microchips como elementos pasivos intracelulares. En particular, se han fabricado códigos de barras de silicio que han sido internalizados por macrófagos[8], de tal modo que permiten su etiquetado y rastreo. Además, se ha probado que los dispositivos basados en materiales como el silicio pueden ser internalizados por células eucariotas vivas sin interferir en su viabilidad[9]. Estas ideas exploratorias fueron la semilla de una importante línea de investigación cuyo foco es el desarrollo de MEMS y NEMS con la potencial contribución de su aplicación en el campo

de la biología, la nanobiotecnología y la nanomedicina. Así pues, desarrollar chips que combinen múltiples propiedades como tamaños inferiores al de las células, que permitan su internalización, posibilitando el estudio de poblaciones celulares y de células individuales a través de actuaciones mecánicas, bioquímicas, térmicas y/o magnéticas, presenta un alto interés científico.

Históricamente, la investigación acerca del comportamiento celular se ha abordado desde el punto de vista de la química, lo cual ha generado importantes resultados en la investigación para el desarrollo de fármacos y el progreso de la medicina[10]. Sin embargo, en las últimas décadas se está realizando un gran esfuerzo para estudiar el comportamiento mecánico de las células[11–16]. La mecánica celular es una de las líneas de investigación actuales más prometedora dentro de la biología celular[17]. Las propiedades mecánicas y el comportamiento mecánico de las células tienen un impacto relevante en las malformaciones celulares y están involucrados en múltiples enfermedades humanas como los desórdenes vasculares[18], el cáncer[19] y las afectaciones neuronales[20]. De este modo, la mecanobiología, como nexo entre la biología y la ingeniería, se ha convertido en una de las áreas de investigación emergentes que despierta mayor interés científico. Con dispositivos del campo de las micro- y nanotecnologías se contribuye al estudio de la interrelación de las fuerzas y las propiedades mecánicas de las células vivas y su función[11, 12, 21].

En este sentido, el progreso en la investigación de nuevas herramientas permitió el desarrollo (dentro del grupo MNLT) de un chip formado por dos membranas paralelas de polisilicio de 50 nm de espesor (como sensor mecánico) y un resonador óptico Fabry-Perot (como transductor). Este dispositivo, cuyas dimensiones son $6 \mu\text{m} \times 4 \mu\text{m} \times 0.4 \mu\text{m}$, fue capaz de medir cambios en la presión en el interior de una célula viva[22], y fue el origen de una nueva perspectiva en la cual el grupo MNLT avanzó hacia el diseño y la fabricación de nuevos sensores intracelulares para el estudio de la mecánica celular.

Por un lado, para cuantificar las fuerzas que producen las células durante su migración, contracción o desarrollo, las técnicas actuales están principalmente basadas en la medida de la deformación de materiales cuyas propiedades son inicialmente conocidas, como los Microscopios de Fuerza de Tracción (TFM, del inglés *Traction Force Microscopes*) o las Matrices de micropostes[23–26]. Estos sistemas consisten en un sustrato polimérico con esferas incrustadas o matrices de micropostes, normalmente fabricadas con polydimethylsiloxano (PDMS). Las células de interés se siembran sobre el dispositivo y las fuerzas ejercidas se pueden medir indirectamente a través de la medida del desplazamiento de las esferas y los micropostes en su posición. Sin embargo, estas técnicas, a pesar de ser comúnmente utilizadas, solo permiten el estudio de las células desde el exterior, proveyendo información de la interacción entre las células y el entorno que las rodea. Por otro lado, las técnicas intracelulares puede ayudar a explicar el comportamiento mecánico celular con métodos de detección directos desde el interior de las

mismas. De este modo, se han empleado herramientas basadas en técnicas ópticas y magnéticas para medir directamente las fuerzas que actúan en el interior celular[27]. Por ejemplo, herramientas como las pinzas ópticas se han utilizado en distintas investigaciones como en el estudio de la respuesta mecánica del citoesqueleto de F-actina[28] o en el análisis de las diferencias reológicas entre células sanas y células cancerosas[29], atrapando microesferas internalizadas por las células. Además, se ha estudiado el comportamiento viscoelástico del núcleo y el citoplasma con el empleo de esferas magnéticas intracelulares[30] o con nanovarillas magnéticas[31]. Otros métodos basados en la flexión de nanohilos comienzan a surgir como herramientas que permiten monitorizar fuerzas dinámicas inter- o intracelulares de manera sencilla[32]. No obstante, estos métodos normalmente ofrecen información intracelular local que tiene que ser extrapolada para alcanzar la caracterización global, y también, algunos de ellos, presentan limitaciones como el uso de láseres de alta potencia que pueden alterar la normal función celular.

Esta tesis surge del desafío que supone el desarrollo de nuevas herramientas que contribuyan al conocimiento del comportamiento mecánico celular. Los principales objetivos son el diseño, la fabricación, la caracterización y la validación intra- o extracelular de los chips para el análisis la mecánica celular. Nuestros micro- y nanochips se presentan como herramientas alternativas con las que explorar las propiedades mecánicas de las células tanto desde dentro como desde fuera de ellas.

7.2 Objetivos generales

Esta tesis presenta un carácter altamente multidisciplinar, ya que ha sido desarrollada con el principal objetivo de obtener micro- y nanoherramientas que actúen como sensores en la caracterización mecánica de células vivas. Por tanto, las tecnologías de micro- y nanofabricación, la física, la ciencia de materiales y la biología son las principales disciplinas cubiertas.

Para obtener los dispositivos presentados a lo largo de esta tesis, se ha ideado la tecnología de fabricación adecuada basada en técnicas microelectrónicas de silicio. Previamente, se ha realizado el diseño de los micro- y nanodispositivos para después fabricarlos mediante técnicas de fotolitografía y litografía por haz de electrones (EBL, del inglés *Electron Beam Lithography*). Por otro lado, se ha realizado la caracterización física de los dispositivos fabricados, tanto tras su fabricación, para validar su correcto modo de funcionamiento, como también en su aplicación en células vivas. Además, para poder realizar su función, la viabilidad celular ha sido uno de los requisitos necesarios que deben cumplir los dispositivos. Asimismo, las simulaciones basadas en el Método de Elementos Finitos (FEM, del inglés *Finite Element Method*) ha sido una tarea central en casi todos los dispositivos desarrollados, tanto en su concepción como en su aplicación experimental. Así, las micro-

y nanoherramientas fueron simuladas para verificar que los resultados experimentales se correspondían con el comportamiento esperado, siendo un método adicional para optimizar su diseño y fabricación de modo que cumplan con los requisitos tecnológicos y biológicos.

7.3 Descripción general de los capítulos

Los dispositivos presentados en esta tesis han sido concebidos con un objetivo común: su operación en el campo de la biología celular para actuar como sensores mecánicos. Cada capítulo se centra de manera independiente en la presentación de cada uno de los dispositivos desarrollados.

En el Capítulo 2 se muestra el progreso en la integración de funcionalidades magnéticas en chips intracelulares para la manipulación mecánica de células. Proponemos chips con capacidades magnéticas para la manipulación celular, combinando etiquetado y capacidades magnéticas, gracias al desarrollo de la tecnología basada en procesos fotolitográficos en combinación con métodos de galvanizado (*electroplating*) para el crecimiento de capas de cobalto/níquel (CoNi) y níquel (Ni). Se han obtenido un gran número de microcódigos de barras en suspensión tras la su liberación de la oblea mediante un proceso *ad hoc* que combina un choque térmico y un su posterior pelado. Asimismo, se ha comprobado la viabilidad celular, demostrando que los dispositivos de Ni son internalizados por las células sin interferir en su viabilidad. Finalmente, se realizó una prueba de concepto con códigos de Ni para la manipulación de células de un cultivo.

En el Capítulo 3, hemos mejorado la tecnología de un sensor de presión intracelular, anteriormente desarrollado por el grupo[22], para aumentar su límite de detección a través de procesos basados en la tecnología microelectrónica de silicio. El sensor consta de dos membranas de polisilicio paralelas separadas por un espacio de aire. Para conseguirlo, el sellado de la cavidad del sensor se tuvo que realizar a temperatura ambiente y condiciones de presión atmosférica, con un tapón de poliimida recocido tras un proceso fotolitográfico. El riesgo ante la posibilidad de que la poliimida fluya al interior de la cavidad del sensor hace que el sellado sea uno de los pasos más delicados. Además de la fabricación del sensor, se ha trabajado en el análisis mecánico del comportamiento de la cavidad gracias al uso de simulaciones FEM con las que se ha calculado la desviación de las membranas para diferentes valores de una presión externa aplicada. El funcionamiento de sensores correctamente fabricados podido ser demostrado, aunque la producción de grandes cantidades de chips es una tarea pendiente.

En el Capítulo 4 se presenta una nueva herramienta intracelular de polisilicio para la determinación de las propiedades mecánicas y el seguimiento de la fuerza en un embrión de ratón durante la primeras etapas de la fertilización. Este dispositivo tiene 22 μm de largo y 10.5 μm de ancho, y es

extremadamente delgado, tan solo 25 nm de grosor, lo que permite su flexión dentro del embrión minimizando su impacto en el citoplasma. Las cargas citoplasmáticas se han estimado midiendo la curvatura del dispositivo dentro del embrión y mediante el análisis FEM. Esta herramienta nos ha permitido llevar a cabo la caracterización mecánica del citoplasma embrionario a lo largo de las etapas iniciales de la fertilización hasta la primera división celular. Además, se ha podido concluir que el programa de fuerzas intracelulares y cambios en las propiedades mecánicas se ve alterado en embriones tratados con un inhibidor de actomiosina. Asimismo, se ha establecido un modelo mecánico del comportamiento del citoplasma durante la fase de migración de los pronúcleos.

Finalmente, el Capítulo 5 explora el desarrollo de un nuevo chip extracelular que operará como detector de la Fuerza de Tracción Máxima (UTF, del inglés *Ultimate Traction Force*) ejercida por las células vivas en su entorno extracelular. Este trabajo se inició con la fabricación de un TFM (basado en los métodos convencionales) estampando un patrón de puntos cuánticos (QD, del inglés *Quantum Dot*) en un sustrato. Este método fue ideado para optimizar los tiempos de fabricación, de modo que en un único paso de estampado se obtuviera todo el sistema TFM. Sin embargo, este objetivo no se pudo alcanzar con la tecnología de la que disponíamos y no fue posible obtener un método mejorado en comparación con los sistemas ya existentes. De este modo, basándonos en los chips intracelulares, diseñamos y fabricamos un UTF altamente sofisticado que consta de pilares de silicio en forma de seta con diferentes valores en sus diámetros de anclaje. La tecnología de micro- y nanofabricación fue la clave para el afilado de los anclajes mediante el uso de procesos de grabado seco de capas. Estos nanodispositivos fueron caracterizados mecánicamente en una prueba preliminar de nanoindentación, y se simularon mediante FEM. Así, se elaboró un catálogo con la correspondencia entre el tamaño y la fuerza de fractura de los pilares. Finalmente, se demostró la interacción entre células HeLa y los pilares de silicio, validando su funcionamiento con la medida de las fuerzas de tracción ejercidas al arrancar los chips de los anclajes al sustrato.

7.4 Conclusiones y perspectivas

Esta tesis investiga el desarrollo de diferentes herramientas extra- o intracelulares que actúan como sensores mecánicos. A lo largo de la tesis, se discute sobre el trabajo desarrollado y los resultados obtenidos en cada capítulo. A continuación, resumo las principales conclusiones, discutiendo la relevancia de los resultados obtenidos dentro del campo de la manipulación mecánica de células y la mecánica celular.

En el Capítulo 2, presentamos el desarrollo tecnológico para integrar capacidades de manipulación magnética en microcódigos de barras intracelulares. Códigos de barras de CoNi se co-cultivaron con células HeLa, demostrando que no son compatibles con la viabilidad celular. Se probaron

dos procesos tecnológicos diferentes para encapsular estos códigos de barras de CoNi mediante una capa de oro. No obstante, estos recubrimientos no llegaron a ser una barrera para prevenir la toxicidad de los dispositivos para las células HeLa. La búsqueda continua de herramientas capaces de integrar capacidades magnéticas, con la cualidad de ser biocompatibles en su aplicación en células vivas, nos llevó a buscar un nuevo material. Se fabricaron con éxito dispositivos de Ni mediante técnicas de galvanizado (*electroplating*) y se demostró que no afectaban la viabilidad de las células HeLa. Más allá de esta prueba de viabilidad, fue posible demostrar el uso de los códigos de barras magnéticos de Ni en cultivos de células HeLa para la separación de aquellas células que habían internalizado los códigos de las que no lo habían hecho. Esta prueba de concepto es un paso más en el desarrollo de chips multifuncionales que integren múltiples capacidades como elemento clave en el campo de los dispositivos intracelulares. Los códigos de barras magnéticos de Ni contribuyen al desarrollo tecnológico de herramientas que permiten la manipulación mecánica de células vivas, un requisito fundamental en el estudio de la mecanobiología[33].

Con la intención de mejorar el límite de detección de los sensores de presión intracelular desarrollados previamente por el grupo MNTL[22], en el Capítulo 3, se propone un nuevo diseño con el desafío del desarrollo tecnológico del proceso de sellado. Este reto supuso alcanzar la fabricación de un dispositivo cuyo espesor fuera menor de $0.5 \mu\text{m}$, formado por dos cavidades, una de detección, para la realización de las medidas, y otra de referencia, para corregir la inclinación del dispositivo, ambas selladas para que su interior contenga aire. El comportamiento mecánico de las membranas de polisilicio se realizó con simulaciones FEM y se comparó con los resultados analíticos de deformación de las membranas. Dado que la cavidad se comporta como un resonador Fabry-Perot, también se realizó el análisis óptico de la reflectividad. Durante los procesos de fabricación, se realizó un gran esfuerzo para lograr la correcta ejecución de varios pasos críticos en el desarrollo tecnológico. En primer lugar, las capas de polisilicio se fabricaron para conseguir membranas no granuladas, ajustando las condiciones de depósito en un proceso LPCVD. En segundo lugar, la tecnología de fabricación del proceso para abrir el orificio por el que se atacará el óxido del interior de las cavidades, se abordó con éxito mediante un grabado en seco sin productos poliméricos, que son complicados de eliminar y obstaculizan el posterior grabado de óxido de silicio. Finalmente, se llevó a cabo una investigación en profundidad sobre el uso de polímeros de diferentes viscosidades para la fabricación de un tapón hermético con el que sellar las cavidades. Este paso es crucial para la integridad de los dispositivos, ya que la entrada de la resina en las cavidades compromete el correcto funcionamiento de los sensores. A pesar de la baja productividad en la fabricación, se consiguieron obtener sensores correctamente fabricados que se caracterizaron sometidos a cambios de presión en un microscopio óptico. A través de los dispositivos se pudieron detectar cambios aplicados en la presión externa de hasta 25 mbar, alcanzando sensibilidades de 1.59 mbar/u.a. con desviaciones de ± 2.52 mbar. El

siguiente paso en esta investigación será la fabricación de dispositivos reproducibles, de modo que solo sea necesaria la calibración de un único dispositivo, y se puedan usar en la medida de los cambios de presión en el interior células vivas.

En el Capítulo 4, hemos contribuido a la caracterización del comportamiento mecánico del embrión de ratón mediante el desarrollo de una nanoherramienta intracelular capaz de medir un programa de cambios mecánicos y fuerzas dentro del citoplasma de un embrión de ratón. El diseño en forma de peine (*H-comb*), a diferencia de un voladizo simple, evita la ambigüedad cuando el dispositivo se proyecta en 2D de modo que se puede distinguir entre su flexión e inclinación o rotación. La producción de millones de dispositivos se logró de manera exitosa a través de las técnicas de fabricación de los sistemas microelectrónicos. Los nanodispositivos, después de ser cuidadosamente microinyectados en un embrión unicelular de ratón, han permitido el estudio de las propiedades mecánicas del citoplasma mediante el rastreo y la medida de los cambios en su curvatura. Los *H-comb* midieron un programa activo de fuerzas intracelulares y cambios en las propiedades mecánicas citoplasmáticas durante las diferentes etapas del desarrollo temprano del embrión de ratón, lo que sugiere que estas fuerzas intracelulares y cambios en las propiedades mecánicas citoplasmáticas son necesarias para completar las etapas secuenciales de la fase inicial del desarrollo. Esta premisa fue probada cuando, tras el tratamiento de los embriones con un inhibidor de actomiosina, la blebbistatina, el programa mecánico de los embriones se vio alterado ya que los nanodispositivos reportaron una reducción del nivel de fuerza basal del citoplasma. Además, se pudieron deducir dos parámetros mecánicos teóricos para explicar la rigidez del citoplasma: ζ_k , para informar sobre la resistencia a la reorganización del citoplasma, y ζ_{mact} , que da información sobre las transiciones en la actividad mecánica en promedio temporal.

Por otro lado, el modelo GES, basado en un gradiente de rigidez efectiva del citoplasma embrionario, demostró que las leyes físicas universales son totalmente adecuadas para explicar qué impulsa algunos procesos y etapas del desarrollo embrionario unicelular. Por ejemplo, el modelo GES explicó la convergencia pronuclear durante la fase de migración de los pronúcleos y, por primera vez, se pudo predecir el centrado y la expansión de los pronúcleos durante esta fase, así como la relación entre la velocidad de las partículas intracelulares y su tamaño.

Globalmente, este trabajo presenta resultados de gran relevancia para los objetivos de la mecanobiología[34], que se relacionan con cómo las fuerzas físicas y las propiedades mecánicas afectan al comportamiento celular, su desarrollo y a la aparición de algunas enfermedades. Este dispositivo se presenta como un método muy novedoso para la medición directa de las propiedades mecánicas, revelando la importancia de los hallazgos en el campo en comparación con las técnicas indirectas tradicionales. Por tanto, los *H-comb* suponen un estímulo para el desarrollo de nuevas herramientas,

más pequeñas que una célula, con el objetivo de medir las fuerzas intracelulares. De este modo, los dispositivos en forma de estrella surgieron como una nueva herramienta para ser probada en el interior de células vivas. Estas nuevas herramientas han sido fabricadas con éxito y, además, se han estudiado mecánicamente mediante simulaciones FEM. Los dispositivos en forma de estrella explorarán la idea de un chip de silicio, tan pequeño como una célula eucariota, que permita su el sensado de fuerzas y cambios mecánicos intracelulares. De ahí que, basándonos en las tecnologías micro- y nanoelectrónicas del silicio, el desarrollo de estos chips contribuirá con un nuevo enfoque a la mecanobiología desde una acción mecánica, en lugar de química, y actuando sobre una sola célula.

Además de las herramientas intracelulares presentadas anteriormente, hemos complementado el estudio de la mecánica celular con el desarrollo de una herramienta extracelular basada en chips intracelulares anclados al sustrato. En el Capítulo 5, se ha desarrollado un sistema para determinar las fuerzas de tracción máximas ejercidas por células vivas. La exploración inicial se abordó mediante la fabricación de un sistema formado por un patrón de QD distribuido periódicamente sobre un sustrato blando que permite calcular las fuerzas aplicadas por las células en su entorno extracelular midiendo los cambios en las posiciones de los puntos impresos. Sin embargo, la obtención final del patrón de QD no se pudo lograr ya que la tecnología disponible limita la fabricación correcta de este dispositivo. De este modo, se diseñaron pilares de silicio nanoestructurados con una alta relación de aspecto, y se alcanzó el desarrollo tecnológico para su fabricación investigando dos métodos diferentes para afilar el pie de anclaje de los pilares. Estos métodos permitieron la fabricación de pilares cuyos anclajes alcanzan dimensiones nanométricas, lo que facilita la obtención de estructuras cuyas fuerzas de fractura van desde nN a μN . La caracterización mecánica de los pilares se realizó mediante ensayos de nanoindentación in situ. Estas pruebas mecánicas se presentaron como un estudio preliminar donde el control de la posición de la sonda es un proceso crítico complicado de controlar.

Para conocer las fuerzas necesarias para la fractura de los pilares, las pruebas de nanoindentación se complementaron con simulaciones FEM. Los dispositivos fueron probados en su aplicación en la medida de las fuerzas ejercidas por células vivas, validando el modo de funcionamiento para el que fueron diseñados. Fuerzas de hasta $10 \mu N$ fueron registradas 48 h después de inicio del experimento. Estos valores de fuerza se calcularon con simulaciones FEM asumiendo que la tracción se ejerce en la parte más alta de la cabeza del pilar. Además, entre 96 h y 168 h, se registraron fuerzas de hasta $25.20 \mu N$. Estos resultados sin precedentes evidencian fuerzas extremadamente altas, lo que representa una gran contribución al campo sobre la caracterización del comportamiento mecánico celular. La principal incertidumbre que hay que analizar es si las fuerzas son ejercidas de manera individual o colectiva por las células. No obstante, hemos demostrado la aplicación de este original dispositivo para la medición de fuerzas celulares. Para completar el estudio, y con el objetivo de diferenciar entre células normales y células

cancerosas, una parte del trabajo futuro se basará en probar otras líneas celulares.

La principal contribución de la investigación desarrollada durante esta tesis está enmarcada en las micro- y nanotecnologías del silicio, a través del desarrollo de la tecnología de fabricación para la obtención de nuevos dispositivos con los que afrontar el estudio de la mecánica celular con métodos más sencillos e innovadores. Dado que la biología no se puede analizar solo desde un punto de vista químico, la física debe considerarse una herramienta fundamental con la que analizar el comportamiento celular. Se ha demostrado que las fuerzas mecánicas son decisivas en el destino de células metastásicas diseminadas[35]. De ahí la importancia de determinar las propiedades mecánicas del núcleo celular, del citoesqueleto o de la membrana celular, pero también la necesidad de dilucidar cuáles son las señales mecánicas que regulan, median o afectan el comportamiento celular, requiere el desarrollo de herramientas biocompatibles[21]. De esta manera, este trabajo contribuye al enriquecimiento del conocimiento en el campo de la mecanobiología, siempre desde un marco físico y tecnológico, abriendo un nuevo campo de aplicación para los chips.

Bibliography

- [1] Daojing Wang and Steven Bodovitz. Single cell analysis: the new frontier in 'omics'. *Trends in biotechnology*, 28(6):281–290, 2010.
- [2] Yves F Dufrêne, Toshio Ando, Ricardo Garcia, David Alsteens, David Martinez-Martin, Andreas Engel, Christoph Gerber, and Daniel J Müller. Imaging modes of atomic force microscopy for application in molecular and cell biology. *Nature nanotechnology*, 12(4):295–307, 2017.
- [3] BJ Haupt, AE Pelling, and MA Horton. Integrated confocal and scanning probe microscopy for biomedical research. *TheScientificWorld-JOURNAL*, 6, 2006.
- [4] Kristina Haase and Andrew E Pelling. Investigating cell mechanics with atomic force microscopy. *Journal of The Royal Society Interface*, 12(104): 20140970, 2015.
- [5] Petra S Dittrich. Research highlights. *The Royal Society of Chemistry. Lab Chip*, 10:541–543, 2010. <https://doi.org/10.1039/C000521P>.
- [6] S Durán, Sergi Novo, M Duch, R Gómez-Martínez, M Fernández-Regúlez, A San Paulo, C Nogués, J Esteve, E Ibañez, and JA Plaza. Silicon-nanowire based attachment of silicon chips for mouse embryo labelling. *Lab on a Chip*, 15(6):1508–1514, 2015.
- [7] Andreas Schmid, Hendrik Kortmann, Petra S Dittrich, and Lars M Blank. Chemical and biological single cell analysis. *Current opinion in biotechnology*, 21(1):12–20, 2010.
- [8] Elisabet Fernandez-Rosas, Rodrigo Gomez, Elena Ibanez, Leonardo Barrios, Marta Duch, Jaume Esteve, Carme Nogués, and José Antonio Plaza. Intracellular polysilicon barcodes for cell tracking. *Small*, 5(21): 2433–2439, 2009.
- [9] Rodrigo Gómez-Martínez, Patricia Vázquez, Marta Duch, Alejandro Muriano, Daniel Pinacho, Nuria Sanvicens, Francisco Sánchez-Baeza, Patricia Boya, Enrique J de la Rosa, Jaume Esteve, et al. Intracellular silicon chips in living cells. *Small*, 6(4):499–502, 2010.
- [10] Jürgen Drews. Drug discovery: a historical perspective. *Science*, 287 (5460):1960–1964, 2000.
- [11] Pere Roca-Cusachs, Vito Conte, and Xavier Trepap. Quantifying forces in cell biology. *Nature cell biology*, 19(7):742–751, 2017.
- [12] Marita L Rodriguez, Patrick J McGarry, and Nathan J Sniadecki. Review on cell mechanics: experimental and modeling approaches. *Applied Mechanics Reviews*, 65(6), 2013.
- [13] Daniel A Fletcher and R Dyche Mullins. Cell mechanics and the cytoskeleton. *Nature*, 463(7280):485–492, 2010.

- [14] Jochen Guck. Some thoughts on the future of cell mechanics. *Biophysical Reviews*, 11(5):667–670, 2019.
- [15] CT Lim, EH Zhou, and ST Quek. Mechanical models for living cells—a review. *Journal of biomechanics*, 39(2):195–216, 2006.
- [16] Charlotte Alibert, Bruno Goud, and Jean-Baptiste Manneville. Are cancer cells really softer than normal cells? *Biology of the Cell*, 109(5):167–189, 2017.
- [17] Emad Moeendarbary and Andrew R Harris. Cell mechanics: principles, practices, and prospects. *Wiley Interdisciplinary Reviews: Systems Biology and Medicine*, 6(5):371–388, 2014.
- [18] Cornelia Hahn and Martin A Schwartz. Mechanotransduction in vascular physiology and atherogenesis. *Nature reviews Molecular cell biology*, 10(1):53–62, 2009.
- [19] Sarah E Cross, Yu-Sheng Jin, Jianyu Rao, and James K Gimzewski. Nanomechanical analysis of cells from cancer patients. *Nature nanotechnology*, 2(12):780–783, 2007.
- [20] Martin Chalfie. Neurosensory mechanotransduction. *Nature reviews Molecular cell biology*, 10(1):44–52, 2009.
- [21] Mustafa Unal, Yunus Alapan, Hao Jia, Adrienn G Varga, Keith Angelino, Mahmut Aslan, Ismail Sayin, Chanjuan Han, Yanxia Jiang, Zhehao Zhang, et al. Micro and nano-scale technologies for cell mechanics. *Nanobiomedicine*, 1(Godište 2014):1–5, 2014.
- [22] Rodrigo Gómez-Martínez, Alberto M Hernández-Pinto, Marta Duch, Patricia Vázquez, Kirill Zinoviev, J Enrique, Jaume Esteve, Teresa Suárez, and José A Plaza. Silicon chips detect intracellular pressure changes in living cells. *Nature nanotechnology*, 8(7):517, 2013.
- [23] Huw Colin-York, Christian Eggeling, and Marco Fritzsche. Dissection of mechanical force in living cells by super-resolved traction force microscopy. *Nature protocols*, 12(4):783–796, 2017.
- [24] Martin Bergert, Tobias Lendenmann, Manuel Zündel, Alexander E Ehret, Daniele Panozzo, Patrizia Richner, David K Kim, Stephan JP Kress, David J Norris, Olga Sorkine-Hornung, et al. Confocal reference free traction force microscopy. *Nature communications*, 7(1):1–10, 2016.
- [25] Manuel Zündel, Alexander E Ehret, and Edoardo Mazza. Factors influencing the determination of cell traction forces. *PLoS One*, 12(2):e0172927, 2017.
- [26] Sujin Lee, Juhee Hong, and Junghoon Lee. Cell motility regulation on a stepped micro pillar array device (smpad) with a discrete stiffness gradient. *Soft Matter*, 12(8):2325–2333, 2016.

- [27] Dedy Septiadi, Federica Crippa, Thomas Lee Moore, Barbara Rothen-Rutishauser, and Alke Petri-Fink. Nanoparticle–cell interaction: a cell mechanics perspective. *Advanced Materials*, 30(19):1704463, 2018.
- [28] Schanila Nawaz, Paula Sánchez, Kai Bodensiek, Sai Li, Mikael Simons, and Iwan AT Schaap. Cell visco-elasticity measured with afm and optical trapping at sub-micrometer deformations. *PloS one*, 7(9):e45297, 2012.
- [29] Kalpana Mandal, Atef Asnacios, Bruno Goud, and Jean-Baptiste Manneville. Mapping intracellular mechanics on micropatterned substrates. *Proceedings of the National Academy of Sciences*, 113(46):E7159–E7168, 2016.
- [30] Marie Versaevel, Maryam Riaz, Tobias Corne, Thomas Grevesse, Joséphine Lantoine, Danahe Mohammed, Céline Bruyère, Laura Alaimo, Winnok H De Vos, and Sylvain Gabriele. Probing cytoskeletal pre-stress and nuclear mechanics in endothelial cells with spatiotemporally controlled (de-) adhesion kinetics on micropatterned substrates. *Cell adhesion & migration*, 11(1):98–109, 2017.
- [31] Alfredo Celedon, Christopher M Hale, and Denis Wirtz. Magnetic manipulation of nanorods in the nucleus of living cells. *Biophysical journal*, 101(8):1880–1886, 2011.
- [32] John F Zimmerman, Graeme F Murray, Yucai Wang, John M Jumper, Jotham R Austin, and Bozhi Tian. Free-standing kinked silicon nanowires for probing inter-and intracellular force dynamics. *Nano letters*, 15(8):5492–5498, 2015.
- [33] Carlos Matellan and Armando E del Río Hernández. Where no hand has gone before: probing mechanobiology at the cellular level. *ACS Biomaterials Science & Engineering*, 5(8):3703–3719, 2018.
- [34] Jeroen Eyckmans, Thomas Boudou, Xiang Yu, and Christopher S Chen. A hitchhiker’s guide to mechanobiology. *Developmental cell*, 21(1):35–47, 2011.
- [35] Marco Montagner and Sirio Dupont. Mechanical forces as determinants of disseminated metastatic cell fate. *Cells*, 9(1):250, 2020.

Collaborations and Stays in Research Institutions

Due to the multi- and interdisciplinary nature of this thesis, we have collaborated with several partners from other fields of the scientific knowledge. In addition, I have made stays and visits in different research institutions to complete my education, but also to complete the research projects.

Collaborations

- The 3D: *Desarrollo, Diferenciación y Degeneración* Laboratory of Dr. Teresa Suárez, from the *Centro de Investigaciones Biológicas Margarita Salas (CIB, CSIC)*, Madrid, Spain.
- The Laboratory of Mammalian Molecular Embryology led by Dr. Prof. Tony Perry from the Department of Biology and Biochemistry, University of Bath, Bath, England.
- The group of Llüisa Pérez from the *Departament de Farmacologia, Toxicologia i Química Terapèutica* from the *Universitat de Barcelona*, Barcelona, Spain and from School of Pharmacy, University of Nottingham, Nottingham, UK.
- Dr. Rafael Pérez del Real, from the group of Nanomagnetism and Magnetization processes at the *Instituto de Ciencia de Materiales de Madrid (ICMM, CSIC)*, Madrid, Spain.
- Dr. Roberto Castilla López, from the group of Department of Fluid Mechanics at the *ESEIAAT-Universitat Politecnica de Catalunya*, Terrassa, Spain.
- The Micro and Nanomechanics group led by Dr. Jon M. Molina Aldareguia at the IMDEA Materials Institute, Madrid, Spain.

Stays in Research Institutions

- In the framework of my education as a doctoral research, I was a research stay student in the group 3D from the *CIB Margarita Salas (CSIC)* with Dr. Teresa Suárez. For two months, I could expand my knowledge in operation of a cellular biology laboratory in the basis of the appropriate manipulation of cellular cultures in their interaction with the micro- and nanotools developed during my thesis. I performed several experiments related to the field of cell mechanics behaviour related with the devices presented in Chapters 2 and 5.

- I was visiting for two days with Dr. Miguel Monclús and Dr. Jon M. Molina-Aldareguia, who lead the Micro and Nanomechanics group at the *IMDEA Materials Institute*. They are specialists in the mechanical behaviour of advanced structural materials from the nanoscale to the macroscale. There, several experiments, to mechanically characterized the specimens introduced in Chapter 5, were carried out by an in situ nanoindentation equipment.

Scientific Contribution

Publications

1. María Isabel Arjona, Consuelo González-Machón, Sara Durán, Marta Duch, Rafael Pérez del Real, Abhinav Kadambi, Juan Pablo Agusil, Mariano Redondo, Llúisa Pérez, Elvira Gómez, Teresa Suárez & José Antonio Plaza. *Technology development for on-barcode integrating magnetic capabilities to intracellular chips*. **Submitted to: *Smart Materials and Structures***.
2. Marta Duch, Núria Torras, Maki Asami, Toru Suzuki, María Isabel Arjona, Rodrigo Gómez-Martínez, Matthew D. VerMilyea, Robert Castilla, José Antonio Plaza & Perry, Anthony CF. *Tracking intracellular forces and mechanical property changes in mouse one-cell embryo development*. **Nature Materials**, 1-10, 2020. <https://doi.org/10.1038/s41563-020-0685-9>. *Impact factor: 38.663*.

In Preparation Publications

1. From the results obtained within the investigation to improve the detection limit of an intracellular pressure sensor presented along Chapter 3, we expect to submit an article to a high impact journal in the following months about *High sensitive suspended intracellular pressure sensors with a reference cavity*.
2. From the results obtained with the star-shaped device presented at the end of Chapter 4, we expect to submit an article to a high impact journal in the following months about *Star-shaped intracellular chips for cell force tracking*.
3. From the results obtained on Chapter 5, we expect to submit an article to a high impact journal in the following months about *Anchored silicon chips for cell traction force determination*.

Publications out of the scope of the thesis

1. Juan Pablo Agusil, María Isabel Arjona, Marta Duch, Naüm Fustè & José Antonio Plaza. *Multidimensional Anisotropic Architectures on Polymeric Microparticles*. **Small**, 16(46), 2004691, 2020. <https://doi.org/10.1002/sml1.202004691>. *Impact factor: 11.459*.

Conferences

1. María Isabel Arjona, Ana Sánchez, Marta Duch, Rodrigo Gómez-Martínez, Teresa Suárez & José Antonio Plaza. *Suspended intracellular pressure sensor with a reference cavity*. 45th International Conference on Micro & Nano Engineering. MNE2019. Rhodes, Greece. September, 23rd-26th, 2019. *Oral contribution*.
2. María Isabel Arjona, Juan Pablo Aguil, Ana Sánchez, Marta Duch & José Antonio Plaza. *Electron Beam Lithography Patterning for a Cell Traction Force Microscope*. 11th Ibero-American Congress on Sensors. Barcelona, España. September, 17th-18th, 2018. *Poster presentation*.
3. María Isabel Arjona, Juan Pablo Aguil, Ana Sánchez, Marta Duch & José Antonio Plaza. *Electron Beam Lithography Patterning for a Cell Traction Force Microscope*. 3rd Scientific Meeting of BCN-b Students JPhD2017. Cerdanyola del Vallès, Barcelona, España. November, 7th-8th, 2017. *Oral contribution*.

Projects

1. **Title:** Nanoelectromechanical Systems for Intracellular Measurements (INTRANENS).
Financial Entity: Swiss National Science Foundation (SNSF), Synergia.
Funded Entity: Instituto de Microelectrónica de Barcelona-Centro Nacional de Microelectrónica (CSIC). Barcelona, Cataluña, España.
Principal Research: Prof. José Antonio Plaza Plaza.
Time: March 2020 - March 2024.
Total Amount: 950.000 €
2. **Title:** Micro y Nanoherramientas Avanzadas en Suspensión para Aplicaciones Intra y Extracelulares (MINAHE 6).
Financial Entity: Ministerio de Economía y Competitividad.
Funded Entity: Instituto de Microelectrónica de Barcelona-Centro Nacional de Microelectrónica (CSIC). Barcelona, Cataluña, España.
Principal Research: Prof. José Antonio Plaza Plaza.
Time: January 2018 - December 2020.
Total Amount: 267.168 €
3. **Title:** Suspensions of MicroNanoTools for applications in living cells (MINAHE 5).
Financial Entity: Ministerio de Economía y Competitividad.
Funded Entity: Instituto de Microelectrónica de Barcelona-Centro Nacional de Microelectrónica (CSIC). Barcelona, Cataluña, España.
Principal Research: Prof. José Antonio Plaza Plaza.
Time: January 2015 - December 2017.
Total Amount: 257.730 €

Scientific Dissemination

Transferring the results obtained in scientific research to the general public is a responsibility that researchers have with the society. Hence, during the development of this thesis, I have participated to this commitment with the following activities or contributions in the media:

- **Event:** Participation with a video of scientific dissemination in the contest: *Yo investigo. Yo soy CSIC. II Edition, 2020*
link: <https://www.youtube.com/watch?v=REXbWX112aM>.
- **Event:** Interview for media news about a scientific publication
link: <https://canal.ugr.es/noticia/cientificos-espanoles-fabrican-chips-que-son-inyectados-en-ovulos-para-medir-las-primeras-fases-del-desarrollo-embrionario/>
- **Event:** Talk in the frame of *Jornada de la Mujer y la Niña en la Ciencia*.
Audience: High School students (Institut Lluís Vives, Barcelona, España).
Title: Mi carrera científica.
Date: 11/02/2020
Duration: 1 h
- **Event:** Imparted seminar.
Audience: 4th course students of the bachelor's degree in Nanoscience and Nanotechnology (Universitat Autònoma de Barcelona).
Title: Aplicación de las micro- y nanotecnologías al campo de la biología.
Date: 17/12/2018
Duration: 1 h
- **Event:** Imparted seminar.
Audience: 4th course students of the bachelor's degree in Nanoscience and Nanotechnology (Universitat Autònoma de Barcelona).
Title: Aplicación de las micro- y nanotecnologías al campo de la biología.
Date: 16/12/2016
Duration: 1 h